MULTI-OBJECTIVE MODEL PREDICTIVE CONTROL OF GRID-TIED SOLAR PHOTOVOLTAIC SYSTEM

Submitted in partial fulfilment of requirement
for the award of the degree of

Doctor of Philosophy

By
Bonala Anil Kumar
(Roll No.: 701406)

Under the supervision of
Dr. S. Srinivasa Rao
Professor

DEPARTMENT OF ELECTRICAL ENGINEERING
NATIONAL INSTITUTE OF TECHNOLOGY
(An Institution of National Importance)
WARANGAL, Telangana State, India – 506004
DECEMBER - 2019

Approval Sheet

This Thesis entitled "**Multi-Objective Model Predictive Control of Grid-Tied Solar Photovoltaic System**" by **Bonala Anil Kumar, Roll No.: 701406** is approved for the degree of Doctor of Philosophy

Examiners

_____

_____

Supervisor

Dr. S. Srinivasa Rao
Professor

Chairman

Dr. S. Srinivasa Rao
Professor & Head
Department of Electrical Engineering
NIT Warangal

Date: _____

DEPARTMENT OF ELECTRICAL ENGINEERING
NATIONAL INSTITUTE OF TECHNOLOGY
(An Institution of National Importance)
WARANGAL, Telangana State, India – 506004

Certificate

This is to certify that the thesis entitled **"Multi-Objective Model Predictive Control of Grid-Tied Solar Photovoltaic System**", submitted by **Bonala Anil Kumar,** Roll No.: 701406, to the Department of Electrical Engineering, National Institute of Technology, Warangal in partial fulfilment of the requirements for the award of the degree of **Doctor of Philosophy** in Electrical Engineering is a record of bonafide research work carried out by him under my supervision and guidance. The contents of this thesis, in full or in parts have not been submitted simultaneously to any other institute or university for the award of any degree or diploma.

Station :
Date :

Dr. S. Srinivasa Rao
(Thesis Supervisor)
Professor
Department of Electrical Engineering.
NIT Warangal – 506004.

Declaration

This is to certify that the work presented in the thesis entitled "**Multi-Objective Model Predictive Control of Grid-Tied Solar Photovoltaic System"** is a bonafide work done by me under the supervision of **Dr. S. Srinivasa Rao,** Professor, Department of Electrical Engineering, National Institute of Technology, Warangal, India and was not submitted elsewhere for the award of any degree.

I declare that this written submission represents my ideas in my own words and where others ideas or words have been included, I have adequately cited and referenced the original sources. I also declare that I have adhered to all principles of academic honesty and integrity and have not misrepresented or fabricated or falsified any idea/data/fact/source in my submission. I understand that any violation of the above will be a cause for disciplinary action by the institute and can also evoke penal action from the sources which have thus not been properly cited or from whom proper permission has not been taken when needed.

Bonala Anil Kumar

(Roll No: 701406)

Date:

Place: NIT Warangal

Acknowledgements

First and foremost, I would like to express my deep sense of gratitude to my thesis supervisor **Dr. S. Srinivasa Rao**, Professor in the Department of Electrical Engineering for his continuous monitoring, moral support, patience, encouragement and timely inputs throughout my research work. His commitment towards research work is always been a source of inspiration for rest of my life.

I would like to extend my gratitude to my Doctoral Scrutiny Committee members **Dr. B. K Murthy**, Professor, Department of Electrical Engineering, **Dr. N. Bheema Rao**, Professor & Head, Department of Electronics & Communication Engineering and **Dr. A. Kirubakaran** Associate Professor Department of Electrical Engineering for their continuous monitoring, keen interest, insightful comments and encouragement.

My Sincere thanks to **Prof. N.V. Ramana Rao**, Director NIT Warangal for providing all the necessary facilities to carry out my research work.

My special thanks to **Dr. V.T. Somasekhar,** Professor, Department of Electrical Engineering for his support, encouragement and valuable suggestions during various stages of research work progress presentations as a Chairman of Doctoral Scrutiny Committee.

I thank all the faculty members in the Department of Electrical Engineering for their support, encouragement and valuable suggestions during various stages of my work.

I thank all the supporting staff in the Department of Electrical Engineering for their help, support and co-operation during my research work in the laboratory.

I thank **Dr. M. Vishnu Prasad, Dr. Y. Hareesh Kumar, Dr. B. Durga Hari Kiran** and **Mr. Y Bhaskar S S Gupta** for their constant support throughout this work and also I would like to thank all my fellow scholars from Department of Electrical Engineering who are always ready to share their ideas and extend their support.

I would like to thank all the members who are directly or indirectly involved and supported me in successful completion of this work.

Last but not the least; I would like to thank my parents, **Balaiah** and **Vimala**, my sister **Malleshwari** and my brother-in-law **Dr. Ch. Praveen Kumar** for their understanding, support and patience which has helped me in the successful completion of work.

Bonala Anil Kumar

List of Figures

List of Tables

List of Symbols

ξ	Objective function
i_α^*, i_β^*	Reference currents in stationary reference frame
i_α^p, i_β^p	Predicted currents in stationary reference frame
v_{dc1}, v_{dc2}	DC-link capacitor voltages
v_{cm}	Common mode voltage
S_d	Number of switching transitions
$k+1$	Next sampling period
λ_{dc}	Weighting factor for DC-link capacitor voltage balancing
λ_{cm}	Weighting factor for common mode voltage
λ_{sfw}	Weighting factor for switching frequency
P^*, Q^*	Reference active reactive powers
P, Q	Active reactive powers
i_{sn}	Source nominal current
V_{dcn}	DC-link capacitor nominal voltage
ε	Objective error
$G_x, \overline{G}_x$	Switching devices of NPC phase leg
P, N, O	Device switching states
$\vec{v}$	NPC inverter output voltage vector
v_{ia}, v_{ib}, v_{ic}	NPC inverter phase voltages
v_{iao}, v_{ibo}, v_{ico}	NPC inverter pole voltages
C_1,C_2	NPC inverter DC-link capacitors
V_{dc}	NPC inverter DC-link voltage
V_n	NPC inverter neutral point voltage
i_{c1}, i_{c2}	NPC inverter capacitors currents
i_o	NPC inverter midpoint DC-link current
r_{c1}, r_{c2}	Equivalent series resistance of NPC inverter capacitors
T_s	Sampling time
L_f	Filter inductance
R_f	Filter resistance

v_g	Grid voltage
i_g	Grid current
S_{opt}	Optimal switching state
i_{pv}	PV array current
v_{pv}	PV array voltage
i_{pvg}	Light generated current
i_0	Saturation current
i_{0n}	Nominal saturation current
i_{pvn}	PV array nominal current
i_{scn}	Short circuit current
V_{pv}	PV output voltage
T	PV cell temperature
T_n	Reference temperature
G	Solar irradiance
G_n	Reference irradiance
E_g	Band gap energy
q	Electron charge
k	Boltzmann's constant
K_i	Short circuit temperature coefficient
a	Diode ideality constant
V_{ocn}	Open circuit voltage
R_s	PV cell series resistance
R_p	PV cell parallel resistance
m_{mi}	Maximum modulation index
C_{eff}	Effective capacitance across DC-link
K_{RHP}	Safety factor
K_i	Cloud enhancement factor
V_{pv_min}	Minimum cut-in voltage of PV array
ω_C	Crossover frequency of outer DC-link voltage control loop
ω_{grid}	Fundamental frequency of grid
K_{grid}	Grid frequency gain

K_S	Coefficient that determines share of converter rating
S_{rated}	Converter rated power
T_{trans}	Transition period
Δi_{rp}	Desired maximum current ripple
f_{sm}	Maximum switching frequency
a	Scaling/overloading factor
T_c	Integral time constant
$T_{i\sigma}$	Equivalent time constant of inner power loop
k_p	Proportional gain
γ	Phase margin
$v_{g\alpha}^{+}, v_{g\beta}^{+}$	Fundamental positive sequence voltages
ϕ	Position of the reference voltage vector
n	Sector number
φ_{rc}	Critical power factor angle
I_m	Maximum current
C_v	Control variable
X_{ij}	Dataset
r_{ij}	Normalized dataset
$\mathrm{K_j}$	Linear correlation coefficient
σ_j	Contrast intensity
R_{jk}	Pearson's linear correlation coefficient
λ_j	Criterion weight
Pv_j	Preference variation value
$\overline{r}$	Mean of normalized value
φ	Deviation in preference value
I	Preference selective index

List of Abbreviations

AC	Alternating Current
ANN	Artificial Neural Network
CCS-MPC	Continuous Control Set Model Predictive Control
CHB	Cascaded H-Bridge
CMPC	Centralized Model Predictive Control
CMV	Common Mode Voltage
CRITIC	Criteria Importance through Inter-Criteria Correlation
DC	Direct Current
DMC	Direct Matrix Converter
DSP	Digital Signal Processor
DSO	Digital Storage Oscilloscope
DWMPC	Dynamic Weighted Model Predictive Control
ESR	Equivalent Series Resistance
FC	Flying Capacitor
FCS-MPC	Finite Control Set Model Predictive Control
FLC	Fuzzy Logic Controller
FMCDM	Fuzzy Multi-Criteria Decision Making
GRA	Grey Relational Analysis
HF	High Frequency
IEA-PVPS	International Energy Agency-Photovoltaic Power System
IGBT	Insulated Gate Bipolar Transistor
LUT-DPC	Lookup Table Direct Power Control
MCDM	Multi-Criteria Decision Making
MLP	Multilayer Perceptron
MPC	Model Predictive Control
MPCC	Model Predictive Current Control
MPDPC	Model Predictive Direct Power Control
MPPT	Maximum Power Point Tracking
MOSFET	Metal Oxide Semiconductor Field Effect Transistor
NDO	Nonlinear Disturbance Observer

NMPC	Nonlinear Model Predictive Control
NNPC	Nested Neutral Point Clamped
NPC	Neutral Point Clamped
PI	Proportional-Integral
PR	Proportional-Resonant
PSI	Preference Selective Index
PWM	Pulse Width Modulation
P&O	Perturb and Observe
SAW	Simple Additive Weighting
SMD	Standard Mean Deviation
SO	Symmetrical Optimum
SPV	Solar Photovoltaic
SPECS	Solar Photovoltaic Energy Conversion System
STATCOM	Static Synchronous Compensator
SVM	Space Vector Modulation
TOPSIS	Technique for Order of Preference by Similarity to Ideal Solution
VIKOR	VlseKriterijuska Optimizacija I Komoromisno Resenje
VOC	Voltage Oriented Control
VSI	Voltage Source Inverter
UPS	Uninterruptable Power Supply
WECS	Wind Energy Conversion System

Abstract

Over the last few years, the largest ever increasing installed capacity of solar photovoltaic (SPV) energy sources has attracted the attention of global electrical power generation market. The large penetration of grid-interactive SPV systems has enforced strict grid-codes to concern about the stable and secure operation of the existing grids. The stochastic behaviour and the strict grid-codes of SPV systems necessitate power electronic based energy conversion systems. Further, increase in the power levels of SPV systems enjoins the need for multi-level inverters and their control techniques. Multi-level inverters are well proven technology for efficient energy conversion in high power industrial applications. Neutral point clamped (NPC) topology is one of the most widely used and commercially accepted multi-level inverters of grid-tied SPV systems. Control schemes for these grid-tied NPC inverters are crucial for efficient energy conversion. The design and development of new control schemes for the grid-tied SPV inverters is an ongoing research topic.

The major control requirements of a general grid-tied inverter includes an ideal current/power tracking, fast dynamic response, better utilization of DC-link voltage, lower current THD, and lower switching losses. However, in addition to these the specific objectives of grid-tied three-level NPC (3L-NPC) PV inverters include maximum power extraction, DC-link capacitor voltage balancing and leakage current reduction etc. Several classical control schemes are available in the literature, out of which voltage oriented control (VOC) with space vector modulation (SVM) and direct power control (DPC) based on lookup-table (LUT) approach are the most widely used control schemes of the SPV system. However, due to the complexity in the design procedure for these control schemes to include multiple objectives of SPV system has motivated the investigation of advanced control schemes.

Finite control set model predictive control (FCS-MPC) is a class of predictive control approach which have emerged recently for the applications of power converters and energy conversion systems. FCS-MPC refers to a controller that explicitly uses the discrete-time model of the system to directly generate the switching state required for the converter defined with various constraints. The control variables required for the desired objectives are modeled in terms of the inverter switching states and the future behaviour of these variables are predicted by using the number of admissible switching states of the inverter. An

objective function is formulated by using these predicted values and corresponding reference value. A suitable control action for the inverter is selected by minimising the objective function. However, inclusion of diverse control parameters like inverter current/power, DC-link voltage, leakage current/common-mode voltage (CMV), and switching frequency into single objective function requires a suitable selection of weighting factors to maintain the relative importance between them. Usually, empirical method is used for the selection of weighting factors, which is a heuristic process and requires more number of simulation and experimental trials. This method becomes more complex and further time-consuming with the increase in number of control objectives. Selection of weighting factors is one of the challenging tasks in the design of FCS-MPC technique. Despite of multi-objective control capability, FCS-MPC still includes a classical proportional-integral (PI) controller for the DC-link voltage regulation of single-stage grid-tied SPV inverter. The outer DC-link voltage has to be regulated to its reference obtained from the MPPT algorithm to extract the maximum power from the PV array. This DC-link voltage control loop is in cascade with the inner predictive current/power control loop. Hence, the dynamics of this DC-link voltage controller influences the overall system performance.

In this research work, efforts are made to address these limitations by introducing simplified methods for weighting factor selection with a centralized model predictive control (CMPC) approach. A simple direct optimization method and two dynamic objective prioritisation approaches of MCDM methods are proposed to simplify the selection of weighting factors. The proposed techniques presented are: selective FS-MPC under direct optimisation, CRITIC and PSI based objective prioritisation approaches under MCDM methods. Further, CMPC with decoupled active-reactive power control is proposed for regulating the floating DC-link of single-stage grid-tied SPV inverter for eliminating the cascaded structure of the FCS-MPC. All the proposed techniques eliminate the heuristic offline selection of weighting factors. The simulation model for single-stage grid tied 3L-NPC PV inverter is developed by using MATLAB/Simulink to test both the classical and proposed control techniques under various operating conditions. The results are validated experimentally by using test setup developed in the laboratory. Based on the results obtained, it is observed that the proposed techniques offer an improved objective tracking and comparative dynamic response with respect to the classical approaches.

CONTENTS

Chapter-1
Introduction

1.1 Background

Increased demand for electrical energy and obligations on greenhouse gas emission has drawn the attention of renewable energy sources in the power sector. The steady gain in the prominence of renewable energy, especially the solar photovoltaic (SPV) energy source is playing an important role in the energy generation. According to the International Energy Agency – Photovoltaic Power System (IEA-PVPS), the global PV installed capacity has represented 403.3 GW of cumulative PV installations and an annual installed capacity close to 100 GW at the end of 2017 as shown in Fig.1.1. This largest ever increasing installed capacity of SPV energy source indicates its role in the modern power supply system's [1]. The major countries that have accounted for the highest cumulative & percentage annual installations at the end of 2017 are China with 53.1 GW with 54%, USA with 10.7 GW with 11%, and India with 9.1 GW with 9% as shown in Fig.1.2. The Cumulative installation of top five leading countries including Japan and European Union represented 88% of all installations recorded in 2017 and 90% in terms of installed capacity, with mostly utility-scale plants. Taking into account of the stochastic behaviour and the requirement of maintaining strict grid codes [2], power electronic based energy conversion systems and their control plays a vital role in the integration of photovoltaic energy source to the utility grid [3].

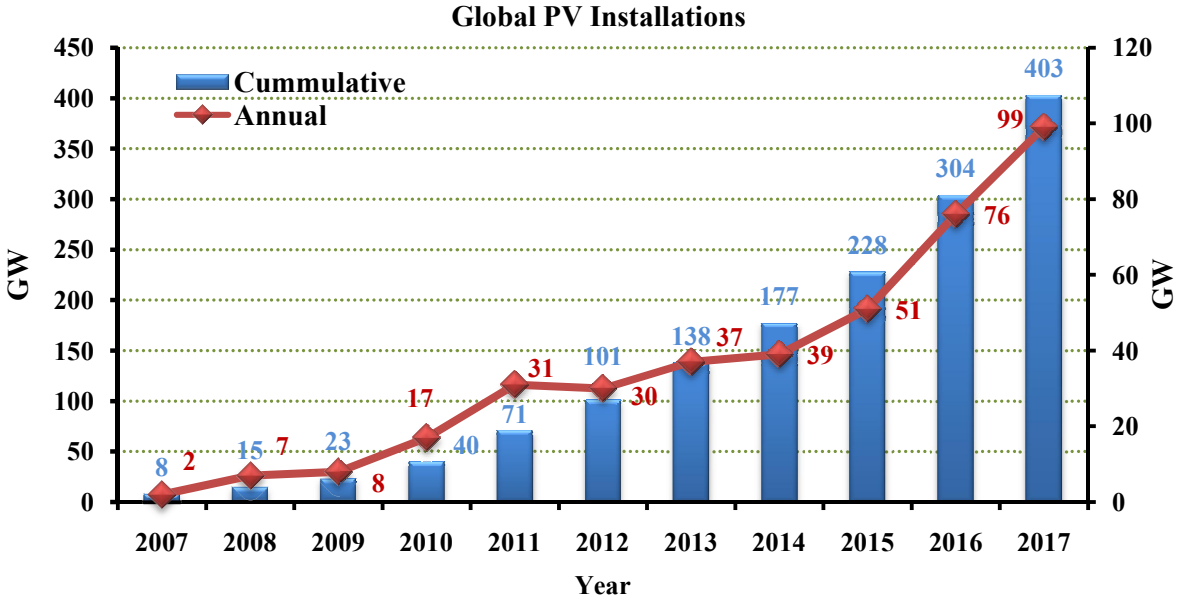

Fig.1.1. Global installed solar power from 2007 to 2017 [1].

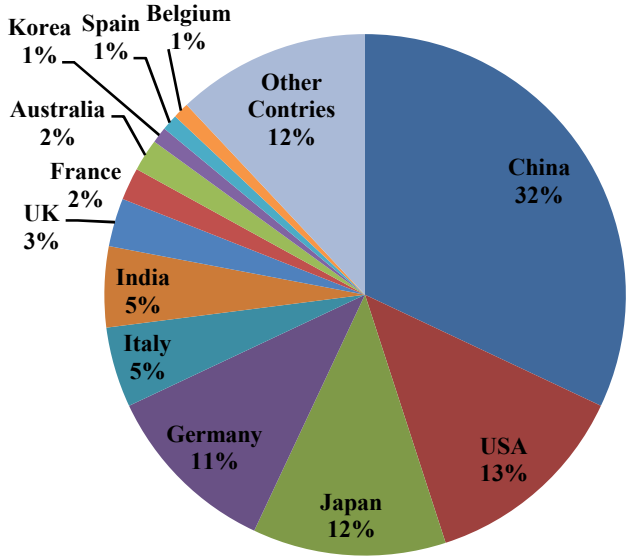

(a)

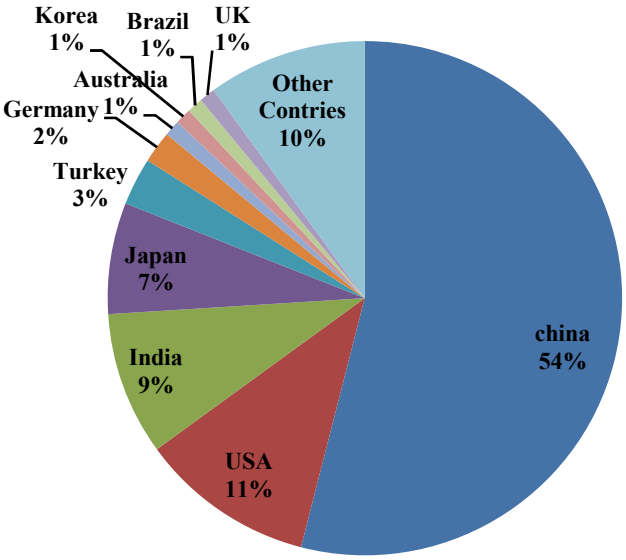

(b)

Fig.1.2. SPV Installation in Top 5 countries (a) cumulative (b) annual [1]

1.2 Solar Photovoltaic Energy Conversion Systems (SPECS)

A generic structure of a grid-tied SPV system has well defined stages as shown in Fig.1.3. Firstly, the system consists of a PV array which harvests the solar energy into an electrical energy. Second a DC–DC stage, which generally comprises of boost or buck-boost type of DC-DC converter topologies to boost the PV voltage and perform the MPPT for extracting

the maximum power. This stage can be further used to distribute the power conversion, control the DC side and also provide a galvanic isolation. This second stage can be omitted depending on the application and configuration of the PV array used for the system. In the third stage, a DC-AC inverter is used to interface the PV system to the grid directly or via a DC-DC stage. This DC-AC inverter used for interfacing the PV array is referred as PV inverter. Based on the number of stages incurred in interface, the PV inverters are broadly classified into (i) Single-Stage grid-tied PV inverter (ii) Two-stage grid-tied PV inverter. The typical structure of a single-stage and two-stage grid-tied PV inverter is shown in Fig.1.4. Despite of the configuration, the overall functionalities of grid-tied PV systems are given as

- Basic Functions
- PV Specific Functions
- Ancillary Services.

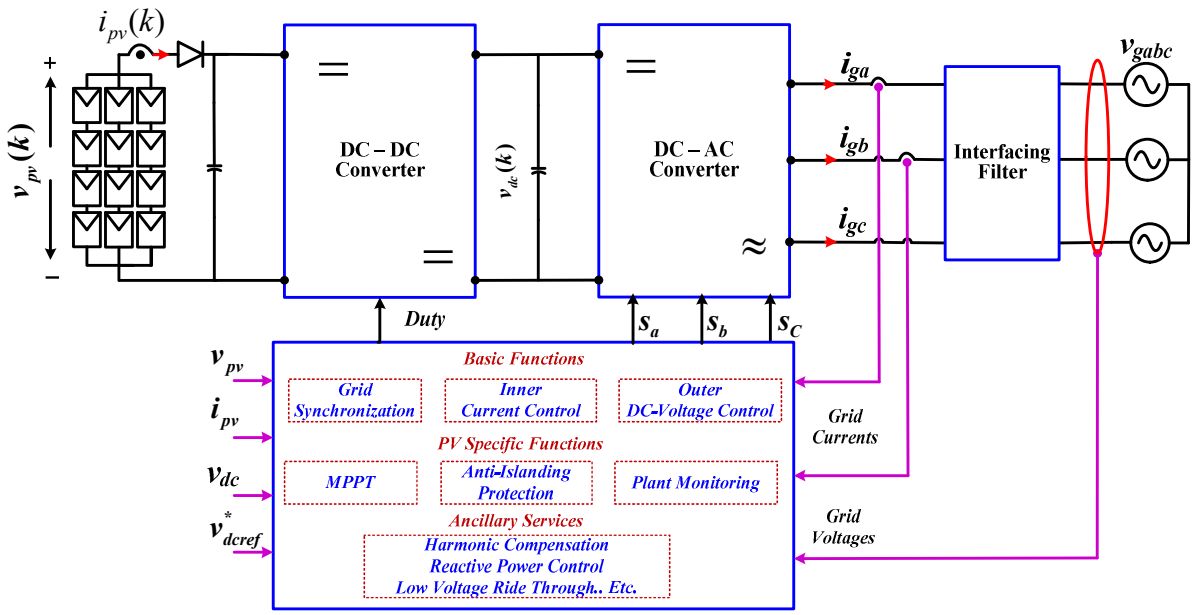

Fig.1.3. Generic structure of grid tied SPECS.

In general, the grid-tied PV inverters have a cascaded control structure which includes the outer DC-link voltage control and inner current/power control. In order to interface the PV inverter to the grid, the control algorithm requires a grid synchronization scheme. These functional requirements of PV inverters are classified under the basic functions of SPECS. The grid-tied PV inverter specific functionalities include plant monitoring system, protection for anti-islanding operation and maximum power extraction using MPPT algorithm. Further,

enhanced controllability of PV inverters can be achieved by providing the ancillary services.

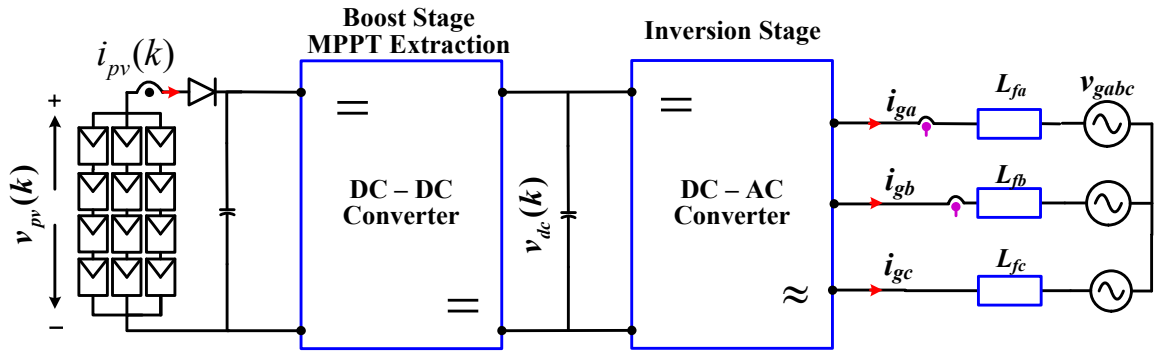

(a)

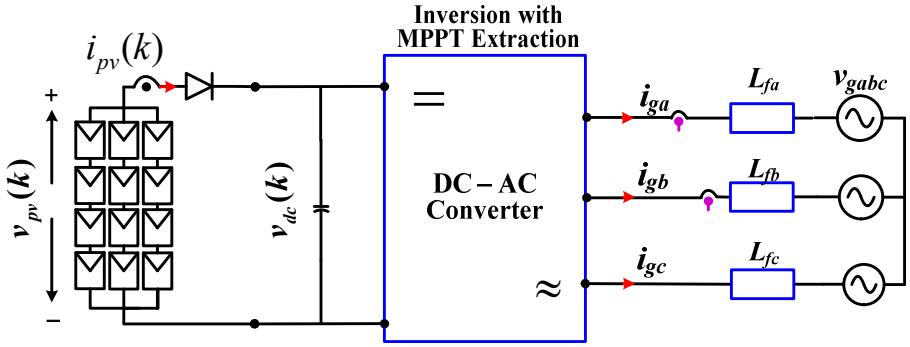

(b)

Fig.1.4. Grid-tied SPV inverters (a) two-stage (b) single-stage.

The grid-connected SPECS vary significantly in terms of size and installed power. They can be grouped into four different types of configurations: (i) centralized for three-phase large-scale plants (ii) string configuration for single-phase/three-phase small and medium-scale plants (iii) multi-string for single-phase/three-phase small to large-scale plants and (iv) AC-module for small-scale systems [4]–[7]. Simplified block diagram of these configurations are shown in Fig.1.5. Details of these configurations are given in the following subsections.

1.2.1 Centralized configuration

It is one of the most widely adopted configurations for large-scale PV plants. This configuration has a single three-phase inverter interfacing the PV plant to the grid. The PV modules are directly connected across the DC-link of the inverter; where, the required DC voltage is obtained by connecting the number of PV modules in series and enough number of parallel strings is connected to meet the required power. As there is only single power converter in this configuration, the power conversion efficiency is usually high. However, due

to the availability of single DC-link voltage the MPPT capability of this configuration is less compared to the distributed MPPT systems. The typical converter topologies used for this configurations are three-phase two-level voltage source inverter (VSI), three-phase three-level neutral point clamped (3L-NPC) inverter and three-phase three-level T-type (3L-T) inverter [5], [8]–[10]. The schematics of these converter topologies are shown in Fig.1.6.

1.2.2 String configuration

String configuration is a distributed architecture of centralized PV inverters with one inverter per string. Since a single PV string is interfaced to the grid, they are aimed at single-phase low power or three-phase medium power-scale grid systems. This configuration is popular for grid tied roof top PV system. Due to the availability of individual inverters, this configuration enables the independent MPPT extraction which minimizes the power loss due to power mismatch and partial shading. Hence, the modular structure of this configuration yields an increased total energy from the inverters. The typical converter topologies used for this configuration are H-bridge inverter with high frequency isolated and non-isolated DC-DC converter, H4 inverter, H5 inverter, H6 inverters and HERIC etc [6], [7], [11], [12]. Further, various multilevel inverters available in the market under this configuration are 3L-HNPC, 5L-HNPC and T-type inverters [6], [7], [11]–[13]. Simplified schematics of these converter topologies are shown in Fig.1.7 and Fig.1.8.

1.2.3 Multi-string configuration

Multi-string configuration is also a distributed architecture with peculiar two-stage (DC-DC stage + DC-AC stage) central configuration; where, the DC-DC converters are used to connect the PV system or string to a central inverter. Typically, the DC-DC converters used in this configuration are non-isolated simple boost converter or high-frequency (HF) isolated converters. Schematics of these converters are shown in Fig.1.9. The DC-DC converter stage decouples the PV system and the inverter with a DC link. As a result, a robust grid-tied converter control with extended operating voltage range can be achieved. This configuration includes the advantages of both the central and string configurations. Due to the modularity, the effects of partial shading and module power mismatch are mitigated in this configuration and yields high-energy with individual MPPT. This multi-string configuration can be adopted for a single/three-phase grid system ranging from small kW to medium-scale tens of kW [7],

[8], [14], [15].

1.2.4 AC-module configuration

The AC-module configuration is popularly known as module-integrated inverter or micro-inverter. In this configuration, a dedicated grid-tied inverter is used to interface the PV module to the grid. This configuration also includes a DC-DC boost stage to elevate the PV module voltage for grid interface. The most popular converter topologies used in this configuration are fly-back DC-DC converter with an H-bridge interfacing inverter [7], [8], [16], [17]. Schematics of the converters in this configuration are shown in Fig.1.10.

A summary on salient characteristics of these configurations are given in Table.1.1 and examples of commercially available inverters of each configuration are given in Table 1.2. Design and development of new converter topologies are aiming for increasing the energy conversion efficiency, higher power density, improved power quality, lower production cost, and minimized leakage current complying with strict grid code requirements. In regard to the latest developments, several converter topologies are available in the market for central, string, multi-string and AC-module PV applications. Out of these, multi-level converters topologies based on NPC, T-type and H-bridge type has gained the attention in both high power MV applications as well as low power residential applications with kW and LV range.

1.3 Overview on control requirements and techniques

1.3.1 Control requirements of 3L-NPC PV inverter

NPC inverters are widely adopted in the grid-tied PV systems. These inverters require special attention for the design and development of new control strategies to meet the inverter specific requirements, power quality standards and grid codes. In case of single-stage grid-tied PV inverter system, the maximum power extraction and the active-reactive power exchange will takes place simultaneously in single power conversion stage [18]–[21]. Hence, these objectives are considered as the main control objectives. Further, the DC-link capacitor voltage balancing, leakage current mitigation and switching frequency reduction are the additional control objective from the perspective of NPC topology and PV system requirements. However, the 3L-NPC inverter requires DC-link capacitor voltage balancing in concert with the active-reactive power exchange for proper operation, hence both the control

objective are considered as equally important. Whereas, the objectives like leakage current mitigation by reduction in common mode voltage, switching frequency minimization, selective harmonic elimination, maximum current limitation are considered as the secondary objectives. The control requirements of 3L-NPC PV inverter are summarised in Fig.1.11. In order to achieve these objectives several control strategies are presented in the literature [5], [22]–[24]. These strategies include the controller stage and modulator/gating signal generation stage in cascade to achieve most of the objectives. A summary of the well established & emerging controllers and gating signal generation techniques are shown in Fig.1.12.

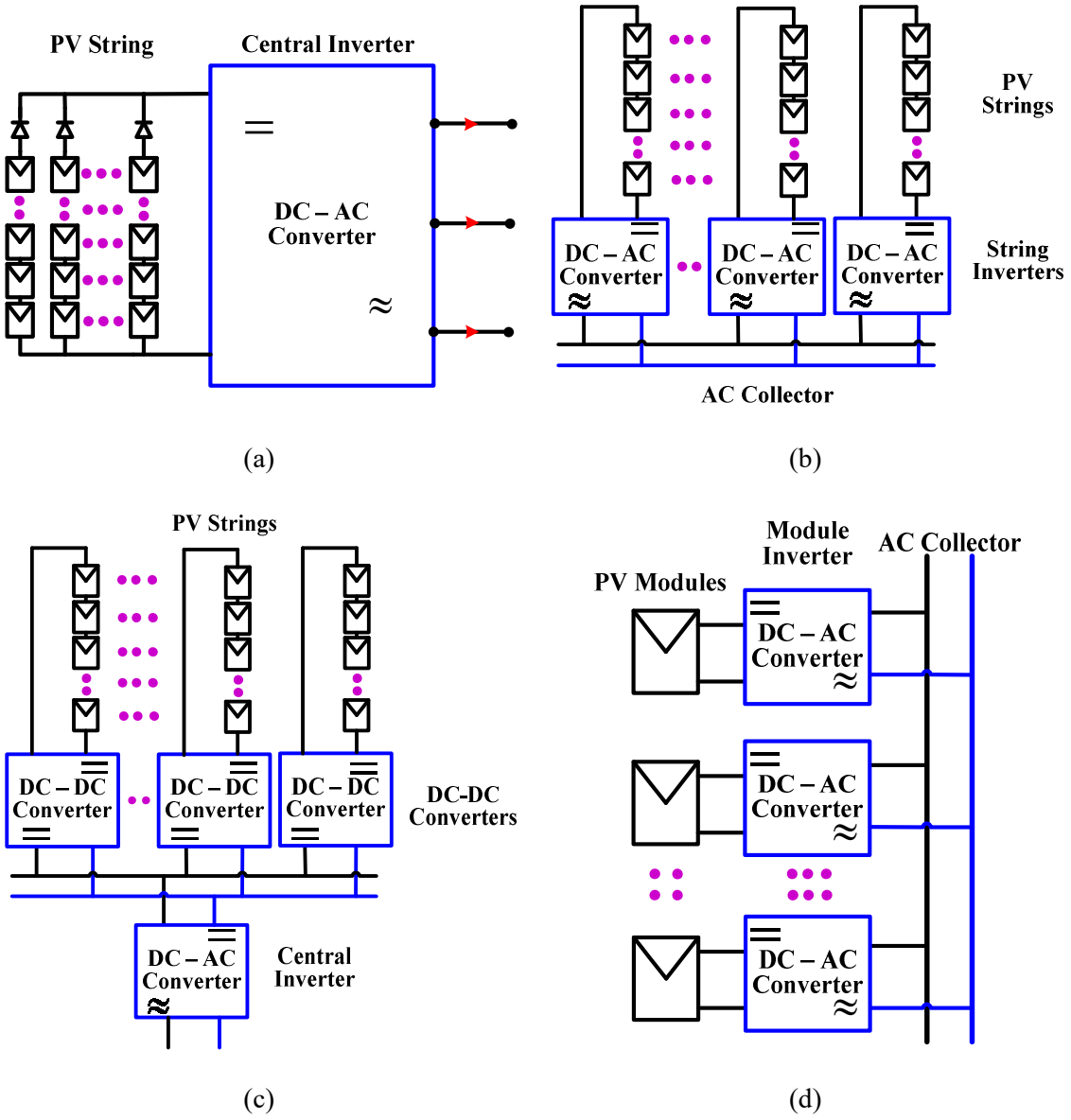

Fig.1.5. Configurations of grid tied SPECS (a) central configuration (b) string configuration (c) multi-string configuration (d) AC-module configuration

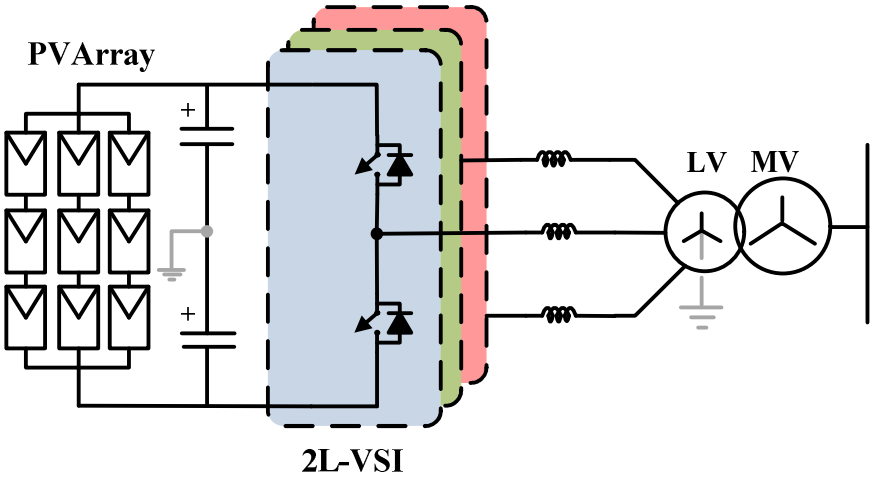

(a)

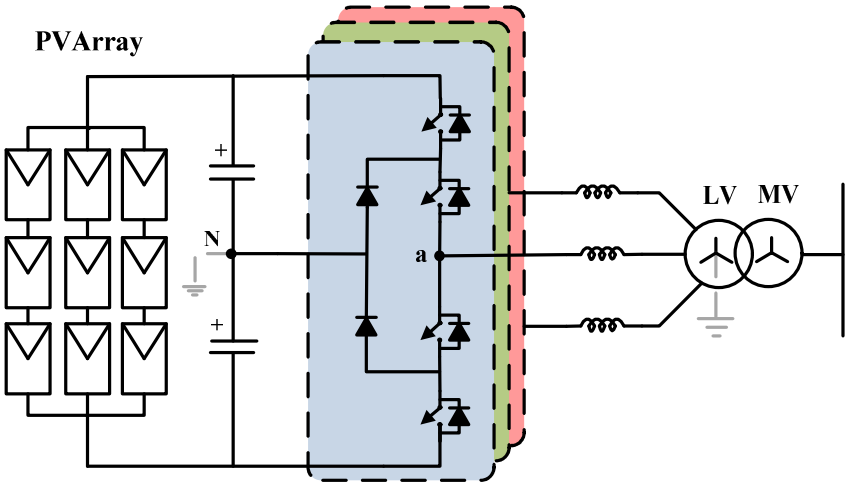

(b)

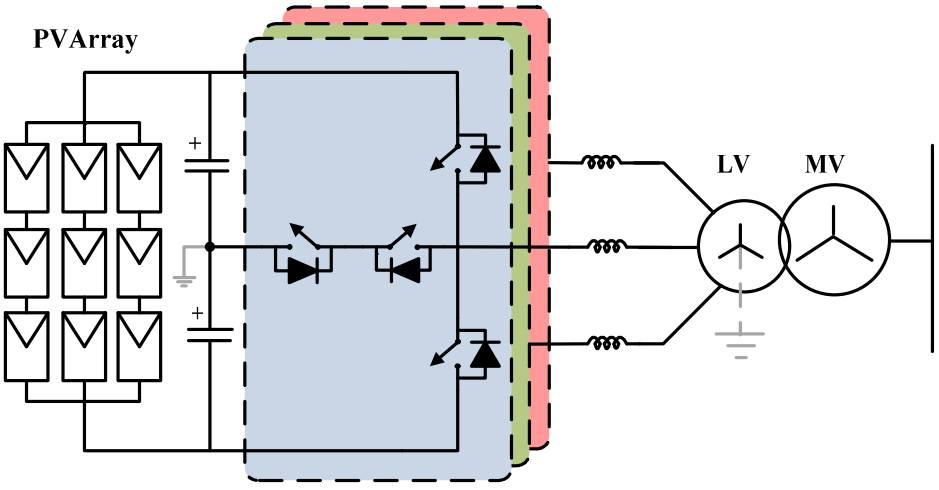

(c)

Fig.1.6. Converter topologies for centralized configuration (a) 2L-VSI (b) 3L-NPC (c) 3L-T type

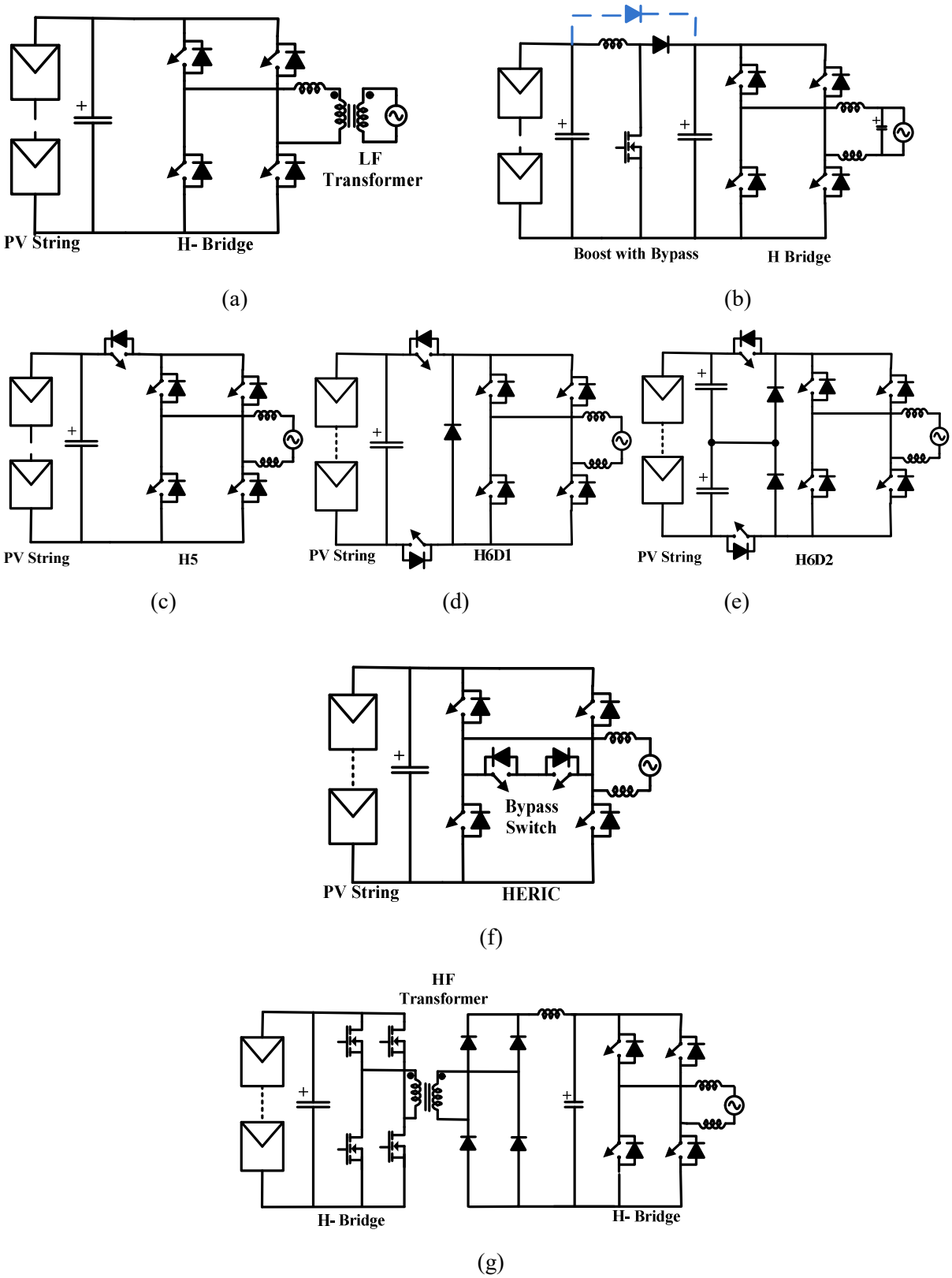

Fig.1.7. Converter topologies for string configuration (a) H-Bridge (b) H4 (c) H5 (d) H6D1 (e)H6D2 (f) HERIC (g) H-Bridge with HF isolation

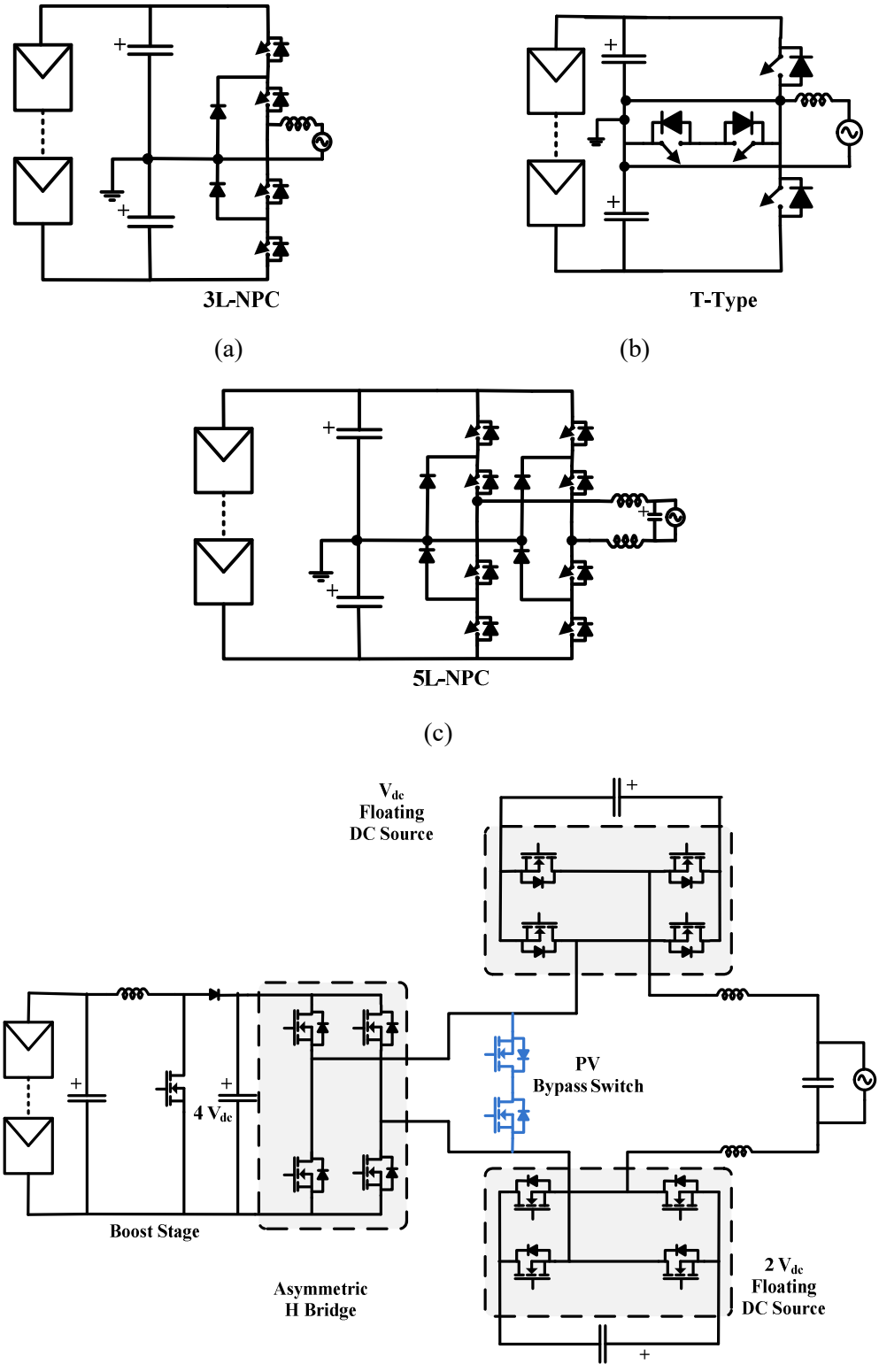

Fig.1.8. Converter topologies for string configuration (a) 3L-NPC (b) 3L-T type (c) 5L-NPC (d) asymmetric H-Bridge

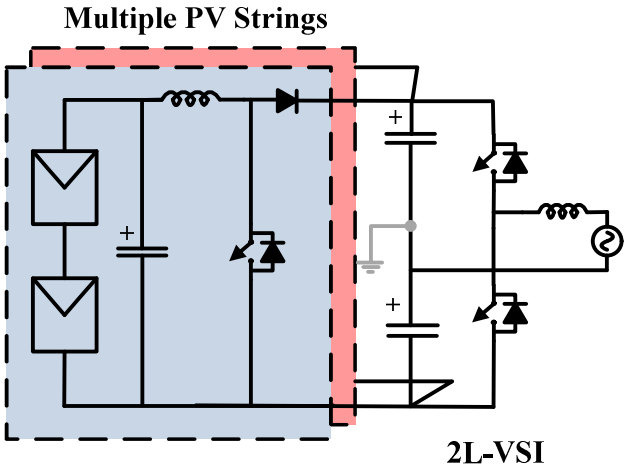

(a)

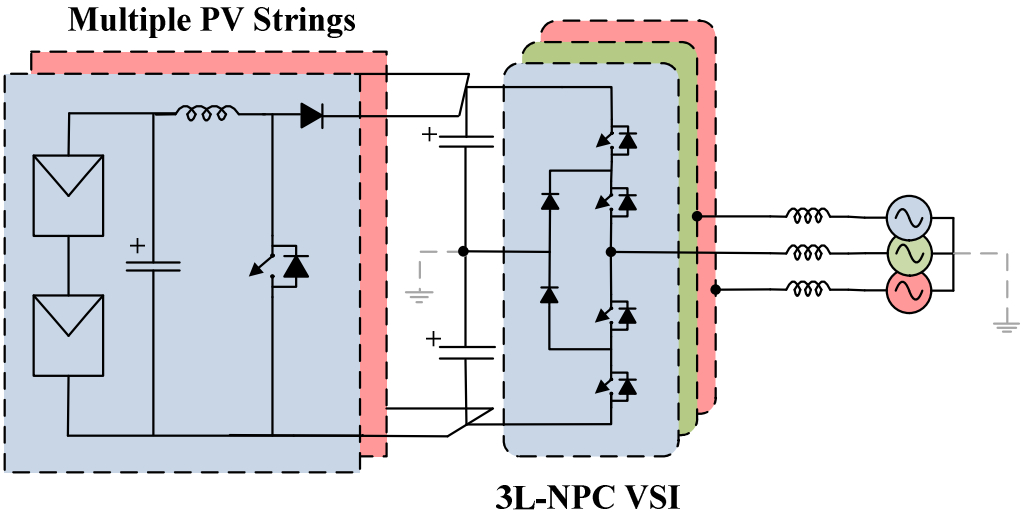

(b)

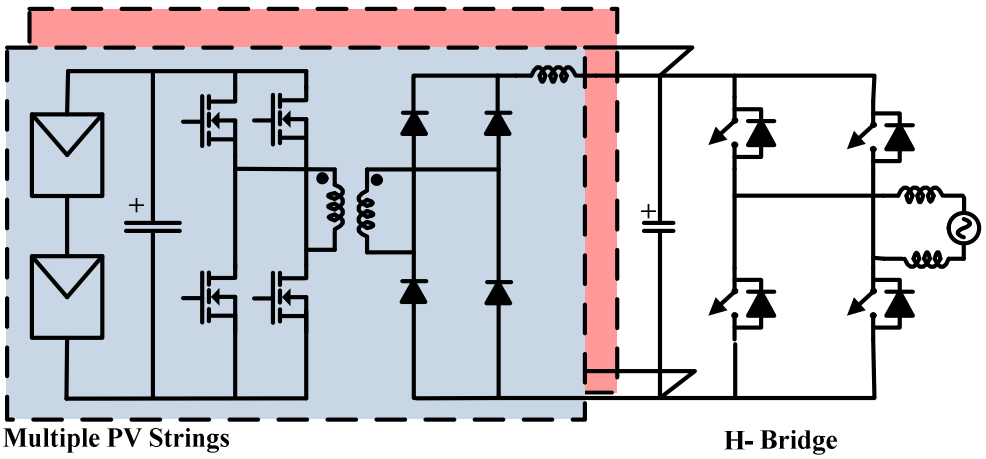

(c)

Fig.1.9. Converter topologies for multi-string configuration (a) 2L-VSI (b) 3L-NPC (c) H-Bridge with HF isolation

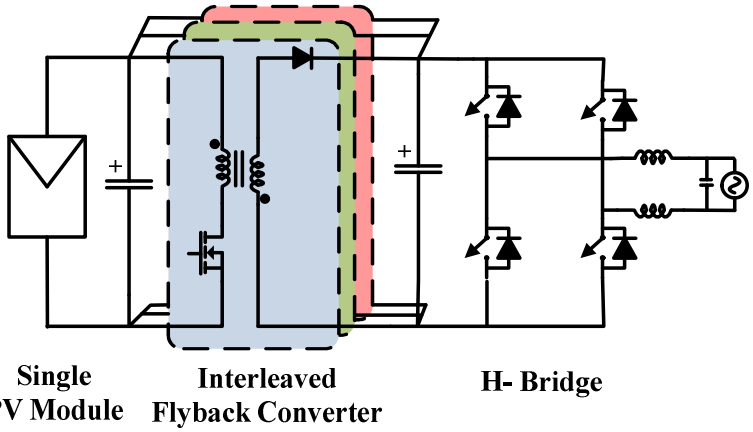

(a)

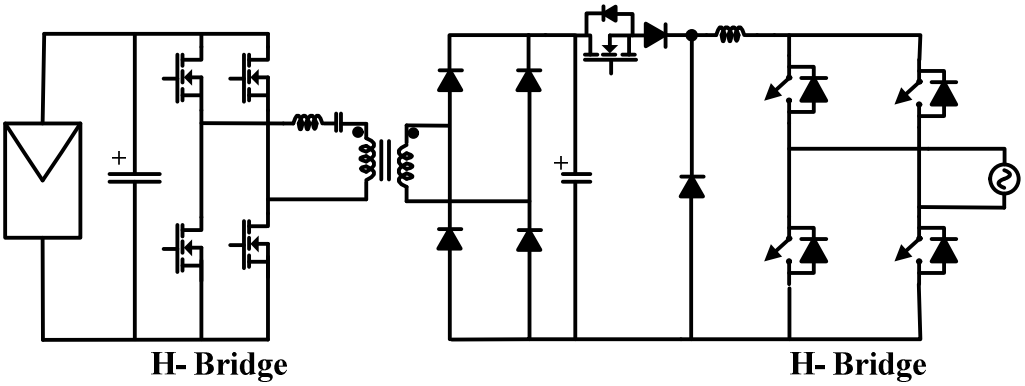

(b)

Fig.1.10. Converter topologies for AC-module configuration (a) 2L-VSI (b) 3L-NPC (c) H-Bridge with HF isolation

Table.1.1. Characteristics of grid-tied SPECS configurations

Configuration	Power range	Cost/Watt	Semiconductor Devices	Advantages	Disadvantages
Central inverter	<850kW (<1.6MW for Dual)	Low	IGBT	Simple design and control system	Reduced energy yield due to module power mismatch and effect of partial shading.
String inverter	<10 kW	Medium	MOSFET/ IGBT	Individual MPPT	High component counts, complex control issues.
Multi-string inverter	<500 kW	Medium/ Low	MOSFET/ IGBT	Individual MPPT, Simple design and control	Two-stage power conversion, and more number of components
AC-module inverter	<300 W	High	MOSFET	High Energy yield	More number of components and separate control for each module.

Table.1.2. Different commercially available PV inverter configurations

Make/Model	Input voltage	Power	Input current (max)	Efficiency (%)	Isolation	Independent MPPT
Central Inverters						
Satcon/EPP-1500-UL	550-850 V	1.5 MW	2820 A	98.5	Yes	Yes (2)
ABB/PVS800-MWS	525-825 V	1.25 MW	2480	97.8	Yes	Yes (2)
SMA/MVPP 1.6MW	570-820 V	1.6 MW	2800	98.6	Yes	Yes (2)
String Inverters						
Sunways/NT 5000	900 V	4.6 kW	15.4 A	97.8	No	Yes (2)
Danfoss/DLX 4.6	600 V	4.6 kW	23 A	97.3	Yes	Yes (3)
ABB/PVS 200 TL 8000	900 V	8 kW	34.8 A	97	No	Yes (4)
Multi-String Inverters						
SMA/SB 5000TL	750 V	5250 W	15 A	97	No	Yes (2)
Danfoss/TLX 15	700 V	15 kW	36 A	98	No	Yes (3)
SATCON/Solstice	600 V	100 kW	182 A	96.7	No	Yes (6)
AC-module inverters						
Power One Aurora/MICRO-0.3-I	60 V	300 W	10.5 A	96.5	Yes	1 per module
Siemens MIS	45 V	260 W	10.5 A	96.3	Yes	1 per module
Enecsys single micro inverter	44 V	240 W	12 A	95	Yes	1 per module

1.3.2 Overview on existing control techniques

A broad classification of controllers and gating signal generation techniques are shown in Fig.1.12 [25], [26]. The controllers are broadly classified into five major groups such as linear control, hysteresis control, sliding mode control, intelligent control and predictive control [27]–[63]. Similarly, gating signal generation techniques are classified into pulse width modulation (PWM), pseudo modulation and closed loop control with implicit modulator [25], [64]–[69]. Out of these, the classical linear control based on voltage orientation (Voltage Oriented Control – VOC) cascaded with space vector modulation (SVM) technique is widely employed for the SPV systems [29], [32], [38], [39], [42], [44], [58]. The VOC approach guarantee the dynamic and steady state performance via internal current control loops with

linear proportional-integral (PI)/ proportional-resonant (PR) controllers. Selection of these controller parameters for the desired stability criteria is difficult due to the complex design procedure. SVM technique is one of the efficient modulation techniques which offer higher DC-bus utilization, improved harmonic profile and lower losses compared to the general sinusoidal PWM (SPWM) technique [25]. However, to achieve the DC-link capacitor voltage balancing, and minimizing the common-mode voltage, SVM technique involves a complex design procedure [70]–[73].

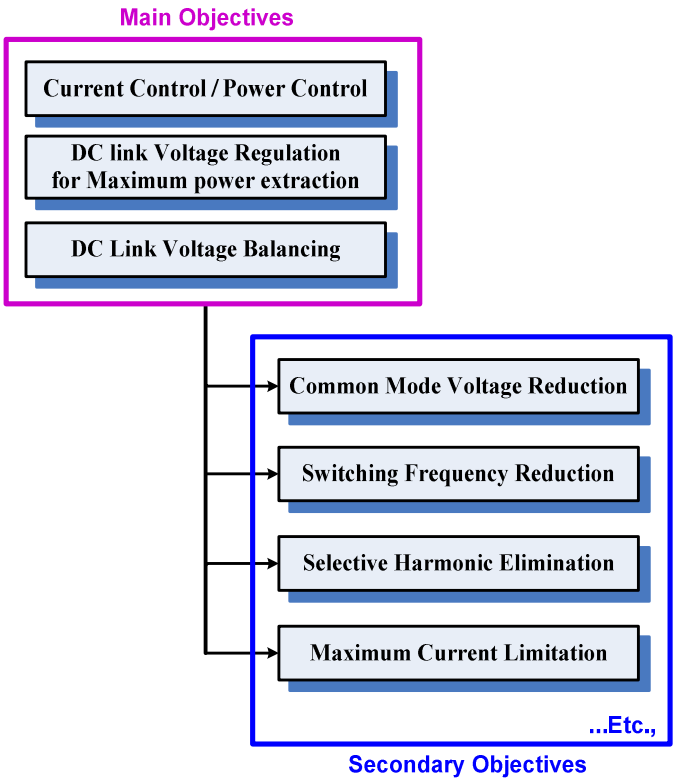

Fig.1.11. Summery of control requirements of 3L-NPC PV inverter

On the other side, a lookup table based direct power control (LUT-DPC) strategy has gained the attention of researchers due to the elimination of inner current/power control loop and pulse width modulator stage [74]–[76]. The LUT-DPC consists of a predefined switching table generated based on the behaviour of switching states to regulate the instantaneous errors between the reference and estimated active power, reactive power, and DC-link capacitor voltage deviation; with respect to the location of the output voltage vector in space vector plane. The switching state selected will regulate the active and reactive powers within the defined hysteresis error band. As the switching state selected directly influences the active

and reactive powers injected by the inverter in each sampling period, this method is called as direct power control. Design simplicity and fast dynamic response are the key features of LUT-DPC. However, DPC suffers from considerable power ripples indeed the distortion in injecting currents, variable switching frequency and inability to control additional control objectives like CMV reduction, switching frequency regulation etc. Several modifications and extensions for DPC were proposed to overcome these problems. In the recent past, model predictive control (MPC) techniques are introduced to grid-tied inverter applications to address various control aspects and to achieve precise control over the control parameters [77]–[80].

1.3.3 Model Predictive Control (MPC)

The concept of MPC refers to a controller that explicitly uses the model of the system to select an optimal control action. The receding horizon policy for MPC technique is shown in Fig.1.13. From this illustration, it can be observed that the input signal u_k at the beginning of the present sampling period k is obtained by predicting the future behaviour of the output y_k for a given range of prediction horizon $k+N_P$. Similarly, an input signal for the next sampling period is obtained by predicting the future behaviour of output for a prediction horizon of $k+N_P+1$. Hence, this policy is known as receding horizon policy [81].

The basic implementing structure for MPC is shown in Fig.1.14. A model of the system is used to predict the future behaviour of outputs based on the past and present values of both input and outputs. Based on the predicted outputs and corresponding reference trajectory, the future errors are obtained and will be given to the optimizer. Depending on the constraints and objectives given to the optimizer, future inputs for the system will be selected. In general, the input is referred as a control signal and output is considered as a control parameter in MPC techniques. The concept of MPC was introduced as an optimal control theory in the 1960s and by the end of 1970s, it was successfully implemented in industrial processes [82]. The slow dynamics and large sampling periods of the chemical process allow enough time for online optimization [83]. The first attempt to use the predictive control in power electronics was made in the early 1980 [84], [85]. This method was not popular at that time due to its high amount of calculations required in each sampling period. In the recent past, the inception of modern digital control platforms with high computational capabilities enabled the implementation of complex control techniques like MPC with more precision and ease.

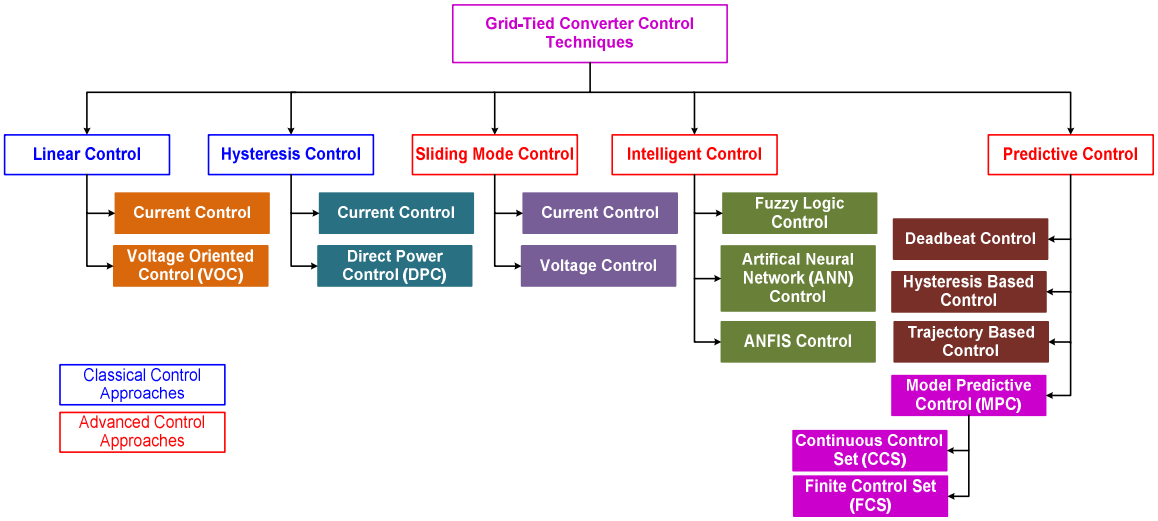

(a)

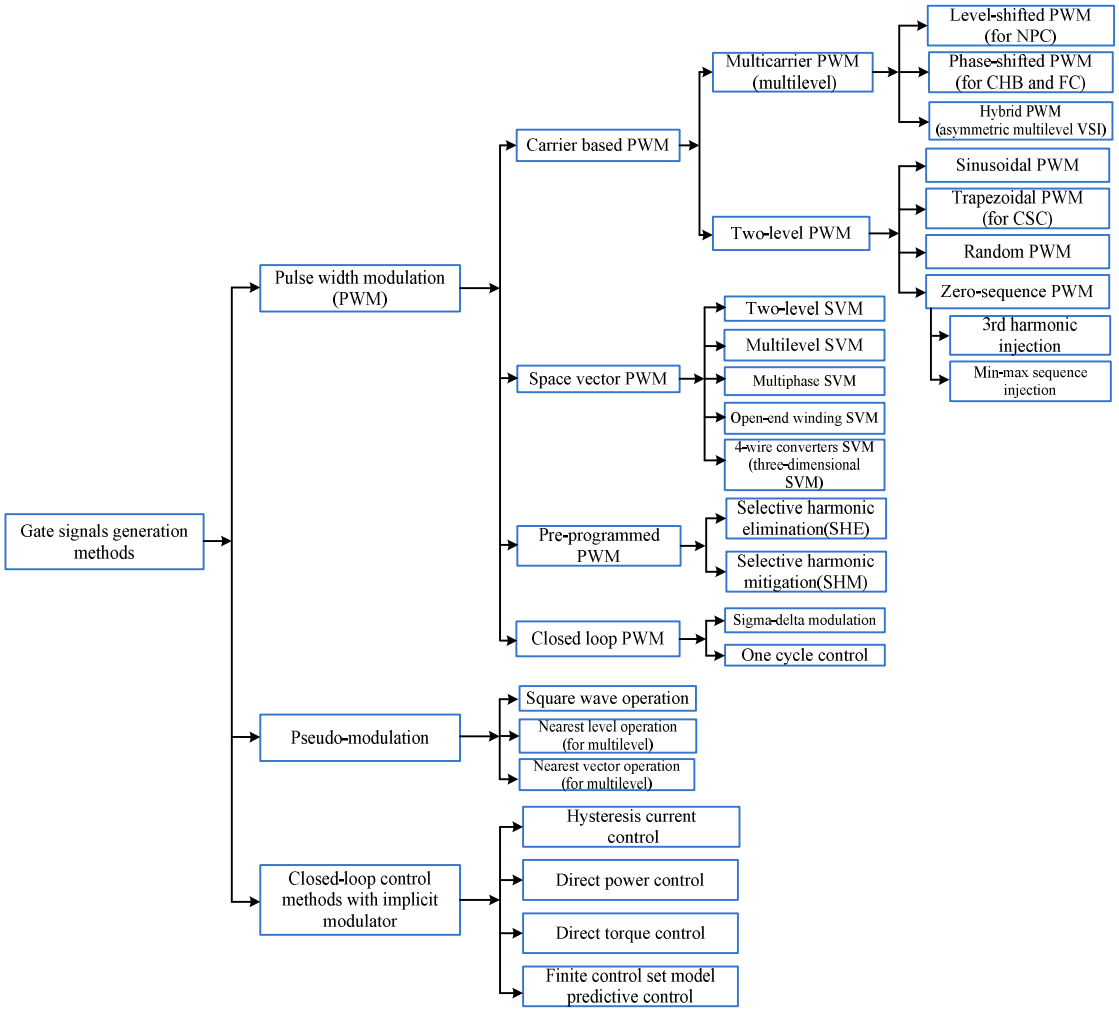

(b)

Fig.1.12. Classification of control techniques for grid-tied inverters (a) controller classification (b) gating signal generation technique classification

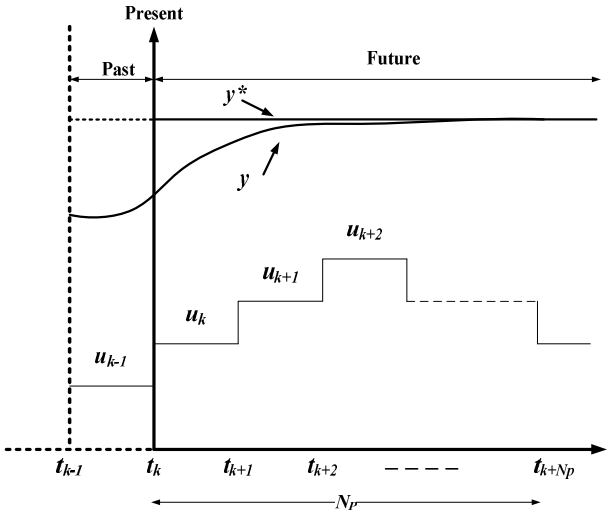

Fig.1.13. Receding horizon policy for model predictive control

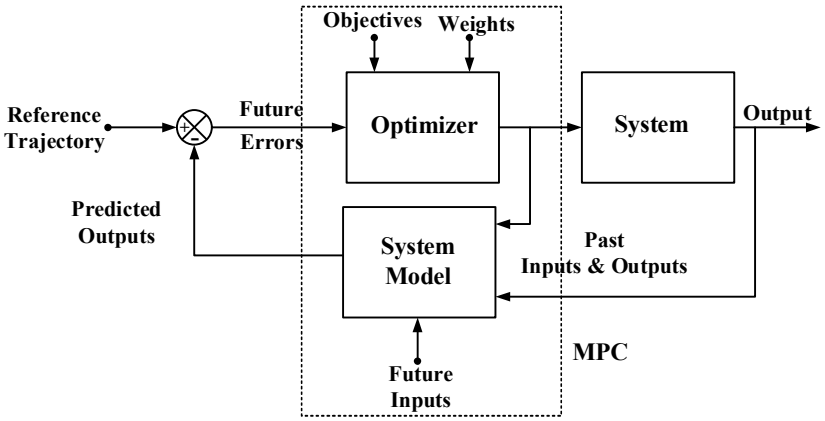

Fig.1.14. Structure for implementing model predictive control

1.3.4 Finite Control-Set Model Predictive Control (FCS-MPC)

MPC techniques used for power electronics and energy conversion systems are mainly classified into two categories; Continuous Control Set Model Predictive Control (CCS-MPC) and Finite Control Set Model Predictive Control (FCS-MPC) [78], [79], [86], [87]. In CCS-MPC, a control signal is computed in a continuous time (usually duty ratio of voltage) and then given to a modulation stage to obtain the desired control action. On the other hand, FCS-MPC directly selects the control signals by optimizing the objective-function which contains the error terms of control parameters and uses the inherent discrete nature of the converters. Because of this, FCS-MPC is an extensively used technique compared to CCS-MPC in power electronics and converter applications. Implementation of FCS-MPC is straightforward as the

finite number of control actions is available for power converters. This control technique has several advantages such as easy to understand, applicable to a wide variety of systems and provision to include additional control parameters and nonlinearities into the objective-function [78], [79].

The generic principle of FCS-MPC for two-level Voltage Source Inverter (VSI) with short prediction horizon (i.e., N_P=1) is shown in Fig.1.15. In this illustration, y^k is considered as a control parameter for the present sampling instant k and it can be estimated based on the past data. As the two-level VSI has eight switching states, the response of control parameter for all these eight switching states can be predicted for the next sampling period *(k+1)*. The switching state which results in close tracking of predicted control parameter with respect to the reference of control parameter y^*(i.e., $|y^*-y^{k+1}|$ is minimum) is considered as an optimal control action for the next sampling period. From Fig.1.15, at the sampling instant *(k+1)*, switching state S_4 leads to close tracking of y^k with respect to y^*. Based on this measure, S_4 is applied at k to obtain the optimal control action. Similarly, S_3 is the suitable control action at *(k+1)* [79].

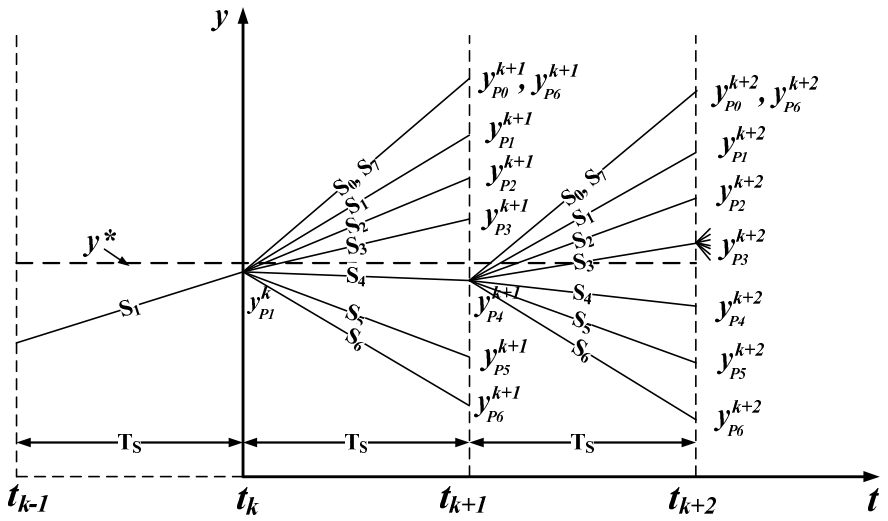

Fig.1.15. Principle of finite control set model predictive control

The block diagram of FCS-MPC for a typical power electronic application is shown in Fig.1.16. In this representation, a VSI is connected to a three phase load with y being the control parameter. To implement FCS-MPC, initially control parameter y^k is to be measured for present sampling instant k. If the direct measurement of control parameter is not possible,

then estimation of control parameter has to be done based on model of the system and past history of control variable. Based on the measured/estimated values, prediction of control parameter can be done for all available inverter control actions. An objective function is formulated by using these predicted values and corresponding reference value. A suitable control action for the inverter is selected by minimising the objective function. However, in power electronics and energy conversion applications; the inclusion of diverse control parameters like inverter current/power, inverter voltage, common-mode voltage, and switching frequency into single objective function requires a suitable selection of weighting factors to maintain the relative importance between them. This is one of the challenging tasks in the design of FCS-MPC technique for power electronic applications [79], [88], [89].

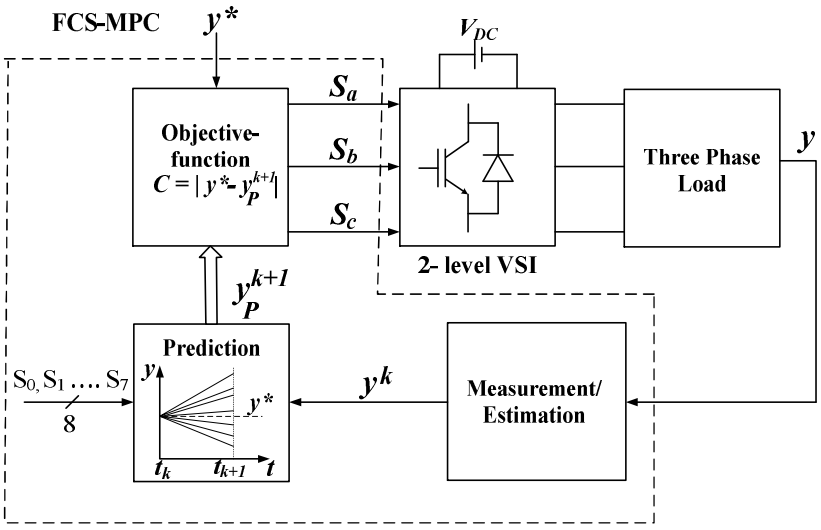

Fig.1.16. Block diagram for finite control set model predictive control

1.4 Literature review

Solar photovoltaic (SPV) is one of the fastest growing renewable energy sources. Large penetration of grid-interactive PV systems with stiff grid-codes has drawn the attention of multilevel inverters, especially the NPC topology in various configurations [6], [7], [90]. The basic objectives of control for PV inverter are to extract the maximum power from the PV array and to regulate the active-reactive power injected to the grid. However, the specific objective of the NPC inverter to balance the DC-link capacitor voltages is also equally important for proper operation of the inverter [65]. Several classical control approaches together with modulation techniques have been reported in the literature to meet the aforementioned objectives. Nevertheless, the control of these multiple control objectives is

quite complex with the classical control techniques. Hence, MPC based control techniques are introduced for the applications of grid-tied inverters to address various control aspects with precise control over the required objectives. MPC techniques used for power electronic applications can be categorized into two groups; such as CCS-MPC and FCS-MPC. However, FCS-MPC is widely accepted by both academia and industrial communities because of its salient features such as; concepts are easy to understand, applicable to wide variety systems, easy inclusion of constraints/nonlinearities and direct selection of switching state without intermediate modulation stage. There are two important variants of FCS-MPC i.e., model predictive current control (MPCC) and model predictive direct power control (MPDPC). A typical block diagram of FCS-MPC with these control variants is shown in Fig.1.17.

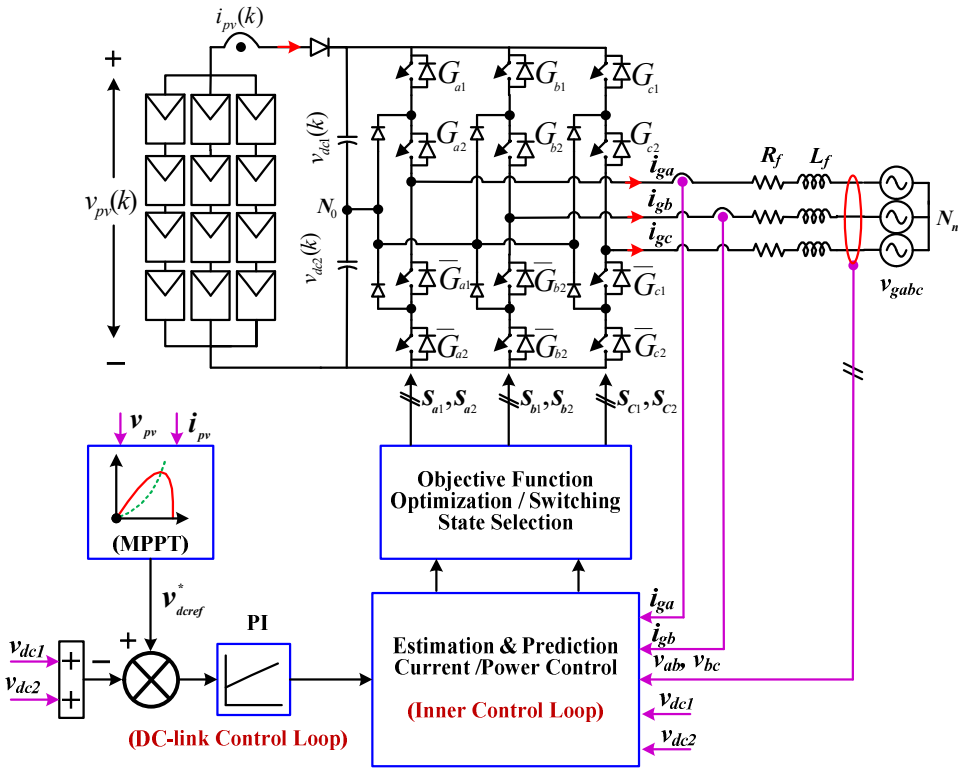

Fig.1.17. Block diagram for FCS-MPC for single stage grid-tied 3L-NPC PV inverter

Despite of its versatile features, FCS-MPC still presents problems while designing the controller for multi-objective control applications. One of the major challenges is the selection of weighting factors to prioritize the control objective in the objective function. Selection of these weighting factors directly affects the system performance. In order to achieve the desired performance, the relative importance between multiple control objectives is maintained by assigning appropriate weighting factor for each objective. Fig.1.18 shows the

control objectives with their respective weighting factors for a single-stage grid-tied 3L-NPC PV inverter.

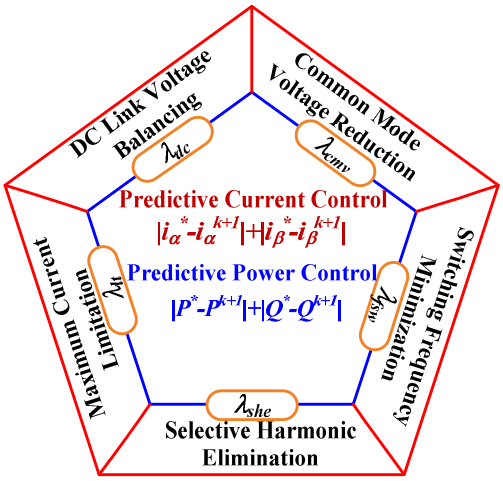

Fig.1.18. Overview of control objectives for objective function

Objective function defined with the possible control objectives of grid-tied 3L-NPC PV inverter are given as follows:

$$\xi_{MPCC}=\left|i_\alpha^{*(k+1)}-i_\alpha^{(k+1)}\right|+\left|i_\beta^{*(k+1)}-i_\beta^{(k+1)}\right|+\lambda_{dc}\left|v_{dc1}^{(k+1)}-v_{dc2}^{(k+1)}\right|+\lambda_{cm}\left|v_{cm}^{(k+1)}\right|+\lambda_{sfw}\left|S_d^{(k+1)}\right|+\cdots \quad (1.1)$$

$$\xi_{MPDPC}=\left|P^{*(k+1)}-P^{(k+1)}\right|+\left|Q^{*(k+1)}-Q^{(k+1)}\right|+\lambda_{dc}\left|v_{dc1}^{(k+1)}-v_{dc2}^{(k+1)}\right|+\lambda_{cm}\left|v_{cm}^{(k+1)}\right|+\lambda_{sfw}\left|S_d^{(k+1)}\right|+\cdots \quad (1.2)$$

Where, λ_{dc}, λ_{cm}, and λ_{sfw} are the weighting factors for DC-link capacitor voltage balancing, common mode voltage reduction and switching frequency minimization.

FCS-MPC lacks with a systematic approach to determine the weighting factors. Generally, the weighting factors are determined empirically which requires extensive time-consuming simulation and experimental trials as there are no definite design procedures to determine the correlation among the objectives of control. Hence, in order to reduce this uncertainty in the empirical process, a set of guidelines are defined in [91] to prioritize the control objectives. In this approach, first the control objectives are classified into equally important objectives and secondary objectives. Equally important objectives are necessary for the proper operation of the inverter, whereas, secondary objectives are the additional constraints. Determining the weighing factor for secondary control objectives is simple. The initial value of the weighing factor is selected zero (λ=0) as this set point measures the behaviour of primary variable, and

the value is increased till the secondary objective reaches its desired value. However, in case of equally important terms the set point of weighing factor is not allowed to be zero (λ=0) as both the objectives are necessary for proper operation of the inverter. Hence, first the objective function is normalized to realize the equal importance among the objectives which sets a starting point for the search. Then, the same procedure as defined for the secondary objectives followed till the desired performance is achieved. An objective function defined with the control objectives of current tracking and DC-link capacitor voltage balancing for a grid-tied 3L-NPC inverter is shown below

$$\xi_{MPCC} = \left|i_{\alpha}^{*(k+1)} - i_{\alpha}^{(k+1)}\right| + \left|i_{\beta}^{*(k+1)} - i_{\beta}^{(k+1)}\right| + \lambda_{dc}\left|v_{dc1}^{(k+1)} - v_{dc2}^{(k+1)}\right| \tag{1.3}$$

These objectives are necessary and equally important for proper operation of the inverter. Further, they are of different nature and magnitude. Hence, the search for λ_{dc} is initiated first by normalizing the objective function as follows:

$$\xi_{MPCC} = \frac{1}{i_{sn}}\left[\left|i_{\alpha}^{*(k+1)} - i_{\alpha}^{(k+1)}\right| + \left|i_{\beta}^{*(k+1)} - i_{\beta}^{(k+1)}\right|\right] + \frac{\lambda_{dc}}{V_{dcn}}\left|v_{dc1}^{(k+1)} - v_{dc2}^{(k+1)}\right| \tag{1.4}$$

or

$$\xi_{MPCC} = \left|i_{\alpha}^{*(k+1)} - i_{\alpha}^{(k+1)}\right| + \left|i_{\beta}^{*(k+1)} - i_{\beta}^{(k+1)}\right| + \frac{i_{sn}\lambda_{dc}}{V_{dcn}}\left|v_{dc1}^{(k+1)} - v_{dc2}^{(k+1)}\right| \tag{1.5}$$

Where, the value of λ_{dc} is adjusted till the objective is achieved with the desired performance. Further, the search processes can be simplified by using the branch and bound algorithm. Though these guidelines reduce the uncertainty in the search process, it still involves time-consuming simulation and experimental trials to determine the optimal solution. Further, this approach becomes more and more tedious with the addition of number of control objectives. This approach has been used by various researches to determine the weighing factors for grid-tied PV inverter applications till the date due to the lack of analytical or numerical methods to determine an optimal solution [92]–[95].

Similar to the normalization approach, a different procedure is explored to determine the weighting factors for a multi-objective MPC of grid-tied NPC PV inverter in [96]. In this approach, an average of acceptable individual objective errors (ε_i) are defined and used in the normalization to make the magnitudes of each objective comparable as shown

$$\alpha = \frac{\varepsilon_i}{i_{sn}}, \beta = \frac{\varepsilon_{vdc}}{V_{dcn}} \tag{1.6}$$

The objective function is defined as

$$\xi_{MPCC} = \lambda_i \left[\left| i_\alpha^{*(k+1)} - i_\alpha^{(k+1)} \right| + \left| i_\beta^{*(k+1)} - i_\beta^{(k+1)} \right| \right] + \lambda_{dc} \left| v_{dc1}^{(k+1)} - v_{dc2}^{(k+1)} \right| \tag{1.7}$$

where, $\lambda_i = \frac{1}{\alpha}$ and $\lambda_{dc} = \frac{1}{\beta}$.

Though this approach is simple, determining the average acceptable error for various objectives with the defined power level of the application requires an experienced design engineer. Further, these weight factors are constant and maintain a fixed correlation among the control objectives irrespective of the operating conditions. In order to overcome this, several MPC methods have been reported in the literature for dynamic selection of weighting factors for FCS-MPC.

In [97], an online auto-tuning method of weighting factor selection is introduced for a grid-tied inverter with distributed generation system. Where, the objective function is defined with active power tracking, reactive power tracking and terminal voltage regulation. In this approach, a range of acceptable error for each control objective is defined with preset initial weighting factors. If the error of individual objectives is within the limits of defined error then the present weighting factor is applied in the next sampling period. Else, a larger weighting factor is selected to give higher priority to the respective objectives for the next sampling period. Similar approach has been extended for grid-tied matrix converter based active shunt compensator [98]. This enumerated search for weighting factor in each control objective affects the dynamic performance of the system.

An analytical approach for dynamic adjustment of weighting factors for a grid-tied 3L-NPC inverter has been presented in [99]. The objective function is defined with the current tracking, DC-link capacitor voltage balancing and switching frequency regulation. Similar to the previous approach, the objective prioritization is done based on the magnitude of existing errors. The weighting factors is adjusted with a dynamic gain defined as

$$gain = \begin{cases} 1, & |\varepsilon| \le \varepsilon_{\max} \\ |\varepsilon| \dfrac{h}{\varepsilon_{\max}} + (1-h), & |\varepsilon| > \varepsilon_{\max} \end{cases} \tag{1.8}$$

Where, $\boldsymbol{\varepsilon}$ is the objective error and h is the gain rate. This dynamic weighted MPC (DWMPC) increases the adaptability of the controller for various operating conditions with the intended behaviour. However, it requires selection of additional parameters per each objective which gain requires an expert design engineer.

In [100], an artificial neural network (ANN) based dynamic objective function for FCS-MPC of grid-tied 3L-NPC inverter has been proposed to determine the online weighting factors. In order to determine the optimal weights, a multilayer perceptron (MLP) ANN is trained in offline to characterize the performance of the system based on the merit figures. The merit figures used to characterize the system performance are average current tracking error, average current total harmonic distortion, average DC-link voltage deviation and average switching frequency. The ANN establishes the correlation between control objectives and the power references by using the merit figures which defines the system behaviour. Similar sort of approach is presented for an uninterruptable power supply (UPS) system application in [101]. These approaches require extensive simulation/experimental trails for possible operating conditions to generate the training data which is again a tedious task similar to the empirical approach.

In [102], a fuzzy FCS-MPC (FFCS-MPC) for a grid-tied three-level nested neutral point clamped converter is presented. A fuzzy logic controller (FLC) is employed to determine the objective weights in online. The objective function of NNPC is defined with active, reactive power and capacitor voltage balancing. A set of fuzzy rules developed based on the mathematical guidelines for these individual objectives dynamically determines the weighting factors to minimize the trajectory slopes of the respective control variables. However, it is difficult to design fuzzy logic controller for a multi-objective system due to the complexity incurred with increase in number of control variables. Further, several attempts are made to completely eliminate the weighting factors selection by taking the advantage of correlation and defining the hierarchy among the control objectives [103]–[106]. However these approaches are limited to specific applications and constraints.

Selection of weighting factors plays a key role in achieving the desired performance with FCS-MPC; however, their selection is limited by the conflicting inter-correlation between the objectives. This can be overcome by using Multi-Criteria Decision Making (MCDM) methods. MCDM methods are used in the complex decision-making problems with conflicting criteria. These methods are well suited for the simplification of weighting factor selection in the objective function [107], [108].

1.5 Weighting factor selection based on MCDM methods

MCDM methods are normally used to select the best solution from the available alternatives in the presence of multiple and conflicting criteria [107], [108]. These MCDM methods are classified into two categories namely; Multi-Objective Decision Making (MODM) methods and Multi Attribute Decision Making (MADM) methods. MODM methods are applied to the problems associated with continuous data and infinite number of alternatives. Whereas, MADM methods are used for the problems associated with discrete data and finite set of alternatives. Considering the finite set of control actions and the control objectives of the power electronic converters as the finite set of alternatives and criteria's respectively, the weighting factor selection problem FCS-MPC can be referred as a MCDM problem. MADM methods are best suited for the simplifying the selection of weighting factors in the objective function. In most of the cases, MADM methods are often referred as MCDM methods. Application of MCDM methods for simplifying the objective prioritisation in the FCS-MPC adds significant computational burden in the implementation. Hence, the selected MCDM methods should be able to implement in the available digital control platforms.

To select appropriate weights for the individual criterion, several weighting factor selections based on subjective and objective approaches are available [108]. In case of subjective approach, the design engineer has to select the priority coefficients to simplify the selection of weighting factors with their expertise. In [109], [110], a Fuzzy Multi-Criteria Decision Making (FMCDM) method based on subjective weighting approach has been proposed to simplify the weighting factor selection of FCS-MPC for grid-tied NNPC converter and direct matrix converter (DMC). This approach eliminates the weighting factors with priority coefficients defined based on analytical hierarchy process (AHP). The membership functions defined in FMCDM approach represents the degree of objective

achievement. Though, these MCDM methods avoid the weighting factors, they require an expert design engineer to select appropriate priority coefficients. Further, these priority coefficients are constant and maintain a fixed correlation among the control objectives irrespective of the operating conditions. As a result, the tracking performance of each control variable varies with the operating conditions.

To overcome these problems, objective weighting methods are used in this research work. To implement these methods for online objective function optimization, the selected methods should be simple, compatible with online optimization and able to implement in available digital control platforms. Several objective weighting factor methods are available in the literature, however based on these measures, two simple MCDM methods namely: criteria importance through inter-criteria correlation (CRITIC) and preference selective index (PSI) based objective weighting methods are implemented for single-stage grid-tied 3L-NPC PV inverter.

1.6 Centralized Model Predictive Control (CMPC) for grid-tied inverter

Despite the capability of controlling multiple constraints, the traditional FCS-MPC uses a cascaded structure of outer DC-link voltage and inner current/power control loop for grid-tied inverters. The outer DC-link voltage control loop regulates the DC-link capacitor voltage to its reference by providing the reference current/power to the inner control loop. Generally, a PI controller is used to regulate the DC-link voltage. Since, the PI controller provides the reference to the inner control loop; the overall system performance will be influenced by the dynamics of PI controller. Tuning of these controller parameters for the desired stability criteria requires a trade-off between steady-state and transient response. To address this issue a cascade-free MPC control approach has been introduced for active front end rectifier in [111]. In this approach, a dynamic active power reference to regulate the outer DC-link voltage is derived based on discrete-time model of the system. This method has eliminated the outer DC-link voltage control loop with centralized control by incorporating the constraint in the objective function. This control strategy has been extended to the grid-tied applications such as shunt active power filter [112], multi-level inverter interfaced distributed generation system [92], and back-to-back converter interfaced wind energy conversion system [33], [113]. In these applications the DC-link voltage is regulated to a fixed value of reference to inject active and reactive power into the grid. However, for a single-stage grid-tied SPV

inverter, the dynamic power reference generation presented in [33], [92], [111]–[113] are not directly applicable to regulate the floating DC-link for extracting the maximum power.

1.7 Motivation

From the literature survey it is observed that, FCS-MPC is a recent advancement in the control of grid-tied inverters and become an attractive alternative for the classical control techniques. This method enables the flexibility in control of multiple control objectives by choosing the suitable weighting factor in the objective-function. In most of the cases empirical methods are used for the selection of weighting factors in the objective-function. Hence, there is a need to introduce generic methods for the selection of appropriate weighting factors with simple approach. Further, despite the capability of controlling multiple constraints, the traditional FCS-MPC uses a cascaded structure of outer DC-link voltage and inner current/power control loop for a grid-tied inverter; where, the overall system performance will be influenced by the dynamics of PI controller.

In this research work, efforts are made to address the issue of selection of weighting factors in multi-objective model predictive control of single-stage grid-tied solar photovoltaic system. A direct optimization method and two objective prioritization methods based on MCDM approach are proposed to simplify the weighting factor selection in multi-objective FCS-MPC. Further, the control of floating DC-link of single-stage grid-tied solar photovoltaic inverter with a modified CMPC approach is presented.

1.8 Scope of the Thesis

The objective of this research work is to simplify the weighting factor selection in multi-objective model predictive control of grid-tied solar photovoltaic inverter. Weighting factor is the only parameter to be tuned in FCS-MPC for maintaining the relative importance between various control objectives. In standard implementation of FCS-MPC, empirical method is used to select the suitable weighting factor in the objective function which requires number of simulation and experimental trails. In this research work, serious attempts are made to simplify the selection of weighting factors for maintaining the relative importance between the control variables such as current/power tracking, DC link capacitor voltage balancing and common mode voltage (CMV) reduction.

In the first method, a selective finite-states model predictive control (FS-MPC) is proposed for a grid interfaced three-level neutral point clamped (3L-NPC) solar photovoltaic (PV) inverter. The proposed control approach eliminates the weighting factor selection for DC-link capacitor voltage balancing and reduces the computational burden for real-time implementation. The switching states required for the prediction and objective function optimisation are selected based on the position of reference voltage vector in the space vector plane, inverter current directions and the charge status of the DC-link capacitors. As a result, the selection of optimal switching state is fast, easy to implement and simplifies the selection of weighting factor problem for capacitor voltage balancing.

In the second method, a centralized model predictive control (CMPC) with criteria importance through inter-criteria correlation (CRITIC) based dynamic weighting factor selection (CRITIC-W-CMPC) for a multi-objective solar photovoltaic (SPV) inverter is proposed. The CRITIC method eliminates the time consuming trail-and-error approach of weighting factor selection by using multivariate descriptive analysis of objective deviations in each sampling period. Thus, weighting factors are dynamically selected depending upon the operating conditions of the inverter for an improved tracking performance of each objective. Further, the CMPC eliminates the cascaded structure of grid tied inverter control by using a decoupled active-reactive power based dynamic reference generation. As a result, the floating DC-link of single-stage SPV inverter is regulated to its reference for extracting the maximum power without using any classical proportional-integral (PI) controller.

In the third method, a preference selective index (PSI) based dynamic weighting factor selection approach (PSI-W-CMPC) is proposed to maintain the relative importance between the power tracking and DC-link capacitor voltage balancing. Similar to the second method, the proposed control approach eliminates the outer DC-link voltage control loop and also the empirical approach required for the selection of weighting factors. A detailed qualitative comparison of these proposed control approaches are presented in Table.1.3.

1.9 Organization of the Thesis

In chapter-1, background of the topic, literature review on FCS-MPC for grid-tied inverters and MCDM methods, motivation for the problem formulation and scope of the thesis are presented.

In chapter-2, modeling of 3L-NPC grid-tied inverter, analysis and implementation of conventional FCS-MPC for grid-tied inverters, simulation and experimental results of PI-SVM, MPCC, LUT-DPC and MPDPC are given for various operating conditions.

In chapter-3, design of single-stage grid tied 3L-NPC PV inverter and implementation of MPCC, MPDPC based control strategies for single-stage grid tied 3L-NPC PV inverter are presented. Simulation and experimental results are presented for MPCC and MPDPC under various operating conditions.

In chapter-4, development of selective FS-MPC for single-stage grid tied 3L-NPC inverter is presented. Simulation and experimental results of selective FS-MPC and conventional MPCC are compared under various operating conditions.

In chapter-5, development of CMPC with CRITIC based objective prioritisation for single-stage grid tied 3L-NPC inverter is presented and its implementation steps are presented. Simulation and experimental results of CRITIC-W-CMPC and conventional MPDPC are compared under various operating conditions.

In chapter-6, PSI based objective prioritisation for single-stage grid tied 3L-NPC inverter and its implementation steps are presented. Simulation and experimental results of PSI-W-CMPC and conventional MPDPC are compared under various operating conditions.

In chapter-7, overall summary of the results, comparison of active and reactive power ripples, % THD of injecting currents for both the conventional and proposed FCS-MPC methods are presented. Finally, conclusions and future scope for the work is suggested.

Table.1.3 A qualitative comparison between the proposed methods

Description	FS-MPC	CRITIC-W-CMPC	PSI-W-CMPC
Constraints Inclusion	Design Specific	Easy to include	Easy to include
Weight Selection	Eliminated	Simple and intuitive	Simple and intuitive
Dynamic performance	Fast	Fast	Fast
Computational Complexity (Comparatively)	Low	High	Medium
Computational burden (Comparatively)	Low	High	Medium
Weights Selection approach	Eliminated	Dynamic & Online	Dynamic & Online

Chapter-2
FCS-MPC for Grid Tied 3L-NPC Inverter

2.1 Introduction

Multi-level inverters are well proven technology for efficient energy conversion in high-power industrial applications [65], [67], [68], [90]. The most popular and well-established multi-level inverter topologies are diode neutral point clamped (NPC), cascaded H-bridge (CHB) and flying capacitor (FC) type. Out of these, NPC topology is one of the most widely used multilevel inverter in the industrial applications. In particular, the three-level NPC (3L-NPC) inverter is most promising due to its higher power capability, higher output levels, small size of DC buses, less number of components required (compared to five-level and seven-level topologies) and reduced total harmonic distortion [114]. The applications of commercially available 3L-NPC inverter includes static synchronous compensators (STATCOMs), electric traction system, marine propulsion system, high power motor drives, wind energy conversion systems (WECS) and solar photovoltaic energy conversion systems (SPECS). Most of these applications include current/power control based on linear proportional integral (PI) controller with carrier/space-vector pulse width modulation (CPWM/SVPWM) techniques or a non-modulator based hysteresis current/power controllers [25]. The typical issues of 3L-NPC inverter are DC-link capacitor voltage balancing, active-reactive power tracking under various power factor operating conditions, high *dv/dt* due to fast switching actions of semiconductor devices and also the higher switching losses. Control of these objectives with the classical controllers and modulation techniques incur high design complexity.

To accomplish the above mentioned requirements in-concert, multi-objective FCS-MPC is one of the attractive control alternative for the classical approaches [77]–[80]. FCS-MPC refers to a controller that explicitly uses the model of the system to select an optimal control action for the defined objective constraints. The enumerated search for optimal control action within the admissible switching states of the converter is simple and straightforward. Hence, the implementation of FCS-MPC can be extended for wide variety of applications with multiple constraints.

In this chapter, a detailed design procedure of generalized FCS-MPC for a grid-tied 3L-NPC inverter is presented. There are two important variants of FCS-MPC for grid-tied inverters namely: model predictive current control (MPCC) and model predictive direct power control (MPDPC) [115]–[117]. The main objectives of these control approaches are current tracking for MPCC, active-reactive power tracking for MPDPC, and DC-link

capacitor voltage balancing. Depending on the requirement, the secondary objectives such as common mode voltage (CMV) reduction and switching frequency minimization can be included into the objective function. The performance of these MPCC and MPDPC approaches are experimentally verified on the laboratory scale setup and the results are compared with the classical PI-SVM and LUT-DPC approaches.

2.2 Modeling of grid-tied neutral point clamped inverter.

FCS-MPC requires the discrete time model of the system and the objectives required to be controlled are expressed in terms of switching states. The detailed models of 3L-NPC inverter, modeling of DC-link, modeling of grid and modeling of CMV are presented in the following sub-sections.

2.2.1 Modeling of 3L-NPC inverter.

The schematic diagram of three-phase grid-tied 3L-NPC inverter is shown in Fig.2.1. This 3L-NPC inverter is composed of three-legs with four controlled switches and two clamping diodes in each leg. Out of the four controlled switches two pair of switches (G_{xy}) has the complementary switching action with the remaining two ($\overline{G}_{xy}$) in each phase $x \in \{a, b, c\}$ and pair $y \in \{1,2\}$. The gating signals for the pair of switches in each phase-x are represented as g_y^x. Further, the DC-link side of the inverter consists of two split-capacitors C_1 and C_2 providing a neutral point N_0 at the centre.

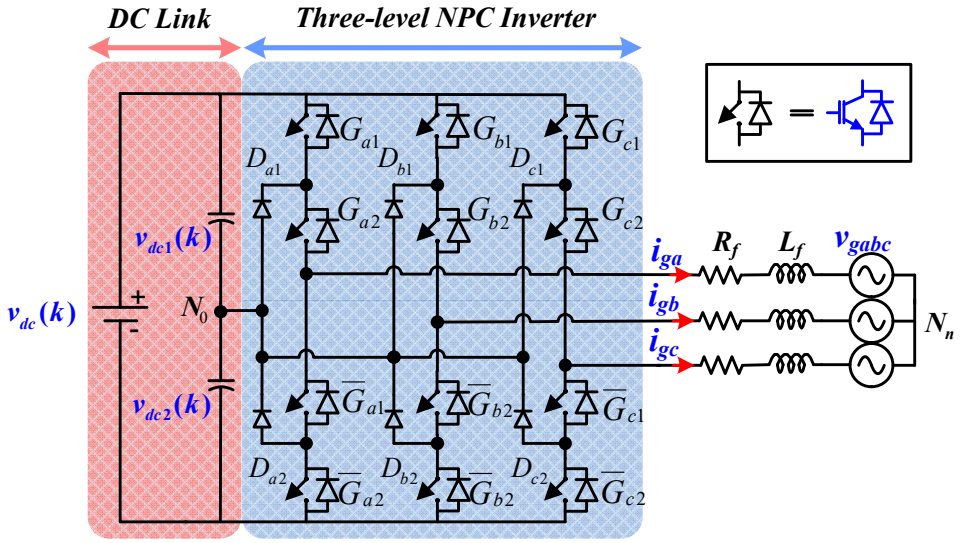

Fig.2.1. Schematic of grid-tied three-phase 3L-NPC.

The voltages across the DC-link capacitors C_1 and C_2 are denoted as V_{dc1} and V_{dc2}, respectively. The clamping diodes of each phase are connected to the neutral point N_0.

The operating states of each phase are represented as [P], [O] and [N], where the switching state u_x is given as

$$u_x = \begin{cases} [P] & if\ g_1^x\ is\ ON \quad \& g_2^x\ is\ ON \\ [O] & if\ g_1^x\ is\ OFF\ \& g_2^x\ is\ ON \\ [N] & if\ g_1^x\ is\ OFF\ \& g_2^x\ is\ OFF \end{cases} \tag{2.1}$$

Fig.2.2 shows the active devices of each switching state u_x. The output voltage of a phase-leg with reference to the neutral point N_0 (pole voltage) for each switching state is given in Table.2.1. As the output voltage levels are $+V_{dc}/2$, 0 and $-V_{dc}/2$, the inverter is referred as a three-level inverter.

Table.2.1. Output voltage of a phase-leg with reference to the neutral point N_0

Switching State	Device Switching Status				V_{ANo}
	g_1^a	g_2^a	$\bar{g}_1^a$	$\bar{g}_2^a$	
P	1	0	0	1	$+V_{dc}/2$
O	0	1	0	1	0
N	0	1	1	0	$-V_{dc}/2$

On considering all the three-phases, there exists 27 (3^3) admissible switching states for a 3L-NPC inverter. The distribution of these switching states in space-vector plane is shown in Fig.2.3. These 27 switching states generate 19 different voltage vectors. Out of these 19 voltage vectors, one zero vector is generated by three switching states {OOO, PPP, and NNN}, six small vectors are generated by twelve switching states {POO, PPO, OPO, OPP, OOP, POP, ONN, OON, NON, NOO, NNO and ONO}, six medium vectors are generated by six switching states {PON, OPN, NPO, NOP, ONP and PNO} and six large vectors are generated by six switching states {PNN, PPN, NPN, NPP, NNP, and PNP}.

The phase voltages and line voltages of the 3L-NPC inverter defined in terms of the capacitor voltages V_{dc1} and V_{dc2} and switching state u_x are given as:

$$\vec{v}_{iabc} = \begin{bmatrix} v_{ia} \\ v_{ib} \\ v_{ic} \end{bmatrix} = \frac{(V_{c1}+V_{c2})}{6} \begin{bmatrix} 2 & -1 & -1 \\ -1 & 2 & -1 \\ -1 & -1 & 2 \end{bmatrix} \vec{u}_x + \frac{(V_{c1}-V_{c2})}{6} \begin{bmatrix} 2 & -1 & -1 \\ -1 & 2 & -1 \\ -1 & -1 & 2 \end{bmatrix} |\vec{u}_x| \tag{2.2}$$

$$\vec{v}_L = \begin{bmatrix} v_{ia} - v_{ib} \\ v_{ib} - v_{ic} \\ v_{ic} - v_{ia} \end{bmatrix} = V_{c1} \begin{bmatrix} 1 & -1 & 0 \\ 0 & 1 & -1 \\ -1 & 0 & 1 \end{bmatrix} \frac{\vec{u}_x + |\vec{u}_x|}{2} + V_{c2} \begin{bmatrix} 2 & -1 & -1 \\ -1 & 2 & -1 \\ -1 & -1 & 2 \end{bmatrix} \frac{\vec{u}_x - |\vec{u}_x|}{2} \quad (2.3)$$

Where $\vec{u}_x = [u_a, u_b, u_c]^{\mathrm{T}}$ and $|\vec{u}_x| = [|u_a|, |u_b|, |u_c|]^{\mathrm{T}}$.

The output voltage vector of the three-phase 3L-NPC inverter in $\alpha\beta$ reference frame is given as:

$$\vec{v} = \frac{2}{3}\left(v_{iao} + \vec{a}v_{ibo} + \vec{a}^2 v_{ico}\right) \quad (2.4)$$

Where $v_{ixo} = \begin{bmatrix} v_{dc1} & v_{dc2} \end{bmatrix} \begin{bmatrix} g_1^x \\ g_2^x \end{bmatrix}$, and $\vec{a} = e^{j\frac{2\pi}{3}}$.

The three-phase inverter output voltages corresponding to each switching state is given in Table.2.2.

2.2.2 Modeling of DC-link

The DC-link model of the 3L-NPC inverter includes, neutral point voltage $V_n(t)$ and the capacitor currents $i_{c1}(t)$ and $i_{c2}(t)$. In order to ensure proper operation of the 3L-NPC inverter, the neutral point voltage $V_n(t)$ must be maintained at zero potential. This can be achieved by regulating the charge status of the capacitors C_1 & C_2 and indeed the voltage across each capacitor V_{dc1} & V_{dc2}, respectively.

The dynamics of neutral point voltage $V_n(t)$ and the capacitor voltages V_{dc1} & V_{dc2} are given as

$$\frac{dV_n(t)}{dt} = \left(\frac{dV_{c1}(t)}{dt} - \frac{dV_{c2}(t)}{dt}\right) \quad (2.5)$$

$$\left.\begin{aligned} \frac{dV_{dc1}(t)}{dt} &= r_{c1}\frac{di_{c1}(t)}{dt} + \frac{i_{c1}(t)}{C_1} \\ \frac{dV_{dc2}(t)}{dt} &= r_{c2}\frac{di_{c2}(t)}{dt} + \frac{i_{c2}(t)}{C_2} \end{aligned}\right\} \quad (2.6)$$

Where, r_{c1}, r_{c2} are equivalent series resistance (ESR) of capacitors C_1 and C_2, respectively.

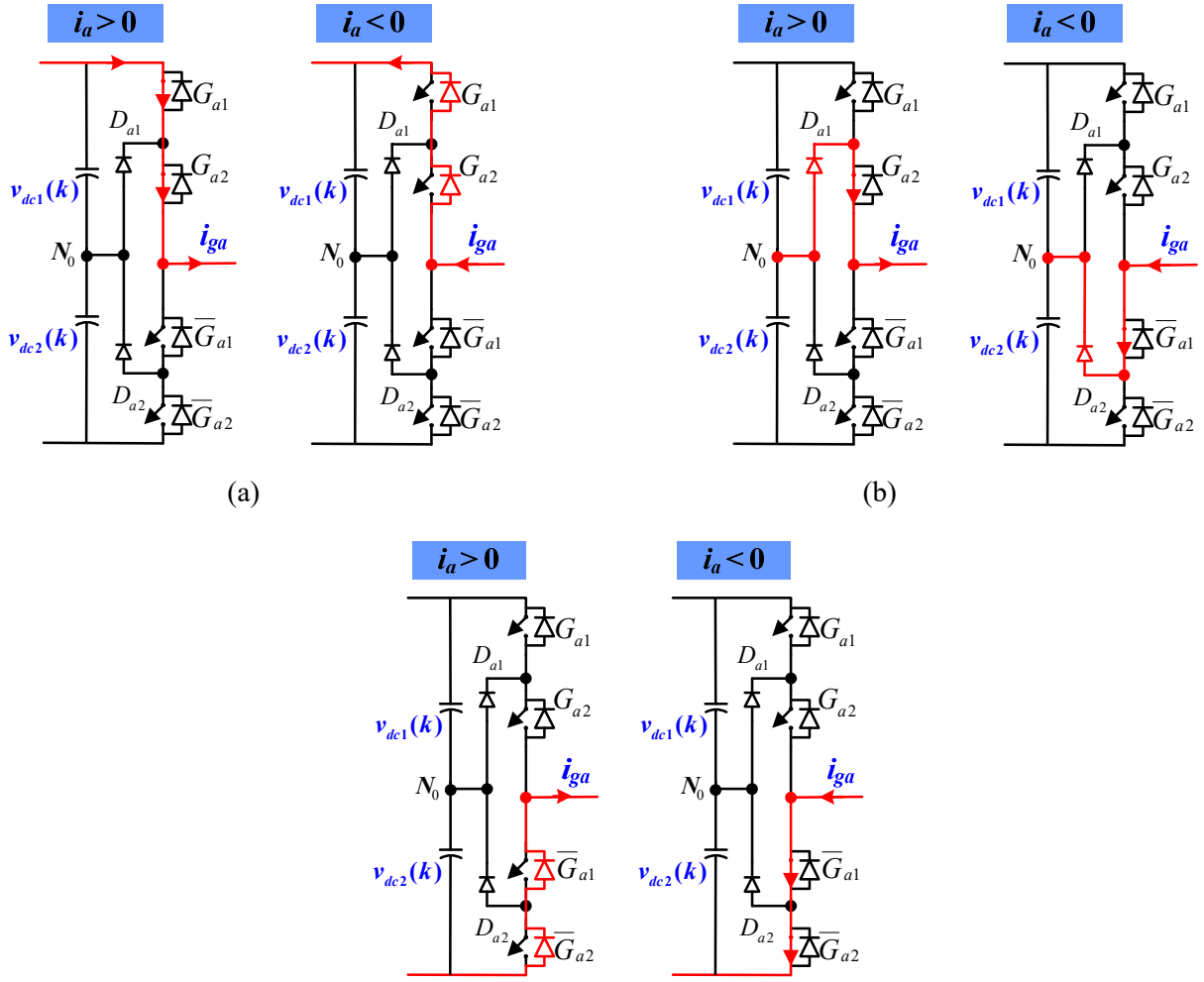

Fig.2.2. Active devices based on direction of current flow for each state

On applying the forward Euler's discretization approach, the discrete-time model of the DC-link capacitor voltages is obtained as:

$$\begin{aligned} V_{dc1}^{p}(k+1) &= V_{dc1}(k) + \frac{T_S}{C_1} i_{c1}(k) + \underbrace{r_{c1}\left(i_{c1}(k+1) - i_{c1}(k)\right)}_{\text{drop due to ESR of } C_1} \\ &= V_{dc1}(k) + \frac{T_S}{2C_1} i_0(k) + \underbrace{\frac{r_{c1}}{2}\left(i_0(k+1) - i_0(k)\right)}_{\text{drop due to ESR of } C_1} \end{aligned} \tag{2.7}$$

$$\begin{aligned} V_{dc2}^{p}(k+1) &= V_{dc2}(k) + \frac{T_S}{C_2} i_{c2}(k) + \underbrace{r_{c2}\left(i_{c2}(k+1) - i_{c2}(k)\right)}_{\text{drop due to ESR of } C_2} \\ &= V_{dc2}(k) - \frac{T_S}{2C_2} i_0(k) + \underbrace{\frac{r_{c2}}{2}\left(i_0(k+1) - i_0(k)\right)}_{\text{drop due to ESR } C_2} \end{aligned} \tag{2.8}$$

where, $v_{dc1}^{p}(k+1)$,and $v_{dc2}^{p}(k+1)$ are the predicted variables with T_s sampling period. The midpoint DC-link current i_0= (i_{C2} – i_{C1}) in (2.7) & (2.8) can be estimated by using the measured line currents and the switching states of the inverter as

$$i_o(k) = g_{oa}(k) \cdot i_{ga}(k) + g_{ob}(k) \cdot i_{gb}(k) + g_{oc}(k) \cdot i_{gc}(k) \tag{2.9}$$

where, g_{ox}=1 if u_x=0 and g_{ox}=0 if u_x≠0.

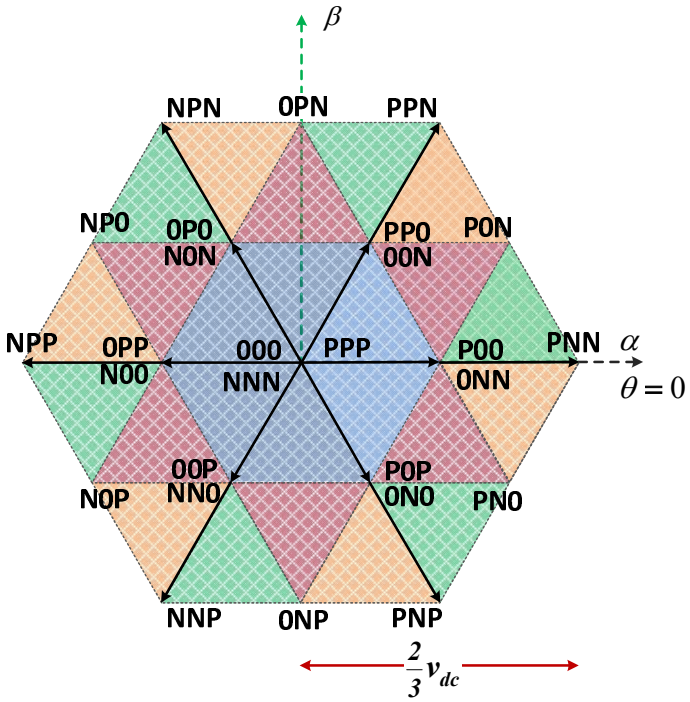

Fig.2.3. Space vector plane of 3L-NPC inverter

2.2.3 Modeling of grid

A simplified representation of a three-phase grid-tied inverter interfaced with *L*-filter is shown in Fig.2.4. The dynamics of the grid-tied inverter is described as:

$$v_{ix}(t) = v_{gx}(t) + R_f i_{gx}(t) + L_f \frac{di_{gx}(t)}{dt} \tag{2.10}$$

Where $v_{ix}(t)$, $v_{gx}(t)$ and $i_{gx}(t)$ are the inverter phase voltage, grid voltage and grid currents, respectively. Here, L_f is the interfacing filter inductor with the parasitic resistance R_f.

From Eq. (2.10), the dynamics of grid currents in *αβ* reference frame is given as:

$$\frac{d\vec{i}_{g\alpha\beta}(t)}{dt} = \frac{1}{L_f}\left(\vec{v}_{i\alpha\beta}(t) - \vec{v}_{g\alpha\beta}(t)\right) - \frac{R_f}{L_f}\vec{i}_{g\alpha\beta}(t) \tag{2.11}$$

Table.2.2. 3L-NPC inverter output voltages for each switching state

Space vector		Switching State		Vector Classification	Vector Magnitude
$\vec{v}_0$		PPP, OOO, NNN		Zero vector	0
		P-type	N-type	Small vector	$\frac{1}{3}V_{dc}$
$\vec{v}_1$	$\vec{v}_{1P}$	POO			
	$\vec{v}_{1N}$		ONN		
$\vec{v}_2$	$\vec{v}_{2P}$	PPO			
	$\vec{v}_{2N}$		OON		
$\vec{v}_3$	$\vec{v}_{3P}$	OPO			
	$\vec{v}_{3N}$		NON		
$\vec{v}_4$	$\vec{v}_{4P}$	OPP			
	$\vec{v}_{4N}$		NOO		
$\vec{v}_5$	$\vec{v}_{5P}$	OOP			
	$\vec{v}_{5N}$		NNO		
$\vec{v}_6$	$\vec{v}_{6P}$	POP			
	$\vec{v}_{6N}$		ONO		
$\vec{v}_7$		PON		Medium vector	$\frac{1}{\sqrt{3}}V_{dc}$
$\vec{v}_8$		OPN			
$\vec{v}_9$		NPO			
$\vec{v}_{10}$		NOP			
$\vec{v}_{11}$		ONP			
$\vec{v}_{12}$		PNO			
$\vec{v}_{13}$		PNN		Large vector	$\frac{2}{3}V_{dc}$
$\vec{v}_{14}$		PPN			
$\vec{v}_{15}$		NPN			
$\vec{v}_{16}$		NPP			
$\vec{v}_{17}$		NNP			
$\vec{v}_{18}$		PNP			

The discrete format of Eq. (2.11) is given as:

$$\vec{i}_{g\alpha\beta}^{\,p}(k+1)=\frac{T_s}{L_f}\left(\vec{v}_{i\alpha\beta}(k)-\vec{v}_{g\alpha\beta}(k)\right)+\left(1-\frac{T_sR_f}{L_f}\right)\vec{i}_{g\alpha\beta}(k) \tag{2.12}$$

Where, $\vec{i}_{g\alpha\beta} = [i_{g\alpha} \quad i_{g\beta}]^{T}$, $\vec{v}_{g\alpha\beta} = [v_{g\alpha} \quad v_{g\beta}]^{T}$ and $\vec{v}_{i\alpha\beta} = [v_{i\alpha} \quad v_{i\beta}]^{T}$ are the grid current vector, grid voltage vector and inverter voltage vector in $\alpha\beta$ frame respectively.

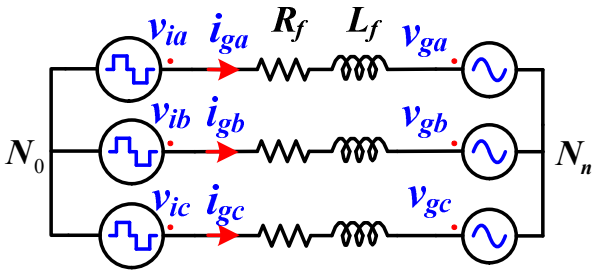

Fig.2.4. Simplified representation of a grid tied inverter.

2.2.4 Modeling of common-mode voltage

The CMV of a grid-tied 3L-NPC inverter exists between the neutral-point of the grid (n) and the split-point of the DC-link capacitors (N_0). The CMV of 3L-NPC inverter is expressed as:

$$v_{cm} = v_{nN_0} = \frac{1}{3}\sum_{x\in abc} v_{ixo} \tag{2.13}$$

From Eq. (2.13), it can be seen that the value of CMV depends on the switching states/gating signals of the inverter. The CMVs for the available switching states of 3L-NPC inverter are given in Table.2.3. It can be observed that the CMV of six medium voltage vectors {PON, PNO, OPN, ONP, NPO, NOP} and three zero vectors {PPP, NNN, OOO} are found to be zero. Hence, with proper selection of switching states, the CMV of the inverter can be reduced to zero.

2.3 Control strategy

FCS-MPC scheme for a grid-tied 3L-NPC is shown in Fig.2.5. The design procedure of FCS-MPC scheme mainly includes three-major stages namely; measurement/estimation of feedback variables, prediction of control variables and optimization of objective-function. In the first stage, the variables required for prediction or reference generation are measured by using the sensors. If the direct measurement is not possible then they are estimated. Further in the second stage, the future behaviour of the required control variables are predicted for finite number of control actuations within the given range of prediction horizon. Finally, an objective function is defined with the control objectives to evaluate the optimal control

action required for the next sampling period. The detailed steps involved in the design of FCS-MPC scheme is presented in the following sub-sections.

Table.2.3. CMVs of 3L-NPC inverter for corresponding switching states

	Switching States	Common-mode voltage (CMV)
Large vectors	PPN, NPP, PNP	$V_{dc}/6$
	NNP, NPN, PNN	$-V_{dc}/6$
Medium vectors	PON, PNO, OPN, ONP, NPO, NOP	*0*
Small Vectors	PPO, OPP,POP	$V_{dc}/3$
	ONN, NON, NNO	$-V_{dc}/3$
	POO, OPO, OOP	$V_{dc}/6$
	OON, ONO, OON	$-V_{dc}/6$
Zero vectors	PPP	$V_{dc}/2$
	NNN	$-V_{dc}/2$
	OOO	*0*

2.3.1 Measurement/estimation of variables

The direct measurement of feedback variables is required for the implementation of FCS-MPC technique. However, if the measurement is not possible then the signals are required to be estimated. The main objective of grid-tied inverters is to regulate the active and reactive power injected into the grid. The active and reactive power injecting into the grid can be regulated directly by using currents or powers as the control variables. Further, from the perspective of NPC topology, DC-link capacitor voltage balancing is also equally important for the proper operation of the inverter. Hence, the objectives of current/power tracking and DC-link capacitor voltage balancing are considered as the main control objectives in the implementation of FCS-MPC for grid-tied 3L-NPC inverter. In order to achieve these control objectives, the instantaneous grid voltages, grid currents, DC-link capacitor voltages and the neutral point current are required to be measured. Though the neutral point current is directly available for the measurement, the value of neutral point current required for the present sampling period can be estimated by using Eq. (2.9), hence the cost incurred for the measurement can be avoided.

2.3.2 Prediction of control variables

The implementation of FCS-MPC for grid-tied inverter requires the prediction of control variables for the admissible switching states of the inverter. The future behaviour of control

variables are predicted for the given range of prediction horizon of the control algorithm. One-step ahead prediction (i.e., N_p=1) is the simplest predictive control technique used for power converters. The 3L-NPC inverter consists of 27 admissible switching states generating a total of 19 voltage vectors as given in Table.2.2. Prediction of grid-currents and DC-link capacitor voltages with one-step ahead prediction can be obtained by using following relations

$$\left\langle \vec{i}^{\,p}_{g\alpha\beta}(k+1)\right\rangle_m = \frac{T_s}{L_f}\left(\left\langle \vec{v}_{i\alpha\beta}(k)\right\rangle_m - \vec{v}_{g\alpha\beta}(k)\right) + \left(1-\frac{T_s R_f}{L_f}\right)\vec{i}_{g\alpha\beta}(k) \tag{2.14}$$

$$\left\langle V^{p}_{C1}(k+1)\right\rangle_m = V_{c1}(k) + \frac{T_S}{2C_1}\left\langle i_0(k)\right\rangle_m \tag{2.15}$$

$$\left\langle V^{p}_{C2}(k+1)\right\rangle_m = V_{c2}(k) - \frac{T_S}{2C_2}\left\langle i_0(k)\right\rangle_m \tag{2.16}$$

Where m represents the inverter switching states $\{S_1, S_2, \ldots. S_{27}\}$.

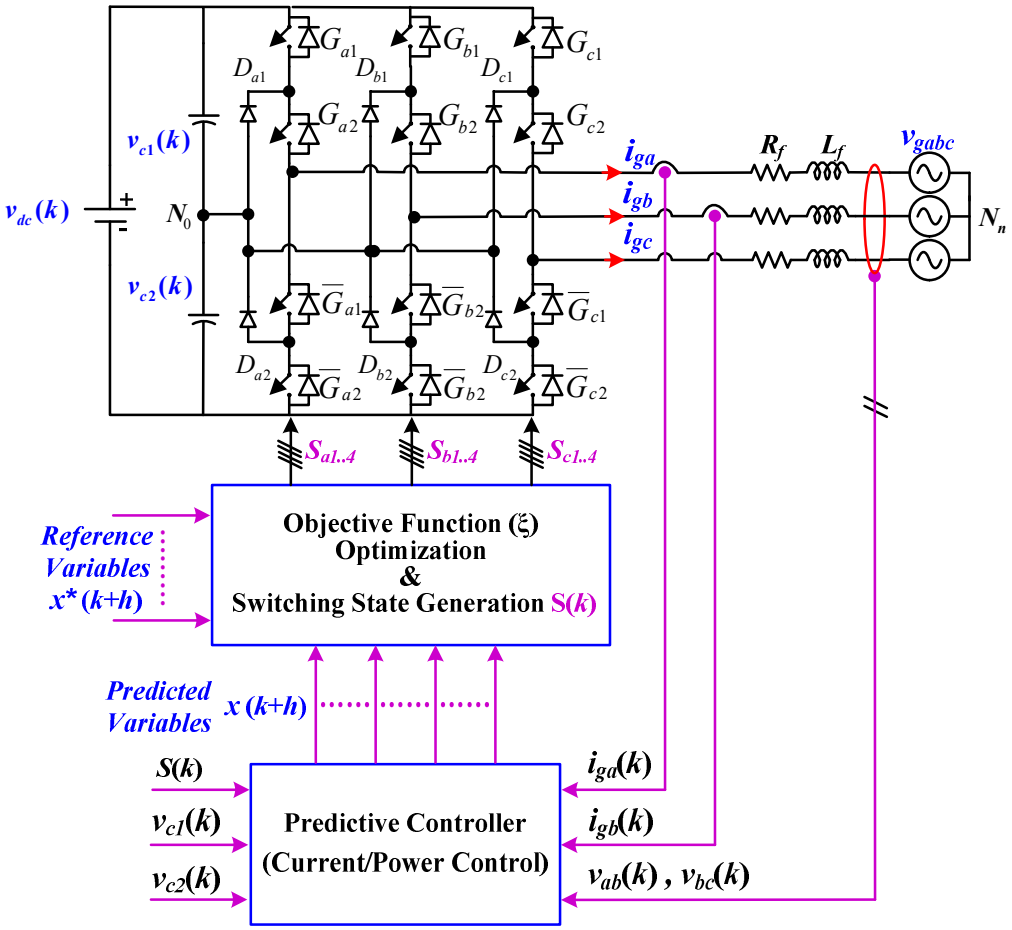

Fig.2.5. Predictive control of grid tied 3L-NPC inverter

2.3.3 Objective function optimization

An objective function is formulated to track the relative closeness of the predicted control variables with respect to their reference for each control action of the inverter. The optimal control action is the one which gives the minimum value of the objective function. In FCS-MPC for grid-tied inverters, injecting currents/power and DC-link capacitor voltages are the two main control variables to regulate, where the corresponding control objectives are defined as:

$$\xi_i(k) = \left|i^*_{g\alpha}(k+1) - i^p_{g\alpha}(k+1)\right| + \left|i^*_{g\alpha}(k+1) - i^p_{g\alpha}(k+1)\right| \tag{2.17}$$

$$\xi_S(k) = \left|P^*_g(k+1) - P^p_g(k+1)\right| + \left|Q^*_g(k+1) - Q^p_g(k+1)\right| \tag{2.18}$$

$$\xi_{vdc}(k) = \left|v^p_{dc1}(k+1) - v^p_{dc2}(k+1)\right| \tag{2.19}$$

Since the magnitudes and units of these control variables are diverse from each other, weighting factors are assigned to maintain the relative importance among the objectives in the objective function. An objective function defined with these control objectives for one-step ahead prediction is given as:

$$\xi(k) = \xi_i(k) + \lambda_{dc}\xi_{vdc}(k) \tag{2.20}$$

$$\xi(k) = \xi_S(k) + \lambda_{dc}\xi_{vdc}(k) \tag{2.21}$$

where, λ_{dc} is the weighting factor for DC-link capacitor voltage balancing. The optimal switching state is obtained by minimizing the objective function as given below

$$S_{opt} = \arg \min_{(s_1,\ldots..s_{27})} \xi(k) \tag{2.22}$$

2.3.4 Delay compensation

In case of computer based simulation of FCS-MPC, the time incurred in the measurement of feedback signals, predictions and optimization of objective function is zero. Hence the optimal switching state determined is applied at (k^{th}) sampling instant which minimizes the error at (k + 1) sampling instant as shown in Fig.2.6 (a). This is usually known as one-step ahead prediction algorithm. All the 27 switching states of the 3L-NPC will be used for predictions and objective function optimization.

On the other hand, implementation of FCS-MPC in real-time processor requires considerable time for the measurement, computation and generation of switching states [118]. This time delay involved in the realization of optimal switching state deteriorates the performance of the inverter [119]. Hence, the concept of delay compensation is introduced in the FCS-MPC to overcome the delay caused by the digital signal processor (DSP). The implementation of delay compensation is shown in Fig.2.6 (b).

In general, a two step ahead prediction horizon is considered for delay compensation. In order to realize two-step ahead prediction horizon for 3L-NPC, a total of 729 (27^2) switching combinations will be considered for predictions and objective function optimization.

$$\left\langle \vec{i}_{g\alpha\beta}^{\,p}(k+2)\right\rangle_m = \frac{T_s}{L_f}\left(\left\langle \vec{v}_{i\alpha\beta}(k+1)\right\rangle_m - \vec{v}_{g\alpha\beta}(k+1)\right) + \left(1-\frac{T_s R_f}{L_f}\right)\vec{i}_{g\alpha\beta}(k+1) \tag{2.23}$$

$$\left\langle V_{C1}^{p}(k+2)\right\rangle_m = V_{c1}(k+1) + \frac{T_S}{2C_1}\left\langle i_0(k+1)\right\rangle_m \tag{2.24}$$

$$\left\langle V_{C2}^{p}(k+2)\right\rangle_m = V_{c2}(k+1) - \frac{T_S}{2C_2}\left\langle i_0(k+1)\right\rangle_m \tag{2.25}$$

However, this type of approach leads to the high computational burden on the DSP. To overcome this problem, a modified two-step ahead prediction algorithm is proposed in [120]. In this approach, the same switching state is used for prediction in (k + 1) and (k + 2) sampling instants. As a result, the number of switching state combinations in the modified two-step ahead prediction algorithm is reduced to 27 as shown in Fig.2.6 (c).

$$\left\langle \vec{i}_{g\alpha\beta}^{\,p}(k+2)\right\rangle_m = \frac{T_s}{L_f}\left(\left\langle \vec{v}_{i\alpha\beta}(k)\right\rangle_m - \vec{v}_{g\alpha\beta}(k)\right) + \left(1-\frac{T_s R_f}{L_f}\right)\vec{i}_{g\alpha\beta}(k+1) \tag{2.26}$$

$$\left\langle V_{C1}^{p}(k+2)\right\rangle_m = V_{c1}(k) + \frac{T_S}{2C_1}\left\langle i_0(k+1)\right\rangle_m \tag{2.27}$$

$$\left\langle V_{C2}^{p}(k+2)\right\rangle_m = V_{c2}(k) - \frac{T_S}{2C_2}\left\langle i_0(k+1)\right\rangle_m \tag{2.28}$$

2.4 Significance of weighting factor selection

FCS-MPC is one of the advanced control technique which provides a systematic solution for multi-variable constrained control of power electronic applications. In order to achieve

multi-objective control with FCS-MPC, an objective function is defined with the desired control objectives. Since the control objectives are of different nature (voltage/ current/ power/ switching states etc.,), the relative importance between these objectives are maintained by using the weighting factors. These weighting factors directly impact the selection of switching state required for the inverter. Hence, the weighting factors have to be selected properly.

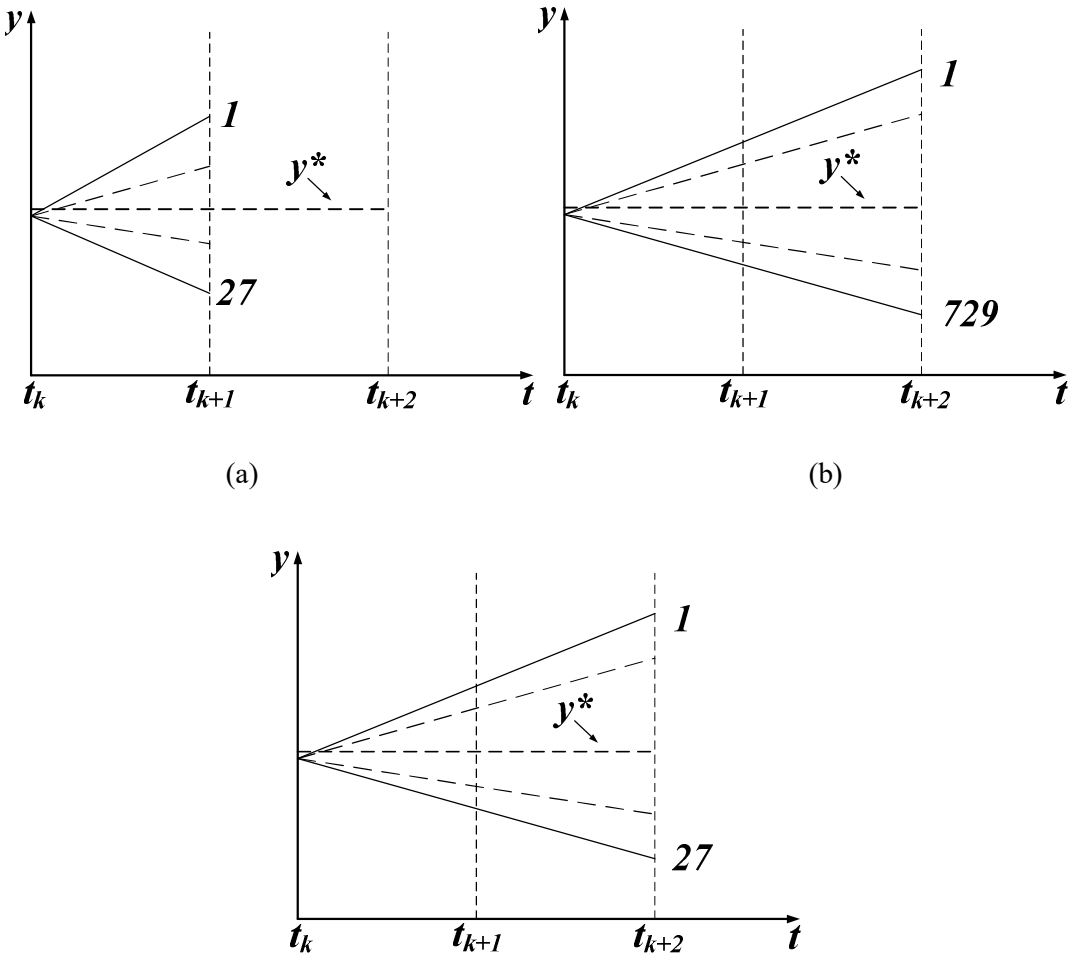

Fig.2.6. (a) One step ahead prediction (b) two step ahead prediction (c) simplified two step ahead predictions

In general the control objectives are classified into two types i.e., equally important and secondary objective terms. As a case of grid-tied 3L-NPC inverter in this work, the current/power tacking objective and DC-link capacitor voltage balancing objective are considered as the equally important objectives; whereas, the objectives of CMV reduction, switching frequency reduction etc., are considered as secondary objectives. The correlation

between these objectives is intermittent; hence, increase in weighting factor of one control objective doesn't necessarily lead to an optimal control. This conflicting characteristics and intermittent correlation between the various control objectives makes the selection of weighting factors more complex.

In most of the cases empirical method is used for the selection of suitable weighting factor which requires a number of simulation and experimental trails. To address this, few guidelines were presented based on branch and bound algorithm [91] and weighting factor based on nominal values of individual control objectives was given in [96]. These two approaches require further tuning of weighting factors in the real-time implementation. Further, selection of suitable weighting factor becomes difficult with inclusion of additional control objective into the objective function. Hence, MCDM methods are introduced for the selection of weighting factors as it becomes simple and straightforward compared to previous two methods.

2.4.1 Branch and bound algorithm

Branch and bound algorithm is used to reduce the number simulation and experimental trails for the selection of suitable weighting factor [91]. The implementation of the branch and bound algorithm is shown in Fig.2.7. Here, M^1 and M^2 are the control parameter errors in the objective-function. M^1 is considered as primary control parameter error term and M^2 is considered as secondary control parameter error term. λ is the weighting factor used for the secondary error term to maintain the relative balance between control parameters in the objective-function. In this method initially, λ is selected with a couple of initial values (λ = 0.1 and 10). Based on these initial values, different orders of λ are selected for the evaluation of error terms M^1 and M^2 in the objective-function. The values for λ are selected as 0.1, 1 and 10. Based on the values obtained for M^1 and M^2, the range of λ is rearranged to $0.1 \leq \lambda \leq 1$ and the values for M^1 and M^2 are evaluated for $\lambda = 0.5$ (i.e., half of the selected range). By repeating this procedure, the final range for weighting factor is selected as $0.1 \leq \lambda \leq 0.25$. By selecting the λ value in between the above ranges, satisfactory error limits are obtained for both M^1 and M^2. However, this approach becomes complex due to the inclusion of additional control parameters into the objective-function.

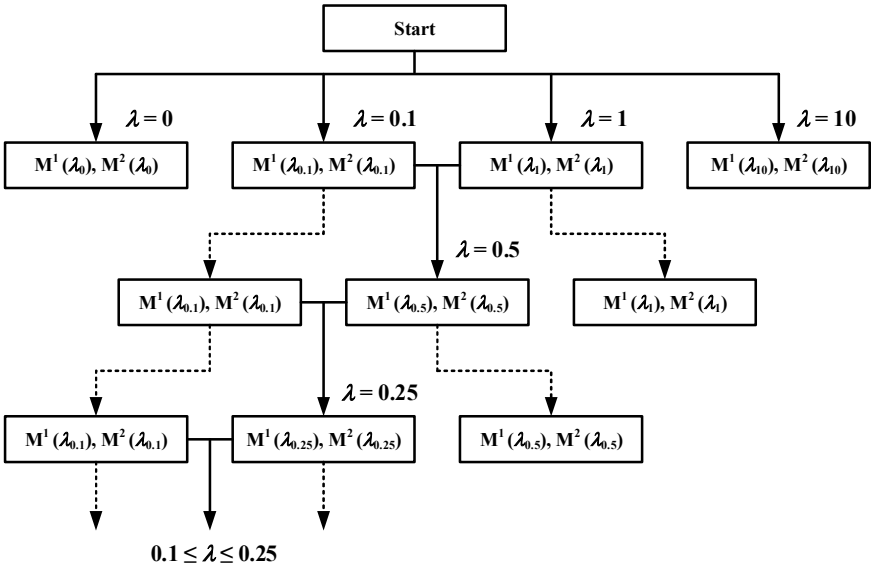

Fig.2.7. Branch and bound algorithm for weighting factor selection

2.4.2 Weighting factor selection based on MCDM methods

Multi-criteria decision making (MCDM) methods are mainly used for complex decision-making problems with conflicting criteria. MCDM methods can be used to simplify the weighting factor selection in the objective function of FCS-MPC due to its ability to select an optimal alternative from various available alternatives to achieve the required criteria. To implement MCDM methods, a single performance index is obtained by assigning the suitable weights to the individual criterion. In each MCDM method, different approaches are used to obtain the single performance index. To select appropriate weights for the individual criterion in the performance index, several weighting selections based on subjective and objective approaches are available [108]. In case of subjective approach, the design engineer has to select the priority coefficients to simplify the selection of weighting factors with his expertise. The selected weights are fixed irrespective of the operating conditions of the application. Few subjective weighting factor methods based on fuzzy multi-criteria decision making method (FMCDM), analytic hierarchy process (AHP), simple additive weighting (SAW), grey relational analysis (GRA), VlseKriterijuska Optimizacija I Komoromisno Resenje (VIKOR) and technique for order of preference by similarity to ideal solution (TOPSIS) for FCS-MPC are available in the literature [121]–[125]. The priority coefficients are constant and maintain a fixed correlation among the control objectives irrespective of the operating conditions. As a result, the tracking performance of each control variable varies with the operating conditions.

To overcome these problems, objective weighting methods are used in this research work. To implement these methods for online objective-function optimization, the selected methods should be simple, compatible with online optimization and able to implement in available digital control platforms. Several objective weighting factor methods are available in the literature, however based on these measures, two simple MCDM methods namely: criteria importance through inter-criteria correlation (CRITIC) and preference selective weighting methods are implemented for a single-stage grid-tied 3L-NPC PV inverter.

2.5 Implementation of predictive control for grid-tied inverter

The flowchart for the implementation of generalized FCS-MPC approach with two-step ahead prediction for grid-tied 3L-NPC inverter is shown in Fig.2.8 and the corresponding steps are given below.

Step I. Measure instantaneous grid voltages $v_{ab}(k)$ and $v_{bc}(k)$; grid currents i_a (k) and i_b (k) and DC-link capacitor voltages v_{dc1} (k) and v_{dc2} (k).

Step II. Convert the grid voltages and currents from natural (abc) frame to stationary orthogonal ($\alpha\beta$) frame, $\vec{v}_{g\alpha\beta}(k)$, $\vec{i}_{g\alpha\beta}(k)$. Estimate the fundamental positive sequence component of grid voltages $\vec{v}^{+}_{g\alpha\beta}(k)$.

Step III. Obtain the reference control variables ($\vec{i}^{*}_{g\alpha\beta}(k)$, or active power P^* & reactive power Q^*).

Step IV. Estimate the positive sequence voltages for (k + 2) period by using Lagrange's extrapolation approach as given in Eq. (3.26).

Step V. Predict the control variables ($\vec{i}^{\,p}_{g\alpha\beta}(k+2)$, or active power $P^*(k+2)$ & reactive power $Q^*(k+2)$).

Step VI. Define the objective function $\xi(k)$ with the control objectives.

Step VII. Evaluate the objective function defined for all the admissible switching states and obtain the optimal switching state which minimizes the objective function.

2.6 Simulation results

In order to validate the effectiveness of FCS-MPC, a detailed simulation studies are carried by using MATLAB/Simulink. The system parameters used for simulation and experimental studies are given in Table.2.4. The test results for MPCC and MPDPC are

presented for steady-state and dynamic operating conditions. In order to validate its effectiveness, results are compared with classical linear PI controller with SVM (PI-SVM) and lookup table based direct power control (LUT-DPC) for current & power control respectively. The principle of classical control techniques are presented in appendix.

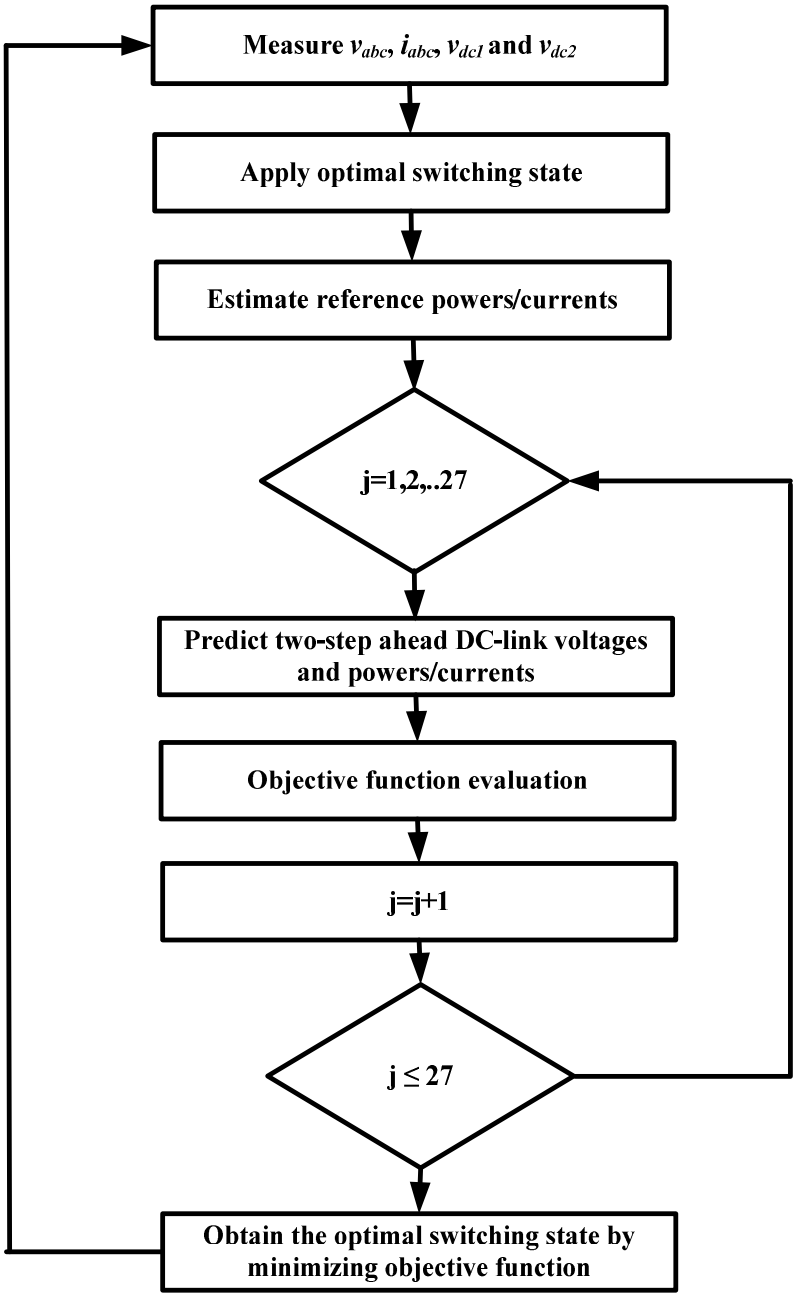

Fig.2.8. Flowchart for generalized implementation of FCS-MPC for grid tied 3L-NPC inverter

2.6.1 Steady state response with current control strategies

The steady state current injection with PI–SVM and MPCC approaches are shown in Fig.2.9. The DC-link voltage is set to 180 V and maintained balanced at 90 V per capacitor.

The switching frequency of PI-SVM approach is taken as 5 kHz. In order to generate the same average switching frequency with MPCC, the sampling rate of the 20 kHz is considered. For a current injection of 4.8 A, the waveforms for PI-SVM and MPCC are illustrated in Fig.2.9 (a) and Fig.2.9 (b), respectively. The objective function in the MPCC is defined with current tracking and DC-link voltage balancing. The percentage total harmonic distortion (%THD) of injecting currents and the inverter voltage are shown in Fig.2.10 and Fig.2.11, respectively. The %THD of the injecting currents and the inverter voltages with both the control approaches are approximately same. However, the MPCC has a spread spectrum compared to PI-SVM.

Table.2.4. System parameters

Parameter	Simulation	Experiment
Grid Details		
Grid voltage	85 V rms (L-L)	85 V rms (L-L)
Grid frequency	50 Hz	50 Hz
Feeder resistance	0.1 Ω	0.1 Ω
Feeder inductance	0.5 mH	0.5 mH
VSC details		
Filter resistance	0.5 Ω	0.5 Ω
Filter inductance	3 mH	3 mH
V_{dc} (min)	150 V	150 V
C_{dc} (C_1=C_2=C)	4700 μF	4700 μF
Sample time	50 μs	50 μs

2.6.2 Dynamic response with current control strategies.

The dynamic response for step-change in current reference with both the control strategies is shown in Fig.2.12. The DC-link voltage is set at 180 V. A step change in current from 3 A to 6 A peak at 0.305s is applied. MPCC will have faster dynamics however for comparison the PI controller values are tuned to obtain the comparable dynamics. The dynamics of injecting currents with both the control approaches are approximately similar and the DC-link voltages are also well balanced. However, MPCC has strictly regulated the capacitor voltage balanced compared to the PI-SVM.

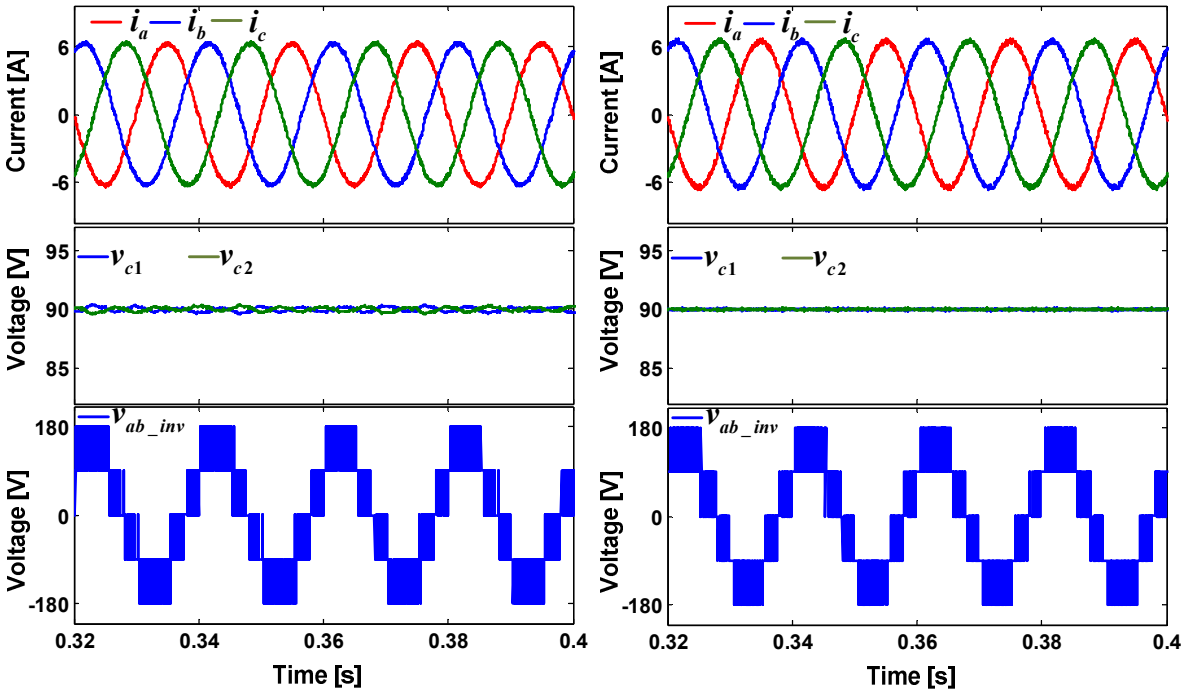

(a) (b)

Fig.2.9. Simulation results for steady state waveforms with (a) PI-SVM (b) MPCC

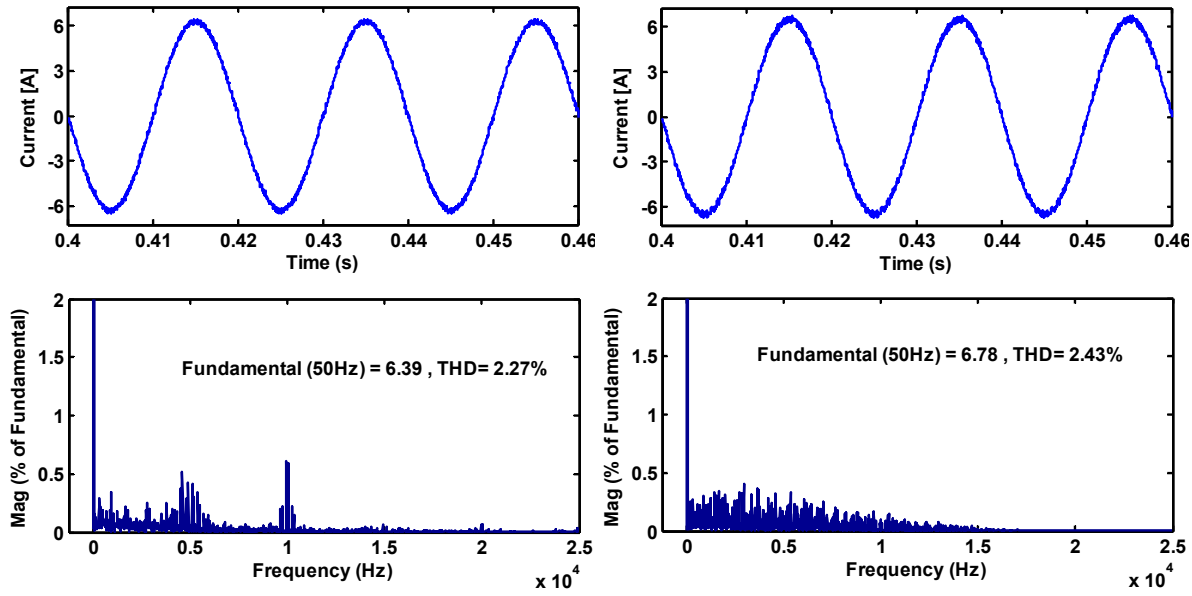

(a) (b)

Fig.2.10. Simulation results for %THD of injecting currents with (a) PI-SVM (b) MPCC.

2.6.3 Steady state response with power control strategies.

The results for steady state power injection with LUT-DPC and MPDPC are shown in Fig.2.13. Both the control strategies are variable switching frequency approaches, hence to achieve same average switching frequency of 5 kHz the sampling frequency is taken as 20 kHz. The results for active power injection of 1200 Watts with reactive power reference of 0

Var for LUT-DPC and MPDPC are shown in Fig.2.13 (a) Fig.2.13 (b), respectively. The DC-link voltage is set to 180 V. The hysteresis band for active power, reactive power and the DC-link voltages in LUT-DPC are considered as 50 Watts, 50 Var and 1V respectively. Similarly, the objective function in MPDPC is framed by using active-reactive power tracking and DC-link capacitor voltage balancing. The weighting factor for the DC-link capacitor voltage balancing is selected based on branch and bound algorithm. It can be observed that both the control approaches have balanced the DC-link capacitor voltages at 90 V. The % THD of injecting currents with LUT-DPC and MPDPC are shown in Fig.2.14 (a) and Fig.2.14 (b), respectively. From the results it can be seen that the MPDPC has a lower current THD and strict DC-link capacitor voltage balancing compared to the classical LUT-DPC.

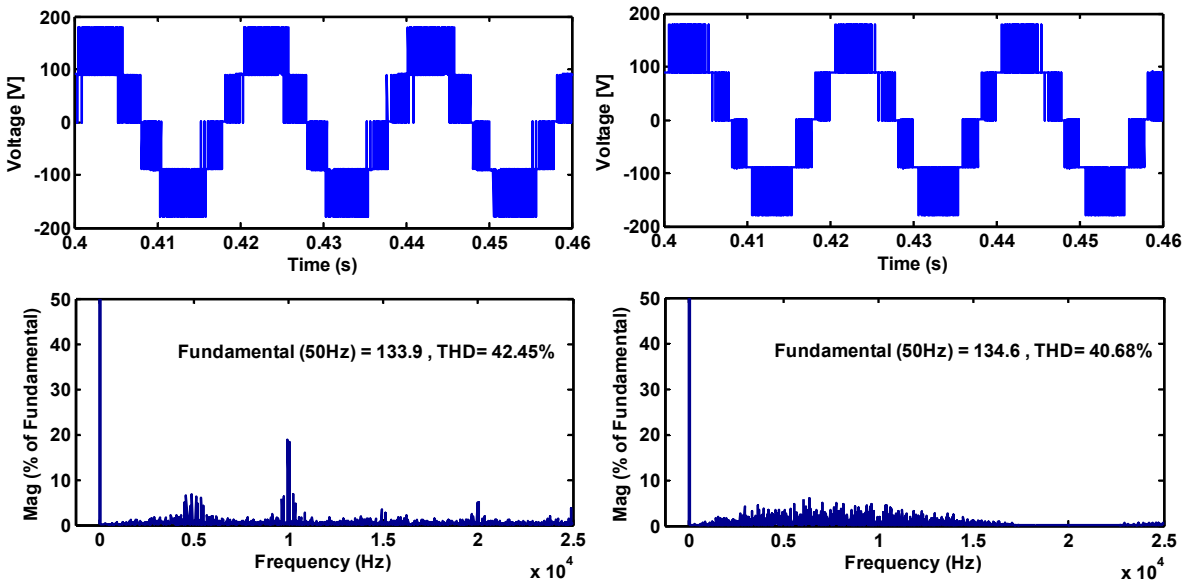

(a) (b)

Fig.2.11. Simulation results for %THD of inverter voltages with (a) PI-SVM (b) MPCC

2.6.4 Dynamic response with power control strategies.

The dynamic response for step-change in reactive power reference from +600 Var to -600 Var with an active power reference of 600 Watts with both the control strategies is shown in Fig.2.15. Similar to the steady state the DC-link voltage is set to 180 V. From the results, it can be seen that the MPDPC has a faster dynamics compared to the LUT-DPC.

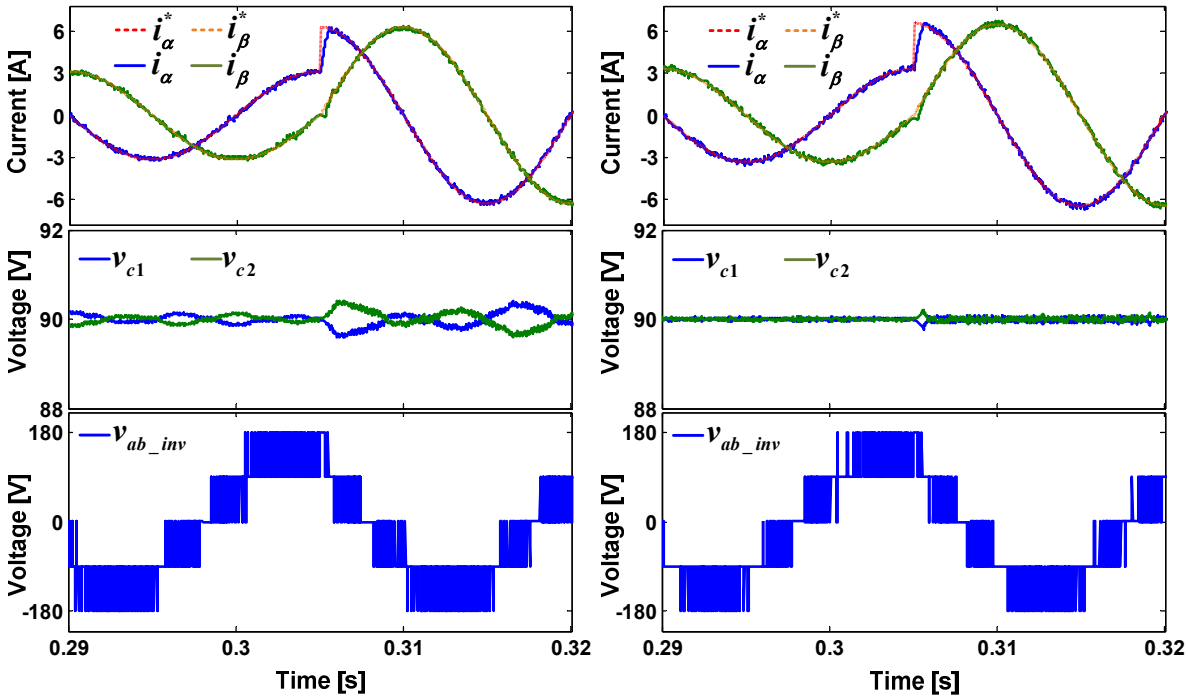

(a) (b)

Fig.2.12. Simulation results for dynamic response of current with (a) PI-SVM (b) MPCC

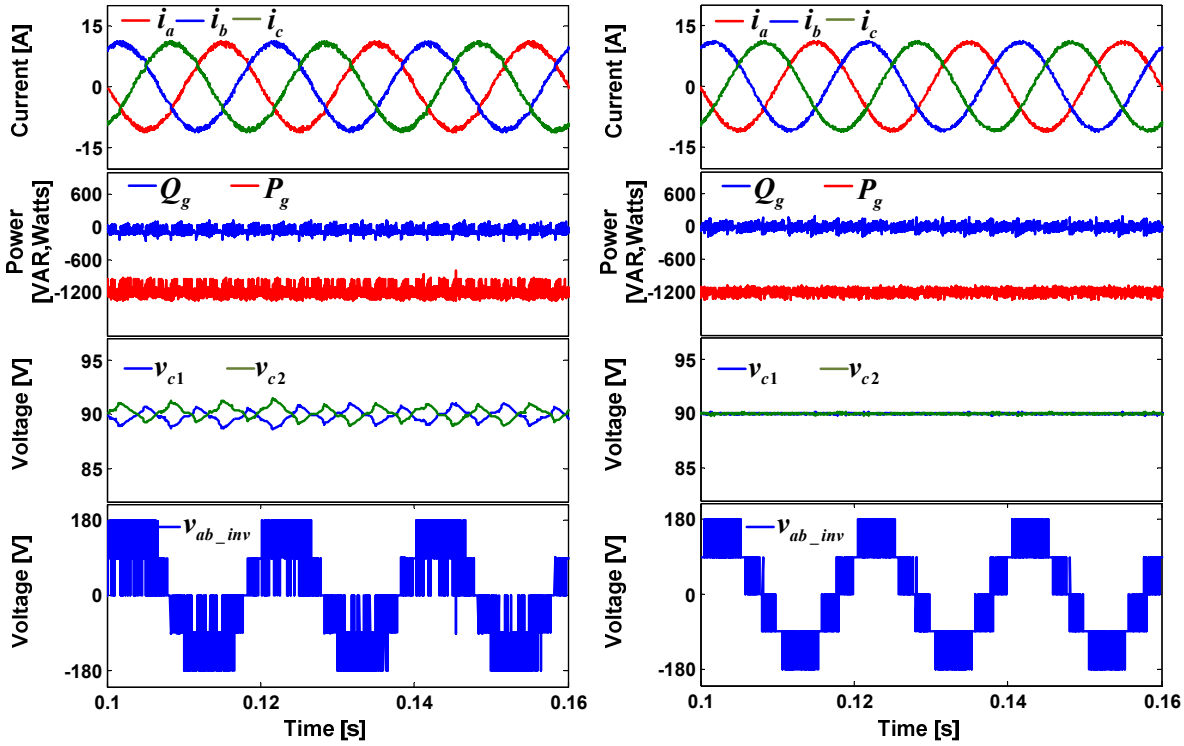

(a) (b)

Fig.2.13. Simulation results for steady-state response of current with (a) LUT-DPC (b) MPDPC

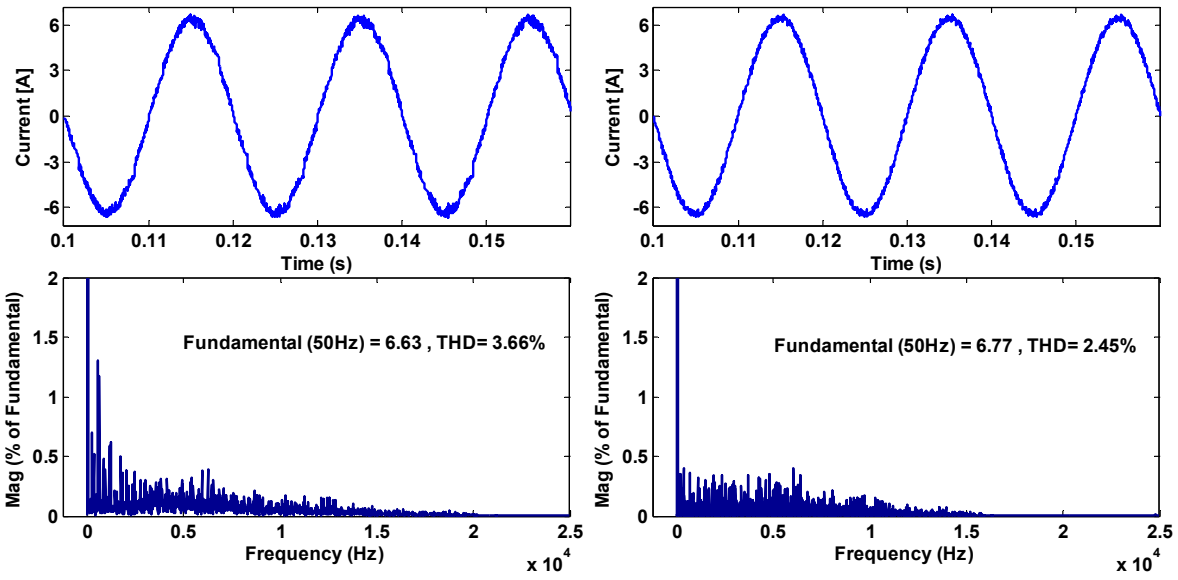

(a) (b)

Fig.2.14. Simulation results for %THD of current with (a) LUT-DPC (b) MPDPC

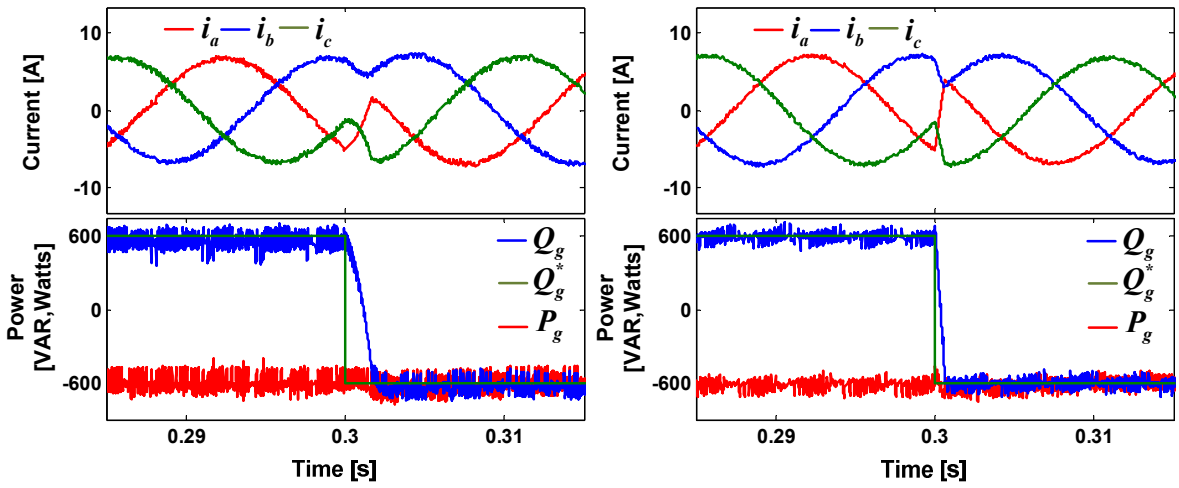

(a) (b)

Fig.2.15. Simulation results for dynamic response of current with (a) LUT-DPC (b) MPDPC

2.6.5 Impact of weighting factor on DC-link capacitor voltage balancing

In order to understand the impact of weighting factor on the capacitor voltage balancing, an unbalanced loading on DC-link is applied. A resistor of 50 Ω is connected across one of the DC-link capacitor and the weighting factor λ_{dc} is changed from 0.1 to 0 and back to 0.1 at time t=0.2 s and 0.24 s, respectively. The result for change in DC-link capacitor voltages with change in weighting factor is shown in Fig.2.16. It can be seen that the DC-link capacitor voltages deviate with its reference as the weighting factor is changed to zero and gets balanced again after applying the weighting factor.

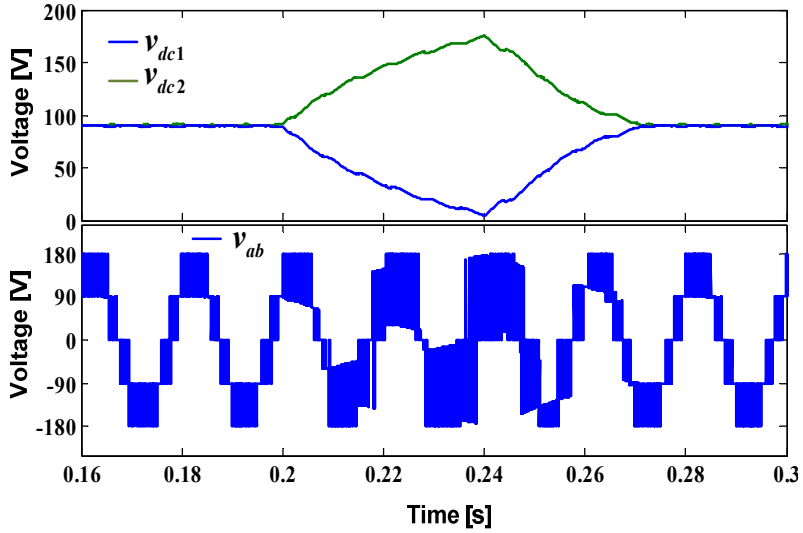

Fig.2.16. Simulation results for DC-link capacitor voltage balancing with change in weighting factor

2.6.6 Impact of weighting factor on CMV mitigation

Fig.2.17 demonstrates the CMV mitigation for 3L-NPC inverter with MPCC. The objective function is defined with current tracking, DC-link capacitor voltage balancing and CMV reduction objectives. The weighting factor for capacitor voltage balancing λ_{dc} is adjusted to maintain the DC-link balance even after including the CMV reduction objective. Initially the λ_{cm} is kept zero, at time t=0.2 s weighting factor λ_{cm} is changed to 0.018 and at t=0.24 s again it is changed to 0.036. The change in CMV with change in λ_{cm} illustrates that, as the weighting factor increases the CMV is reduced.

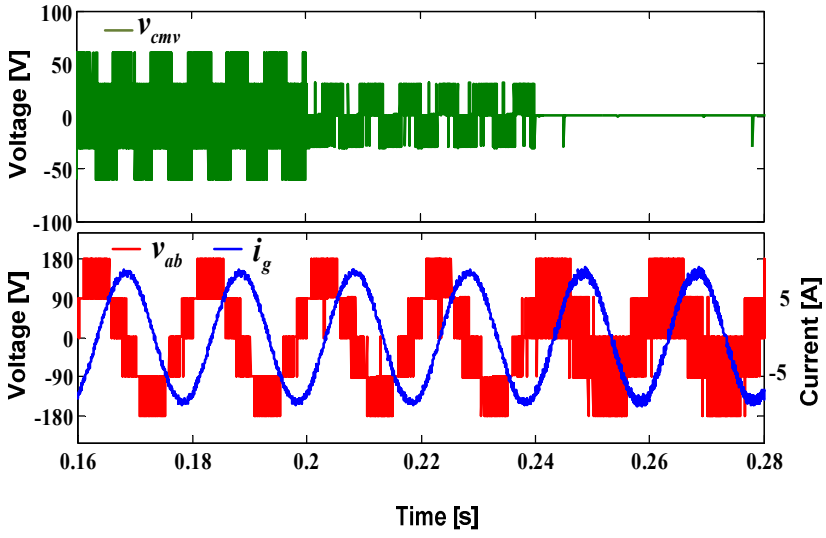

Fig.2.17. Simulation results for CMV mitigation with change in weighting factor

2.6.7 Impact of weighting factor on switching frequency reduction

The change in switching frequency with change in weighting factor λ_{swf} for 3L-NPC inverter is presented in Fig.2.18. The objective function is defined with current tracking, DC-link capacitor voltage balancing and switching frequency reduction objectives. Similar to the previous case studies, the weighting factor λ_{dc} for DC-link capacitor voltage balancing is initially selected based on branch and bound algorithm. Then it is further tuned to balance the capacitors even after inclusion of switching frequency reduction. The change in switching frequency with change in λ_{swf} is illustrated by its impact on converter output. Initially the weighting factor λ_{swf} is kept zero and the average switching frequency F_{swa} of the output voltage is found to be 2.52 kHz. At t=0.2 s the weighting factor is increased to 0.4, the F_{swa} is observed to be 1.68 kHz and at t=0.24 s the weighting factor is further increased to 0.95 the F_{swa} of the inverter is observed to be 982 Hz. It can be seen that as the weighting factor increases the switching frequency of the inverter decreases and correspondingly there is an effect on injecting currents.

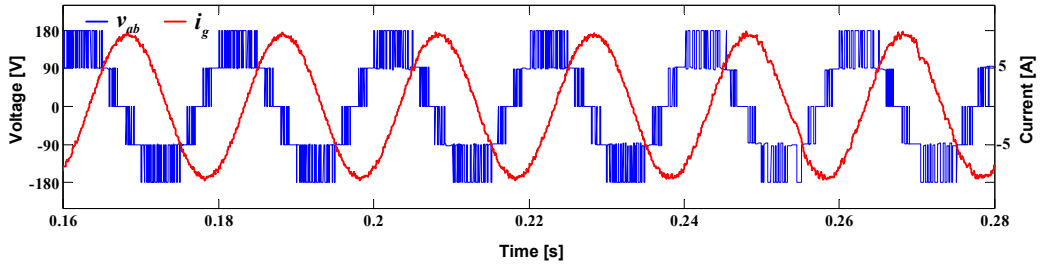

Fig.2.18. Simulation results for switching frequency reduction with change in weighting factor

2.7 Experimental setup.

The block diagram and the experimental setup used to implement the control of grid-tied inverter are shown in Fig.2.19 and Fig.2.20, respectively. The experimental setup consists of Chroma 62050H-S Programmable DC source, a 3L-NPC inverter realized by using Siemens BSM75GB120DN2 IGBT modules, two current sensors (LA-25 NP), four voltage sensors (LV-25) and a dSPACE-DS1104 R&D controller board. A 3L-NPC inverter is interfaced to grid through a three-phase filter inductor. The dSPACE DS1104 R&D real-time controller board is used to execute the developed control algorithms. The feedback signals measured by using voltage and current sensors are fed to the control card via a CP1104 I/O connector board. The gating signals are driven through HCPL-3120 gate drive opto-coupler. A digital storage oscilloscope (DSO) is used to capture the experimental results.

The block diagram of dSPACE-DS1104 R&D controller board is shown in Fig.2.21. The main components of this controller board are main/master processor (MPC8240, PowerPC 603 core, 250 MHz), four multiplexed ADCs (16 - bit), four independent ADCs (12-bit), eight DACs (16-bit), two incremental encoder interfaces, 20-bit digital I/Os, serial interface (RS232, RS485 and RS442) and one slave DSP (TMS320F240) with built-in PWM signals for both three-phase and single-phase PWM outputs. This controller board is placed in the 32-bit PCI slot of the personal computer (PC) and it requires MATLAB/SIMULINK/RTW as a prerequisite. To implement control algorithm in a digital platform, initially it has to be developed in MATLAB/SIMULINK environment. In order to communicate SIMULINK based control algorithm with induction motor drive, it is necessary to introduce I/O interfaces into the model using dSPACE real-time interfacing (RTI) blocks. This will allow the simulation to interface with the hardware. A model will be created with SIMULINK and RTI blocks using the SIMULINK® Coder™. This generates the C code and the RTI build process compiles the generated C code and links the object files and libraries into an executable application. This application directly downloads to the real-time processor after the compilation (build). The build status is displayed in the MATLAB command window and generates four files namely

PPC : The real-time application to be downloaded to a Power PC board

MAP : Map file with address information of variables.

TRC : Variable description files to use by Control Desk.

SDF : System description files with reference to PPC, MAP and TRC files

Using the information from the SDF, control desk can read and write the variables in real-time. Control desk provides numerous instruments to access, measure and display the various parameters in the real-time implementation.

2.8 Experimental results.

To validate the effectiveness of MPCC and MPDPC, the experimental test studies are conducted on the laboratory scale setup developed. The test scenarios of the experimentation are similar to the simulation studies. The results for steady-state and dynamic response of the control approaches are experimentally verified and the results are compared with the classical PI-SVM and LUT-DPC for current and power control, respectively.

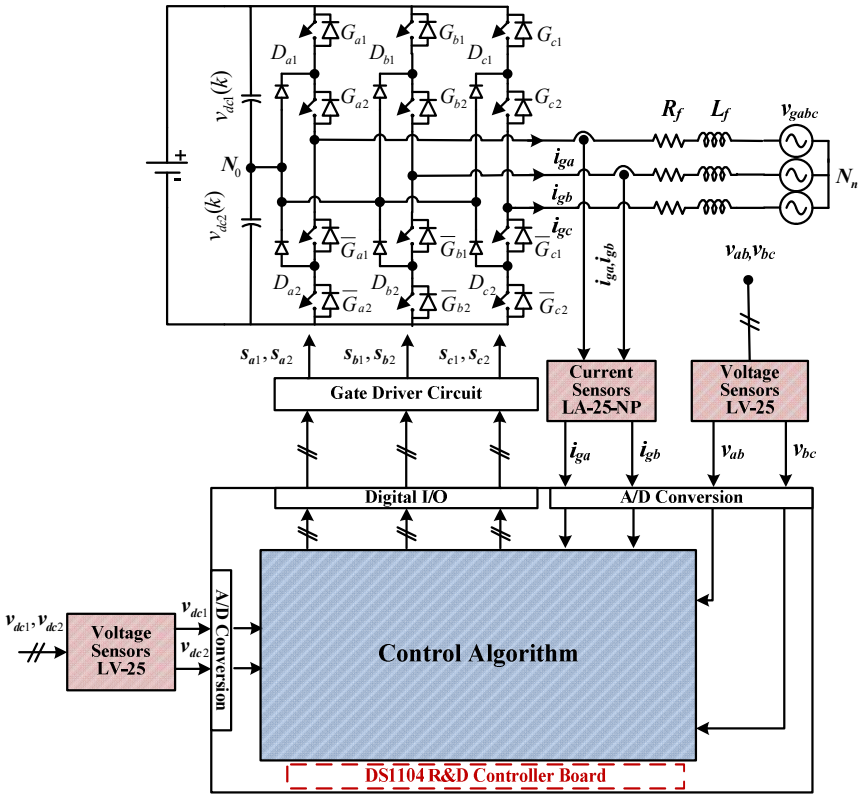

Fig.2.19. Block diagram of the experimental setup of grid-tied 3L-NPC inverter

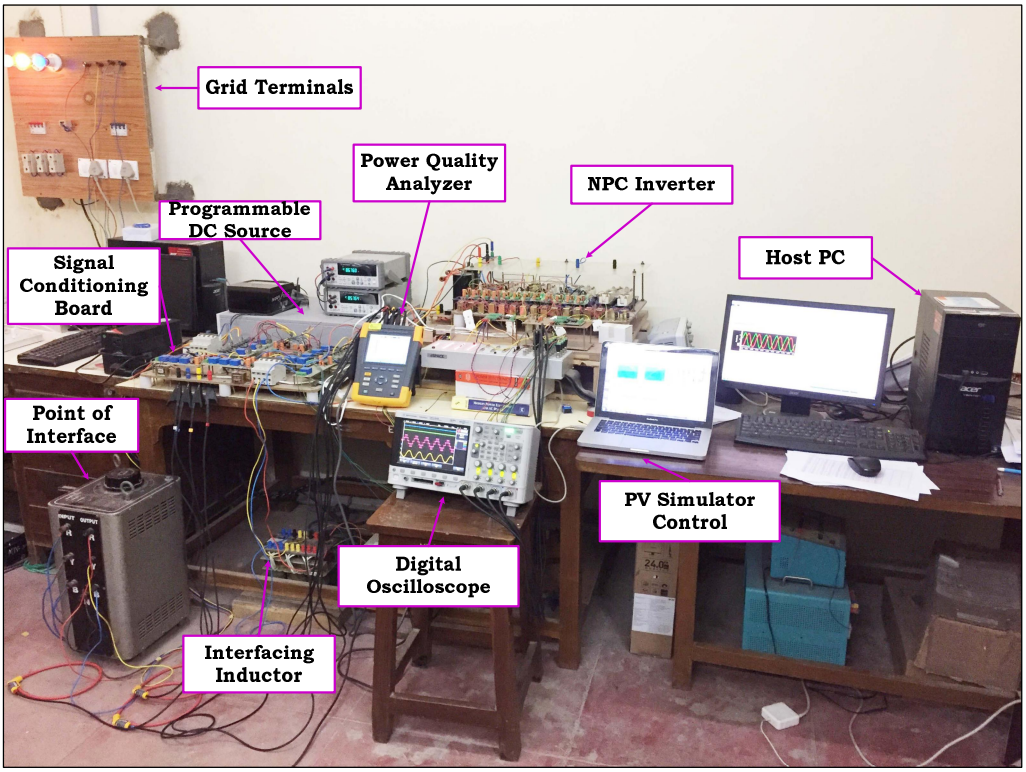

Fig.2.20. Photograph of experimental setup for grid-tied 3L-NPC inverter.

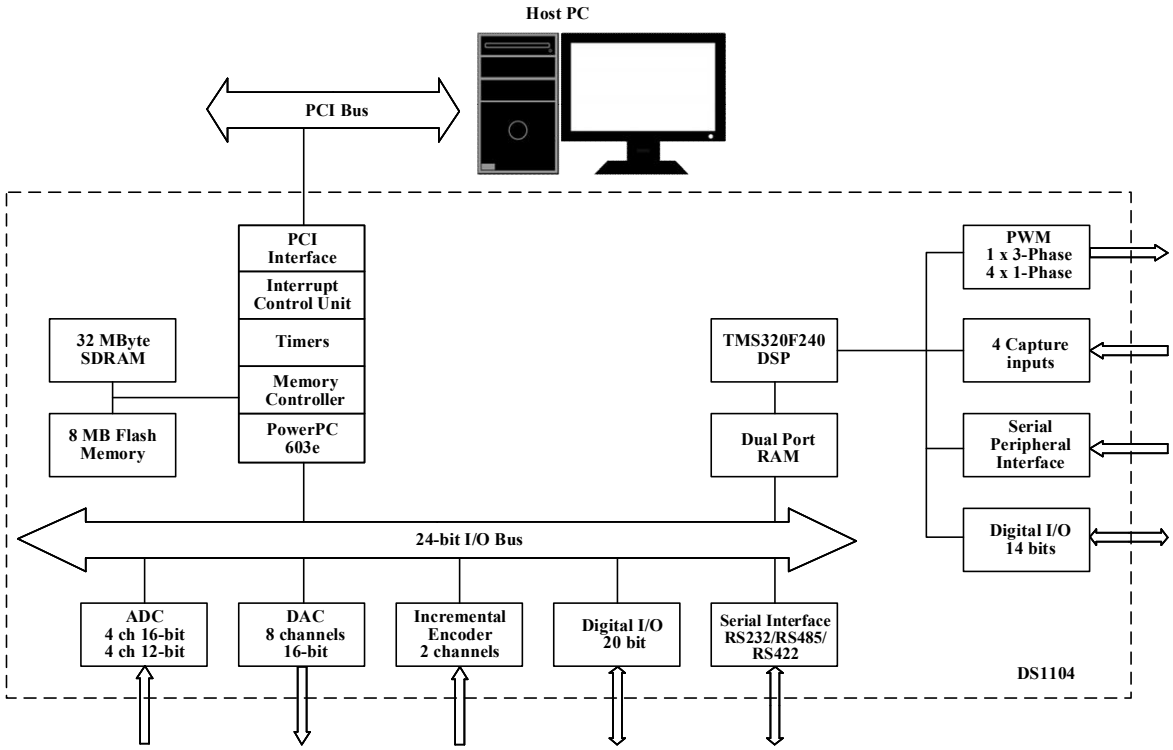

Fig.2.21. Block diagram of dSPACE DS-1104 R&D controller board

The experimental results for steady-state response of PI-SVM and MPCC approaches are shown in Fig.2.22 (a) and Fig.2.22 (b), respectively. The DC-link voltage is set to 180 V and a reference current of 4.8 A is commanded for injection. The FFT of the injecting currents and the inverter output voltage for both the control approaches are shown in Fig.2.23 and Fig.2.24, respectively. These results illustrates that, though the injecting currents and inverter output voltage with MPCC has a wide spectrum spread up to the sampling frequency, the harmonic distortion is low compared to the PI-SVM.

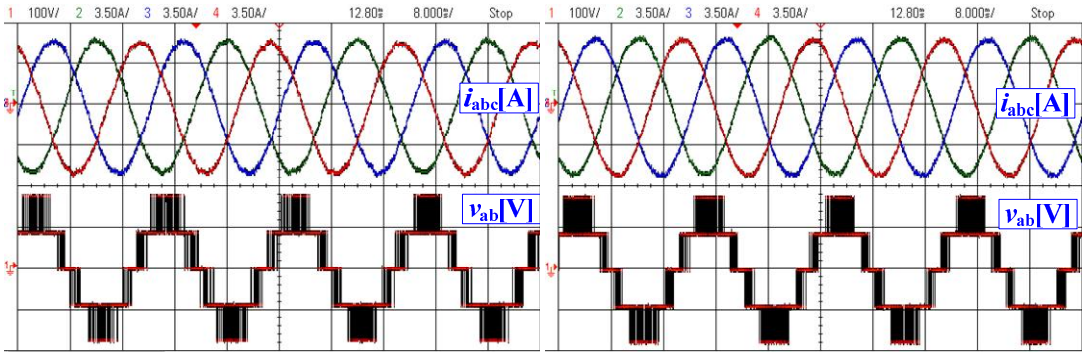

(a) (b)

Fig.2.22. Experimental results for steady-state response of current (a) PI-SVM (b) MPCC

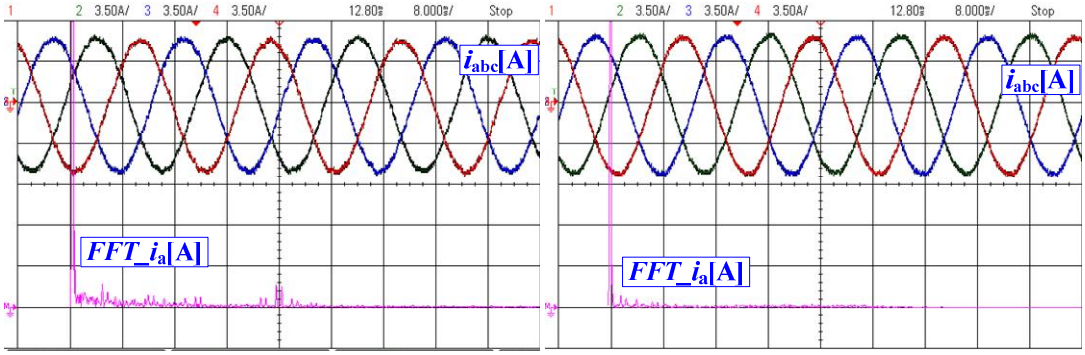

(a) (b)

Fig.2.23. Experimental results for %THD of current (a) PI-SVM (b) MPCC

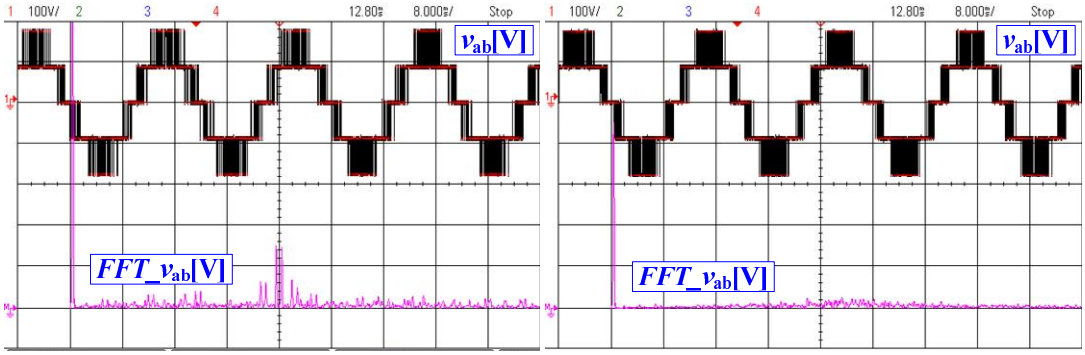

(a) (b)

Fig.2.24. Experimental results for %THD of voltage (a) PI-SVM (b) MPCC

Further, the dynamic response of PI-SVM and MPCC are verified by applying a step-change in current from 4 A to 6 A peak. The controller parameters for PI-SVM are tuned to obtain comparable dynamics however; MPCC has faster current dynamics comparatively which can be seen in Fig.2.25.

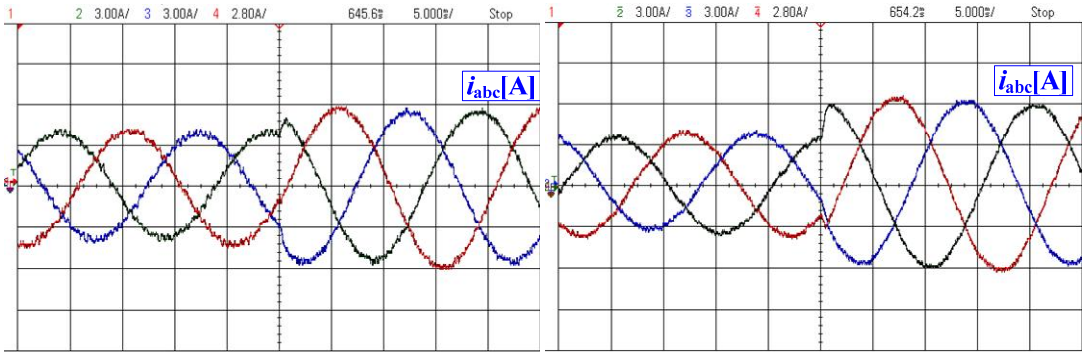

(a) (b)

Fig.2.25. Experimental results for dynamic response of voltage with (a) PI-SVM (b) MPCC

The experimental results for steady state power injection with LUT-DPC and MPDPC are shown in Fig.2.26. Both the control approaches are implemented with a sampling time T_s of

50μs. The DC-link voltage is set to 180 V. The hysteresis band for active power, reactive power and the DC-link voltages in LUT-DPC are considered as 50 Watts, 50 Var and 0.5 V respectively. Similarly, in case of MPDPC the objective function is defined with active-reactive power tracking and DC-link capacitor voltage balancing objectives. The results for active power injection of 800 Watts with reactive power reference of 0 Var for LUT-DPC and MPDPC are shown in Fig.2.26 (a) and Fig.2.26 (b), respectively. The FFT of injecting currents with LUT-DPC and MPDPC are shown in Fig.2.27 (a) and Fig.2.27 (b), respectively. It can be observed that the harmonic spectrum for both the control approaches is wide spread. From the results it can be seen that the MPDPC has a lower current harmonic distortion compared to the classical LUT-DPC.

In order to verify the dynamic response of LUT-DPC and MPDPC, a step-change in reactive power reference Q^*_g from +600 Var to -600 Var is observed by keeping active power P^*_g at 600 Watts. Similar to the steady-state the dynamic response of the system is observed by keeping the DC-link voltage to 180 V. From Fig.2.28, it can be observed that the time taken for the step change in reactive power with MPDPC is approximately 2ms which is very fast compared 8ms of the LUT-DPC. Further, a performance comparison of MPCC and MPDPC is presented in Table.2.5.

In order to validate the impact of weighting factor on the capacitor voltage balancing, a resistor of 50 Ω is connected across one of the DC-link capacitor. The weighting factor λ_{dc} is changed from 0.1 to 0 and back to 0.1. The result for change in DC-link capacitor voltages with change in weighting factor is shown in Fig.2.29. The deviation in DC-link voltage affect the inverter output voltage and hence the injecting currents. It can be seen that the DC-link capacitor voltages deviate with its reference as the weighting factor is changed to zero and gets balanced again after applying the weighting factor.

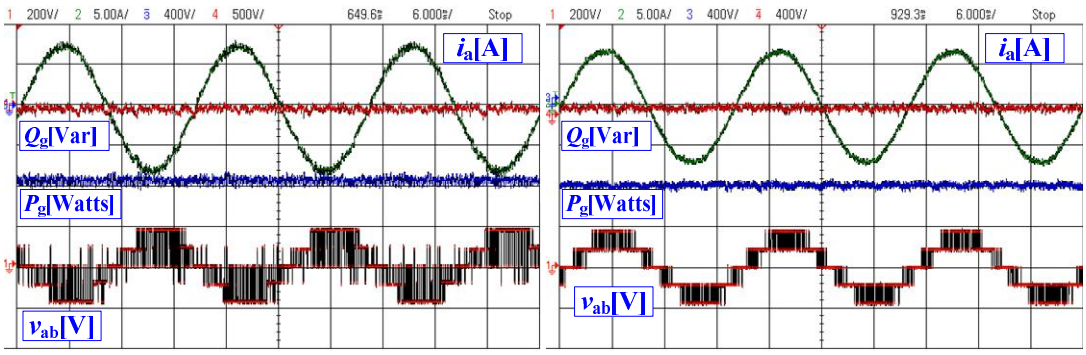

(a) (b)

Fig.2.26. Experimental results for steady-state response of voltage with (a) LUT-DPC (b) MPDPC

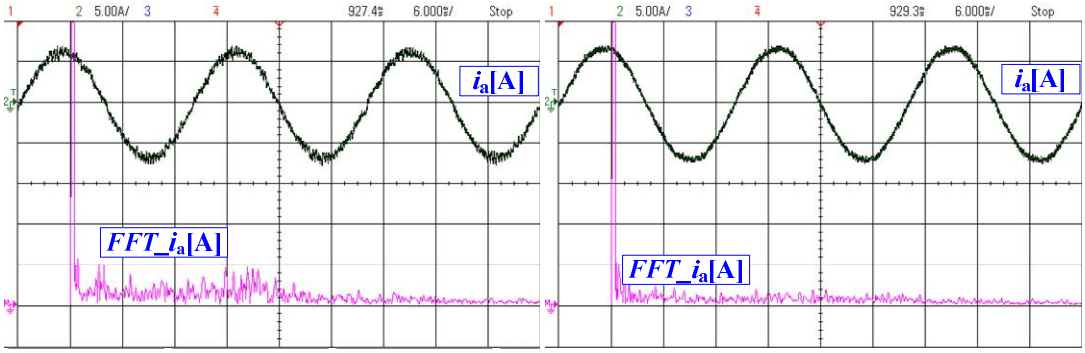

(a) (b)

Fig.2.27. Experimental results for %THD of current with (a) LUT-DPC (b) MPDPC

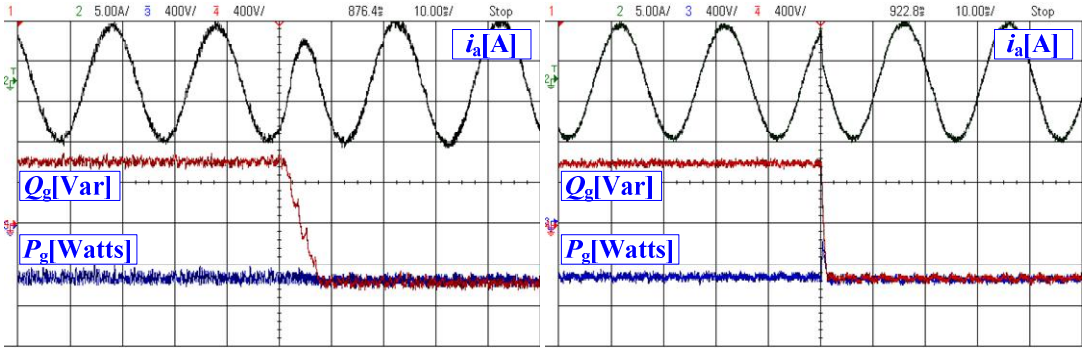

(a) (b)

Fig.2.28. Experimental results for dynamic response of voltage with (a) LUT-DPC (b) MPDPC

Further, Fig.2.30 (a) illustrates the CMV mitigation for 3L-NPC inverter with different weighting factors. The objective function is defined with current tracking, DC-link capacitor voltage balancing and common-mode voltage reduction objectives. The weighting factor for capacitor voltage balancing λ_{dc} is adjusted to maintain the DC-link balance even after including the CMV reduction objective. Initially the λ_{cm} is kept zero and the corresponding CMV is shown in Fig.2.30 (b), then the weighting factor λ_{cm} is changed to 0.12 and further increased to 0.56. The reduction of CMV with λ_{cm} of 0.12 and 0.56 is shown in Fig.2.30 (c) and Fig.2.30 (d), respectively. The reduction in CMV with increase in λ_{cm} validates that as the weighting factor increases the CMV is reduced.

The change in switching frequency with change in weighting factor λ_{swf} for 3L-NPC inverter is shown in Fig.2.31. Similar to the simulation case study initially the weighting factor λ_{swf} is kept zero and the average switching frequency F_{swa} of the output voltage is found to be 1.48 kHz. On increasing λ_{swf} to 0.24 the F_{swa} is observed to be 680 Hz and further increased to 1.2 the F_{swa} of the inverter is observed to be 342 Hz. During this change in weighting factor λ_{swf} the DC-link voltage balanced by appropriately adjusting the

weighting factor λ_{dc}. It can be seen that as the weighting factor increases the switching frequency of the inverter decreases and correspondingly there is an effect on injecting currents.

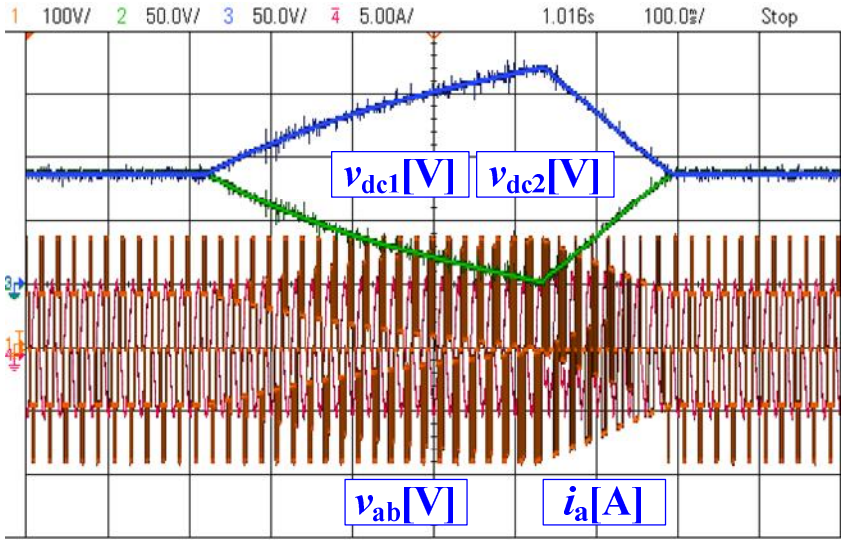

Fig.2.29. Experimental results for DC-link capacitor voltage balancing with change in $\lambda_{dc.}$

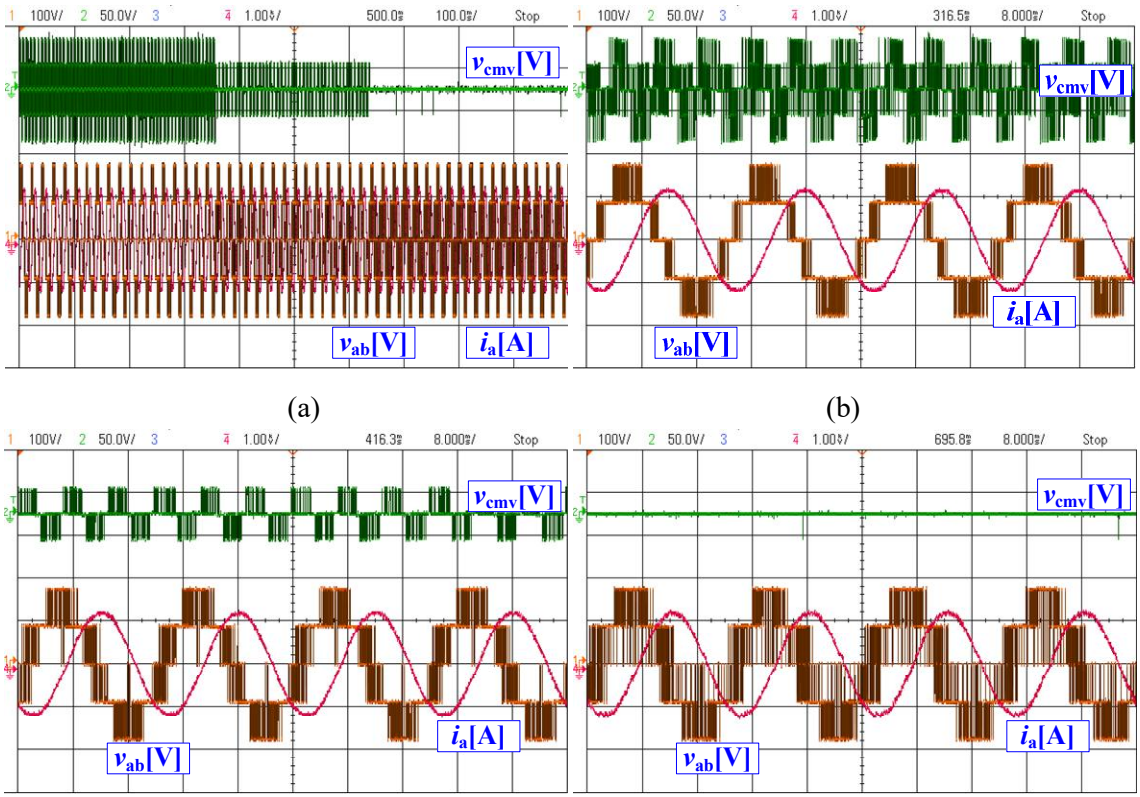

Fig.2.30. Experimental results for CMV mitigation with change in λ_{cm} (a) varying λ_{cm} (b) for λ_{cm}=0 (c) for λ_{cm}=0.12 (d) for λ_{cm}=0.56

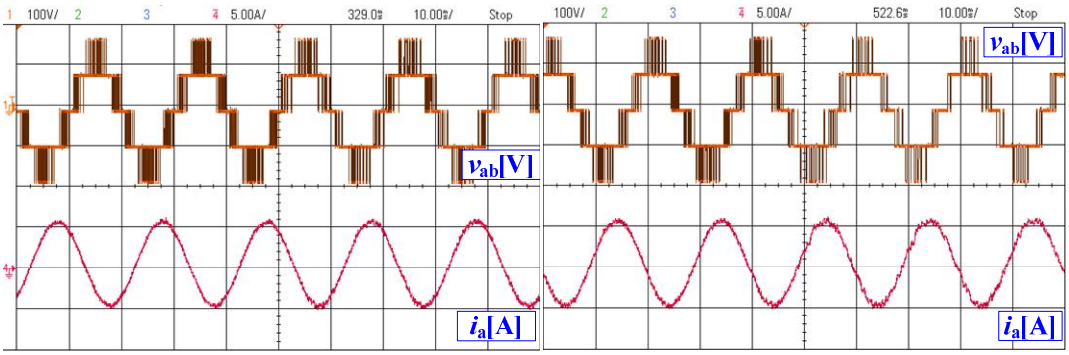

(a) (b)

Fig.2.31. Experimental results for switching frequency minimization with change in λ_{sfw} (a) from 0 to 0.24 (b) from 0.24 to 1.2

Table.2.5. Comparison of system performance with MPCC and MPDPC

Parameter	Indices	MPCC		MPDPC	
		Sim.	Exp.	Sim.	Exp.
Current	% THD	2.43%	2.96%	2.45%	3.01%
	Fund. Mag.	4.79 A	4.45 A	4.78 A	4.36 A
Inverter Voltage	% THD	40.68%	53.24%	46.68%	64.13%
	Fund. Mag.	95.19 V	93.60 V	96.46 V	94.27 V

2.9 Summary

In this chapter, design and implementation of two FCS-MPC schemes namely MPCC and MPDPC for grid tied 3L-NPC inverter are presented. The detailed discrete-time model of 3L-NPC inverter, DC-link, grid and the CMV of the inverter are given in this chapter. The main objectives of control considered are current tracking in MPCC, active-reactive power tracking in MPDPC along with DC-link capacitor voltage balancing. As the objective function contains more than one control variable, the weighting factors are used to maintain the relative importance between these objectives. Selection of weighting factor is the only parameter to be tuned in the multi-objective FCS-MPC. An empirical method is used to select the suitable weighting factor for the DC-link capacitor voltage balancing in the objective function. The simulation and experiments results are presented with the selected weighting factors. These results are compared with the classical PI-SVM and LUT-DPC for current and power control approaches, respectively. The results for steady-state and dynamic response of the system with these controllers are presented. The results validate the effectiveness of the predictive control approaches in terms of the %THD and the time of response. Further, to incorporate the additional control objective like CMV mitigation and switching frequency reduction required for grid tied PV inverters with the classical control

approaches is difficult as their design becomes more complex. Compared to the classical approaches, the inclusion of additional control objectives with FCS-MPC is simple. The additional control objectives are modelled in terms of switching states and included in the objective function. However, selection of weighting factors for these multiple objectives with the empirical approach is complex. To address this issue, direct optimization method and MCDM methods are investigated for the simplification in selection of weighting factors.

Chapter-3
FCS-MPC for Single-Stage Grid-Tied SPECS

3.1 Introduction

The rapid development of solar photovoltaic energy resources has enabled a wide scope for the evolution of multi-level inverter topologies and their control techniques. Especially with the increase in power ratings, the requirement of high power multi-level inverters guarantee lower harmonic distortion, minimization of leakage currents, and higher power conversion efficiency etc., to meet the strict grid-codes. Control of multi-level inverter based solar photovoltaic energy conversion systems (SPECS) require advanced control strategies to meet these requirements. FCS-MPC is one of the advanced control strategies which have been emerged recently for the applications of power converters and energy conversion systems. The inimitable features of FCS-MPC are: intuitive concept, inherent discrete nature, easy inclusion of constraints and fast dynamic response. Compared to the classical approaches, FCS-MPC combines the controller and modulation into a single objective function optimization to directly generate the switching state. Hence, FCS-MPC is also known as "direct model predictive control" (DMPC). A generalized procedure to implement the FCS-MPC for grid-tied 3L-NPC inverter is presented in Chapter 2. In this chapter, application of MPCC and MPDPC approaches for a single-stage grid-tied 3L-NPC PV inverter are introduced and experimentally evaluated.

3.2 Modeling and design of single-stage grid-tied SPECS.

A schematic diagram of a single-stage grid-tied 3L-NPC PV inverter is shown in Fig.3.1. This system consists of a PV array connected across the floating DC-link of 3L-NPC inverter, 3L-NPC VSI, DC-link capacitors C_1 and C_2, and interfacing filter inductor L_f with its internal resistance R_f. The 3L-NPC PV inverter is connected to a three phase grid whose voltages and currents are represented as v_{gx} & i_{gx} of phase $x \in \{a, b, c\}$ respectively. The PV array is composed of series (n_s) and parallel (n_p) connected PV panels. Each PV panel consists of series-connected (N_{ss}) PV cells. Where, v_{pv} and i_{pv} are the voltage across and current through the PV array. The closed loop control of single-stage grid-tied SPECS necessitates the regulation of floating DC-link to its reference obtained from the MPPT algorithm. A simple perturb & observe (P&O) MPPT algorithm is used to determine the reference and a linear PI controller is used to regulate the DC-link voltage. The interfacing filter inductor L_f is connected on the AC-side of 3L-NPC inverter. The function of interfacing filter inductor is to limit the current ripple in the injected currents. The modeling

of PV array and the detailed design of inverter DC-link, interfacing filter inductor (L_f) and the DC-link voltage controller are presented in the following sub-sections.

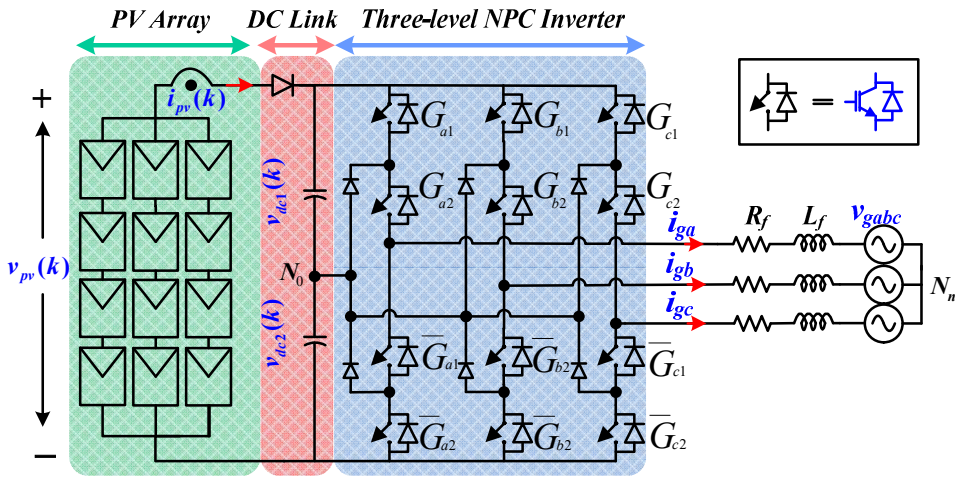

Fig.3.1. Schematic diagram of grid tied 3L-NPC PV inverter

3.2.1 Modeling of PV array

The electrical equivalent circuit of the solar PV array is shown in Fig.3.2. The mathematical model of the PV array is given as:

$$i_{pv} = i_{pvg} - i_0 \left[\exp\left(\frac{v + R_s i_{pv}}{v_t \alpha} \right) - 1 \right] - \left(\frac{v_{pv} + R_s i_{pv}}{R_p} \right) \tag{3.1}$$

Where i_{pvg} and i_0 are the light-generated current and saturation current of PV cell respectively which are given as:

$$i_{pvg} = \left(i_{pvn} + K_i (T - T_n) \right) \frac{G}{G_n} \tag{3.2}$$

$$i_0 = i_{0n} \left(\frac{T_n}{T} \right)^3 \exp\left[\frac{qE_g}{\alpha k} \left(\frac{1}{T_n} - \frac{1}{T} \right) \right] \tag{3.3}$$

$$i_{0n} = \frac{i_{scn}}{\exp\left(V_{ocn} / \mathrm{a} V_{tn} \right) - 1} \tag{3.4}$$

$$v_t = \frac{N_s k T}{q} \tag{3.5}$$

Where $i_{scn}, V_{pv}, T, T_n, G, G_n, E_g, q, k, K_i, \mathrm{a}, V_{ocn}, i_{0n}, R_s$ and R_p are the short circuit current,

PV output voltage, cell temperature, reference temperature, solar irradiance, reference irradiance, band gap energy, electron charge, Boltzmann's constant, short circuit temperature coefficient, diode ideality constant, open circuit voltage, nominal saturation current, series and parallel resistance of PV cell respectively. Fig.3.3 illustrates the current *vs* voltage (I-V curve) and power *vs* voltage (P-V curve) characteristics of PV array at different irradiance and temperature levels.

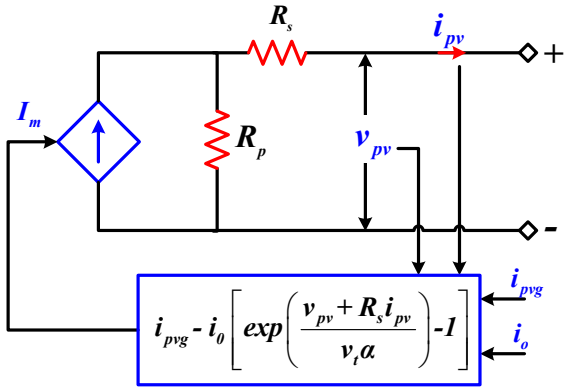

Fig.3.2. Electrical equivalent circuit of PV-array

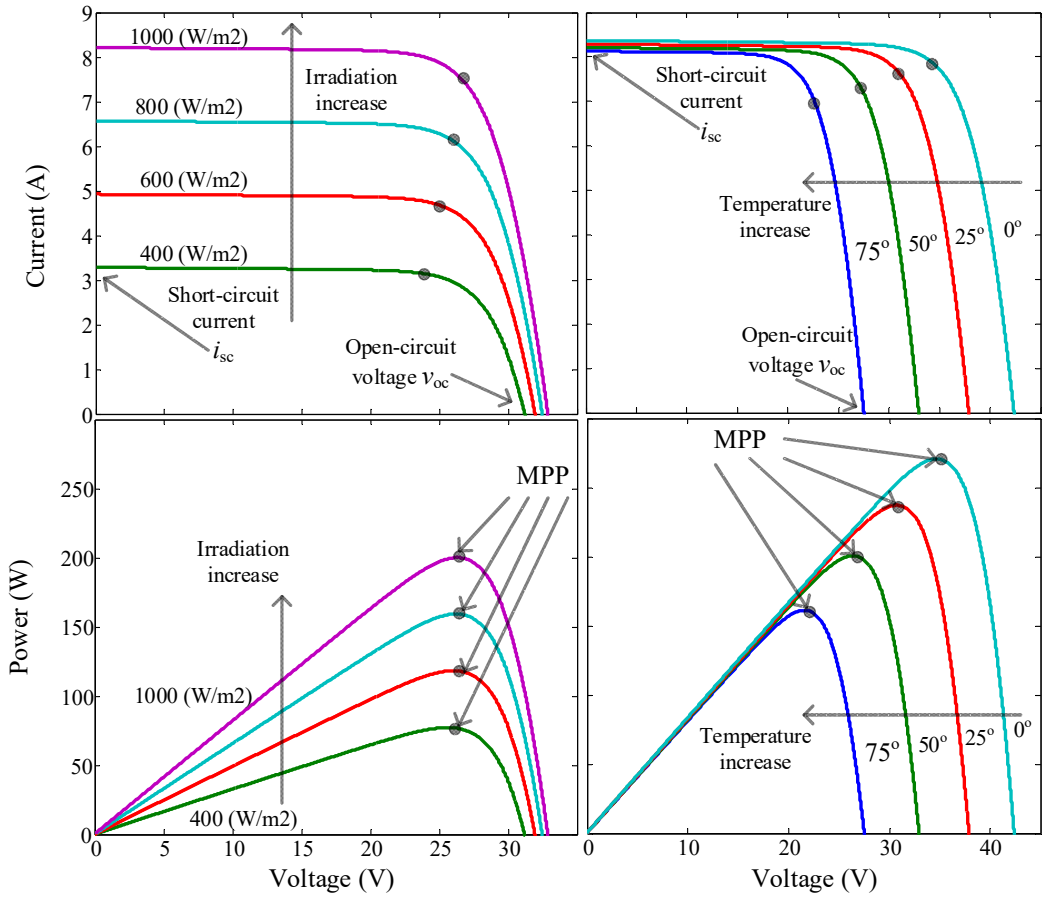

Fig.3.3. PV-array characteristics

3.2.2 Design of DC-link voltage and capacitance

In order to ensure proper operation of a single-stage grid-tied PV inverter, the minimum DC-link voltage (also known as PV cut-in voltage) has to be higher than twice the peak line-to-line voltage of the grid. An analytical expression describing the selection of minimum DC-link voltage of a single-stage grid-tied PV inverter by considering a sinusoidal pulse width modulation (SPWM) approach [126] is given as

$$V_{dc\_\min} = \frac{2\sqrt{2}V_{L-L}}{\sqrt{3}m_{mi}} \tag{3.6}$$

Where, $V_{L\text{-}L}$ is the line-line RMS voltage of the grid, and 'm_{mi}' is the maximum modulation index of the inverter. Generally, the maximum modulation index of the single-stage PV inverter is selected well below the maximum linear modulation index of m=1 (with reference to SPWM) to ensure proper margin for the adjustments in DC-link voltage during the transients.

The DC-link of 3L-NPC inverter consists of two identical split-capacitors C_1 and C_2 sharing equal voltages v_{dc1}=v_{dc2}=v_{dc}/2. The effective capacitance (C_{eff}) across the DC-link is C_{eff} = C_1/2 or C_2/2. The value of the DC-link capacitance has significant affect on the performance of the DC-link voltage controller. In this work, the size of the capacitors is selected to meet the criteria's of 1) stability related to control performance of the application and 2) voltage ripple during the transients and abnormal operation. The details are as follows:

***1) Stability criteria related to control performance of the application*:** Single-stage grid-tied PV inverters are controlled by using a cascaded control scheme. The cascaded control scheme consists of outer DC voltage control loop to regulate the DC-link voltage for extracting the maximum power and inner current/power control to regulate the active and reactive powers injected to the grid. It is been explored that there exist a right-half-plane (RHP) pole in the control dynamics of photovoltaic inverter effecting the minimum required DC-link capacitance. To achieve the stability in the control and enhance the reliability, significant design rules to select the DC-link capacitance are presented in [127]. The design criteria and the selection of minimum capacitance required to ensure stable operation as presented in [127] are as follows:

The minimum value of capacitance is given as

$$C_{\min} = K_{RHP} K_i \frac{I_{SC}}{V_{pv\_\min} \omega_C} \tag{3.7}$$

Where K_{RHP} is the safety factor and K_i is the cloud enhancement factor considering the worst-case output current of PV generator. I_{SC} and V_{pv_min} are the short circuit current and minimum cut-in voltage of the PV array. Further, ω_C is the crossover frequency of the outer DC-link voltage control loop and ω_{grid} is the fundamental frequency of the grid. Both the crossover frequency and grid frequency are related as $\omega_C = K_{grid}\omega_{grid}$. Here, K_{grid} is the grid frequency gain. The parameters K_{RHP}, K_i and K_{grid} are considered as 2, 1.5 and (0.2–0.7) respectively as per the guidelines provided in [127].

***2) Voltage ripples during the transients and abnormal operation*:** In this work, the grid-interfaced 3L-NPC PV inverter is also works as shunt compensator to provide the reactive power support to the grid. The main criterion for DC link capacitor sizing is to make sure about the converter capability in the regulation of voltage during the transients. The main principle involved is the energy stored in the capacitor to a multiplication of the converter rated power (S_{rated}) by a specified period of time e.g. 0.5 – 1 cycle [128] The typical relation is as follows:

$$C_{eff} = \frac{2K_S S_{rated} T_{trans}}{\left(V_{dc,\max}^2 - V_{dc,\min}^2\right)} \tag{3.8}$$

Where, K_S is the coefficient that determines the share of converter rating for a specified transition period (T_{trans}).

3.2.3 Selection of interfacing filter inductor

In order to ensure proper tracking of reference injecting currents, the selection of interfacing filter inductor value plays a vital role. Interfacing filter inductor is selected based on the desired maximum current ripple (Δi_{rp}) of injecting currents for a given switching frequency and also based on the magnitude of DC-link voltage [129]. The analytical expression for the selection of filter inductor can be obtained by volt-second balance of inductor dynamics for a given time period as [36], [126], [129], [130]

$$L_f = \frac{\sqrt{3} m_{mi} V_{dc}}{12 a f_{sm} \Delta i_{rp}} \tag{3.9}$$

Where, '*a*' is the scaling/overloading factor, f_{sm} is the maximum switching frequency, and m_{mi} is maximum modulation index considered for the inverter.

3.2.4 Design of DC-link voltage controller

Design of DC-link voltage controller is one of the key aspects of single-stage grid-tied solar photovoltaic systems. In this work, a symmetrical optimum (SO) technique is used to design the controller gains [131]. The dynamics of the DC-link voltage controller influences the performance of control algorithm. The DC-link voltage dynamics of single-stage grid-tied SPV inverter is modeled as

$$\frac{1}{2} C_{dc} \frac{dv_{dc}^2}{dt} = P_{pv} - P_{inv} \tag{3.10}$$

Where, C_{dc} is the equivalent DC-link capacitance given as $C_{dc}=C_1/2=C_2/2$

From Eq. (3.10), the charge status of the DC-link capacitor can be regulated by controlling the net power at the DC-link. A controller which regulates the DC-link voltage will provide the reference power (P_g^*) to the inner control loop.

Considering a PI controller which processes the voltage error with power quantity (P_g^*) as the reference is given as:

$$H_{Vdc} = \frac{P_g^*(s)}{\left(v_{dc}^*(s)\right)^2 - \left(v_{dc}(s)\right)^2} = \frac{k_p(1+T_c s)}{T_c s} \tag{3.11}$$

Where, k_p is the proportional gain and T_c is controller time constant.

The block diagram of the DC-link voltage control loop with power reference is shown in Fig.3.4. The inner current/power controller dynamics is given as:

$$G_i(s) = \frac{1}{(1+T_{i\sigma} s)} \tag{3.12}$$

Where, $T_{i\sigma}$ = 4(Ts +T_{PWM}) is the inner-loop time constant which is designed based on SO criterion.

The open loop transfer function $H_{oVdc}(s)$ is given as:

$$H_{oVdc}(s) = \frac{2k_p(1+T_c s)}{T_c s(1+T_{i\sigma} s)C_{dc} s} \tag{3.13}$$

According to SO, the amplitude and phase plot of $H_{oVdc}(s)$ are symmetrical about the crossover frequency ω_c. For a given phase margin, the crossover frequency ω_c is given as:

$$\omega_c = \frac{1}{aT_{i\sigma}} \tag{3.14}$$

$$a = \frac{1+\cos\gamma}{\sin\gamma} = \sqrt{\frac{T_c}{T_{i\sigma}}} \Rightarrow a > 1 \tag{3.15}$$

Where, γ - given phase-margin and a - is the corresponding factor.

The controller gain k_p at gain crossover frequency ω_c is given as:

$$k_p = \frac{C_{dc}}{a2T_{i\sigma}} \tag{3.16}$$

Finally, the closed loop transfer function of the DC-link voltage loop is given as:

$$H_{cVdc}(s) = \frac{(1+T_c s)}{a^3 T_{i\sigma}^3 s^3 + a^3 T_{i\sigma}^2 s^2 + a2T_{i\sigma} s + 1} \tag{3.17}$$

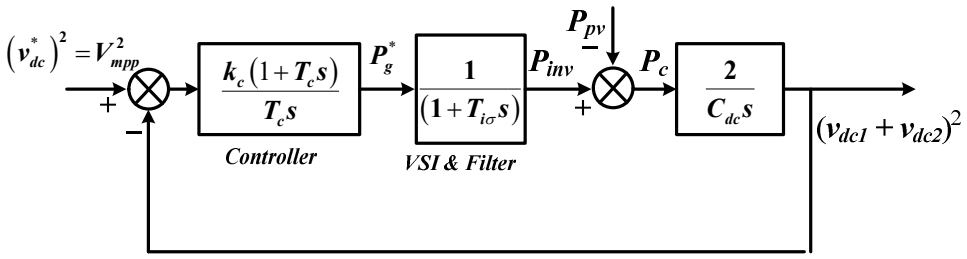

Fig.3.4. Block diagram of DC-link voltage control loop

3.2.5 Maximum power point tracking algorithm

Perturb and Observe (P&O) is one of the simplest and commercially accepted MPPT algorithms. In this algorithm, the change in PV power upon change in PV voltage is used to determine the slope of the operating point. The correction in reference MPPT voltage can be achieved in both positive and negative slope regions. The correction in reference MPPT voltage is made at a constant sampling rate to track the MPPT irrespective of change in operating conditions. This P&O MPPT algorithm is employed to determine the reference

voltage for floating DC-link of the inverter. Fig.3.5 shows the flow chart of the P&O MPPT algorithm.

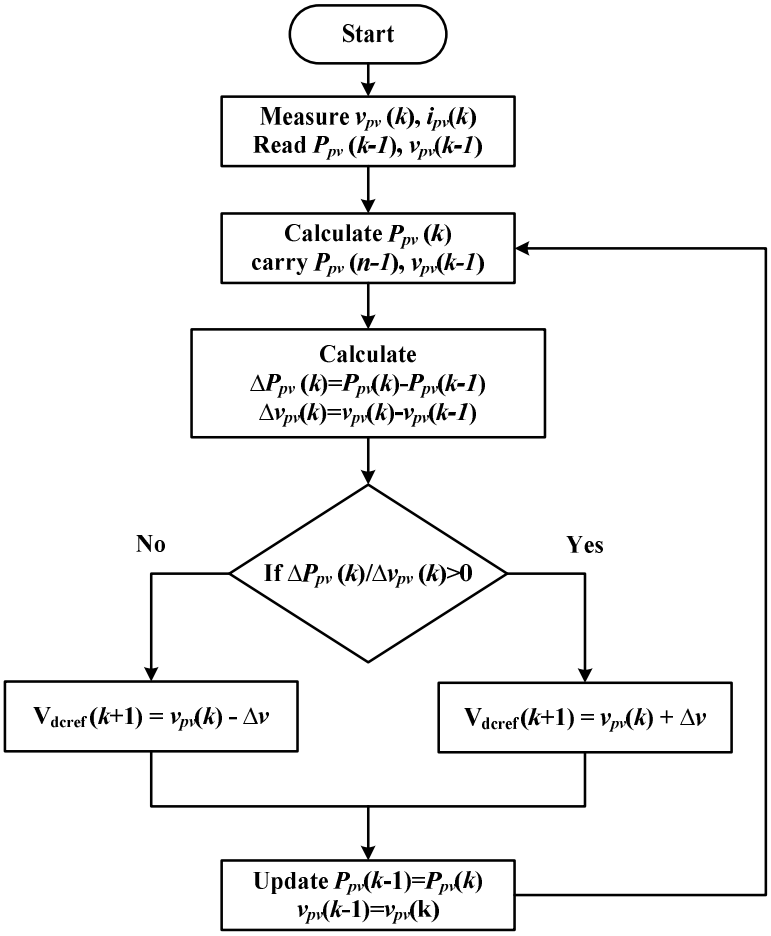

Fig.3.5. Flowchart for P&O MPPT algorithm

3.3 MPCC for 3L-NPC PV inverter.

The MPCC scheme for a single-stage grid-tied 3L-NPC PV inverter is shown in Fig.3.6. The PV array with a series diode is connected across the floating DC-link of the inverter to have a unidirectional power flow. The control scheme consists of two-cascaded loops i.e., inner predictive current control loop and an outer DC-link voltage control loop. In order to extract the maximum power from the PV array, the DC-link voltage has to be regulated to its reference obtained from P&O based MPPT algorithm. The DC-link voltage is regulated by using the classical proportional-integral (PI) controller. The outer DC-link voltage controller provides the reference active power (P^*) required to be injected into the grid whereas the reactive power reference (Q^*) is provided by the grid operator.

The reference current components for active and reactive power injection are given as

$$i_{g\alpha}^{*}(k)=\frac{2}{3}\left(\frac{v_{g\alpha}^{+}(k)P^{*}(k)+v_{g\beta}^{+}(k)Q^{*}(k)}{v_{g\alpha}^{+2}(k)+v_{g\beta}^{+2}(k)}\right) \tag{3.18}$$

$$i_{g\beta}^{*}(k)=\frac{2}{3}\left(\frac{v_{g\beta}^{+}(k)P^{*}(k)-v_{g\alpha}^{+}(k)Q^{*}(k)}{v_{g\alpha}^{+2}(k)+v_{g\beta}^{+2}(k)}\right) \tag{3.19}$$

Where $v_{g\alpha}^{+}$, $v_{g\beta}^{+}$ are the fundamental positive sequence voltages estimated by using second-order generalized integrator (SOGI) [132] at k^{th} instant.

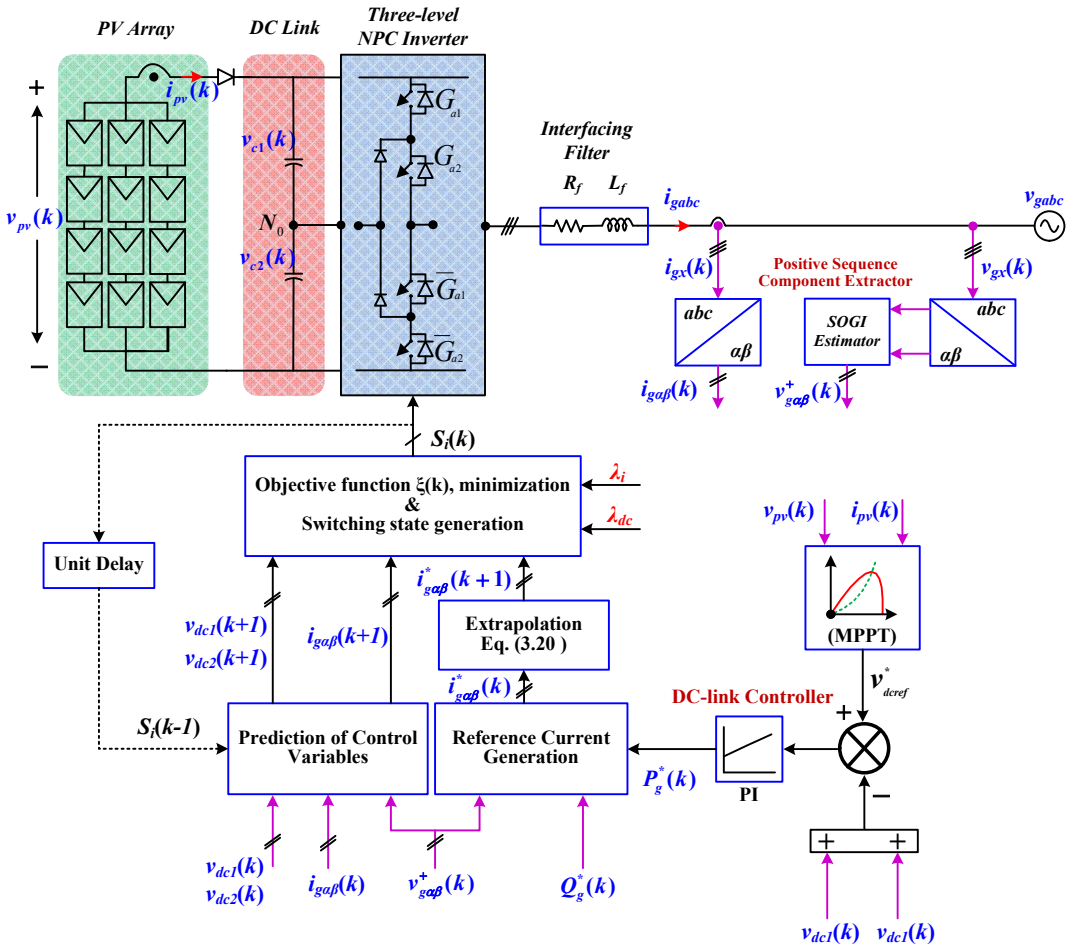

Fig.3.6. MPCC scheme for single stage grid-tied 3L-NPC PV inverter

The reference currents obtained are extrapolated by using Lagrange's method to estimate their values at $(k+1)$ and $(k+2)$ ahead samples by using present and previous sample values of currents as presented below

$$\vec{i}_{g\alpha\beta}^{*}(k+1)=3\vec{i}_{g\alpha\beta}^{*}(k)-3\vec{i}_{g\alpha\beta}^{*}(k-1)+\vec{i}_{g\alpha\beta}^{*}(k-2) \tag{3.20 a}$$

$$\vec{i}_{g\alpha\beta}^{*}(k+2)=6\vec{i}_{g\alpha\beta}^{*}(k)-8\vec{i}_{g\alpha\beta}^{*}(k-1)+3\vec{i}_{g\alpha\beta}^{*}(k-2) \tag{3.20 b}$$

These reference currents are traced by applying the appropriate voltage vector to the inverter. The predictive currents $\vec{i}^{\,p}_{g\alpha\beta}(k+1)$ in Eq. (2.12) are used to determine voltage vector required in (k + 1) state using 27 admissible switching states. However, from the perspective of NPC topology, the DC-link capacitor voltage balancing is also an equally important objective for achieving the desired performance of the inverter. Hence, the discrete-time model of the DC-link capacitor voltages in eq. (2.7) & (2.8) are also used to determine the required voltage vector.

In order to achieve the current tracking and DC-link capacitor voltage balancing in concert, their objectives $\xi_i(k)$ and $\xi_{vdc}(k)$, respectively are included in the objective function $\xi(k)$. Objective function $\xi(k)$ defined with these control objectives are given as

$$\xi(k) = \underbrace{\left|i^{*}_{g\alpha}(k+1) - i^{p}_{g\alpha}(k+1)\right| + \left|i^{*}_{g\alpha}(k+1) - i^{p}_{g\alpha}(k+1)\right|}_{\xi_i(k)} + \lambda_{dc}\underbrace{\left|v^{p}_{c1}(k+1) - v^{p}_{c2}(k+1)\right|}_{\xi_{vdc}(k)} \quad (3.21)$$

Where, λ_{dc} is the weighting factor for DC-link capacitor voltage balancing. Since, the two control objectives are equally important, the weighting factor λ_{dc} is used to maintain the relative importance between the control objectives. The objective function defined is evaluated for 27 admissible switching states and the switching state which minimizes the objective function is selected for generating the voltage vector in the (k +1) sampling period.

The flowchart for the implementation of MPCC approach for single-stage grid-tied 3L-NPC PV inverter is shown in Fig.3.7 and the corresponding steps are given as follows.

Step I. Measure instantaneous grid voltages $v_{ab}(k)$ and $v_{bc}(k)$; grid currents i_a (k) and i_b (k); DC-link capacitor voltages v_{dc1} (k) and v_{dc2} (k); PV voltage $v_{\mathrm{pv}}(k)$, and PV current $i_{\mathrm{pv}}(k)$.

Step II. Convert the grid voltages and currents from natural (abc) frame to stationary orthogonal ($\alpha\beta$) frame, $\vec{v}_{g\alpha\beta}(k)$, $\vec{i}_{g\alpha\beta}(k)$. Estimate the fundamental positive sequence component of grid voltages $\vec{v}^{+}_{g\alpha\beta}(k)$.

Step III. Obtain the required active power (P*) from floating DC-link voltage controller and reactive power (Q*) from the grid operator, calculate the reference injecting currents $\vec{i}^{\,*}_{g\alpha\beta}(k)$ using Eq. (3.18) & (3.19).

Step IV. Estimate the reference currents for (k + 1) states by using Lagrange's extrapolation approach as given in Eq. (3.20a).

Step V. Predict the grid injecting currents and DC-link capacitor voltages for all the admissible switching states of the inverter by using Eq. (2.12), (2.7) & (2.8), respectively.

Step VI. Define the objective function $\xi(k)$ with the control objectives of $\xi_i(k)$ and $\xi_{vdc}(k)$ as given in Eq. (3.21).

Step VII. Evaluate the objective function defined in Eq. (3.21) for all the switching states and obtain the switching state which minimizes the objective function. The optimal switching state which minimizes the objective function is applied to the inverter in the $(k + 1)$ state.

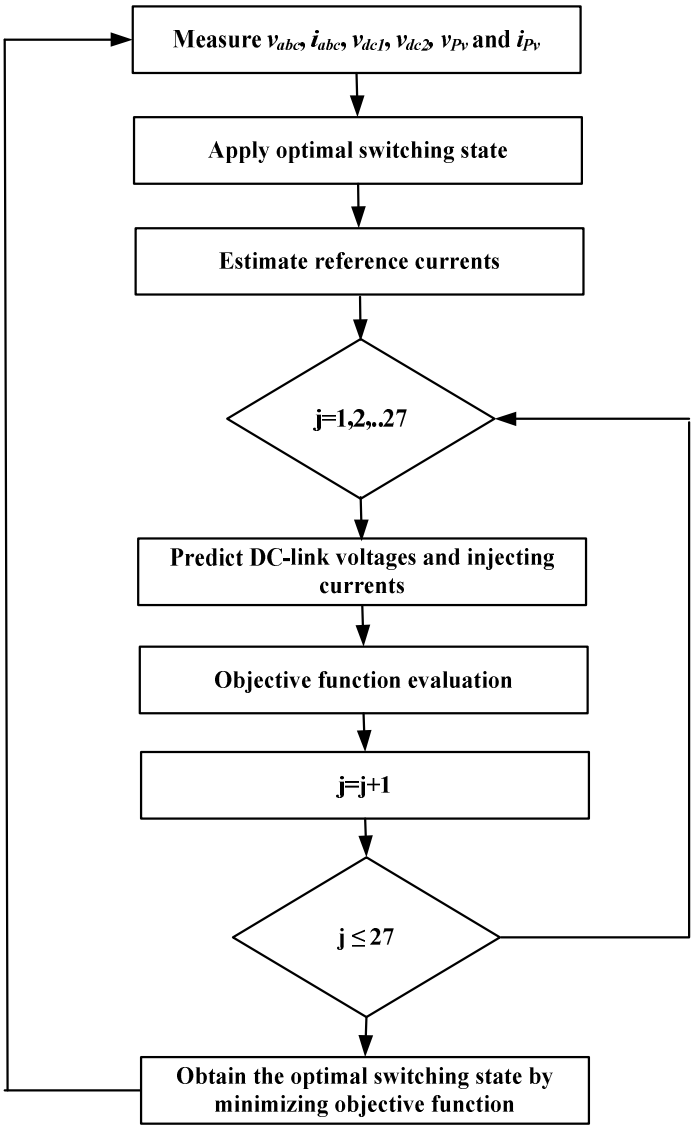

Fig.3.7. Flow chart for MPCC for grid tied 3L-NPC PV inverter

3.4 MPDPC for 3L-NPC PV inverter.

The MPDPC scheme for a single-stage grid-tied 3L-NPC PV inverter is shown in Fig.3.8. Similar to the MPCC, the MPDPC scheme also consists of two-cascaded loops i.e., inner predictive power control loop and an outer DC-link voltage control loop. In order to extract the maximum power from the PV array, the DC-link voltage is regulated to its reference obtained from P&O based MPPT algorithm.

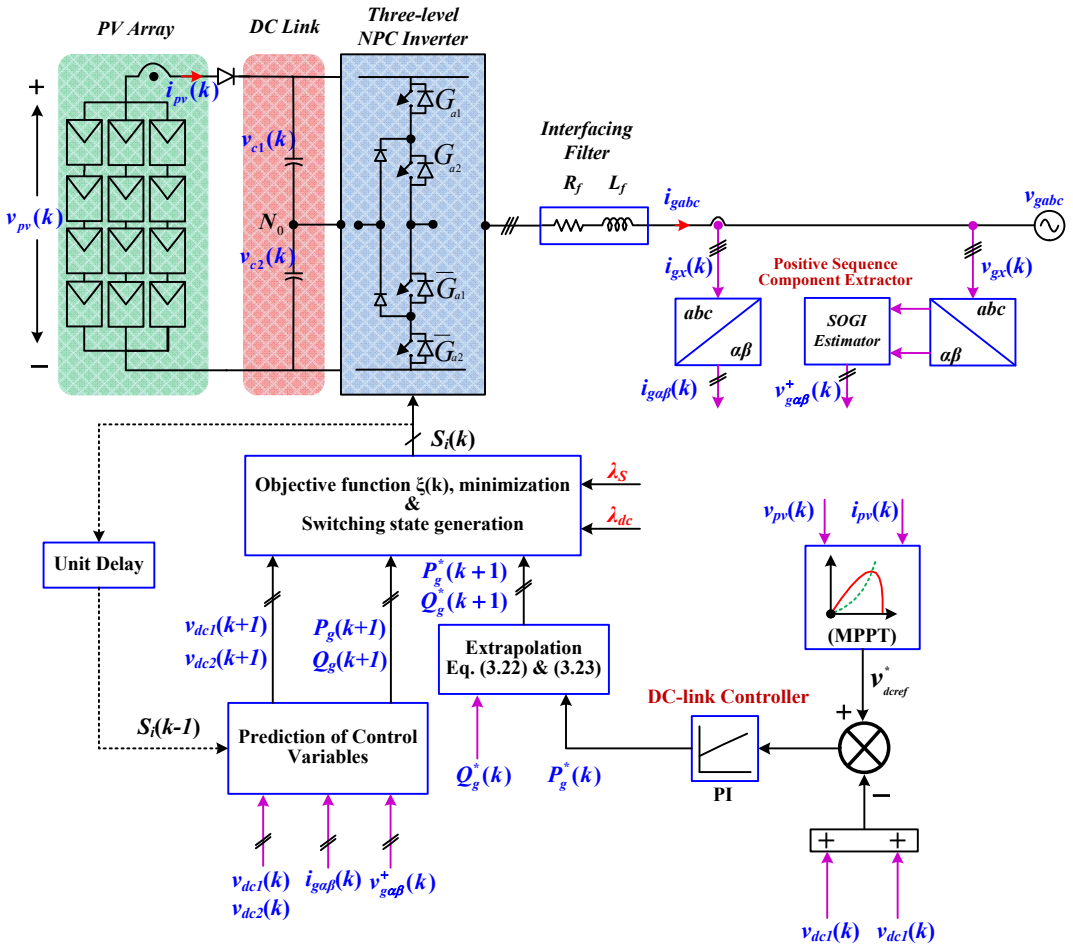

Fig.3.8. MPDPC scheme for single-stage grid tied 3L-NPC PV inverter

The DC-link voltage is regulated by using the classical PI controller. The outer DC-link voltage controller provides the reference active power (P^*) required to be injected into the grid whereas the reactive power reference (Q^*) is provided by the grid operator. Since, the reference active and reactive powers obtained are DC quantities; they can be simply extrapolated to (k + 1) state as

$$P_g^*(k+1) = P_g^*(k) = P_g^*(k-1) \tag{3.22}$$

$$Q_g^*(k+1) = Q_g^*(k) = Q_g^*(k-1) \tag{3.23}$$

The predictive powers $P_g^p(k+1)$ and $Q_g^p(k+1)$ are calculated as

$$P_g^p(k+1) = \frac{3}{2}\left(v_{g\alpha}^+(k+1)i_{g\alpha}^p(k+1) + v_{g\beta}^+(k+1)i_{g\beta}^p(k+1)\right) \tag{3.24}$$

$$Q_g^p(k+1) = \frac{3}{2}\left(v_{g\beta}^+(k+1)i_{g\alpha}^p(k+1) - v_{g\alpha}^+(k+1)i_{g\beta}^p(k+1)\right) \tag{3.25}$$

Where $\vec{i}_{g\alpha\beta}^{\,p}(k+1)$ is the predictive current obtained from eq. (2.12), and $\vec{v}_{g\alpha\beta}^{+}(k+1)$ is extrapolated grid positive voltage vector as given below

$$\vec{v}_{g\alpha\beta}^{+}(k+1) = 3\vec{v}_{g\alpha\beta}^{+}(k) - 3\vec{v}_{g\alpha\beta}^{+}(k-1) + \vec{v}_{g\alpha\beta}^{+}(k-2) \tag{3.26}$$

Objective function $\xi(k)$ defined with the power tracking $\xi_s(k)$ and voltage balancing $\xi_{vdc}(k)$ is given as

$$\xi(k) = \underbrace{\left|P_g^*(k+1) - P_g^p(k+1)\right| + \left|Q_g^*(k+1) - Q_g^p(k+1)\right|}_{\xi_s(k)} + \lambda_{dc}\underbrace{\left|v_{c1}^p(k+1) - v_{c2}^p(k+1)\right|}_{\xi_{vdc}(k)} \tag{3.27}$$

Where, λ_{dc} is the weighting factor for DC-link capacitor voltage balancing.

The objective function defined is evaluated for 27 admissible switching states and the switching state which minimizes the objective function is selected for generating the voltage vector in the (k + 1) sampling period.

The flowchart for the implementation of MPDPC approach for single-stage grid-tied 3L-NPC PV inverter is shown in Fig.3.9 and the corresponding steps are given below.

Step I. Measure instantaneous grid voltages $v_{ab}(k)$ and $v_{bc}(k)$; grid currents i_a (k) and i_b (k); DC-link capacitor voltages v_{dc1} (k) and v_{dc2} (k); PV voltage $v_{\text{pv}}(k)$, and PV current $i_{\text{pv}}(k)$.

Step II. Convert the grid voltages and currents from natural (abc) frame to stationary orthogonal ($\alpha\beta$) frame, $\vec{v}_{g\alpha\beta}(k)$, $\vec{i}_{g\alpha\beta}(k)$. Estimate the fundamental positive sequence component of grid voltages $\vec{v}_{g\alpha\beta}^{+}(k)$.

Step III. Obtain the reference active power (P*) from floating DC-link voltage controller and reactive power (Q*) from the grid operator.

Step IV. Estimate the positive sequence voltages for (k + 1) period by using Lagrange's extrapolation approach as given in Eq. (3.26).

Step V. Predict the active, reactive powers and DC-link capacitor voltages for all the admissible switching states of the inverter by using Eq. (3.24), (3.25), (2.7) & (2.8), respectively.

Step VI. Define the objective function $\xi(k)$ with the control objectives of $\xi_s(k)$ and $\xi_{vdc}(k)$ as given in Eq. (3.27).

Step VII. Evaluate the objective function defined in Eq. (3.27) for all the admissible switching states and obtain the optimal switching state which minimizes the objective function. The optimal switching state obtained is applied to the inverter in the (k + 1) state.

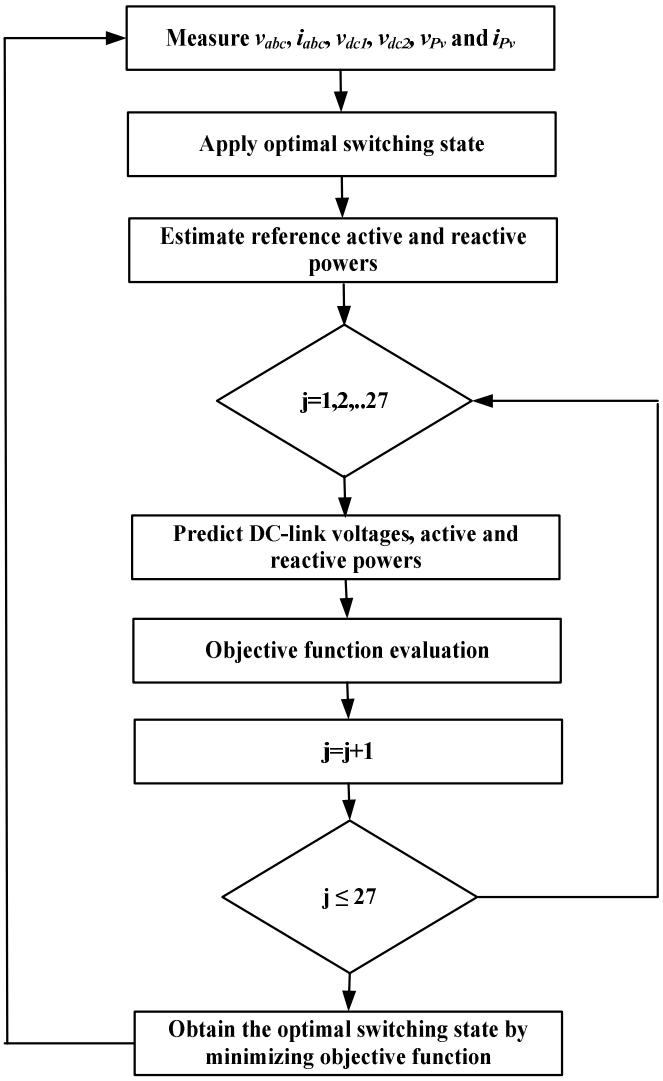

Fig.3.9. Flow chart for MPDPC for grid tied 3L-NPC PV inverter

3.5 Simulation results

In order to illustrate the performance of MPCC and MPDPC, a detailed simulation studies are conducted on a single-stage grid-tied 3L-NPC PV inverter modeled in MATLAB/Simulink. The simulations for both the control approaches are carried with a sampling period of T_s = 80μs. The system parameters for the simulation and experimental studies are given in Table.3.1.

Table.3.1. System Parameters

Parameter	Simulation	Experiment
Grid Details		
Grid voltage	85 V rms (L-L)	85 V rms (L-L)
Grid frequency	50 Hz	50 Hz
Feeder resistance	0.1 Ω	0.1 Ω
Feeder inductance	0.5 mH	0.5 mH
VSC details		
Filter resistance	0.5 Ω	0.5 Ω
Filter inductance	3 mH	3 mH
V_{dc} (min)	150 V	150 V
C_{dc} (C_1=C_2=C)	4700 μF	4700 μF
Sample time	80 μs	80 μs
DC-link controller	K_p=0.45, K_i=2.5	K_p=0.8, K_i=2
PV-array details	(KC200GT at 1000 W/m^2)	(Sandia model at 1000 W/m^2)
V_{oc}	194.4 V (32.9V x 6)	231 V
I_{sc}	8.21 A	7.505 A
V_{mp}	158 (26.33 V x 6)	180 V
I_{mp}	7.61 A	6.67 A
P_{max}	1201 W (200.14 W x 6)	1200 W
N_s	54	--
N_{ss}	6	--
N_{pp}	1	--

A 1.2 kW PV array is considered for the simulation whose current *vs* voltage (I-V curve) and power *vs* voltage (P-V curve) characteristics at 400 Watts/m^2, 700 Watts/m^2, 800 Watts/m^2 and 1000 Watts/m^2 for are shown in Fig.3.10. For evaluating the performance, the system is subjected to various operating conditions. The detailed simulation results for MPCC and MPDPC are presented in following sub-sections

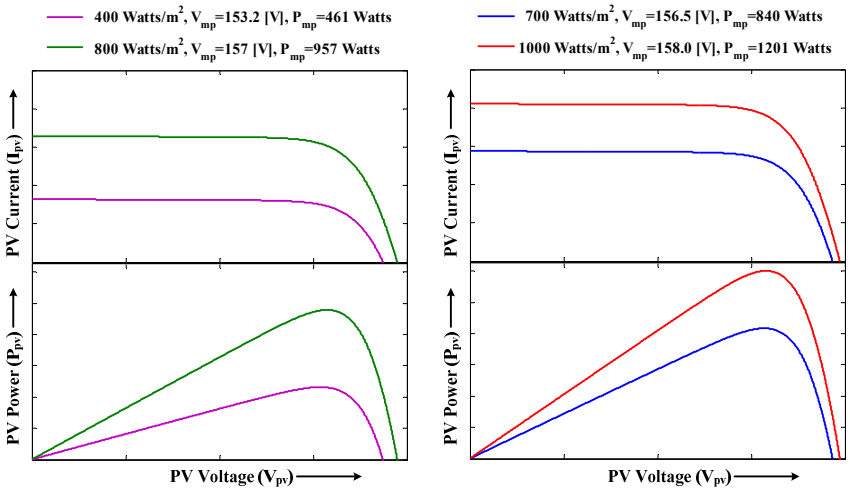

Fig.3.10. I-V and P-V characteristics of PV array at different irradiance levels

3.5.1 Simulation results for MPCC

In this section, the simulation results for MPCC approach are presented. The objectives of current tracking and DC-link capacitor voltage balancing are considered for the investigation. Initially, in order to validate the maximum power extraction with presented MPCC, the single-stage grid-tied SPECS is subjected to change in irradiance as illustrated in Fig.3.11. The change in irradiance profile is as follows: the irradiance (G) is kept constant at 400 Watts/m^2 from [0-0.4] s. At 0.4s the irradiance (G) is increased to 800 Watts/m^2 and reduced back to 400 Watts/m^2 at 1 s. The maximum power extracted with 400 Watts/m^2 is 460.5 Watts at 153.2V DC-link voltage and 951.45 Watts with 156.8V at 800 Watts/m^2. In Fig.3.11, the sub-plots of grid current i_{ga}, grid voltage v_{ga}, the DC-link voltage V_{dc}, and the capacitor voltages V_{dc1} and V_{dc2} are plotted corresponding to the change in irradiance. The steady state waveforms of these intermediate signals at 800 Watts/m^2 with UPF operation and 800 watts/m^2 with Q^* =±600 Var are shown in Fig.3.12, and Fig.3.13, respectively. From these results, it can be confirmed that the presented MPCC approach has extracted the maximum power corresponding to change in irradiance and also injected the reactive power to support the grid based on the reference provided. Further, it can also be observed that the objectives of DC-link voltage balancing and current tracking are simultaneously achieved.

The percentage total harmonic distortion (%THD) of injecting currents with the MPCC control approach is shown in Fig.3.14. The %THD of the injecting current is 3.29% which is well below the IEEE Std. 1547.

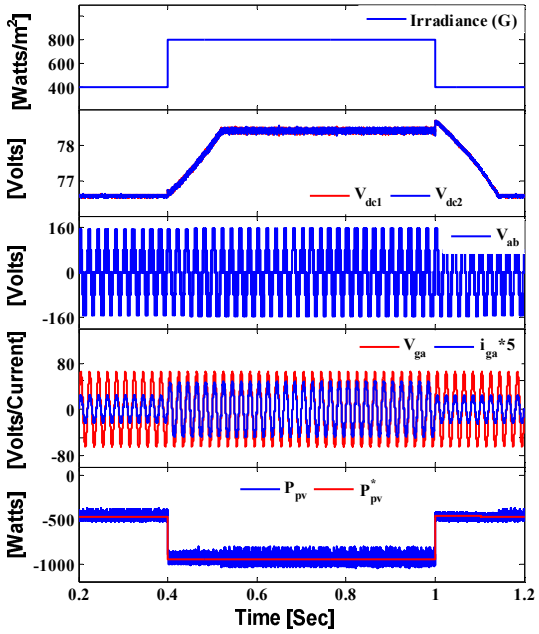

Fig.3.11. Simulation results for Power evolution of 3L-NPC PV inverter with MPCC

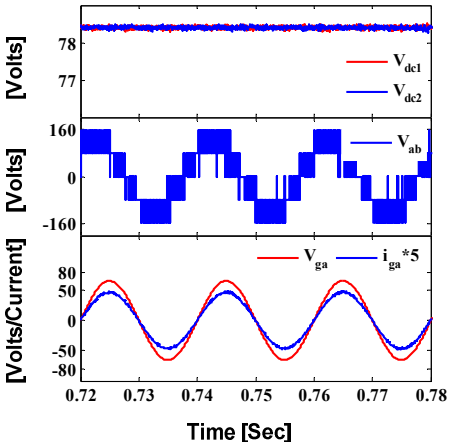

Fig.3.12. Simulation results of intermediate signals at 800 Watts/m^2 with MPCC

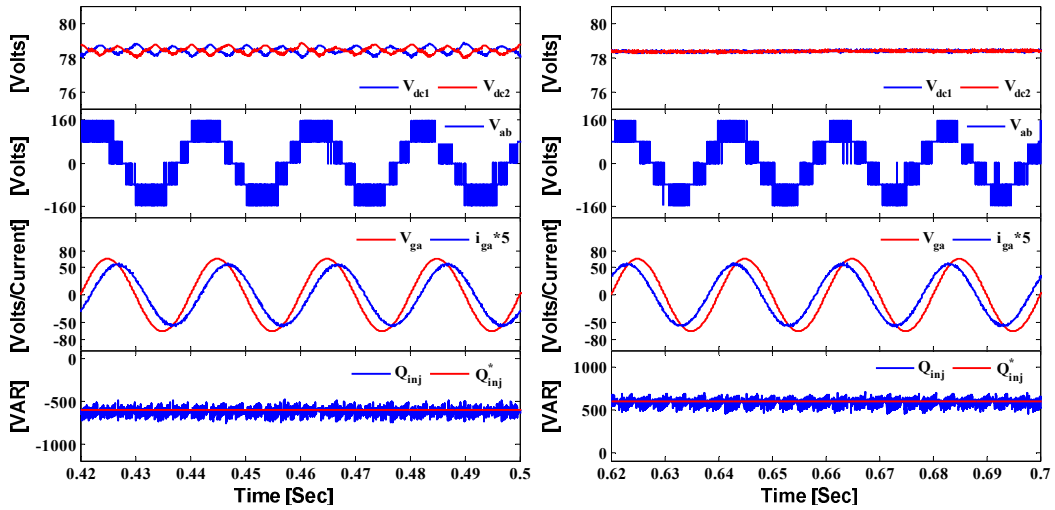

Fig.3.13. Simulation results for DC-link capacitor voltage balancing with MPCC (a) Q*= 600 Var, at G= 800 Watts/m^2 (b) Q*= - 600 Var, at G= 800 Watts/m^2

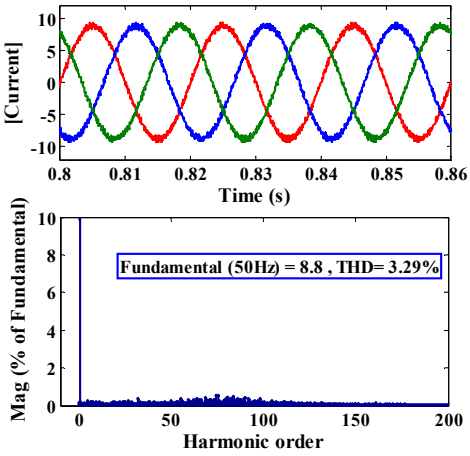

Fig.3.14. Simulation results for %THD of injecting currents with MPCC

3.5.2 Simulation results for MPDPC

In order to validate the maximum power extraction of the SPV system with MPDPC, the results for active power evolution with change in irradiance conditions is investigated. The PV array in the system is subjected to varying irradiance by keeping reactive power reference Q^* = 0 Var. The objective function is defined with the active-reactive power tracking and DC-link capacitor voltage balancing. The scenario of irradiance variation is as follows: initially the irradiance is kept at zero Watts/m^2 for a time interval of [0-0.2]s during which the DC-link voltage is maintained at 150 V (v_{pv_min}). At 0.2 s, the irradiance is changed to 400 Watts/m^2 and is kept constant until 0.6 s; then it is increased to 700 Watts/m^2 at 0.6 s and then to 1000 Watts/m^2 at 1 s. After 1.45 s the irradiance is brought down to 400 Watts/m^2 and then to zero Watts/m^2 at 1.75 s. The DC-link voltage is tracked to 153.2 V, 156.4 V and 157.4 V at 400 Watts/m^2, 700 Watts/m^2 and 1000 Watts/m^2, as a result the maximum power of 460 Watts, 840 Watts and 1200 Watts are extracted, respectively. From Fig.3.15, it can be observed that the MPDPC scheme has tracked the reference voltage provided by the MPPT algorithm and has extracted the maximum power corresponding to subjected irradiance. The steady state waveforms of phase voltage (v_{ga}), phase current (i_{ga}), inverter line voltage (V_{ab}) and the active-reactive powers at 400 Watts/m^2, 700 Watts/m^2 and 1000 Watts/m^2 are shown in Fig.3.16.

Similar to the active power, the reactive power evolution of PV inverter is shown in Fig.3.17. The scenario of change in reactive power reference Q^* is as follows: a step change from 0 Var to -720 Var is applied at 0.8 s, then from -720 Var to +720 Var at 1.6 s and back to 0 Var at 2.4 s. During this change in reactive power, a constant 960 W of active power is

injected by maintaining the irradiance constant at 800 Watts/m^2. It can be seen that, the MPDPC control approach has regulated the DC-link voltage of the inverter to 156.9 V even after the application of step change in reactive power. The steady state waveform of phase voltage (v_{ga}), phase current (i_{ga}), inverter line voltage (V_{ab}) and the active-reactive powers at an irradiance of 800 Watts/m^2 with ±720 Var are shown in Fig.3.18.

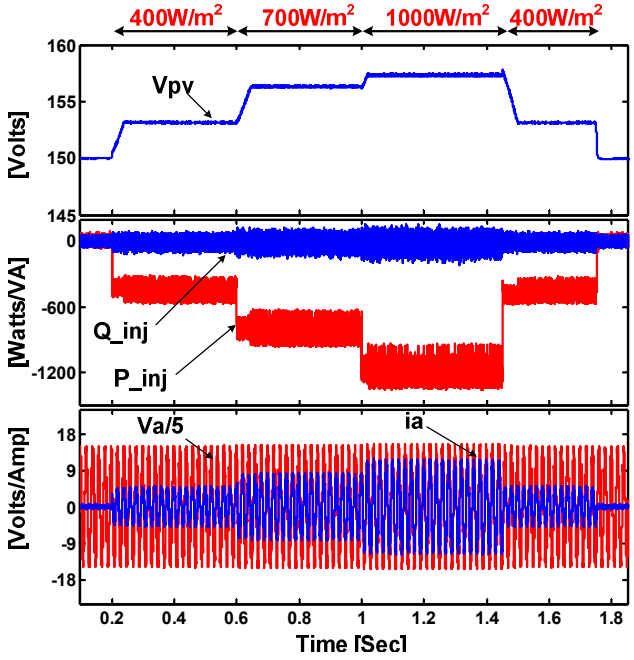

Fig.3.15. Simulation results for active power evolution of 3L-NPC PV inverter with MPDPC

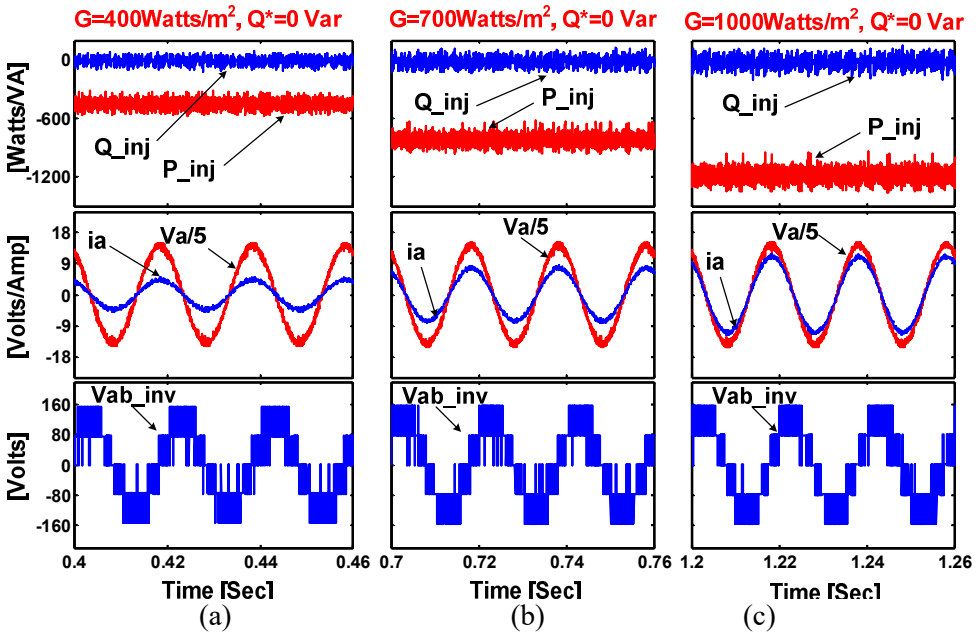

Fig.3.16. Simulation results at steady-state active power at various irradiances with MPDPC (a) 400 Watts/m^2 (b) 700 Watts/m^2 (c) 1000 Watts/m^2.

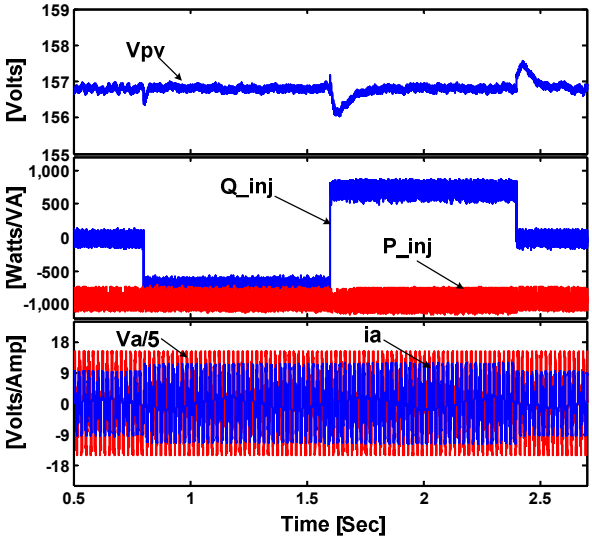

Fig.3.17. Simulation results for reactive power evolution of 3L-NPC PV inverter with MPDPC

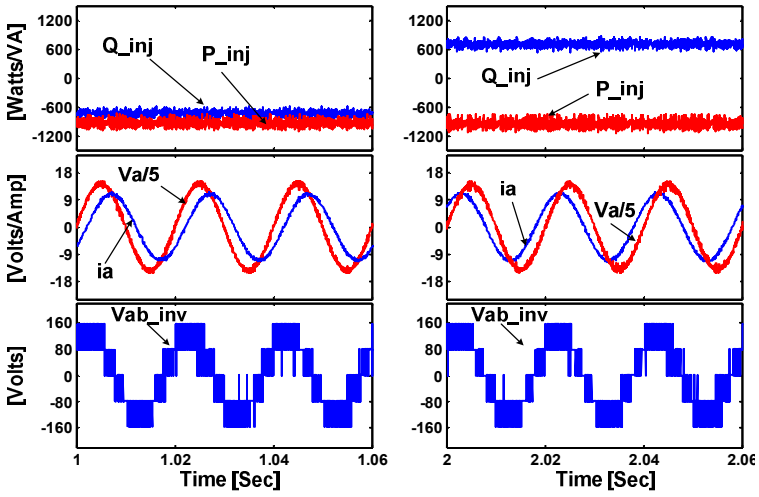

(a) (b)

Fig.3.18. Simulation results at steady-state reactive power at various irradiances with MPDPC (a) Q*= -720 Var, at G= 800 Watts/m^2 (b) Q*= 720 Var, at G= 800 Watts/m^2.

The %THD of injecting currents with the MPDPC control approach is shown in Fig.3.19. The %THD of the injecting current is 3.50% which is also well below the IEEE Std. 1547.

3.6 Experimental setup

The schematic representation of laboratory scale experimental setup is shown in Fig.3.20. The experimental study is conducted on a 1.2 kW single-stage grid-tied 3L-NPC PV inverter. The PV array in the system is emulated by using Chroma 62050H-S solar array simulator. A pre-existing SANDIA model of 1200 Watts at 1000 Watts/m^2, with V_{mp} =180 V and I_{mp} =6.667 A is used as the PV configuration. The 3L-NPC inverter is developed by

using Siemens BSM75GB120DN2 IGBT modules. This 3L-NPC PV inverter is interfaced to grid through a three-phase filter inductor. The dSPACE DS1104 R&D real-time controller board is used to execute the developed control algorithms. The grid voltage, grid current, DC-link voltages and PV currents are the feedback signals measured by using LEM LV-25 voltage sensors and LA 25-NP current sensors. These feedback signals are fed to the control card via a CP1104 I/O connector board. The gating signals for the IGBT switches are driven through HCPL-3120 gate drive opto-coupler.

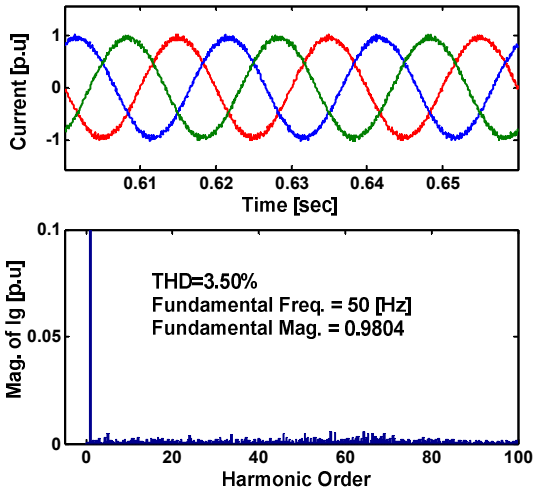

Fig.3.19. Simulation results for %THD of injecting currents with MPDPC

3.7 Experimental results

The experimental results presented for MPCC and MPDPC approaches are to validate the functionalities of maximum power extraction, active power injection and reactive power support to the grid with the grid-tied PV inverter. Further, from the perspective of 3L-NPC inverter, the DC-link capacitor voltage balancing is also illustrated for validating the proper operation of the inverter.

3.7.1 Experimental results for MPCC

The experimental results for the change in irradiance from 400 Watts/m^2 to 800 Watts/m^2 and vice versa are shown in Fig.3.21 (a). The steady state waveforms of phase current (i_{ga}), line voltage (v_{ab}) and the DC-link capacitor voltages (v_{dc1} and v_{dc2}) for 800 Watts/m^2 are shown in Fig.3.21 (b). The DC link capacitor voltage v_{dc} (v_{dc1} + v_{dc2}) is tightly regulated to 174.4 V for extracting a maximum power of 960 Watts from the PV array. The results confirm the maximum power extraction and DC-link capacitor voltage balancing.

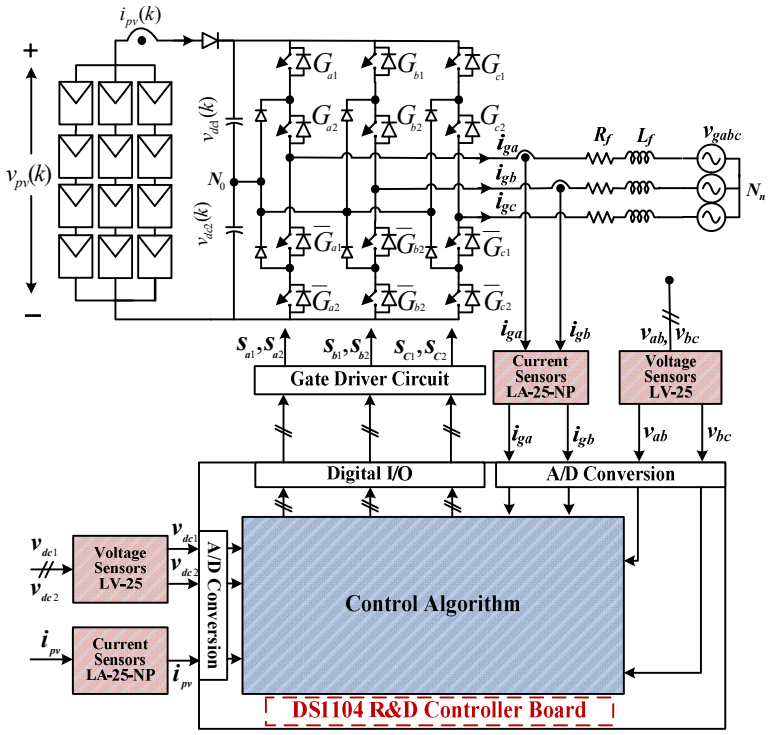

Fig.3.20. Grid tied three-level NPC solar photovoltaic inverter

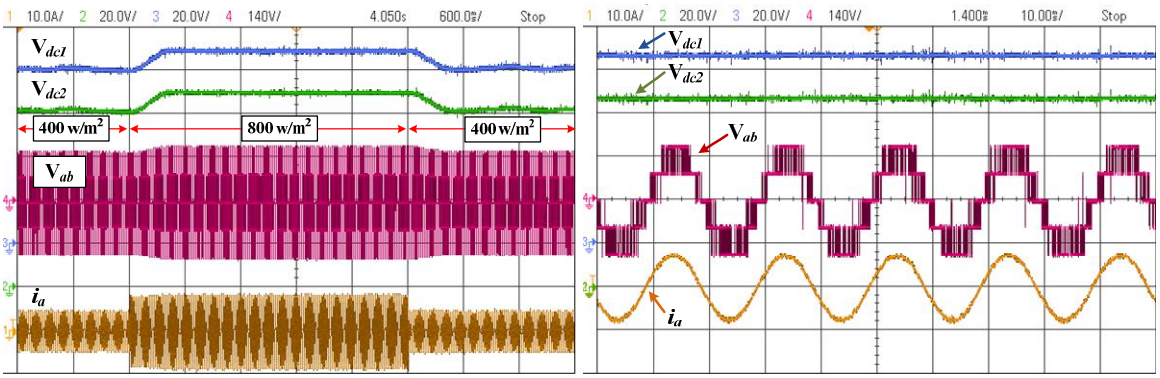

(a) (b)

Fig.3.21. Experimental results for power evaluation of MPCC (a) change in irradiance (b) at 800 Watts/m^2.

The experimental results for reactive power injection with MPCC are presented in the Fig.3.22. The steady state waveforms for operating condition of 800 Watts/m^2 with Q* = -600 Var and Q* = 600 Var are shown in Fig.3.22 (a) and Fig.3.22 (b), respectively. For an irradiance of 800 Watts/m^2 the active power of 960 Watts are injected by regulating the DC-link voltage to 174.4 volts. The steady state waveforms include phase current (i_{ga}), line voltage (v_{ab}) and the DC-link capacitor voltages (v_{dc1} and v_{dc2}). Further, Fig.3.23 illustrates the % THD of the injecting current which is observed as 3.45% which is comparable with the simulation result.

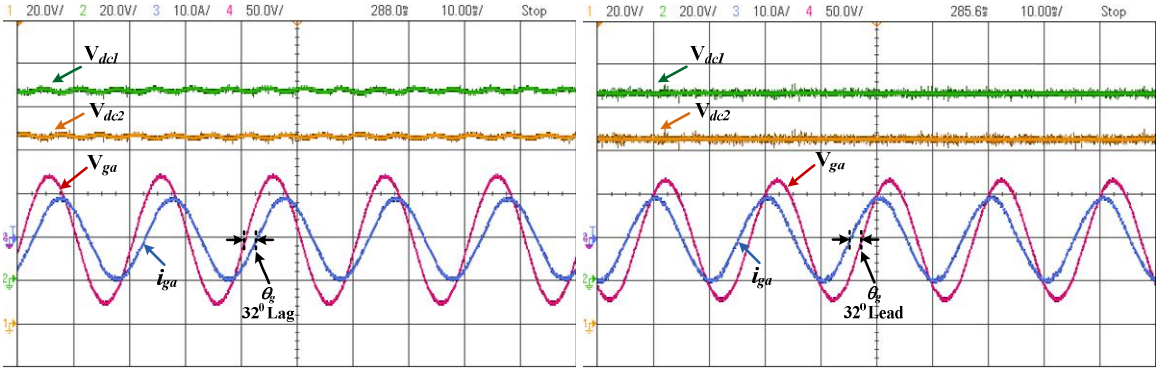

(a) (b)

Fig.3.22. Dc-link voltage balancing during interfacing converter mode with MPCC (a) Q*= 600 Var, at G= 800 Watts/m^2 (b) Q*= - 600 Var, at G= 800 Watts/m^2

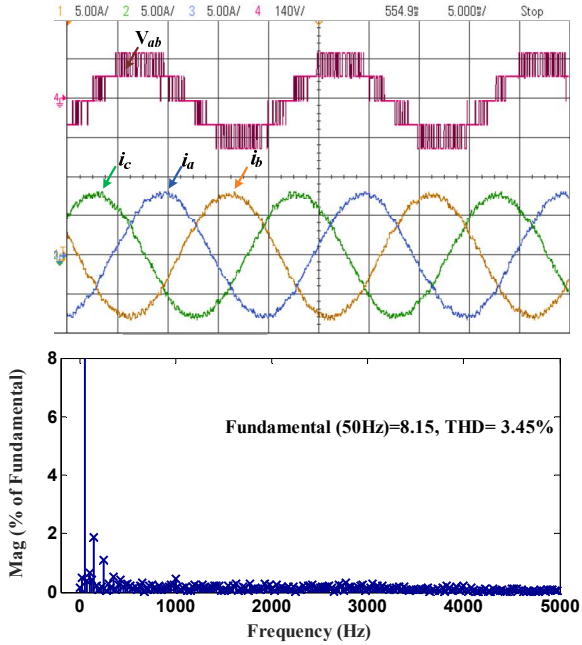

Fig.3.23. Experimental results for %THD of injecting currents with MPCC

3.7.2 Experimental results for MPDPC

To verify the maximum power extraction with MPDPC, the test scenario of maximum power extraction with rapid change in irradiance by keeping the reactive power reference Q^*=0 Var are illustrated in Fig.3.24. The test scenario of varying irradiance is as follows: initially the irradiance is kept as zero Watts/m^2, after 2s the irradiance is changed to 400 Watts/m^2 and 700 Watts/m^2 at 6s. At 10s the irradiance is changed to 1000 Watts/m^2 and brought down to 400 Watts/m^2 after 16s. The DC-link voltages are tracked to 156.1 V, 170.7 V, and 180 V at 400 Watts/m^2, 700 Watts/m^2 and 1000 Watts/m^2 to extract 460 Watts, 830 Watts and 1200 Watts, respectively. It can be observed that the outer DC-link voltage is

continuously regulated to its reference for extracting the maximum power.

The reactive power evolution of the PV inverter with MPDPC for sudden change in reactive power from -720 Var to +720 Var by keeping irradiance constant at 800 Watts/m^2 are shown in Fig.3.25. The step change in reactive power applied at various time instants are as follows: from 0 Var to -720 Var at 2s , -720 Var to 720 Var at 5s and then back to 0 Var at 8s. It can be observed that the DC-link voltage has a momentary change, however the voltage is regulated back to V_{mp}=174.4 V for extracting the maximum power of 960 Watts. The results validate that the MPDPC approach is extracting the maximum power from the PV array even after the inverter is subjected to sudden change in reactive power.

The steady state waveforms of active power (P_{inj}), reactive power (Q_{inj}), injecting currents (i_{ga}), capacitor voltages (V_{dc1} *and* V_{dc2}) and the inverter line voltage (V_{ab_inv}) at various operating conditions are shown in Fig.3.26 and Fig.3.27. Further, Fig.3.28 shows the % THD of the injecting current which is observed as 4.57% which is comparable with the simulation result. Further, a performance comparison of MPCC and MPDPC is presented in Table.3.2.

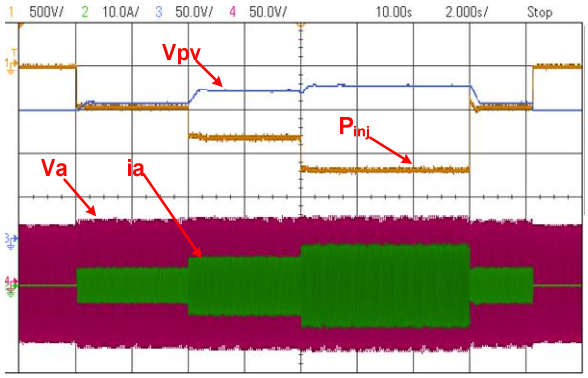

Fig.3.24. Experimental results for active power evolution with MPDPC

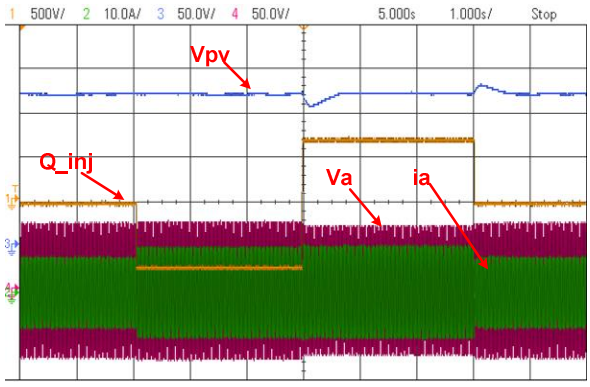

Fig.3.25. Experimental results for reactive power evolution with MPDPC

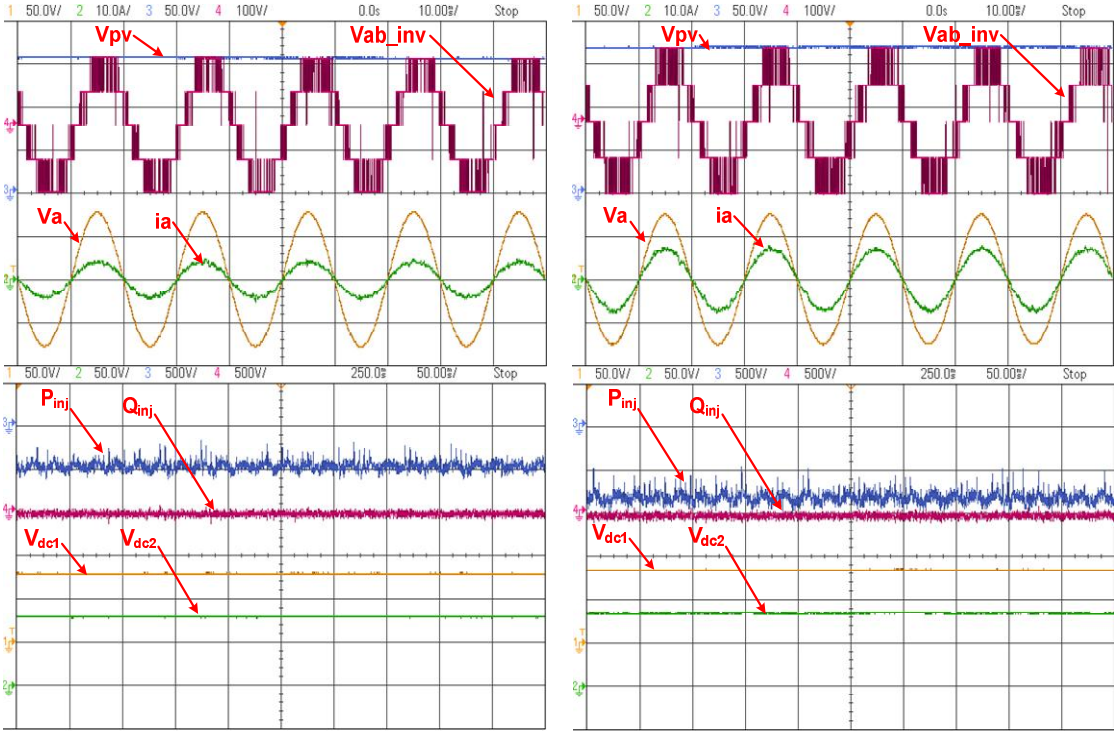

(a) (b)

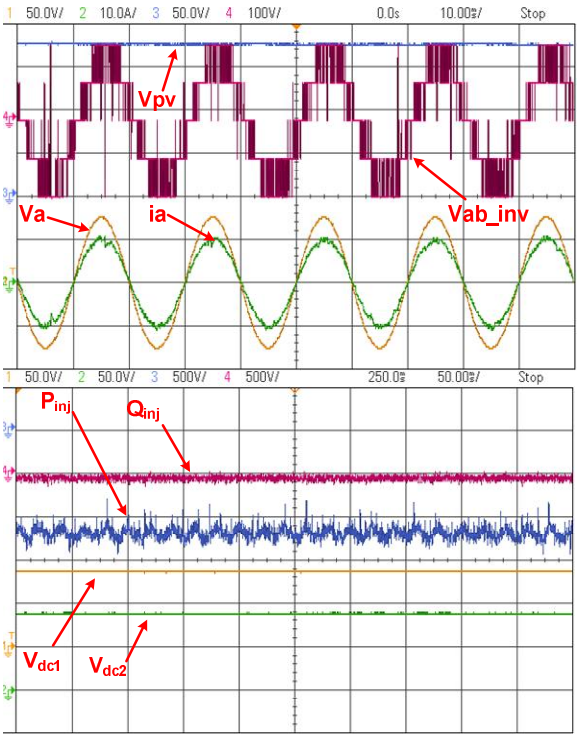

(c)

Fig.3.26. Experimental results at steady-state for various irradiances with MPDPC (a) 400 Watts/m^2 (b) 700 Watts/m^2 (c) 1000 Watts/m^2.

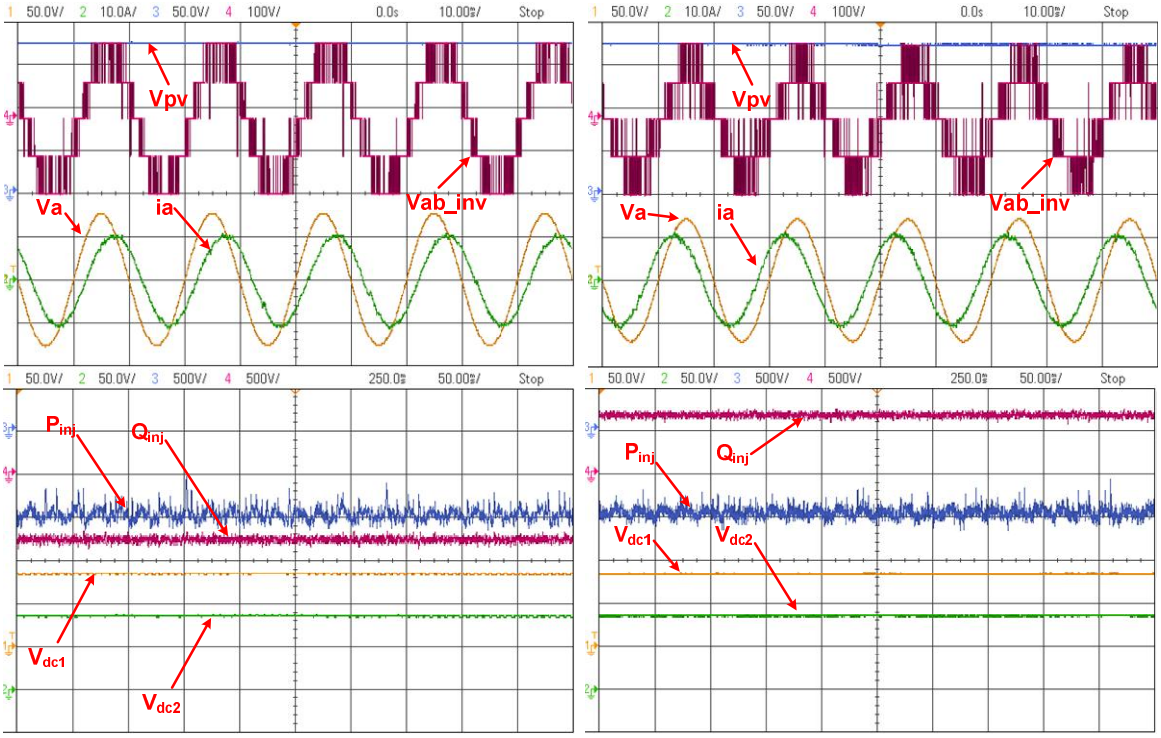

(a) (b)

Fig.3.27. Experimental results for steady-state waveforms with classical MPDPC (a) -720 Var at 800 watts/m^2 (b) +720 Var at 800 watts/m^2.

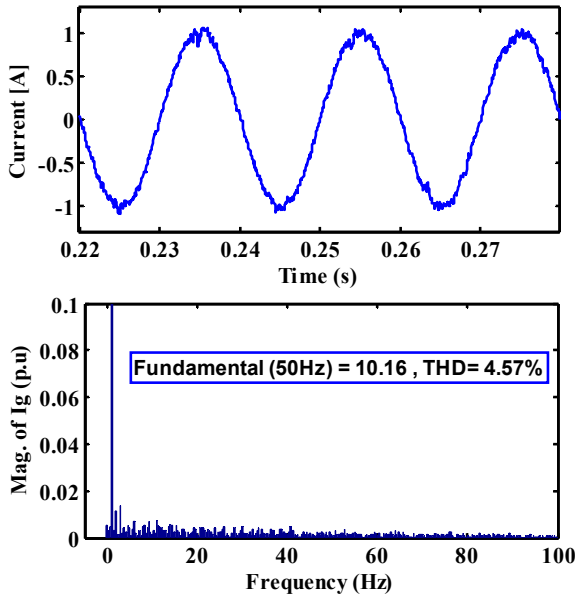

Fig.3.28. Experimental result for %THD of injecting currents with MPDPC

3.7 Summary

In this chapter, implementation of MPCC and MPDPC approaches for single-stage grid tied 3L-NPC PV inverter are presented. The detailed design of SPECS parameters such as selection of DC-link voltage, selection of DC-link capacitor value, design of DC-link voltage

controller and design of filter inductor to interface the PV inverter is presented. The objectives of control are current tracking in MPCC, active-reactive power tracking in MPDPC along with DC-link capacitor voltage balancing. An empirical method is used to select the suitable weighting factor for the DC-link capacitor voltage balancing in the objective function. Both the approaches are tested for injection mode and shunt compensator mode. In case of injection mode, the PV array is subjected to varying irradiance to verify the maximum power extraction capability. Whereas, in case of shunt compensator mode the reactive power injection along with the maximum power extraction is tested. In both the cases, the DC-link capacitors voltages are well balanced and the currents injected are also within the limits of IEEE Std. 1547.

Further, to incorporate the additional control objectives like CMV mitigation and switching frequency reduction required for grid tied PV inverters are found to be difficult due to the complexity in the selection of weighting factors with the empirical approach. To address this issue, direct optimization method based on selective finite-states approach is proposed in Chapter-4.

Table.3.2. Comparison of system performance with MPCC and MPDPC

Parameter	Indices	MPCC		MPDPC	
		Sim.	Exp.	Sim.	Exp.
Current	% THD	3.29%	3.45%	3.5%	4.57%
	Fund. Mag.	8.8 A	8.15 A	8.46 A	8.22 A
Grid Voltage	% THD	2.46%	2.6%	2.52%	2.65%
	Fund. Mag.	87.4 V	86.04 V	87.12 V	86.21 V
Avg. Switching Frequency		2.6 kHz	2.242 kHz	2.38 kHz	2.198 kHz

Chapter-4
Selective FS-MPC for Single-Stage Grid-Tied SPECS

4.1 Introduction

FCS-MPC is an attractive control approach for multilevel inverters. However, the computational complexity and weighting factor selection for multi-objective control are the major drawbacks. In order to address these limitations, a selective finite-states (FS) MPC is proposed for a grid-tied 3L-NPC PV inverter. The main objectives of grid-tied 3L-NPC PV inverter are current tracking and DC-link capacitor voltage balancing. These two control objectives are necessary and are equally important for proper operation of the inverter. An objective function defined with these control variables necessitates weighting factors to maintain the relative importance among them. The dissimilar physical nature with unequal magnitude levels and the intermittent correlation between the control variables make the selection of weighting factor more intricate. Further, the objectives are predicted and the objective function defined is evaluated for all the admissible switching states of the inverter which indeed incur large computational efforts. To overcome these, the FS-MPC selects a specified set of candidate switching states for the prediction and objective-function optimization. These candidate switching states are selected based on the position of reference voltage vector in the space vector plane, inverter current directions and the charge status of the DC-link capacitors. As a result, the selection of optimal switching state is fast, easy to implement and achieves an inherent DC-link capacitor voltage balance. This indeed eliminates the selection of weighting factor for capacitor voltage balancing objective. Further, the impact of selective finite-states on common-mode voltage (CMV) reduction objective is investigated to validate the multi-objective optimization.

4.2 Proposed Selective Finite States approach

The DC-link capacitor voltage balancing and current tracking are the two main control objectives considered in the objective function of MPCC for grid-tied 3L-NPC PV inverter. The future behaviour of these control objectives is determined with the help of discrete-time model of the system by using admissible switching states of the converter. The switching state which minimizes the objective function is applied in the next sampling period. Since the 3L-NPC inverter consists of 27 admissible switching states; the prediction and evaluation of each individual control objective are made for 27 times in each sampling period. As a result, the control of power converter requires higher sampling rate. Accommodating these many numbers of calculations in the given sampling period increases the computational

burden on the processor. Further, due to the non-linearity of the converter, the correlation between the control variables (injecting currents and DC-link capacitor voltages) is intermittent. Therefore, the selection of weighting factors to maintain the relative importance between these objectives is quite a difficult task. Hence, a direct optimization based on selective finite-states approach is proposed and discussed in detail in this chapter.

In the proposed selective FS-MPC, the number of switching states required for prediction and objective function optimization are simplified by providing the priority among the control objectives. Out of the two control objectives, current tacking is given high priority to have a high quality power injection. Hence, initially a voltage vector required to drive the injecting currents to its reference is determined based on the deadbeat approach. The reference voltage vector obtained is realized with the optimal nearest switching state. However, in order to achieve inherent DC-link capacitor voltage balancing, the charging/discharging behaviour of each individual switching state is investigated. Based on the position of reference voltage vector, the candidate region (i.e., the sector and the triangular region) are determined. The switching states associated with candidate triangular region are classified based on the charge regulation behaviour with respect to the current direction of each pole in the inverter. Finally, the candidate switching states are defined based on the position, present charge status of the DC-link capacitors and the direction of phase currents. As a result, the proposed FS-MPC approach achieves an inherent DC-link capacitor voltage balancing of 3L-NPC PV inverter for the wide operating power factor with appropriate selection of switching states. The specified set of selective switching states is fully dedicated to minimize the current tracking objective. Hence, the objectives of current tracking and DC-link capacitor voltage balancing are simplified to a single objective. By this, the efforts required for the selection of weighting factor to balance the DC-link capacitor voltages is completely eliminated. In addition, as the number of switching states required for prediction and optimization are minimized. Hence, the number of computations and corresponding time required for real-time implementation is significantly reduced. The block diagram of the proposed selective FS-MPC approach is shown in Fig.4.1. The detailed steps involved in the design of proposed control approach are given as follows:

4.2.1 Determination of reference voltage vector

The reference voltage vector $v_{i\alpha\beta}^{*}(k+1)$ which minimizes the error between the predicted

current $\vec{i}_{g\alpha\beta}(k+2)$ and the reference current $\vec{i}^{*}_{g\alpha\beta}(k+2)$ is obtained by re-arranging the Eq. 2.23 and replacing $\vec{i}_{g\alpha\beta}(k+2)$ with $\vec{i}^{*}_{g\alpha\beta}(k+2)$, as given below:

$$\vec{v}^{*}_{i\alpha\beta}(k+1)=\vec{v}_{g\alpha\beta}(k+1)+\frac{L_f}{T_s}\left(\vec{i}^{*}_{g\alpha\beta}(k+2)-\vec{i}_{g\alpha\beta}(k+1)\right)+R_f\vec{i}_{g\alpha\beta}(k+1) \tag{4.1}$$

The position of the reference voltage vector in the space vector plane is given as

$$\phi=\tan^{-1}\left(\frac{v^{*}_{i\beta}(k+1)}{v^{*}_{i\alpha}(k+1)}\right) \tag{4.2}$$

4.2.2 Determining candidate triangular region

The space vector plane of the 3L-NPC inverter is divided into six sectors as shown in Fig.4.2. Each sector consists of four triangular regions. The sector in which the reference voltage vector exists is obtained from Eq. (4.2). Determining the candidate triangular region in each sector individually increases the number of computations. Hence, by taking the advantage of the symmetry of space vector plane of 3L-NPC inverter, a generalized approach is presented to obtain the candidate triangular region. In this approach, all the sectors and the triangular regions are referred to the first sector. The generalized approach to determine the candidate triangular region is given as follows:

Let, the complex notation of the reference voltage vector is given as

$$\vec{v}^{*}_{i}(k+1)=v^{*}_{i\alpha}(k+1)+j\ v^{*}_{i\beta}(k+1) \tag{4.3}$$

Where $v^{*}_{i\alpha}(k+1)$, and $v^{*}_{i\beta}(k+1)$ are the real and imaginary components of the complex reference vector.

The generalized form of real and imaginary components of reference voltage vector ($v^{*}_{i\alpha}(k+1)$, $v^{*}_{i\beta}(k+1)$) referred to the first sector are given as

$$v^{*}_{i\alpha}(k+1)=\left|v^{*}_{i}(k+1)\right|\cos\left(\phi-(n-1)\,\pi/3\right) \tag{4.4}$$

$$v^{*}_{i\beta}(k+1)=\left|v^{*}_{i}(k+1)\right|\sin\left(\phi-(n-1)\,\pi/3\right) \tag{4.5}$$

$$\left|v^{*}_{i}(k+1)\right|=\sqrt{\left(v^{*}_{i\alpha}(k+1)\right)^2+\left(v^{*}_{i\beta}(k+1)\right)^2} \tag{4.6}$$

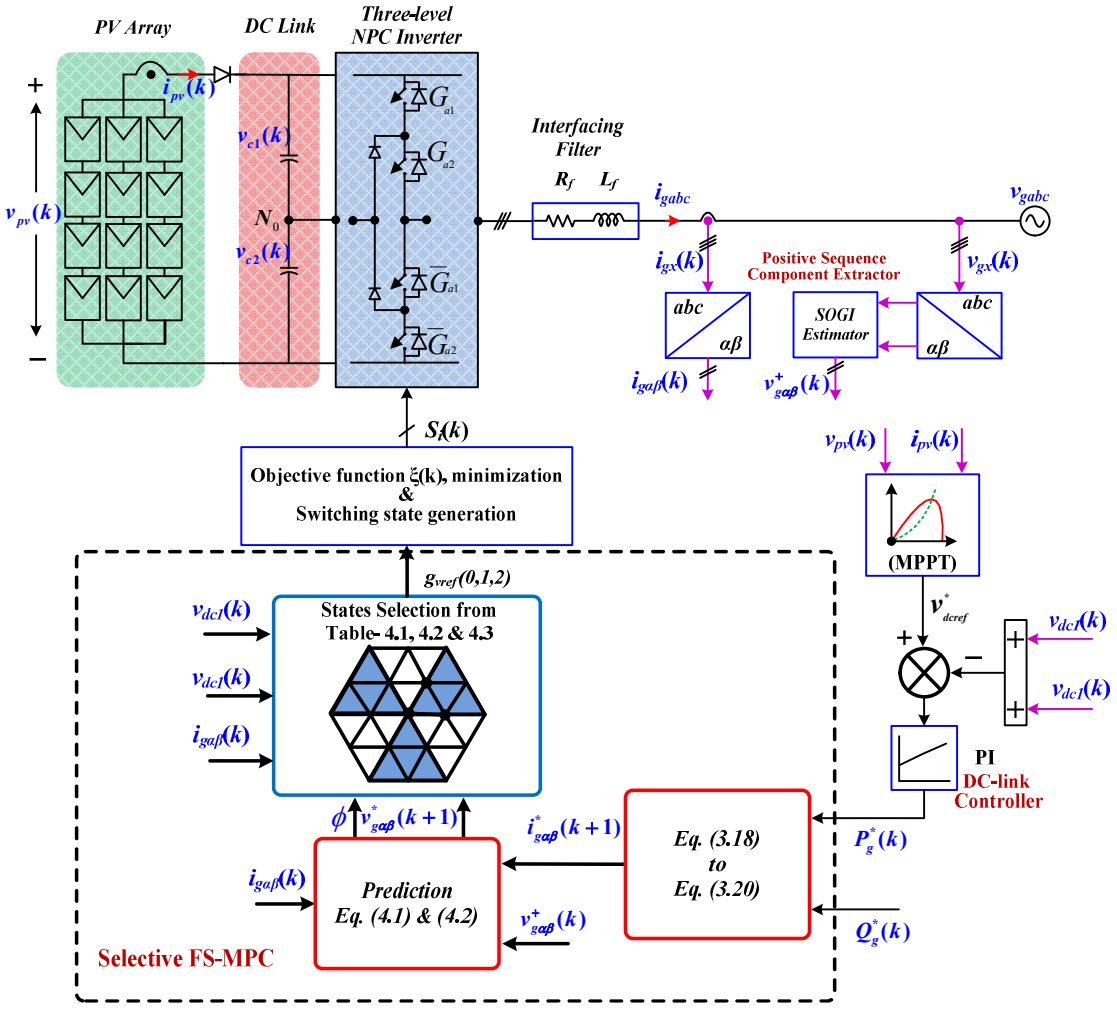

Fig.4.1. Block diagram of proposed selective FS-MPC for single-stage grid-tied 3L-NPC PV inverter

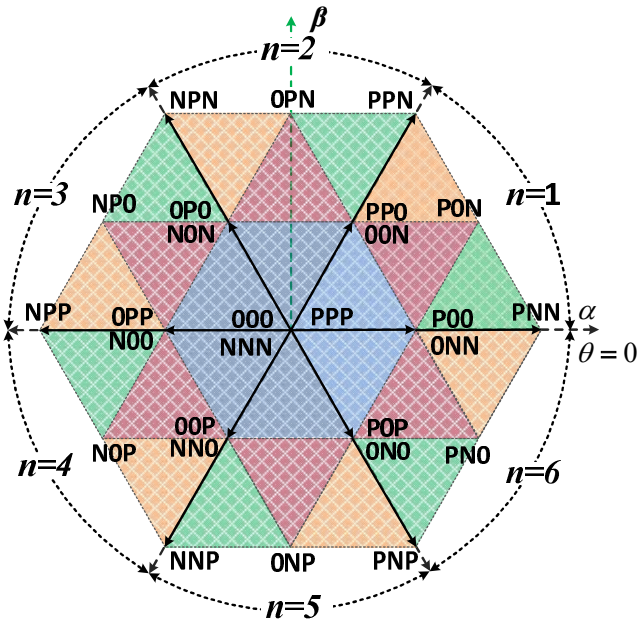

Fig.4.2. Space-vector plane of 3L-NPC inverter with sector classification

Where, $\left|v_i^*(k+1)\right|$, ϕ are the amplitude and phase (as given in Eq. (4.2)) of the reference voltage vector and n is the sector number.

Based on $v_{i\alpha}^*(k+1)$, $v_{i\beta}^*(k+1)$ & ϕ, the candidate triangular region, and the candidate switching states corresponding to each sector are given in Table.4.1 and Table.4.2.

4.2.3 Selection of switching states for inherent neutral point voltage balancing

The 3L-NPC PV inverter operates as a grid interfacing inverter to feed the maximum power extracted from the PV array and also provides reactive power support to the grid as a shunt compensator. Hence, the finite switching states are selected to achieve inherent DC-link capacitor voltage balancing for complete power factor operation of the inverter.

Table.4.1. Candidate triangular region with respect to generalized reference voltage vector

Sl. No.	$v_{i\alpha}^*(k+1)$	$v_{i\beta}^*(k+1)$	Candidate Triangular Region
1	$v_{i\beta}^* > 0$ && $v_{i\beta}^* < \frac{v_{dc}}{2\sqrt{3}}$	$v_{i\alpha}^* \geq \frac{v_{i\beta\_g}^*}{2\sqrt{3}}$ && $v_{i\alpha}^* < \left(-v_{i\beta}^* + \frac{v_{dc}}{3}\right)$	1
2		$v_{i\alpha}^* \geq \left(-v_{i\beta}^* + \frac{v_{dc}}{3}\right)$ && $v_{i\alpha}^* < \left(v_{i\beta}^* + \frac{v_{dc}}{3}\right)$	2
3		$v_{i\alpha}^* \geq \left(v_{i\beta}^* + \frac{v_{dc}}{3}\right)$	3
4	$v_{i\beta}^* \geq \frac{v_{dc}}{2\sqrt{3}}$		4

For analyzing this concept, sector-1 is considered as a sample case and discussed in detail. As shown in Fig.4.3, sector-1 has three null vectors {OOO, PPP, and NNN}, four small vectors {PPO, POO, OON, and ONN}, one medium vector {PON} and two large vectors {PNN, and PPN}. The null vectors, medium voltage vectors and the large voltage vectors do not have effect on DC-link capacitor voltage balancing. Among the three null vectors, PPP and NNN introduce large CMV ($\pm V_{dc}/2$), therefore, only OOO is considered as null vector in the candidate switching states. The small voltage vectors contribute to the DC-link capacitor voltage balancing. The pair of switching states PPO/OON and POO/ONN corresponding to small vectors are redundant and have complementary effect on voltage balancing. The balancing ability of these switching states depends on the direction of current

flow. The current direction is assumed as positive when the current leaves from phase leg of the inverter, and negative when it enters the phase leg. Fig.4.4 shows the change in current direction with respect to change in power factor for the switching states POO/ONN (i_{ga}) and PPO/OON (i_{gc}) in sector-1.

Table.4.2. Candidate switching states with respect to triangular region

Candidate Triangular Region	Sector Number					
	1	2	3	4	5	6
1	POO,ONN PPO,OON PPP,OOO NNN	PPO,OON OPO,NON PPP,OOO NNN	OPO,NON OPP,NOO PPP,OOO NNN	OPP,NOO OOP,NNO PPP,OOO NNN	OOP,NNO POP, ONO PPP,OOO NNN	POP,ONO POO,ONN PPP,OOO NNN
2	POO,ONN PPO,OON PON	PPO,OON OPO,NON OPN	OPO,NON OPP,NOO NPO	OPP,NOO OOP,NNO NOP	OOP,NNO POP, ONO ONP	POP,ONO POO,ONN PNO
3	POO,ONN PON,PNN	PPO,OON PPN,OPN	OPO,NON NPN,NPO	OPP,NOO NPP, NOP	OOP,NNO NNP,ONP	POP,ONO PNP,PNO
4	PPO,OON PON, PPN	OPO,NON OPN,NPN	OPP,NOO NPO,NPP	OOP,NNO NNP,NOP	POP, ONO PNP,ONP	POO,ONN PNO,PNN

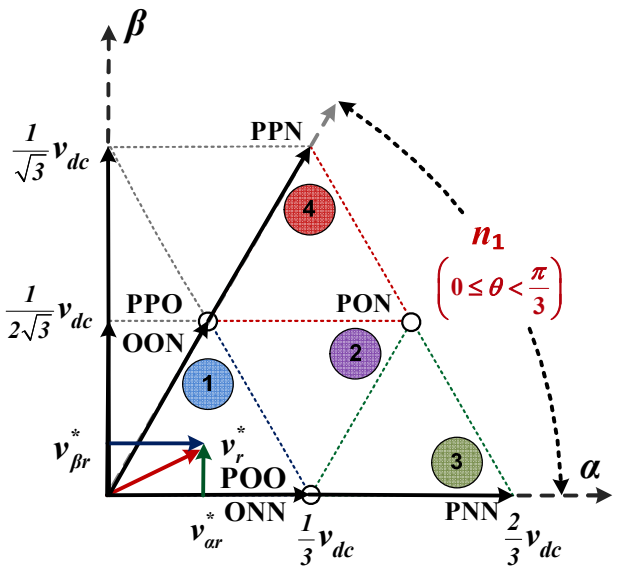

Fig.4.3. Sector – 1 of space vector plane of 3L-NPC

Let φ_{rc_a} and φ_{rc_c} be the critical power factor angle at which the phase currents i_{ga} and i_{gc} changes its direction in sector-1, respectively. These critical power factor angles are obtained as follows:

$$i_{ga}\Big|_{n=1} = I_m \sin\left(\frac{\pi}{2} - \varphi_{rc\_a}\right) = I_m \sin\left(\frac{5\pi}{6}\right) \tag{4.7}$$

$$i_{gc}\Big|_{n=1} = I_m \sin\left(\frac{\pi}{2} - \varphi_{rc\_c} - \frac{4\pi}{3}\right) = I_m \sin\left(\frac{5\pi}{6}\right) \tag{4.8}$$

By solving the Eq. (4.7) and Eq. (4.8), φ_{rc_a} and φ_{rc_c} are obtained as -π/6 and π/6 respectively.

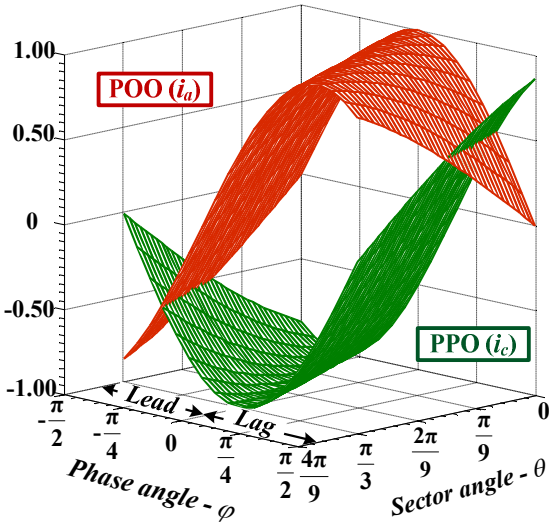

Fig.4.4. Direction of current with change in power factor for sector-1

The phase current i_{ga} corresponding to POO/ONN changes its direction from positive to negative at π/6 lead, similarly, the phase current i_{gc} corresponding to PPO/OON changes from positive to negative at π/6 lag. During positive i_{ga} and i_{gc}, the switching states POO and OON discharges the capacitor C_1 and charges during the negative phase currents. Whereas, the switching states ONN and PPO charges the capacitor C_1 during the positive and discharges the capacitor while negative. Fig.4.5 shows the effect of the current direction on the charging and discharging of capacitors for the switching states POO, PPO, OON and NNO. Hence, proper switching states are to be selected based on the direction of currents and present charge status of the DC-link capacitors to maintain the capacitor voltage balance.

Similar to sector-1, the remaining sectors will also have the same effect on the charge regulation of DC-link capacitors with the selected switching states corresponding to individual sectors. The selective candidate switching states for all the six sectors with respect to the charge status and direction of current flow are given in Table.4.3.

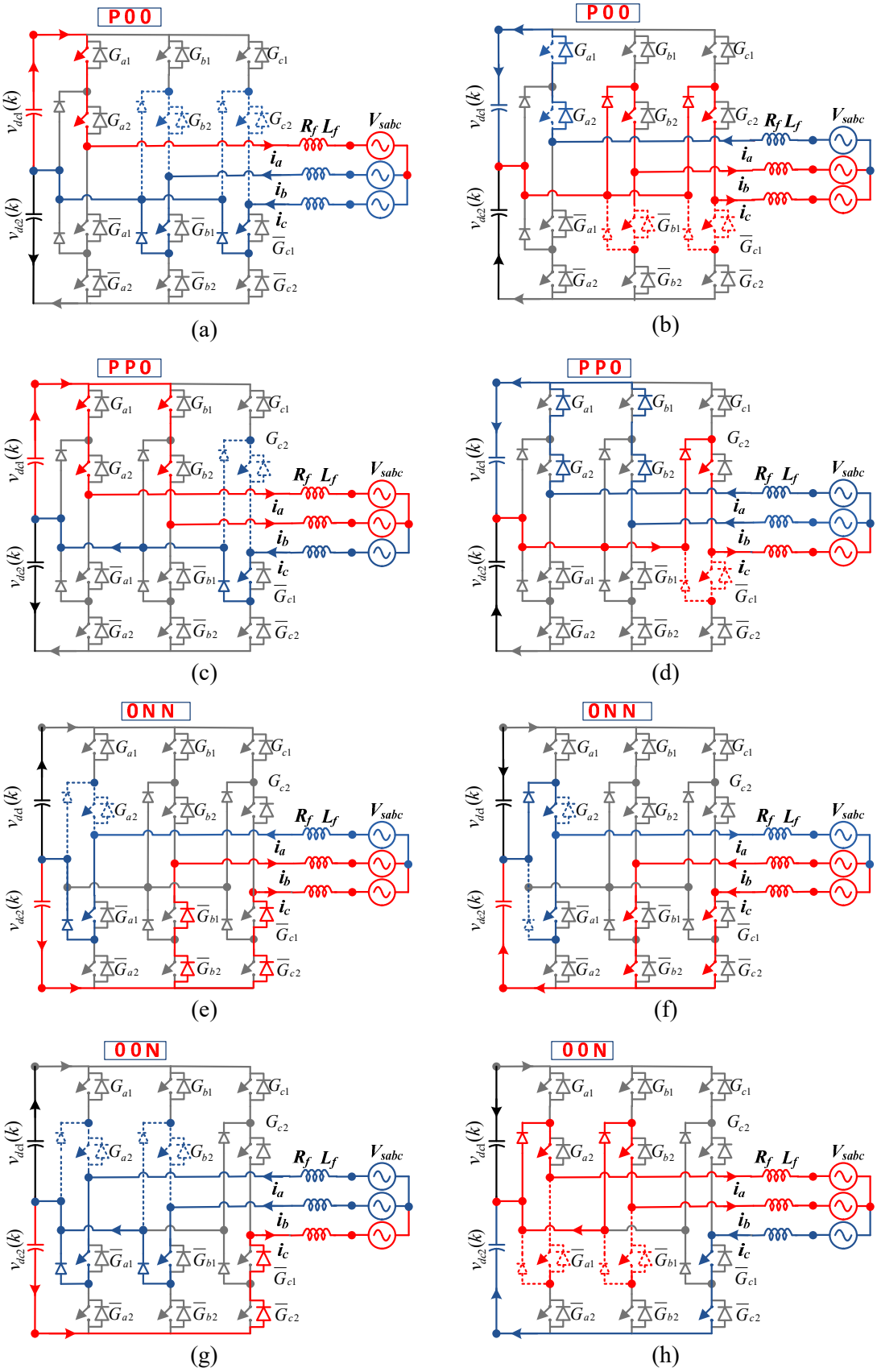

Fig.4.5. Effect of current directions on DC-link capacitor voltage for the switching states POO, PPO, ONN and OON

Table.4.3. Candidate Switching States for all the sectors

Sector No.	Candidate Triangle	Charge Status	Current Direction		Candidate Switching States		
1	1	$V_{dc1} > V_{dc2}$	$i_c < 0$	$i_a > 0$	OOO	POO	PPO
				$i_a < 0$	OOO	ONN	PPO
			$i_c > 0$	$i_a > 0$	OOO	POO	OON
				$i_a < 0$	OOO	ONN	OON
		$V_{dc2} > V_{dc1}$	$i_c < 0$	$i_a > 0$	OOO	OON	ONN
				$i_a < 0$	OOO	OON	POO
			$i_c > 0$	$i_a > 0$	OOO	ONN	PPO
				$i_a < 0$	OOO	POO	PPO
	2	$V_{dc1} > V_{dc2}$	$i_c < 0$	$i_a > 0$	POO	PPO	PON
				$i_a < 0$	ONN	PPO	PON
			$i_c > 0$	$i_a > 0$	POO	OON	PON
				$i_a < 0$	ONN	OON	PON
		$V_{dc2} > V_{dc1}$	$i_c < 0$	$i_a > 0$	ONN	OON	PON
				$i_a < 0$	POO	OON	PON
			$i_c > 0$	$i_a > 0$	ONN	PPO	PON
				$i_a < 0$	POO	PPO	PON
	3	$V_{dc1} > V_{dc2}$		$i_a > 0$	POO	PON	PNN
				$i_a < 0$	ONN	PON	PNN
		$V_{dc2} > V_{dc1}$		$i_a > 0$	ONN	PNN	PON
				$i_a < 0$	POO	PNN	PON
	4	$V_{dc1} > V_{dc2}$	$i_c < 0$		PPO	PPN	PON
			$i_c > 0$		OON	PON	PPN
		$V_{dc2} > V_{dc1}$	$i_c < 0$		OON	PON	PPN
			$i_c > 0$		PPO	PPN	PON
2	1	$V_{dc1} > V_{dc2}$	$i_b > 0$	$i_c < 0$	OOO	OPO	PPO
				$i_c > 0$	OOO	OPO	OON
			$i_b < 0$	$i_c < 0$	OOO	PPO	NON
				$i_c > 0$	OOO	OON	NON
		$V_{dc2} > V_{dc1}$	$i_b > 0$	$i_c < 0$	OOO	OON	NON
				$i_c > 0$	OOO	PPO	NON
			$i_b < 0$	$i_c < 0$	OOO	OON	OPO
				$i_c > 0$	OOO	PPO	OPO
	2	$V_{dc1} > V_{dc2}$	$i_b > 0$	$i_c < 0$	PPO	OPO	OPN

				i_c>0	OON	OPO	OPN
			$i_b<0$	i_c<0	PPO	NON	OPN
				i_c>0	OON	NON	OPN
		$V_{dc2}> V_{dc1}$	$i_b>0$	i_c<0	OON	NON	OPN
				i_c>0	PPO	NON	OPN
			$i_b<0$	i_c<0	OON	OPO	OPN
				i_c>0	PPO	OPO	OPN
	3	$V_{dc1}> V_{dc2}$		i_c<0	PPO	PPN	OPN
				i_c>0	OON	PPN	OPN
		$V_{dc2}> V_{dc1}$		i_c<0	OON	OPN	PPN
				i_c>0	PPO	OPN	PPN
	4	$V_{dc1}> V_{dc2}$	$i_b>0$		OPO	OPN	NPN
			$i_b<0$		NON	NPN	OPN
		$V_{dc2}> V_{dc1}$	$i_b>0$		NON	NPN	OPN
			$i_b<0$		OPO	OPN	NPN
3	1	$V_{dc1}> V_{dc2}$	$i_a<0$	i_b>0	OOO	OPO	OPP
				i_b<0	OOO	NON	OPP
			$i_a>0$	i_b>0	OOO	OPO	NOO
				i_b<0	OOO	NON	NOO
		$V_{dc2}> V_{dc1}$	$i_a<0$	i_b>0	OOO	NOO	NON
				i_b<0	OOO	NOO	OPO
			$i_a>0$	i_b>0	OOO	NON	OPP
				i_b<0	OOO	OPO	OPP
	2	$V_{dc1}> V_{dc2}$	$i_a<0$	i_b>0	OPP	OPO	NPO
				i_b<0	OPP	NON	NPO
			$i_a>0$	i_b>0	OPO	NOO	NPO
				i_b<0	NON	NOO	NPO
		$V_{dc2}> V_{dc1}$	$i_a<0$	i_b>0	NOO	NPO	NON
				i_b<0	NOO	NPO	OPO
			$i_a>0$	i_b>0	NON	OPP	NPO
				i_b<0	OPO	OPP	NPO
	3	$V_{dc1}> V_{dc2}$		i_b>0	OPO	NPO	NPN
				i_b<0	NON	NPO	NPN
		$V_{dc2}> V_{dc1}$		i_b>0	NON	NPN	NPO
				i_b<0	OPO	NPN	NPO

	4	$V_{dc1}> V_{dc2}$	$i_a<0$		OPP	NPP	NPO
			$i_a>0$		NOO	NPO	NPP
		$V_{dc2}> V_{dc1}$	$i_a<0$		NOO	NPO	NPP
			$i_a>0$		OPP	NPP	NPO
4	1	$V_{dc1}> V_{dc2}$	$i_c>0$	$i_a<0$	OOO	OOP	OPP
				$i_a>0$	OOO	OOP	NOO
			$i_c<0$	$i_a<0$	OOO	OPP	NNO
				$i_a>0$	OOO	NOO	NNO
		$V_{dc2}> V_{dc1}$	$i_c>0$	$i_a<0$	OOO	NOO	NNO
				$i_a>0$	OOO	OPP	NNO
			$i_c<0$	$i_a<0$	OOO	NOO	OOP
				$i_a>0$	OOO	OPP	OOP
	2	$V_{dc1}> V_{dc2}$	$i_c>0$	$i_a<0$	OOP	OPP	NOP
				$i_a>0$	OOP	NOO	NOP
			$i_c<0$	$i_a<0$	OPP	NNO	NOP
				$i_a>0$	NOO	NNO	NOP
		$V_{dc2}> V_{dc1}$	$i_c>0$	$i_a<0$	NNO	NOO	NOP
				$i_a>0$	NNO	OPP	NOP
			$i_c<0$	$i_a<0$	NOO	OOP	NOP
				$i_a>0$	OPP	OOP	NOP
	3	$V_{dc1}> V_{dc2}$		$i_a<0$	OPP	NPP	NOP
				$i_a>0$	NOO	NPP	NOP
		$V_{dc2}> V_{dc1}$		$i_a<0$	NOO	NOP	NPP
				$i_a>0$	OPP	NOP	NPP
	4	$V_{dc1}> V_{dc2}$	$i_c>0$		OOP	NOP	NNP
			$i_c<0$		NNO	NNP	NOP
		$V_{dc2}> V_{dc1}$	$i_c>0$		NNO	NNP	NOP
			$i_c<0$		OOP	NOP	NNP
5	1	$V_{dc1}> V_{dc2}$	$i_b<0$	$i_c>0$	OOO	OOP	POP
				$i_c<0$	OOO	NNO	POP
			$i_b>0$	$i_c>0$	OOO	OOP	ONO
				$i_c<0$	OOO	NNO	ONO
		$V_{dc2}> V_{dc1}$	$i_b<0$	$i_c>0$	OOO	ONO	NNO
				$i_c<0$	OOO	ONO	OOP
			$i_b>0$	$i_c>0$	OOO	NNO	POP

				i_c<0	OOO	OOP	POP
	2	$V_{dc1}> V_{dc2}$	$i_b<0$	i_c>0	OOP	POP	ONP
				i_c<0	NNO	POP	ONP
			$i_b>0$	i_c>0	OOP	ONO	ONP
				i_c<0	NNO	ONO	ONP
		$V_{dc2}> V_{dc1}$	$i_b<0$	i_c>0	NNO	ONO	ONP
				i_c<0	OOP	ONO	ONP
			$i_b>0$	i_c>0	NNO	POP	ONP
				i_c<0	OOP	POP	ONP
	3	$V_{dc1}> V_{dc2}$		i_c>0	OOP	ONP	NNP
				i_c<0	NNO	ONP	NNP
		$V_{dc2}> V_{dc1}$		i_c>0	NNO	NNP	ONP
				i_c<0	OOP	NNP	ONP
	4	$V_{dc1}> V_{dc2}$	$i_b < 0$		POP	PNP	ONP
			$i_b > 0$		ONO	ONP	PNP
		$V_{dc2}> V_{dc1}$	$i_b < 0$		ONO	ONP	PNP
			$i_b > 0$		POP	PNP	ONP
6	1	$V_{dc1}> V_{dc2}$	$i_a > 0$	i_b<0	OOO	POO	POP
				i_b>0	OOO	POO	ONO
			$i_a < 0$	i_b<0	OOO	POP	ONN
				i_b>0	OOO	ONO	ONN
		$V_{dc2}> V_{dc1}$	$i_a > 0$	i_b<0	OOO	ONO	ONN
				i_b>0	OOO	POP	ONN
			$i_a < 0$	i_b<0	OOO	ONO	POO
				i_b>0	OOO	POP	POO
	2	$V_{dc1}> V_{dc2}$	$i_a > 0$	i_b<0	POP	POO	PNO
				i_b>0	ONO	POO	PNO
			$i_a < 0$	i_b<0	POP	ONN	PNO
				i_b>0	ONO	ONN	PNO
		$V_{dc2}> V_{dc1}$	$i_a > 0$	i_b<0	ONO	ONN	PNO
				i_b>0	POP	ONN	PNO
			$i_a < 0$	i_b<0	ONO	POO	PNO
				i_b>0	POP	POO	PNO
	3	$V_{dc1}> V_{dc2}$		i_b<0	POP	PNP	PNO
				i_b>0	ONO	PNP	PNO

		$V_{dc2} > V_{dc1}$		$i_b<0$	ONO	PNO	PNP
				$i_b>0$	POP	PNO	PNP
	4	$V_{dc1} > V_{dc2}$	$i_a > 0$		POO	PNO	PNN
			$i_a < 0$		ONN	PNN	PNO
		$V_{dc2} > V_{dc1}$	$i_a > 0$		ONN	PNN	PNO
			$i_a < 0$		POO	PNO	PNN

4.2.4 Objective function

The objective of current tracking is achieved with the application of suitable voltage vector equal to the reference voltage vector obtained from Eq. (4.1). The neutral point voltage balancing is achieved inherently with the selected switching states. Hence, the objective function in Eq. (3.21) is redefined with a single control objective as shown

$$\xi(k+1) = \left|v^*_{i\alpha}(k+1) - v_{i\alpha}(k+1)\right| + \left|v^*_{i\beta}(k+1) - v_{i\beta}(k+1)\right| \tag{4.9}$$

The objective function defined in Eq. (4.9) is evaluated for the selected number of finite switching states to select the optimal voltage vector for the next sampling period. Flowchart for this control approach is shown in Fig.4.6.

4.3 Impact of selective switching states on CMV reduction.

Multi-objective model predictive control of 3L-NPC PV inverter mainly requires the reference current tracking and DC-link capacitor voltage balancing. However, in order to mitigate the leakage current associated with the PV inverter, the CMV reduction constraint is considered in the objective function as given below:

$$\xi(k+1) = \left|v^*_{i\alpha}(k+1) - v_{i\alpha}(k+1)\right| + \left|v^*_{i\beta}(k+1) - v_{i\beta}(k+1)\right| + \lambda_{cm}\left|v_{cm}(k+1)\right| \tag{4.10}$$

Where, λ_{cm} is the weighting factor for CMV reduction.

The objective function in Eq. (4.10) is evaluated for the three selected switching states. The DC-link capacitor voltage is inherently achieved with the selected switching states; hence, the selection of λ_{dc} is eliminated. The CMV reduction is a secondary control objective and the only weighting factor to be selected. Hence, the weighting factor selection becomes very simple. However, the impact of selective switching states on CMV reduction is limited by the DC-link capacitor voltage balancing.

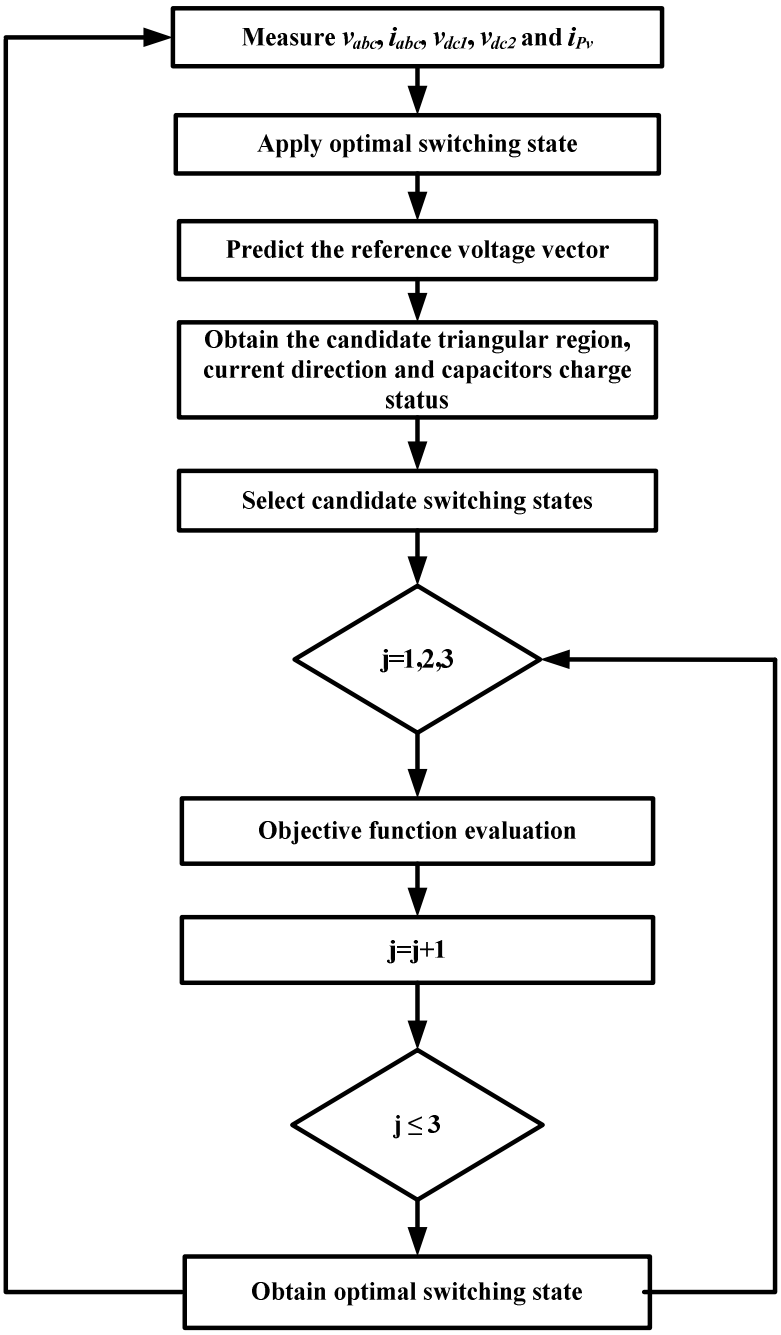

Fig.4.6. Flowchart for selective FS-MPC for single-stage grid-tied 3LNPC PV inverter

The CMVs of the admissible switching states for 3L-NPC inverter are shown in Table.4.4. It can be observed that the switching states of medium voltage vector have zero CMV and are peculiar towards the DC-link capacitor voltage balancing. Hence, the choice of selection of these switching states will impact the DC-link capacitor voltage balancing. Therefore, the selected finite-set switching state approach has a limited control over the CMV reduction.

Table.4.4. Switching states of 3L-NPC inverter and corresponding CMV

Voltage Vectors	Switching States	Common-mode voltage (CMV)
Large vectors	PPN, NPP, PNP	$V_{dc}/6$
	NNP, NPN, PNN	$-V_{dc}/6$
Medium vectors	PON, PNO, OPN, ONP, NPO, NOP	*0*
Small Vectors	PPO, OPP,POP	$V_{dc}/3$
	ONN, NON, NNO	$-V_{dc}/3$
	POO, OPO, OOP	$V_{dc}/6$
	OON, ONO, OON	$-V_{dc}/6$
Zero vectors	PPP	$V_{dc}/2$
	NNN	$-V_{dc}/2$
	OOO	*0*

4.4 Simulation results

To examine the performance of proposed FS-MPC control scheme, a detailed model of single-stage grid-tied 3L-NPC SPV inverter is simulated in MATLAB/Simulink and results are presented with a sampling period of T_s = 80μs. For evaluating the performance, the system is subjected to various operating conditions and the results are compared with the classical MPCC. The performance of the proposed control scheme is assessed in terms of standard mean deviation (SMD) of current tracking error (σ_{ig}), SMD of DC-link capacitor voltage deviation (σ_{vdc}), percentage total harmonic distortion (%THD) of injecting currents and computational burden in terms of execution time.

In order to validate the proposed control approach, the simulation results for inherent capacitor voltage balancing with change in inverter phase current direction (indeed the power factor) are presented. As a case study, the results for change in inverter phase currents i_{ga} and i_{gc} of sector-1 are presented in Fig.4.7 and Fig.4.8 for power injection and shunt compensation modes, respectively. The irradiance of SPV system is maintained at 500 Watts/m^2 to extract an active power of 600 Watts and a reference reactive power (Q^*) of ±1040 *Var* is injected to operate at $\pi/3$ leading/lagging power factor. Fig.4.7 (a) and Fig.4.7 (b) show the simulation results for the inverter operating at $\pi/3$ lagging and $\pi/3$ leading, respectively. It can be observed that the injecting current i_{gc} changes from positive to negative during lagging power factor and i_{ga} changes from positive to negative during leading power factor in sector-1. However, even after the change in direction of currents in the same sector, the DC-link capacitor voltages are inherently balanced with optimal switching state among the selected candidate switching states.

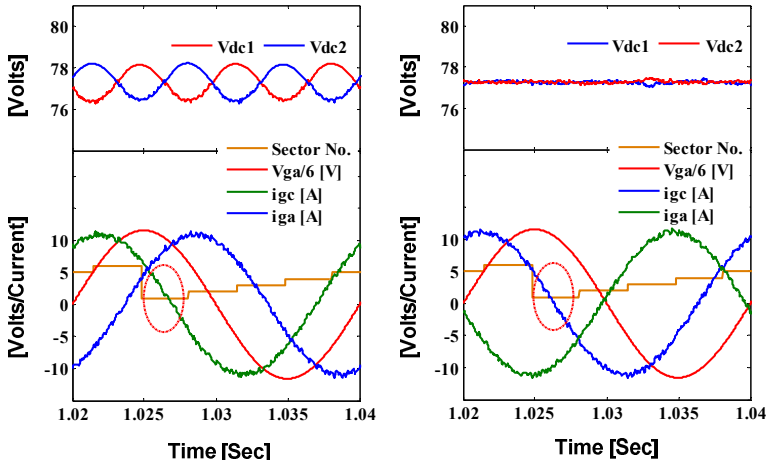

(a) (b)

Fig.4.7. Simulation results for inherent DC-link capacitor voltage balancing with change in current direction in sector-1 under power injection mode for (a) π/3 lag (b) π/3 lead.

The simulation of the inverter operating as a shunt compensator is shown in Fig.4.8. During this mode of operation, the irradiance is kept zero and reactive power reference (Q^*) of ±800 Var is injected. The injecting currents i_{ga} and i_{gc} are positive during lagging power factor and negative during leading power factor operation of the inverter in sector-1. It can be observed that the DC-link capacitor voltages are balanced during these conditions.

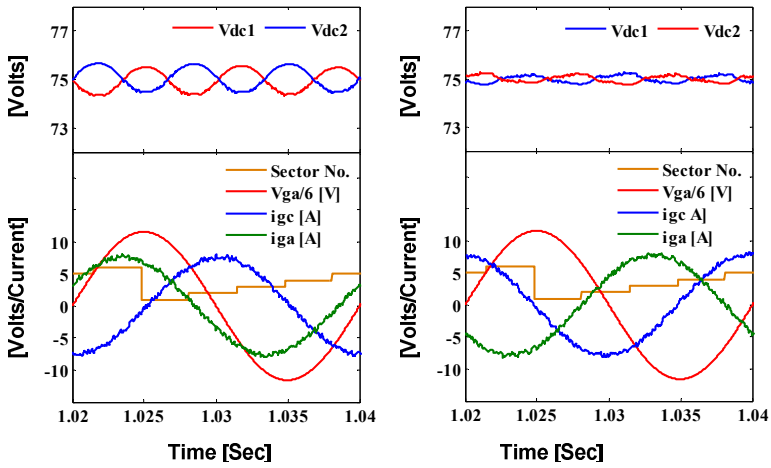

(a) (b)

Fig.4.8. Simulation results for inherent DC-link capacitor voltage balancing under shunt compensator mode (a) π/2 lag (b) π/2 lead.

The maximum power tracking performance of the classical MPCC and proposed selective FS-MPC for change in irradiance are illustrated in Fig.4.9. The change in irradiance profile is as follows: the irradiance (G) is kept constant at 400 Watts/m^2 up to 0.4s. At 0.4s the

irradiance (G) is increased to 800 Watts/m^2 and reduced back to 400 Watts/m^2 at 0.6 s. The maximum power extracted with 400 Watts/m^2 is 460.5 Watts at 153.2V DC-link voltage and 951.45 Watts with 156.8V at 800 Watts/m^2. The subplots of grid current i_{ga}, grid voltage v_{ga}, and the capacitor voltages V_{dc1} and V_{dc2} are plotted corresponding to the change in irradiance for both the controllers as shown in Fig.4.9 (a) and Fig.4.9 (b), respectively. The steady state waveforms of these intermediate signals at 800 Watts/m^2 for both the controllers are shown in Fig.4.10. The results show that the current trace, DC-link voltage tracking and active power evolution of both the controllers are almost similar.

In order to study the effect of operating power factor on capacitor voltage balancing, the reactive power reference of Q^* = -600 Var and Q^* = 600 Var with an irradiance (G) of 800 Watts/m^2 and 0 Watts/m^2 is shown in Fig.4.11 and Fig.4.12. The performance of classical FCS-MPC for G = 800 Watts/m^2 with +600 Var and -600 Var are shown in Fig.4.11 (a) and Fig.4.11 (b) respectively. Further to validate for shunt compensator mode, the change in reactive power from Q^* = -600 Var and Q^* = 600 Var is shown in Fig.4.11 (c). The grid current i_{ga}, grid voltage v_{ga}, and the capacitor voltages v_{dc1} and v_{dc2} corresponding to reference reactive power are shown in the sub-plots. Similarly, the performance of proposed selective finite-states MPC is shown in Fig.4.12 (a), Fig.4.12 (b) and Fig.4.12 (c). From the results it is clear that the DC-link capacitor voltages remain balanced during the grid injection mode (Q^* = ± 600 Var and G = 800 Watts/m^2) and shunt compensator mode (Q^* = ± 600 Var and G = 0 Watts/m^2) for both the controllers. Fig.4.13 shows the results for dynamic response of both the controllers with a step-change in reactive power reference. The percentage total harmonic distortion (%THD) of injecting currents for both the control approaches is shown in Fig.4.14 (a) and Fig.4.14 (b). It can be seen that the response time and %THD of both the control approaches are almost equal.

Fig.4.15 and Fig.4.16 show the results for common-mode voltage reduction constraint. In case of classical MPCC, the objective function is defined with three control objectives i.e., current tracking, voltage balancing and common-mode voltage reduction. The voltage balancing objective and CMV reduction objective are penalized by using the weighting factors λ_{dc} and $\lambda_{cm.}$ In this work the weighting factor for capacitor voltage balancing λ_{dc} is selected first based on branch and bound algorithm. Further, a series of simulations are conducted to fine tune the weighting factors λ_{dc} and λ_{cm}. Fig.4.15 (a-c) show the results for the classical MPCC with λ_{cm}=0, 0.018 and 0.036, respectively.

The objective function in Eq. (4.10) defines the CMV reduction by using the proposed control algorithm. The objective of voltage balancing is inherently achieved with the selective switching states; hence, λ_{cm} is the only weighting factor to be tuned. The result for CMV reduction using the proposed control algorithm for λ_{cm} = 0, 2 and 4 are shown in Fig.4.16. Further increase in λ_{cm} has lead to the imbalance in DC-link capacitor voltages. Due to limited switching states, the CMV reduction by using the proposed control algorithm is comparatively less with respect to the conventional MPCC.

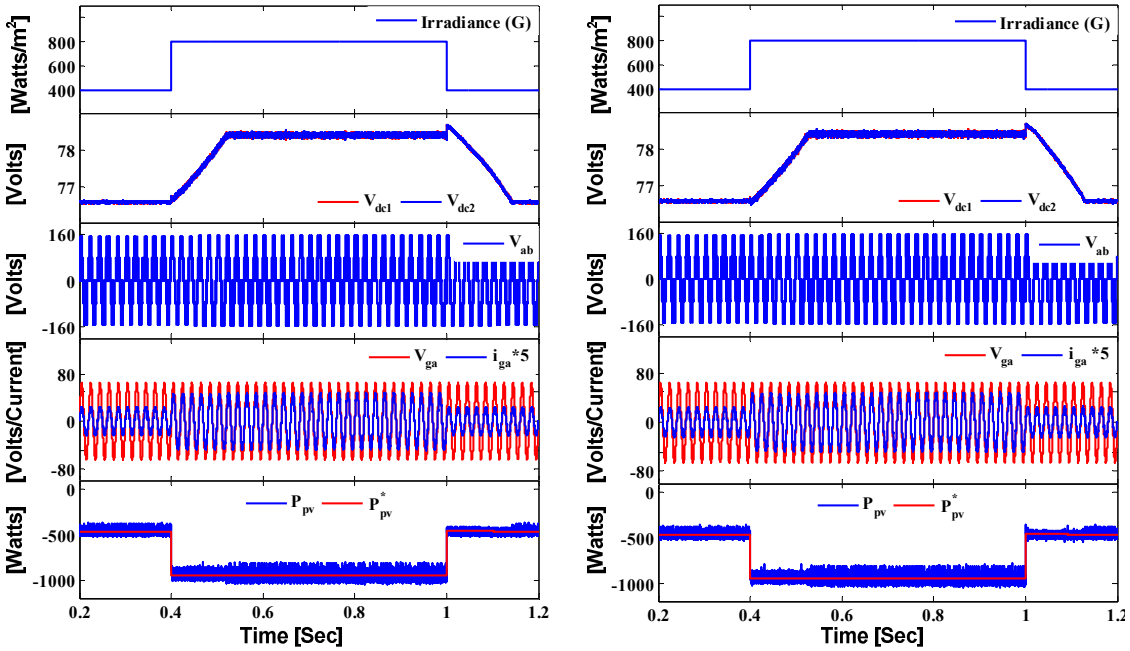

Fig.4.9. Simulation results for power evolution of 3L-NPC PV inverter (a) MPCC and (b) Selective FS-MPC

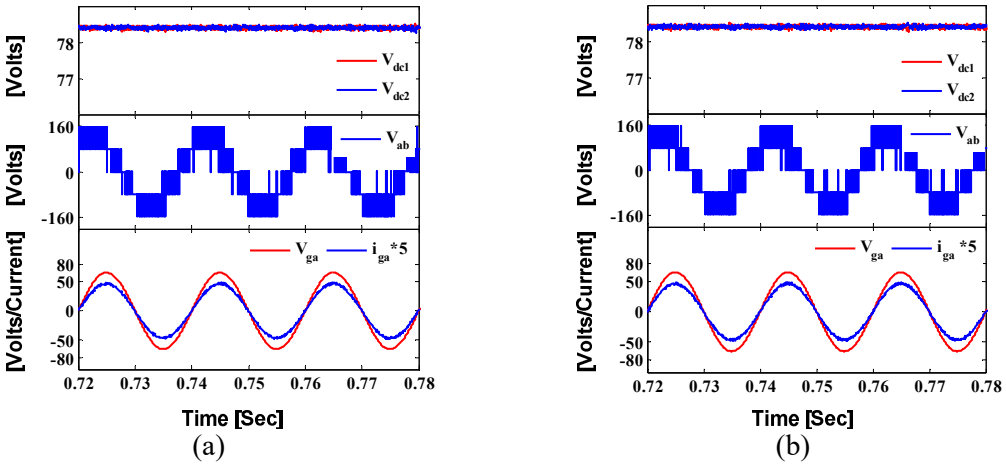

Fig.4.10. Simulation results of intermediate signals at 800 Watts/m^2 (a) MPCC and (b) Selective FS-MPC

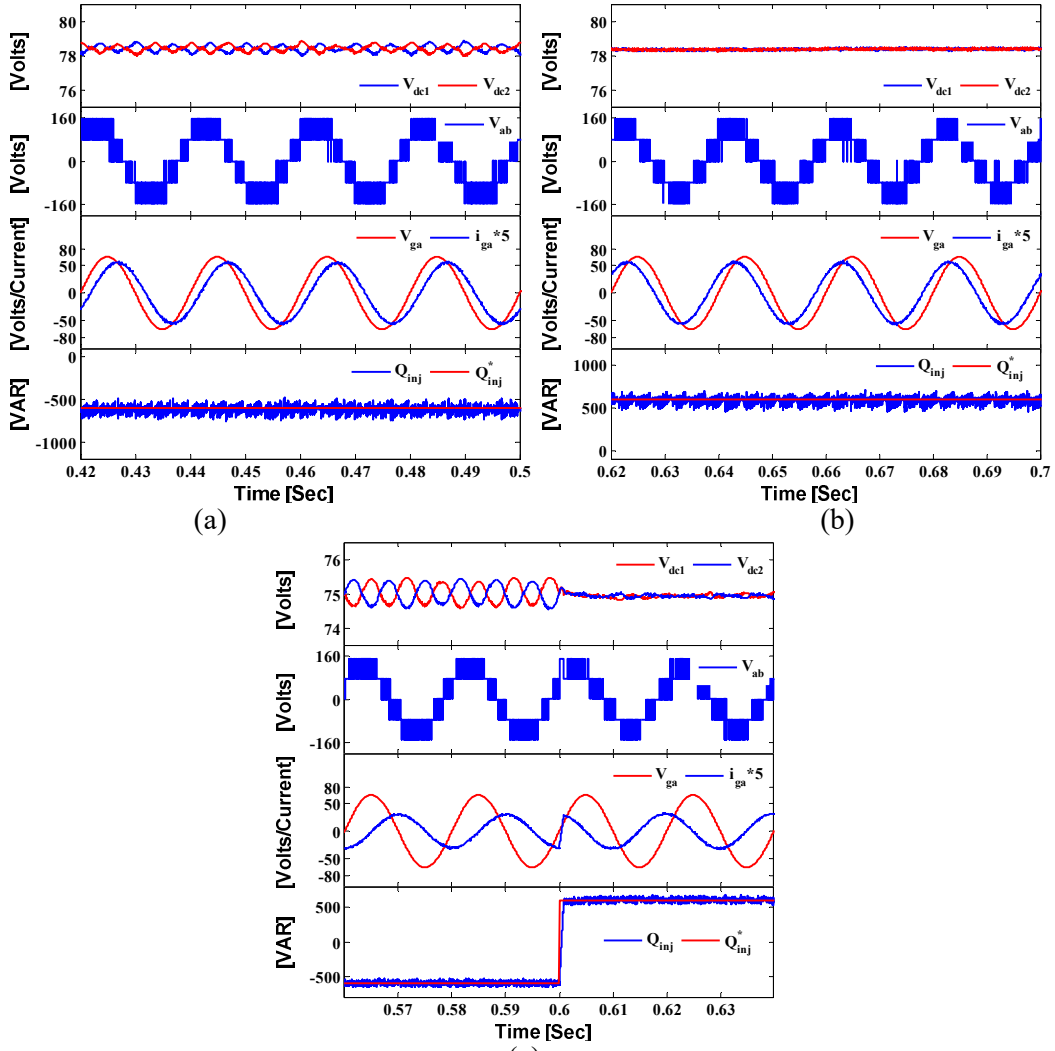

Fig.4.11. Simulation results for DC-link capacitor voltage balancing with MPCC (a) Q*= 600 Var, at G= 800 Watts/m^2 (b) Q*= - 600 Var, at G= 800 Watts/m^2 (c) Q*= -600 Var to +600 Var, at G= 800 Watts/m^2

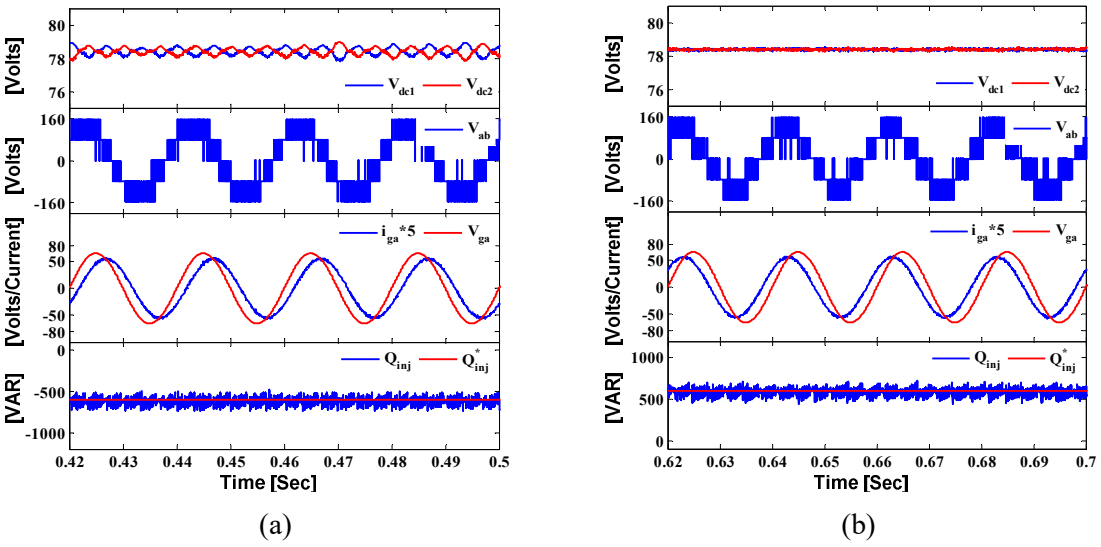

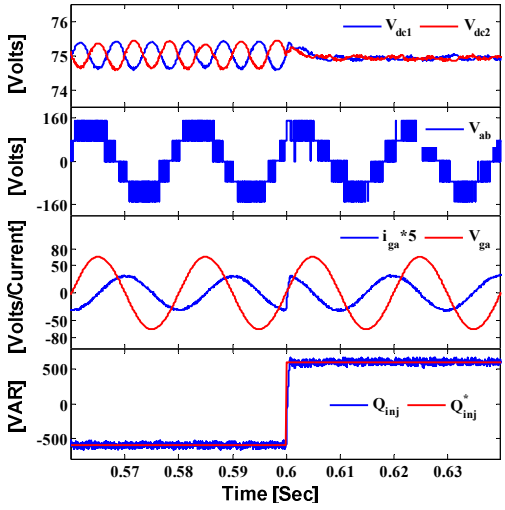

(c)

Fig.4.12. Simulation results for DC-link capacitor voltage balancing with selective FS-MPC (a) Q*= 600 Var, at G= 800 Watts/m^2 (b) Q*= - 600 Var, at G= 800 Watts/m^2 (c) Q*= -600 Var to +600 Var, at G= 800 Watts/m^2

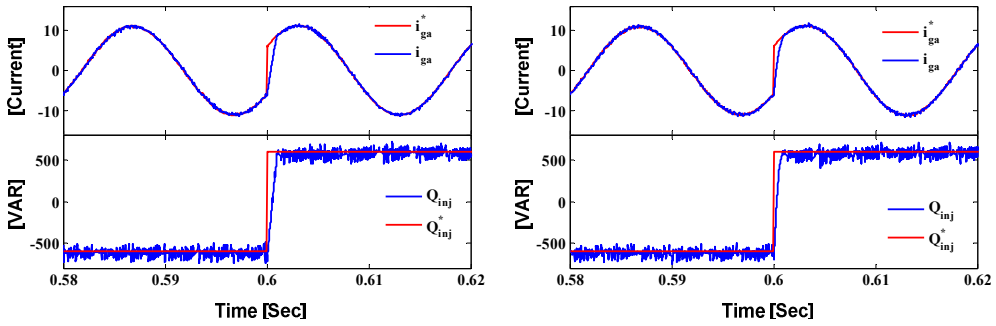

(a) (b)

Fig.4.13. Simulation results for dynamic performance of both the controllers with step-change in reactive power (a) MPCC (b) selective FS-MPC

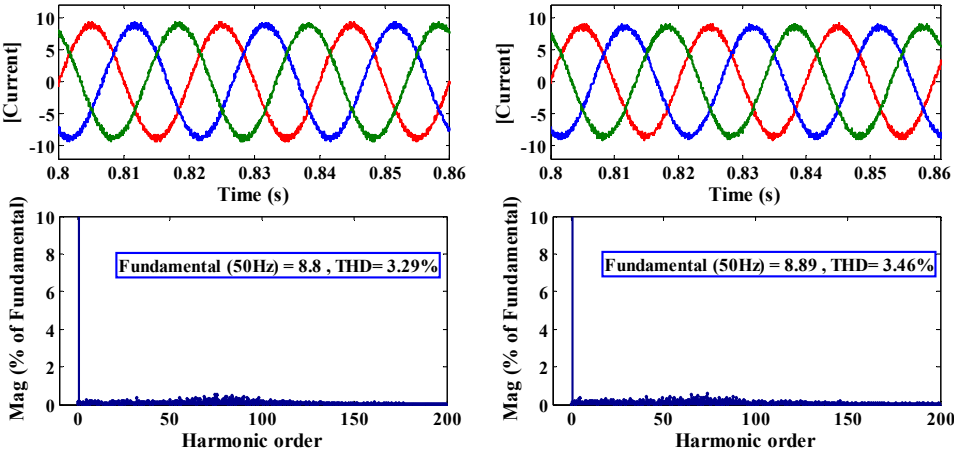

(a) (b)

Fig.4.14. Simulation for %THD of injecting currents (a) FCS-MPC (b) selective FS-MPC

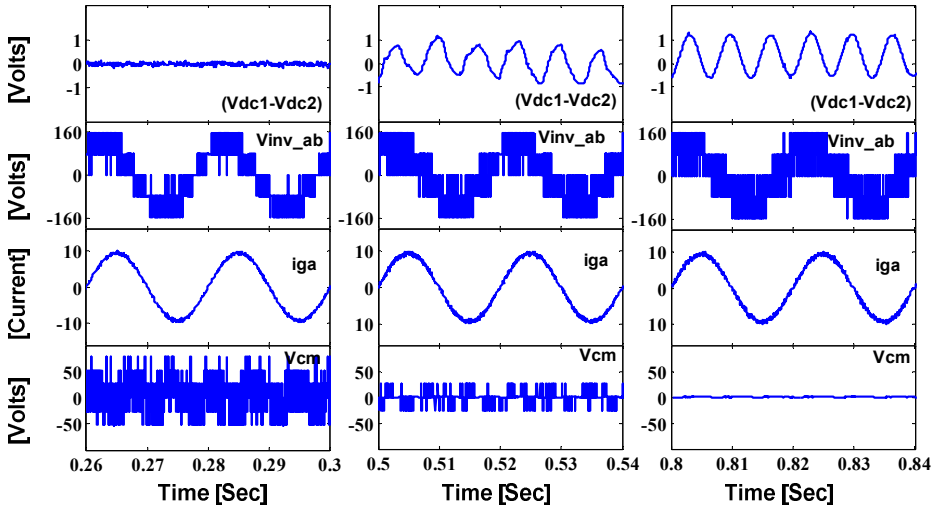

(a) (b) (c)

Fig.4.15. Simulation results for common mode voltage reduction with MPCC (a) λ_{cm}=0, (b) λ_{cm}=0.018 and (c) λ_{cm}=0.036

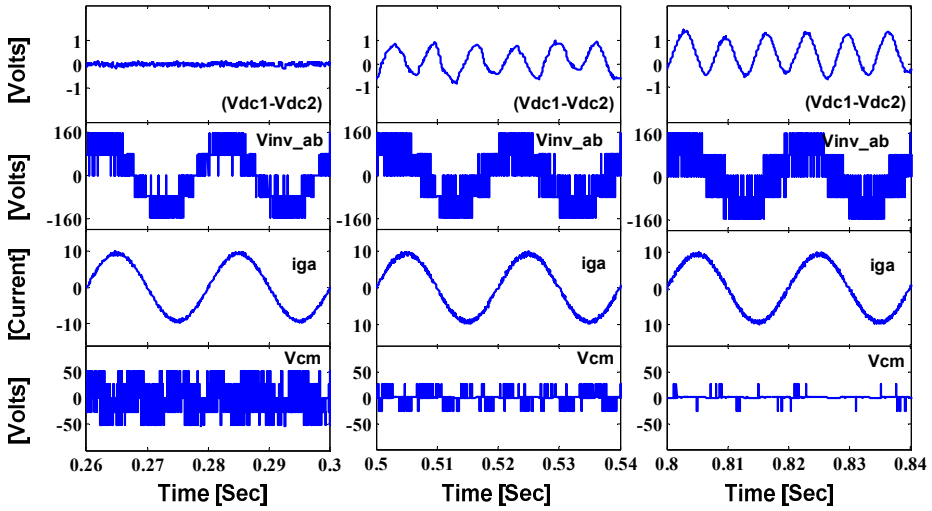

(a) (b) (c)

Fig.4.16. Simulation results for common mode voltage reduction with selective FS MPC (a) λ_{cm}=0, (b) λ_{cm}=2 and (c) λ_{cm}=4

4.5 Experimental results

In order to validate the proposed control approach in real-time, the experimental results for sector-1 are presented in Fig.4.17 and Fig.4.18. Similar to the simulation test scenario, the experiments are conducted for injection mode and shunt compensator mode. In case of PV power injection mode, the irradiance of SPV system is maintained at 500 Watts/m^2 to extract an active power of 600 Watts and a reference reactive power (Q^*) of ±1040 Var is injected to operate at π/3 leading/lagging power factor. Whereas for shunt compensator mode the irradiance is kept zero, and reference reactive power (Q^*) of ±800 Var is injected.

The change in the direction of injecting currents i_{ga} and i_{gc} in the sector-1 is shown in Fig.4.17. It can be seen that the injecting current i_{gc} changes from positive to negative during lagging power factor and i_{ga} changes from positive to negative during leading power factor. Similarly, the results for the inverter operating as a shunt compensator are shown in Fig.4.18. The injecting currents i_{ga} and i_{gc} are positive during lagging power factor and negative during leading power factor operation of the inverter in sector-1. It can be observed that the DC-link capacitor voltages are balanced during these conditions. From the results it can be observed that, irrespective of direction of currents the DC-link capacitor voltages are inherently maintained balanced with appropriate selection of candidate switching states.

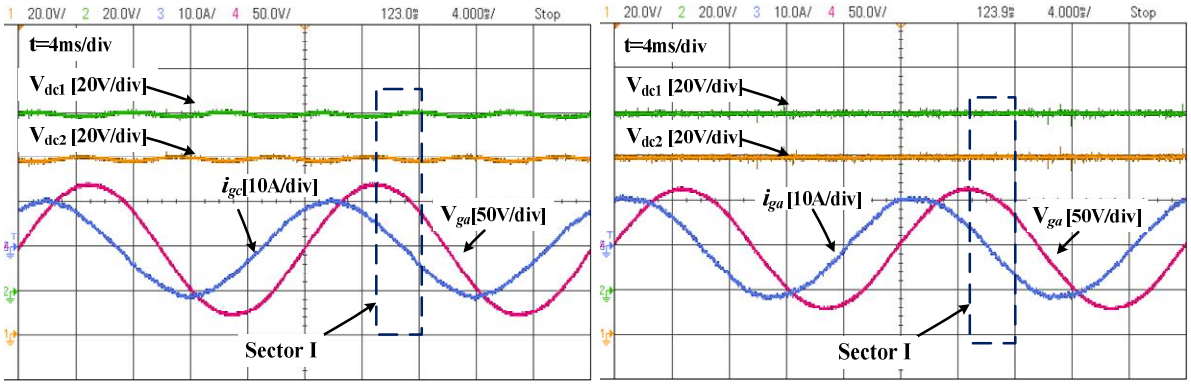

(a) (b)

Fig.4.17. Experimental results for inherent DC-link capacitor voltage balancing with change in current direction in sector-1 under power injection mode (a) π/3 lag (b) π/3 lead.

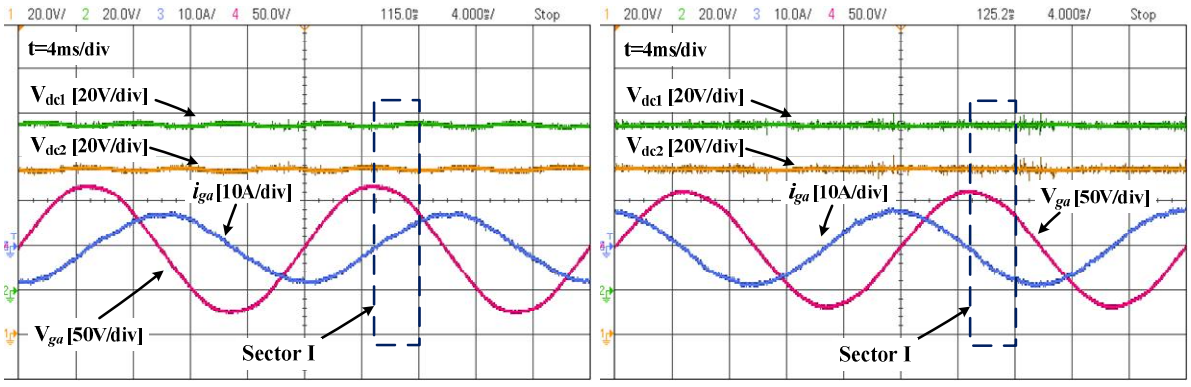

(a) (b)

Fig.4.18. Experimental results for inherent DC-link capacitor voltage balancing under shunt compensator mode (a) π/2 lag (b) π/2 lead.

The experimental results for the change in irradiance from 400 Watts/m^2 to 800 Watts/m^2 and vice-versa for both the control approaches are shown in Fig.4.19 (a) and Fig.4.19 (c),

respectively. The steady state waveforms of phase current (i_{ga}), line voltage (v_{ba}) and the DC-link capacitor voltages (v_{dc1} and v_{dc2}) for 800 Watts/m^2 are shown in Fig.4.19 (b) and Fig.4.19 (d), respectively. The DC-link capacitor voltage v_{dc} (v_{dc1} + v_{dc2}) is tightly regulated to 174.4 volts to extract a maximum power of 960 watts from the PV array. Further, it can be observed that the power evolution of both the control approaches is almost same.

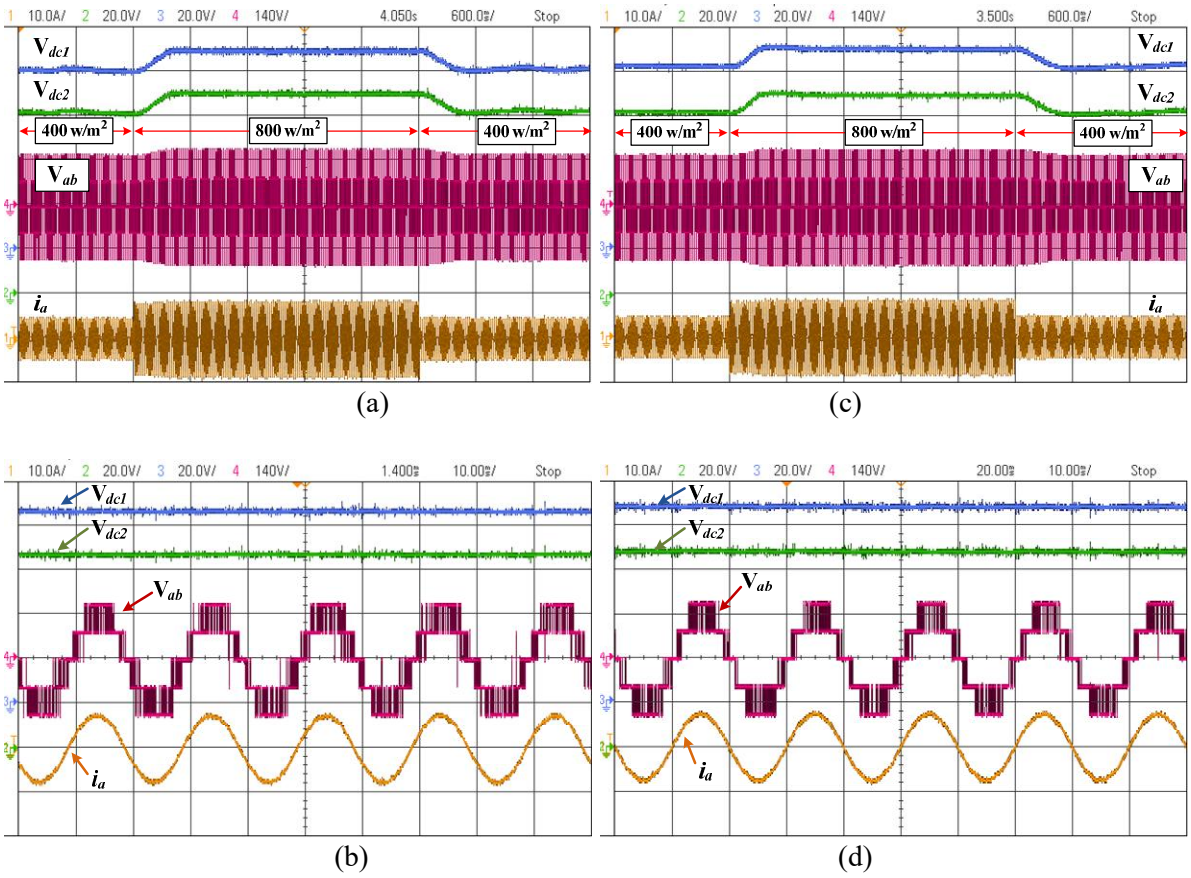

Fig.4.19. Experimental results for power evalution of classical MPCC (a)&(b) and selective FS-MPC (c)&(d)

In order to verify the DC-link capacitor voltage balancing and current tracking ability of both the controllers for various power factor operation of the inverter, a change in reactive power reference from +600 Var to – 600 Var is commanded for various irradiance levels of the inverter. Here, the +Q indicates the lagging power factor operation and -Q indicates the leading power factor operation. Fig.4.20 shows the results for standard deviation in DC-link capacitor voltages and injecting current to its reference with respect to change in active and reactive power injected. Further, the average switching frequency of both the control approaches for a given sampling time is shown in Fig.4.21. From the results, it can be observed that the deviation in DC-link capacitor voltages is less, and the current deviations

are slightly higher for the selective FS-MPC. Further it can also be observed that the average switching frequency of proposed control approach is less compared to the MPCC. The impact of this deviation on the %THD of the injected currents is shown in Fig.4.22. The %THD of injecting a-phase current is found to be 3.45 for the classical MPCC and 3.52 for the proposed selective FS-MPC which are almost similar and are well below the IEEE Std. 1547.

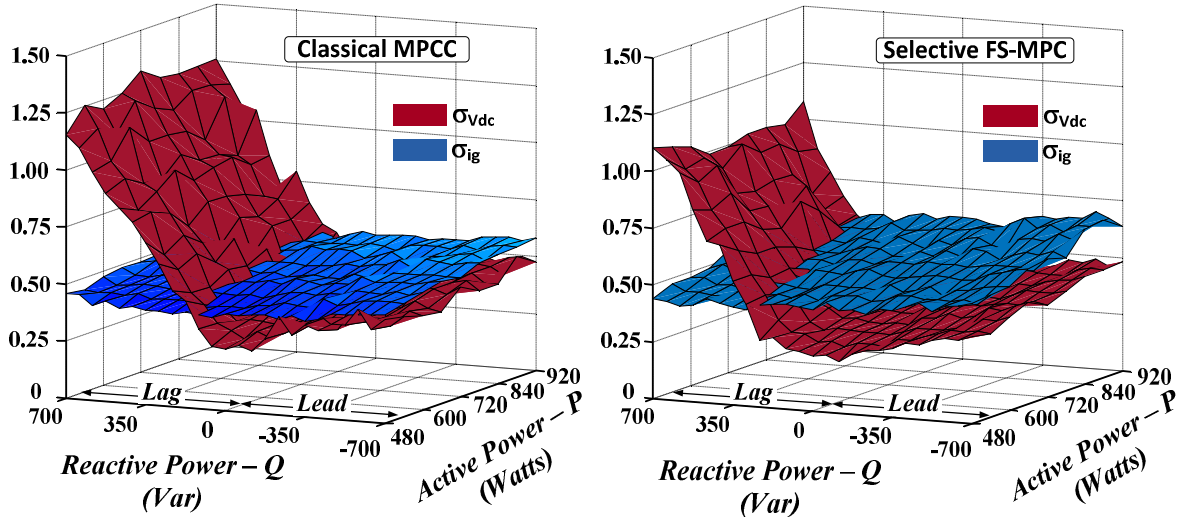

(a) (b)

Fig.4.20. Standard deviation of DC-link capacitor voltages and current tracking errors (a) MPCC (b) selective FS-MPC

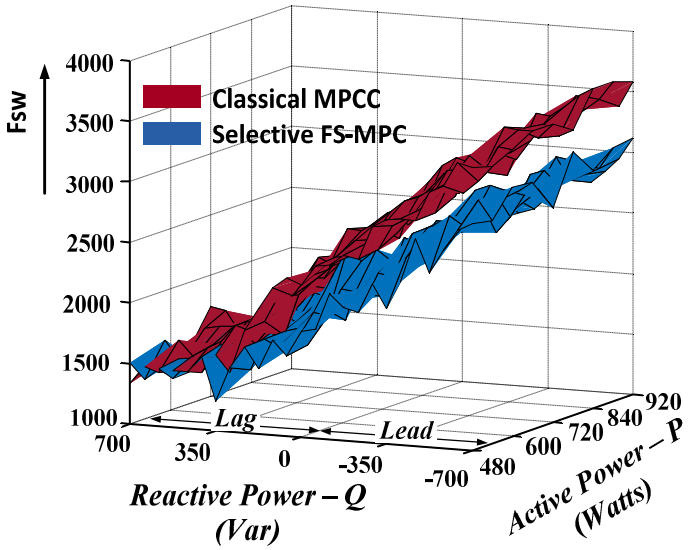

Fig.4.21. Average switching frequency of the MPCC and selective FS-MPC.

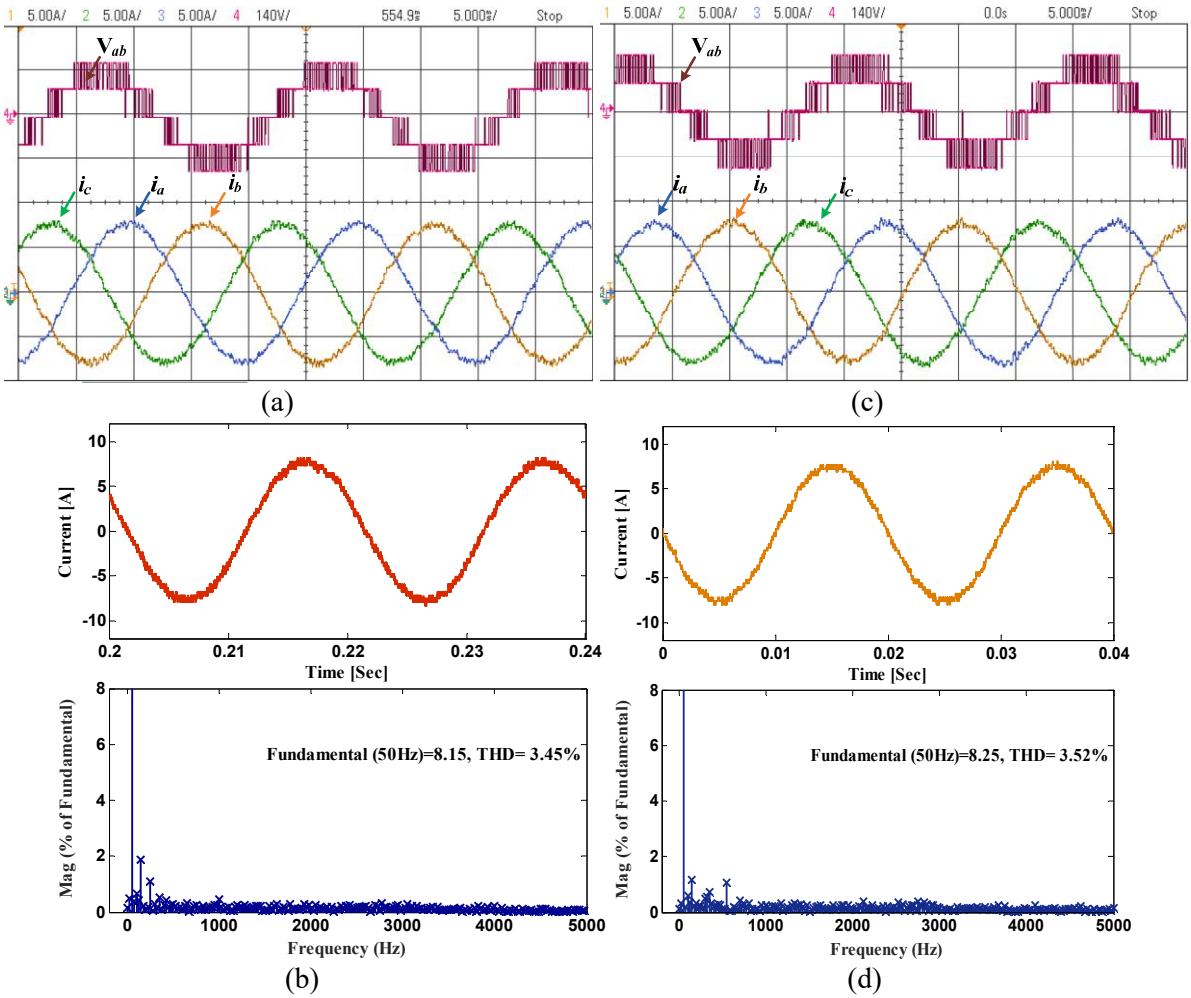

Fig.4.22. Total harmonic distortion of injecting currents with MPCC (a)&(b) and selective FS-MPC (c) & (d)

Sample results for ±600 Var reactive power injection at irradiance of 800 Watts/m^2 with both the control approaches are shown in Fig.4.23. During this condition the DC-link capacitor voltages (v_{dc1} & v_{dc2}) are regulated to 87 V each, which indeed shows that the inverter is extracting the maximum power of 960 Watts from the PV array. Furthermore, sample results for reactive power injection during zero irradiance condition are shown in Fig.4.24. During this condition the inverter is operated as a shunt compensator which provides the reactive power support to the grid.

The dynamic current tracking performance of classical MPCC and proposed selective FS-MPC is shown in Fig.4.25 (a) and Fig.4.25 (b), respectively. The active power component of injecting currents is obtained from the outer DC-link voltage loop where as the reactive power component of current is decided by the grid operator. By keeping the active component of current constant by maintaining the irradiance constant at 800 Watts/m^2, a step change in reactive power reference from -600 Var to 600 Var is commanded. During this

condition the outer DC-link voltage is maintained constant at its reference v_{dcref}= v_{mp}=174 V. The change in reactive power and the tracking of phase-a current is shown in Fig.4.25. The results shows that the control approaches have a similar response and takes around ≈ 2.5ms to reach its reference.

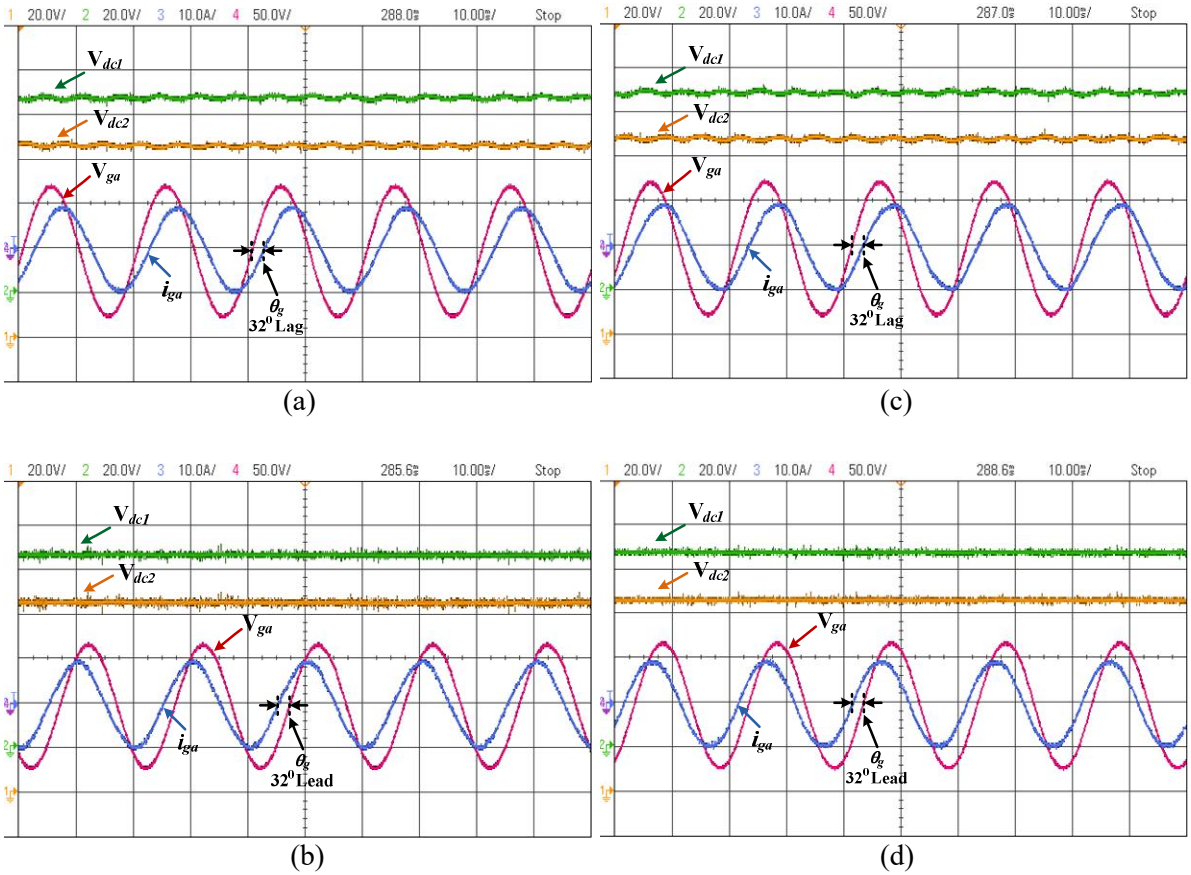

Fig.4.23. DC-link voltage balancing during interfacing converter mode with MPCC(a), & (b) and seletive FS-MPC (c), & (d)

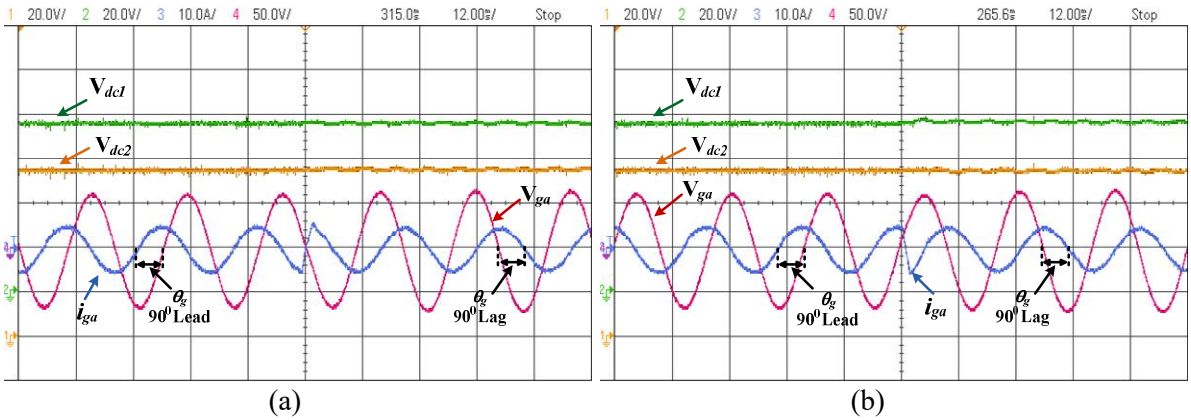

Fig.4.24. DC-link voltage balancing during shunt compensator mode (a) MPCC (b) selective FS-MPC

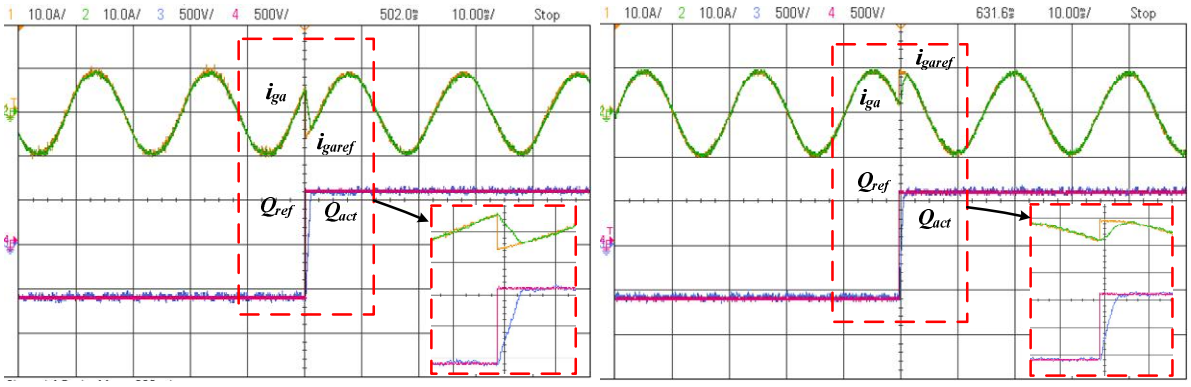

(a) (b)

Fig.4.25. Dynamic current tracking performance of (a) MPCC (b) selective FS-MPC

The results for common-mode voltage reduction constraint with classical MPCC and the proposed selective FS-MPC approach are shown in Fig.4.26 and Fig.4.27, respectively. In case of classical approach, the initial weighting factors of λ_{dc} and λ_{cm} are selected based on branch and bound algorithm. Further, they are tuned based on trial & error approach. Initially, CMV of 3L-NPC PV inverter for λ_{cm} = 0 is shown in Fig.4.26 (a). During this, the DC-link capacitor voltages are maintained balanced. As the weighting factor λ_{cm} is increased to 0.026 the CMV of the inverter is reduced and became zero for the λ_{cm}=0.054. However, during these changes in the λ_{cm} the weighting factor λ_{dc} is adjusted accordingly to maintain the DC-link capacitor voltages balanced. Similar to the classical approach, the weighting factor of λ_{cm} is selected based on empirical approach. Since, the DC-link voltage balance is inherent in the proposed control approach; it requires the selection of weighting factor λ_{cm} for CMV reduction. The response for CMV reduction with weighting factors of λ_{cm} =0, 2.25 and 3.8 are shown in Fig.4.27 (a-c). The CMV is effectively reduced, however further increase in the weighting factor λ_{cm} has lead to complete deviation in the DC-link voltages.

A comparison of computational complexity in terms of execution time required for both the control algorithms are given in Table.4.5. For a fair comparison, a dSPACE DS1104 R&D controller board is used for real-time implementation of both the control algorithm. The execution time of each control algorithm includes the time required for analog-to-digital conversion, reference current extraction, prediction of control variables, objective function minimization and pulse generation. Each individual timings are obtained from the dspace profiler. The number of feedback signals and the reference current generation are same for both the control algorithms. Hence, the time required for analog-to-digital conversion and

reference current generation are same for both the algorithms.

The classical MPCC includess 27 admissible switching states of 3L-NPC inveter for prediction of each control variable. These control variables are evaluated for 27 times in each sampling period. Whereas, in case of proposed control approach, three selected switching states (as discussed in section – IV) are used for prediction and objective function evaluation. Hence, the computations for predictions are reduced by 88.89% for each control variable. Further, due to inherent DC-link capacitor voltage balancing the number of control objectives are further minimized and thereby the computations. The proposed control algorithm requires additional calculation time for the selection of swithcing states. However, it is not significant when compared with the total time of execution.

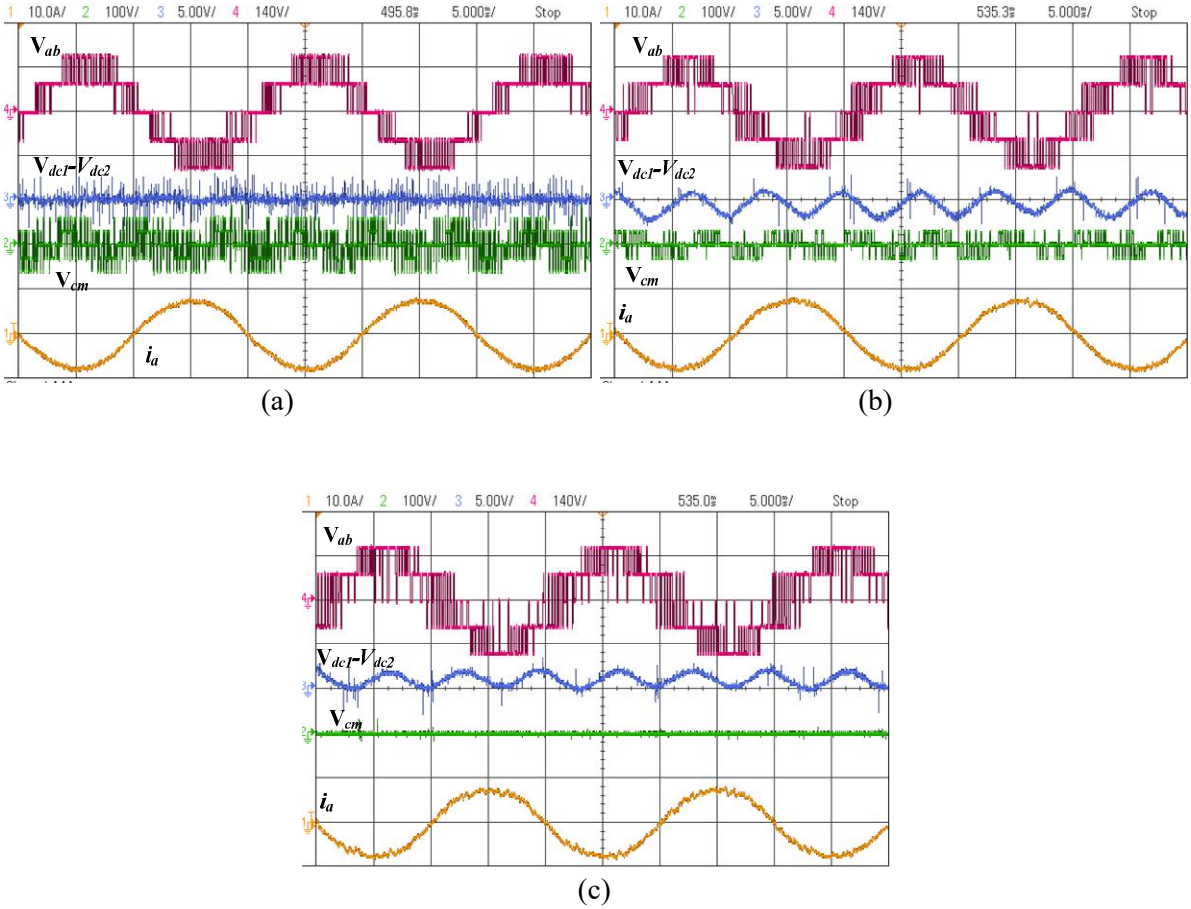

Fig.4.26. CMV reduction with MPCC for (a) λ_{cm} = 0 (b) λ_{cm} =0.026 (c) λ_{cm} = 0.054

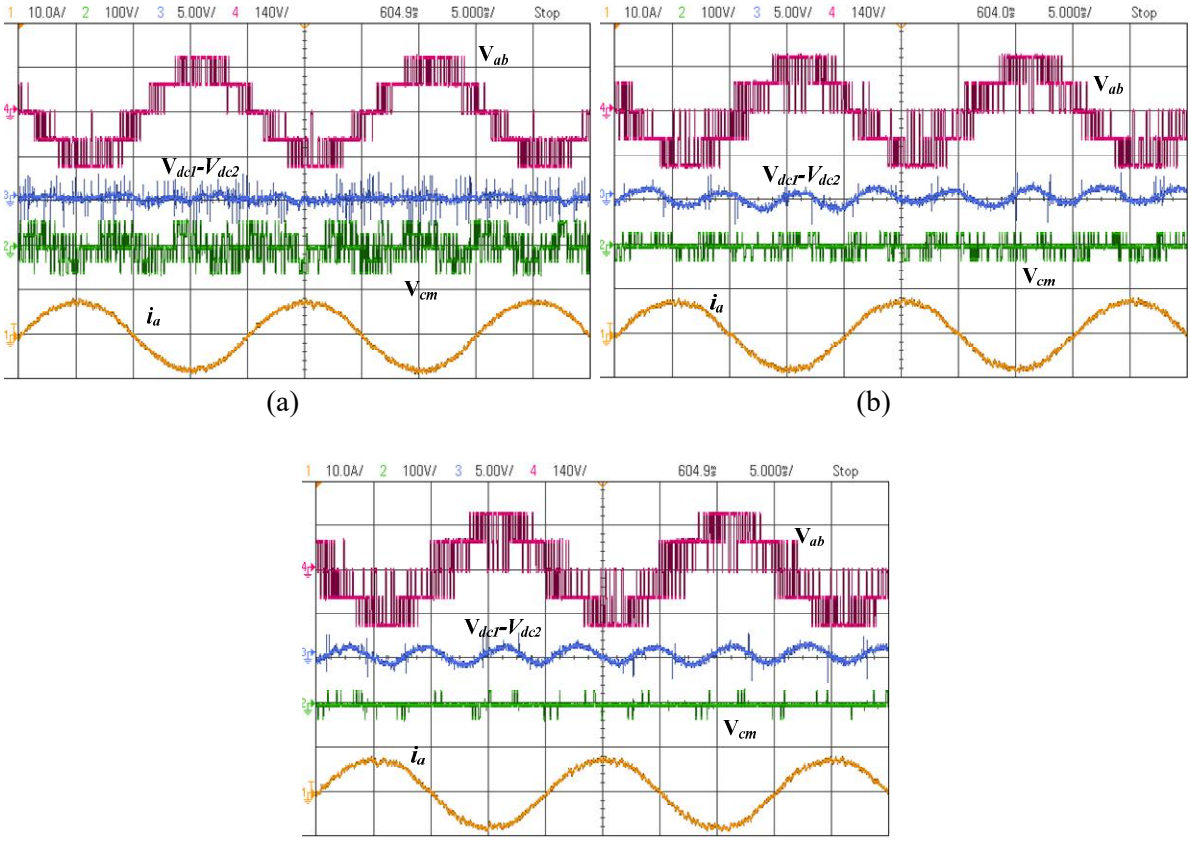

Fig.4.27. CMV reduction with selective FS-MPC (a) λ_{cm} =0 (b) λ_{cm} =2.25 (c) λ_{cm} =3.8

Table.4.5. Comparison of execution time

Event	Classical MPCC	Selective FS-MPC
Analog to Digital Conversion (for feedback signals)	8.23µs	8.23µs
Reference current generation (Includes MPPT algorithm)	15.74µs	15.74µs
Candidate switching states selection	-	5.32µs
Prediction and objective function evaluation	26.42µs	7.35µs
Switching states generation viz Master-bitouts	5.68µs	5.68µs
Total	56.07µs	42.32µs

4.6 Summary

In this chapter, a selective FS-MPC scheme for a 3L-NPC inverter based SPECS is proposed and experimentally verified. A detailed procedure for the selection of switching states to achieve inherent DC-link capacitor voltage balancing is presented. The experimental results of the proposed control approach are compared with the classical

MPCC. From the results, it is observed that the capacitor voltage balancing has been achieved inherently, indeed has eliminated the weighting factor selection issue for equally important control objectives. The overall computation time required for the real-time implementation is reduced by 34.4% in comparison with the classical MPCC and 88.89% for each objective. It can also be observed that the %THD of the injecting currents is 3.52% which is well below the IEEE Std. 1547. The proposed selective FS-MPC scheme has significantly reduced the execution time required for the real-time implementation by retaining the steady state and dynamic current tracking performance. The overall system performance is found to be satisfactory in comparison with the classical MPCC.

Despite of selective FS-MPC merits, the complexity in selection of weighting factors for secondary control objectives are still exists. Further, due to the availability of limited switching states the inclusion of secondary control objectives in the objective function doesn't meet required operating conditions. In order overcome this problem, two generic methods for selection of dynamic weighting factors are introduced in the subsequent chapters.

Chapter-5
CRITIC Weighted Centralized-MPC for Single-Stage Grid-Tied SPECS

5.1 Introduction

FCS-MPC is a class of predictive control approach which has drawn the attention of various researchers with its inimitable features like elimination of modulation stage and flexibility in control of multiple objectives in-concert. Despite of its capability to control multiple constraints, FCS-MPC still has a cascaded structure of control for a single stage grid-tied PV inverter. The cascaded structure of control includes an outer DC-link voltage control loop and inner power control loop. The outer DC-link voltage control loop has a PI controller which compensates the voltage error by providing the power reference for the inner control loop. As a result, the overall system performance will be influenced by the dynamics of PI controller. Tuning of these controller parameters for the desired stability criteria requires a trade-off between steady-state and transient response. In order to overcome this, a cascade-free MPC control approach has been introduced in [111]. In this approach, a dynamic active power reference to regulate the outer DC-link voltage is derived based on discrete-time model of the system. This method has eliminated the outer DC-link voltage control loop with the centralized approach. Further, the similar approach has been extended to various applications [33], [92], [102], [112], [113]. In these applications, the DC-link voltage is regulated to a fixed value of reference to inject active and reactive power into the grid. However, the single-stage grid-tied PV inverter considered for the investigation in this work has a floating DC-link whose voltage should be regulated to the MPPT reference for extracting the maximum power. Hence, the dynamic power reference generation presented in [33], [92], [102], [111]–[113] are not directly applicable to regulate the floating DC-link of the inverter.

The basic objective of FCS-MPC is to determine the switching-state which drives the required control variable to its reference. FCS-MPC is a direct control approach which has eliminated the modulation stage with an objective function to determine the appropriate switching-state. The objective function is defined with multiple control objectives whose control variables are of dissimilar physical nature with unequal magnitude levels. Hence, to maintain the relative importance among the variables a weighting factor is assigned for each control objective. The defined objective function is evaluated with finite number of admissible switching states of the converter. The switching state which minimizes the objective function is applied during the next sampling period.

Let, C_{Oj} for $j = 1,2,...,n$ are the control objectives of the system and, S_i for $i = 1,2,...,m$ are

the admissible finite number of switching states of the power converter. The generalized objective function $\xi(k)$ is defined as

$$\xi\left(S_i\right)\Big|_{i=1,2,\ldots,m} = \sum_{j=1}^{n} \lambda_{COj} \underbrace{\left|C_{vj}^{*} - C_{vj}^{p}\left(S_i\right)\right|}_{C_{Oj}} \tag{5.1}$$

Where, C_{vj} is the control variable and λ_{COj} is the weighting factor of j^{th} objective. Here, the superscript '*' refers to the reference variable and superscript 'p' for the predicted variable.

The control objectives defined in Eq. (5.1) changes with the change in the system; hence the relative importance among these control objectives is intermittent. Further, increase in the weighting factor of one control objective increases its relative importance among the objectives, but it doesn't necessarily lead to a desired performance/operation of the system. This conflicting characteristics and intermittent correlation between the control objectives makes the selection of weighting factors more complex.

In order to address these limitations, a criteria importance through inter-criteria correlation weighted centralized model predictive control (CRITIC-W-CMPC) approach is presented in this chapter. CRITIC is one of the popular objective weighting approaches in the MCDM methods. MCDM methods are widely used to find the optimal solution for problems associated with conflicting criteria and complex decision making. The CRITIC based objective prioritization approach determines the dynamic weights for the control objectives to ensure an improved tracking performance. Further, the proposed CMPC regulates the floating dc-link to its MPPT reference voltage for extracting the maximum power.

5.2 Proposed CMPC for SPV Inverter

The schematic circuit of a single-stage grid-tied 3L-NPC PV inverter with CRITIC-W-CMPC approach is shown in Fig.5.1. The NPC inverter as an interfacing unit necessitates DC-link voltage regulation for extracting maximum power from the PV array, control of active-reactive power injecting into the grid and balancing of split-capacitor voltages. The proposed centralized MPC approach incorporates the objective of outer DC-link voltage regulation into the inner power tracking by using a dynamic power reference generation. For a single-stage PV inverter, the dynamics of floating DC-link voltage is usually coupled to the active and reactive power injected by the inverter [133]. The dynamic power reference

generation for single-stage PV inverter necessitates a decoupled active-reactive power control in the CMPC. Hence, a decoupled active-reactive power control with modified dynamic reference power generation is implemented in the proposed CMPC approach.

5.2.1 Decoupled active-reactive power control

A detailed derivation for the decoupled active-reactive power control is presented in this section. For the ease of modeling and computation, the three phase quantities i_{gx} and v_{gx} for $x \in \{a, b, c\}$ in *a-b-c* reference frame are transformed to stationary orthogonal *α-β* reference frame quantities $i_{g\alpha\beta}$ and $v_{g\alpha\beta}$ by using a Clarke's transformation matrix 'Γ'.

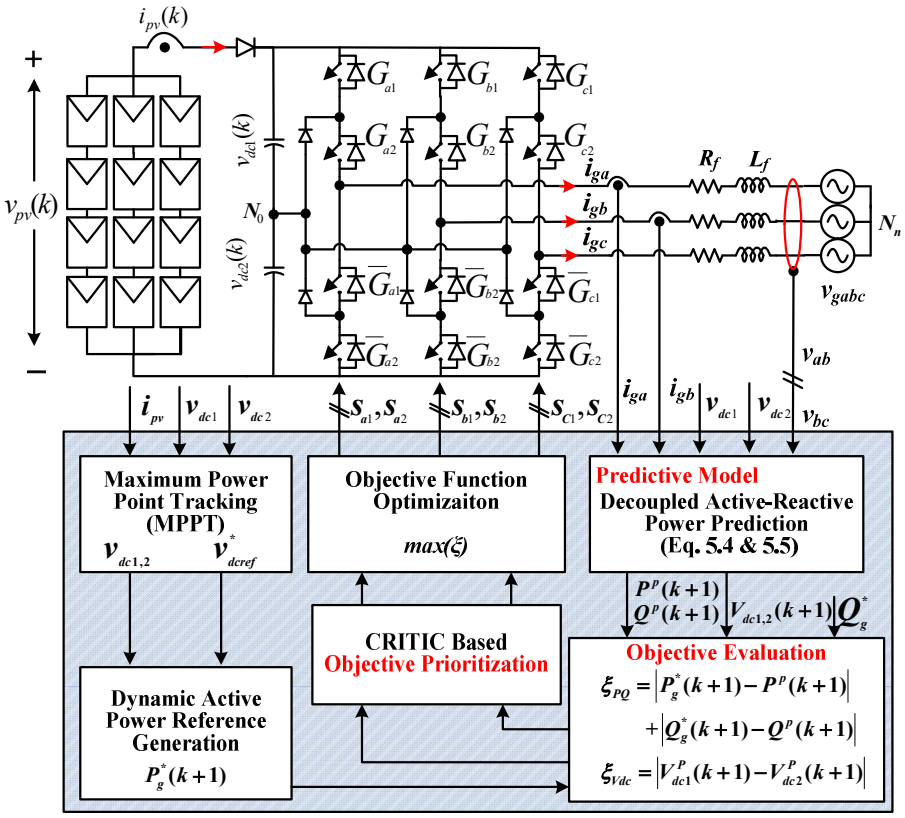

Fig.5.1. Schematic of single-stage grid tied 3L-NPC PV inverter with CRITIC-W-CMPC approach.

The time derivative of instantaneous active and reactive power in *αβ*-frame is given as

$$\frac{dp(t)}{dt} = -\omega q(t) - \frac{R_f}{L_f} p(t) + \frac{3}{2}\hat{v}_{gi} - \frac{3}{2} v_m^2(t) \tag{5.2}$$

$$\frac{dq(t)}{dt} = \omega q(t) - \frac{R_f}{L_f} q(t) + \frac{3}{2}\left[v_{g\beta}(t) v_{i\alpha}(t)\right] - \frac{3}{2}\left[v_{g\alpha}(t) v_{i\beta}(t)\right] \tag{5.3}$$

where, $\hat{v}_{gi} = \left[v_{g\alpha}(t) v_{i\alpha}(t) + v_{g\beta}(t) v_{i\beta}(t) \right]$ and $\omega = 2\pi f$

On discretizing Eq. (5.2) and Eq. (5.3) with forward Euler's approximation the decoupled active and reactive power are obtained as

$$P^{p}(k+1) = \left(1 - \frac{R_f T_s}{L_f}\right) p(k) - \omega T_s q(k) + \frac{3T_s}{2L_f}\left[\left(v_{g\alpha}(k) v_{i\alpha}(k) + v_{g\beta}(k) v_{i\beta}\right) - v_m^2(k)\right] \tag{5.4}$$

$$Q^{p}(k+1) = \left(1 - \frac{R_f T_s}{L_f}\right) q(k) + \omega T_s p(k) + \frac{3T_s}{2L_f}\left[\left(v_{g\chi}(k) v_{i\alpha}(k) - v_{g\alpha}(k) v_{i\beta}\right) - v_m^2(k)\right] \tag{5.5}$$

Where $p(k)$, $q(k)$ are instantaneous active and reactive powers injected by the inverter in the present sampling period and $v_m(k)$ is the amplitude of grid voltage.

5.2.2 Dynamic reference power generation for PV system

The active power reference required to track by the CMPC approach is obtained by balancing the net power available at the DC-link as given below

$$P_g^*(k+1) = P_C^*(k+1) + P_f^*(k+1) - P_{PV}(k+1) \tag{5.6}$$

Where, $P^*_C(k+1)$, $P^*_f\ (k+1)$ and $P_{PV}(k+1)$ are the power references for regulating charging/discharging of DC-link capacitors, loss component incurred by the filter inductor on the AC-side and net power available from the PV array, respectively.

The power reference $P^*_C(k+1)$ of the DC-link capacitor is defined based on gradually approaching manner as presented in [111] with finite number of sampling periods $-N_s$ as given

$$P_C^*(k+1) = C_1\left[\frac{\tilde{v}_{C1}^{*2}(k+1) - v_{C1}^2(k)}{2N_s T_s}\right] + C_2\left[\frac{\tilde{v}_{C2}^{*2}(k+1) - v_{C2}^2(k)}{2N_s T_s}\right] \tag{5.7}$$

$$\tilde{v}_{C1}^{*2}(k+1) = v_{C1}(k) + \frac{v_{C1}^*(k) - v_{C1}(k)}{N_s} \tag{5.8}$$

$$\tilde{v}_{C2}^{*2}(k+1) = v_{C2}(k) + \frac{v_{C2}^*(k) - v_{C2}(k)}{N_s} \tag{5.9}$$

Where, $v_{C1}^{*}(k+1)$ and $v_{C2}^{*}(k+1)$ are the dynamic references of corresponding DC-link voltages. The loss component of filter inductor incurred in Eq. (5.6) is defined as follows

$$P_f^{*}(k+1)=\frac{2R_f}{3v_m^2}\left(P_g^{*2}(k+1)+Q_g^{*2}(k+1)\right) \tag{5.10}$$

By substituting Eq. (5.10) in Eq. (5.6), the net power balance equation becomes a second order quadratic equation as follows

$$P_g^{*2}(k+1)-\frac{3v_m^2}{2R_f}P_g^{*}(k+1)+Q_g^{*2}(k+1)+\frac{3v_m^2}{2R_f}\left(P_C^{*}(k+1)-P_{PV}^{*}(k+1)\right)=0 \tag{5.11}$$

There exits two distinct roots for Eq. (5.11), however the solution which defines the actual reference power is given as

$$P_g^{*}(k+1)=\frac{3v_m^2}{4R_f}-\sqrt{\left(\frac{9v_m^2}{4R_f}\right)^2-\frac{3v_m^2}{2R_f}P_C^{*}(k+1)+\frac{3v_m^2}{2R_f}P_{PV}(k+1)-Q_g^{*2}(k+1)} \tag{5.12}$$

The reference power in Eq. (5.12) is used in the objective function to dynamically regulate the injecting power predicted in Eq. (5.4). The reference power includes the power required to regulate the charge of DC-link in addition to the maximum power which is required to be injected into the grid along with the filter loss. Thus the reference power obtained regulates the DC-link to its reference obtained from the MPPT for extracting the maximum power without using any additional controller or a cascaded loop.

5.3 Dynamic weighting factor selection using CRITIC approach

5.3.1 General implementation steps for CRITIC method.

CRITIC is one of the well established objective weighting approaches of MCDM methods [134]–[138]. In general, MCDM methods are used to identify the optimal solution from the available alternatives to achieve the desired criteria. These MCDM methods describe the relation between the criteria's by using a multivariate descriptive statistical analysis. In this method, the evaluation of performance index defined with various criteria's is viewed as a multi-criteria decision making problem, where the objective weights are determined by CRITIC approach. This approach derives the objective weights based on analytical investigation of the contrast intensity and the conflict inherent between criteria's.

In order to measure the contrast intensity and quantify the conflict between the criteria's, standard deviation approach and a Pearson's linear correlation coefficient are used, respectively.

The generalized steps to find the objective weights of individual criterion are given as follows:

Step 1: In the first step an evaluation matrix is formulated based on the available data as follows:

$$X_{ij} = \begin{bmatrix} x_{11} & x_{12} & \cdots & x_{1n} \\ x_{21} & x_{22} & \cdots & x_{2n} \\ \vdots & \vdots & \ddots & \vdots \\ x_{m1} & x_{m2} & \cdots & x_{mn} \end{bmatrix} \tag{5.13}$$

Where '*m*' represents number of alternatives and '*n*' represents number of criterion.

Step 2: The evaluation matrix obtained in the step-1 is converted into a matrix of relative scores by normalizing the elements to a scale of 0 to 1. The normalization of evaluation matrix is given as

$$r_{ij} = \frac{x_j^{\max} - x_{ij}}{x_j^{\max} - x_j^{\min}} \tag{5.14}$$

Where

$$x_j^{\min} = \min\left\{x_{1j}, x_{2j}, \ldots\ldots x_{mj}\right\}$$

$$x_j^{\max} = \max\left\{x_{1j}, x_{2j}, \ldots\ldots x_{mj}\right\}$$

Step 3: To obtain the objective weights of relative importance, the variance of each criteria and linear correlation coefficient are employed to quantify the contrast intensity and conflict between inter-criteria correlation. The information carried by each criterion is determined by quantifying these factors as follows:

$$K_j = \sigma_j \sum_{i=1}^{m} \left(1 - R_{jk}\right) \tag{5.15}$$

Where, contrast intensity (σ_j) and Pearson's linear correlation coefficient (R_{jk}) are given as

$$\sigma_j = \sqrt{\frac{\sum_{i=1}^{m}\left(r_{ij} - \overline{r}_j\right)^2}{m}} \tag{5.16}$$

$$R_{jk} = \frac{\sum_{i=1}^{m}\left(r_{ij} - \overline{r}_j\right)\left(r_{ik} - \overline{r}_k\right)}{\sqrt{\sum_{i=1}^{m}\left(r_{ij} - \overline{r}_j\right)\sum_{i=1}^{m}\left(r_{ik} - \overline{r}_k\right)}} \tag{5.17}$$

Where $\overline{r}_j$ and $\overline{r}_k$ are the mean values of criterion.

Step 4: Finally, The criteria weights can be determined based on the above evaluation information by using the following relation

$$\lambda_j = \frac{K_j}{\sum_{j=1}^{n} K_j} \tag{5.18}$$

The above weights are used to define the performance index as follows

$$\xi_i = \sum_{j=1}^{n} \lambda_j r_{ij} \tag{5.19}$$

5.3.2 CRITIC based objective prioritization for grid-tied 3L-NPC inverter

To implement CRITIC method in objective function optimization, a single objective function is divided into individual objective function for each control objective as follows,

$$\xi_{pq}\left(S_i\right)\Big|_{i=1,2,\ldots,27} = \left|P^*\left(k+1\right) - P^p\left(k+1\right)\right| + \left|Q^*\left(k+1\right) - Q^p\left(k+1\right)\right| \tag{5.20}$$

$$\xi_{vdc}\left(S_i\right)\Big|_{i=1,2,\ldots,27} = \left|V_{dc1}^p\left(k+1\right) - V_{dc2}^p\left(k+1\right)\right| \tag{5.21}$$

CRITIC is formulated based on the analytical investigation of the evaluation matrix for extracting all the information about evaluation criteria. In order to implement this method, the individual error terms of control objectives are considered as evaluation criteria and corresponding matrix is considered as evaluation matrix. The following steps are involved in the implementation of CRITIC based weighting selection

Step 1: In the first step an evaluation matrix is formulated based on the available data as follows:

$$X_{ij} = \begin{bmatrix} \xi_{S1pq} & \xi_{S1vdc} \\ \xi_{S2pq} & \xi_{S2vdc} \\ \vdots & \vdots \\ \xi_{S27pq} & \xi_{S27vdc} \end{bmatrix} \tag{5.22}$$

In the dataset given in (5.22), twenty seven switching states of the 3L-NPC are considered as available alternatives and minimization of power ripple and DC-link capacitor voltage balancing are considered as required criteria.

Step-2: The obtained information in the step-1 is normalized to a scale of 0 to 1 by using the following normalization.

$$r_{ipq} = \frac{\xi_{pq}^{\max} - \xi_{ipq}}{\xi_{pq}^{\max} - \xi_{pq}^{\min}} \tag{5.23}$$

$$r_{ivdc} = \frac{\xi_{vdc}^{\max} - \xi_{ivdc}}{\xi_{vdc}^{\max} - \xi_{vdc}^{\min}} \tag{5.24}$$

Where

$$\xi_{pq}^{\min} = \min\left\{\xi_{S1pq}, \xi_{S2pq}, \ldots\ldots\ldots \xi_{S27pq}\right\}$$

$$\xi_{pq}^{\max} = \max\left\{\xi_{S1pq}, \xi_{S2pq}, \ldots\ldots\ldots \xi_{S27pq}\right\}$$

$$\xi_{vdc}^{\min} = \min\left\{\xi_{S1vdc}, \xi_{S2vdc}, \ldots\ldots\ldots \xi_{S27vdc}\right\}$$

$$\xi_{vdc}^{\max} = \max\left\{\xi_{S1vdc}, \xi_{S2vdc}, \ldots\ldots\ldots \xi_{S27vdc}\right\}$$

Step 3: To obtain the objective weights of relative importance, the variance of each criteria and linear correlation coefficient are employed to quantify the contrast intensity and conflict between inter-criteria correlation. The information carried by each criterion is determined by quantifying these factors as follows:

$$K_{pq} = \sigma_{pq} \sum_{i=S1}^{S27} \left(1 - R_{pqvdc}\right) \tag{5.25}$$

$$K_{vdc} = \sigma_{vdc} \sum_{i=S1}^{S27} \left(1 - R_{pqvdc}\right) \tag{5.26}$$

Where, contrast intensities (σ_{pq}, σ_{vdc}) and Pearson's linear correlation coefficient (R_{pqvdc}) are given as

$$\sigma_{pq} = \sqrt{\frac{\sum_{i=S1}^{S27} \left(r_{ipq} - \overline{r}_{pq}\right)^2}{27}} \tag{5.27}$$

$$\sigma_{vdc} = \sqrt{\frac{\sum_{i=S1}^{S27} \left(r_{ivdc} - \overline{r}_{vdc}\right)^2}{27}} \tag{5.28}$$

$$R_{pqvdc} = \frac{\sum_{i=S1}^{S27} \left(r_{ipq} - \overline{r}_{pq}\right)\left(r_{ivdc} - \overline{r}_{vdc}\right)}{\sqrt{\sum_{i=S1}^{S27} \left(r_{ipq} - \overline{r}_{pq}\right) \sum_{i=S1}^{S27} \left(r_{ivdc} - \overline{r}_{vdc}\right)}} \tag{5.29}$$

Where $\overline{r}_{pq}$ and $\overline{r}_{vdc}$ are the mean values of powers and capacitor DC-link voltages.

Step 4: Finally, individual weights for active-reactive powers and capacitor DC-link voltage can be obtained as follows,

$$\lambda_{pq} = \frac{K_{pq}}{K_{pq} + K_{vdc}} \tag{5.30}$$

$$\lambda_{vdc} = \frac{K_{vdc}}{K_{pq} + K_{vdc}} \tag{5.31}$$

The above weights are used in a single objective function which is similar to conventional approach as follows,

$$\xi\left(S_i\right)\Big|_{i=1,2,\ldots,27} = \lambda_{pq} r_{ipq} + \lambda_{vdc} r_{vdc} \tag{5.32}$$

Finally, by maximizing the above objective function, optimal switching state is selected for next sampling period.

$$\xi_{opt} = \arg \max_{i=S1,..S27} \xi \tag{5.33}$$

The detailed flowchart for this control approach is shown in Fig.5.2.

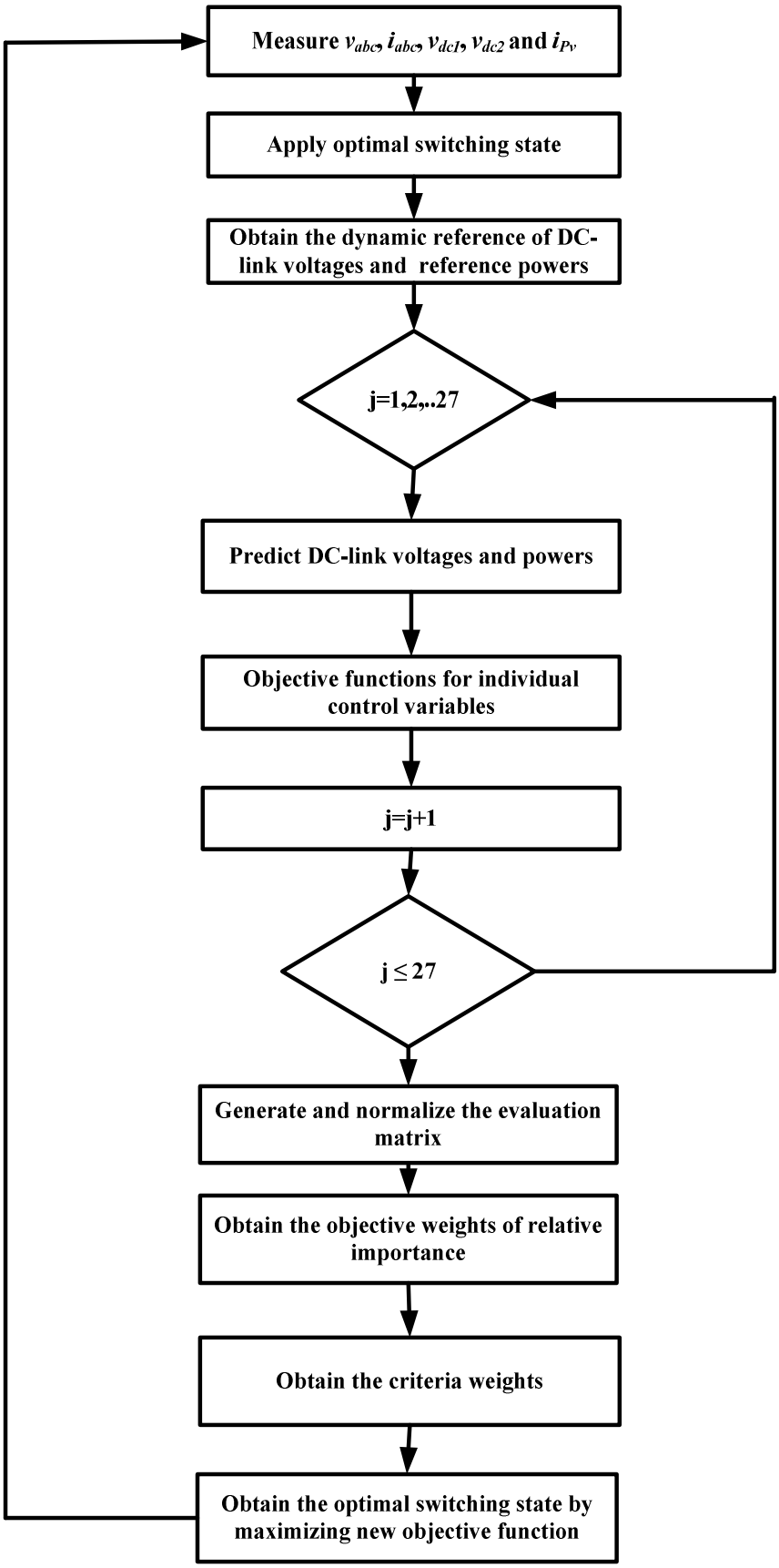

Fig.5.2. Flowchart for single-stage grid tied 3L-NPC PV inverter with CRITIC-WCMPC approach

5.4 Simulation results

To examine the performance of proposed CRITIC-W-CMPC control scheme, a detailed model of single-stage grid-tied 3LNPC SPV inverter is designed in MATLAB/Simulink software. The nominal power of the PV inverter is taken as 1.2 kVA. The simulations are carried with one-step prediction horizon with a sampling period of Ts = 80μs. The system parameters for both the simulation and experimental studies are given in Table.3.1. For evaluating the performance, the system is subjected to various operating conditions and the results are compared with the classical PI-based MPDPC. The performance of the proposed control scheme is assessed in terms of active power ripple, reactive power ripple and %THD of injecting currents.

In order to validate the centralized control of proposed scheme, the active power evolution of the SPV system with both the control approaches are investigated. The PV array in the system is subjected to varying irradiance while keeping the reactive power reference Q^* = 0 Var. The objective function in both the control approaches is defined with the active-reactive power tracking and DC-link capacitor voltage balancing. The scenario of irradiance variation is as follows: initially the irradiance is kept at zero Watts/m^2 for a time interval of [0-0.2]s during which the DC-link voltage is maintained at 150 V (V_{min}). At 0.2 s, the irradiance is changed to 400 Watts/m^2 and is kept constant until 0.6 s; then it is increased to 700 Watts/m^2 at 0.6 s and then to 1000 Watts/m^2 at 1 s. After 1.45 s the irradiance is brought down to 400 Watts/m^2 and then to zero Watts/m^2 at 1.75 s. The DC-link voltage is tracked to 153.2 V, 156.4 V and 157.4 V at 400 Watts/m^2, 700 Watts/m^2 and 1000 Watts/m^2, as a result the maximum power of 460 Watts, 840 Watts and 1200 Watts are extracted, respectively. From Fig.5.3, it can be observed that the proposed control scheme has tracked the reference MPPT voltage without using the outer DC-link voltage controller. Both the control approaches are found to have similar power evolution; on the other hand the power ripple with the proposed control approach is reduced compared to the classical. The steady state waveform of phase voltage, phase current, inverter line voltage and the active-reactive powers of both the control approaches at 400 Watts/m^2, 700 Watts/m^2 and 1000 Watts/m^2 are shown in Fig.5.4.

The harmonic spectrum of the injecting currents for both the methods at 1000 Watts/m^2 is shown in Fig.5.5. The THD is calculated up to 100^{th}-harmonic order. It can be seen that the proposed CRITIC-W-CMPC exhibits the % THD of 2.08 %, which is much smaller than

3.50 % of classical MPDPC. The results show that the proposed scheme has better harmonic performance compared to the classical method.

Similar to the active power, the reactive power evolution of PV inverter with both the control approaches is shown in Fig.5.6. The scenario of change in reactive power reference Q^* is as follows: a step change from 0 Var to -720 Var is applied at 0.8 s, then from -720 Var to +720 Var at 1.6 s and back to 0 Var at 2.4 s. During this change in reactive power, a constant 960 Watts of active power is injected by maintaining the irradiance constant at 800 Watts/m^2. It can be seen that, both the control approaches has regulated the DC-link voltage of the inverter to 156.9 V even after the application of step change in reactive power. In the classical approach the transient seen in the DC-link voltage depends on the choice of controller gains. Whereas, in case of proposed control scheme the DC-link voltage is strictly regulated to the reference MPPT voltage by using the proposed CMPC which has eliminated the need for outer DC-link voltage controller and the efforts required for its tuning. Further, the results confirm that the influence of change in reactive power reference on maximum power tracking is minimized with the decoupled active-reactive power control. The steady state waveform of phase voltage, phase current, inverter line voltage and the active-reactive powers of both the control approaches at an irradiance of 800 Watts/m^2 with ±720 Var are shown in Fig.5.7. The results confirm that the active and reactive power ripples of proposed CRITIC-W-CMPC have lesser power ripple compared to the classical MPDPC.

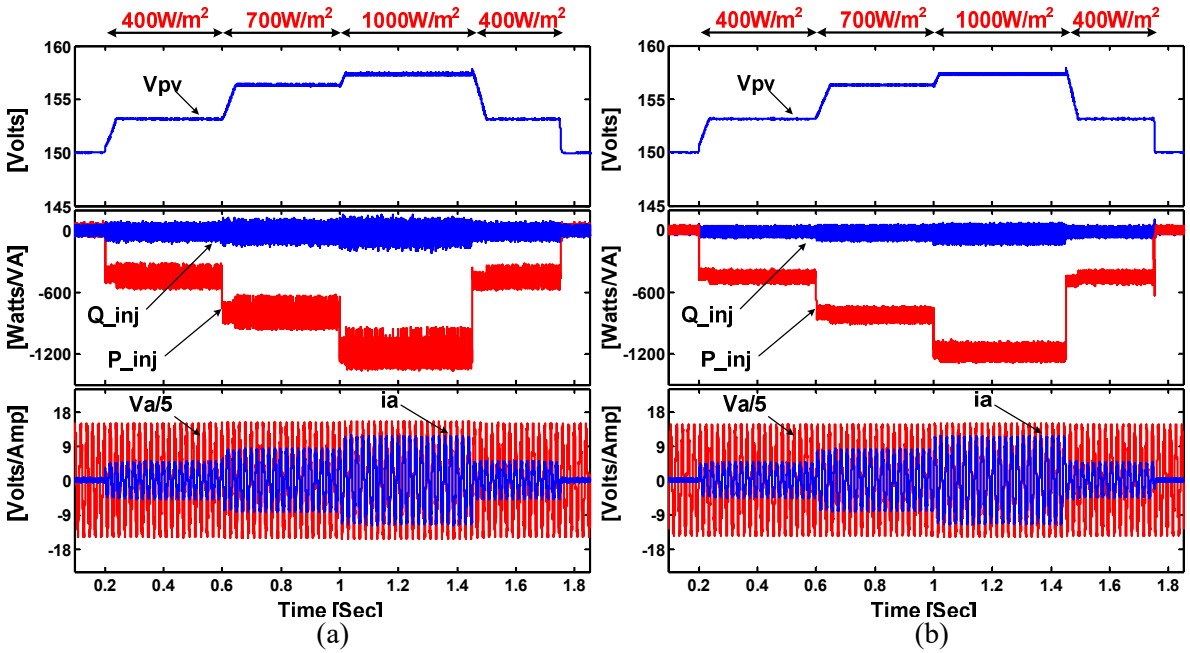

Fig.5.3. Simulation results for active power evolution of 3L-NPC PV inverter (a) MPDPC (b) CRITIC-W-CMPC

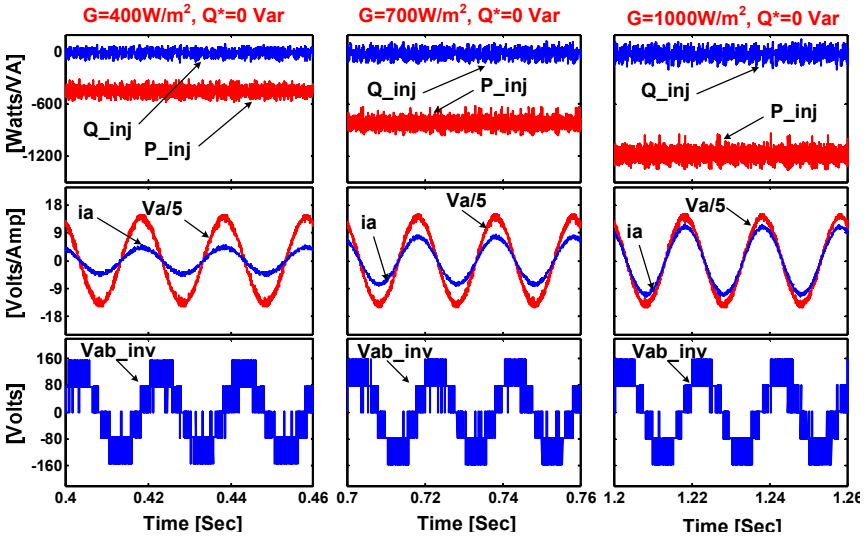

(a)

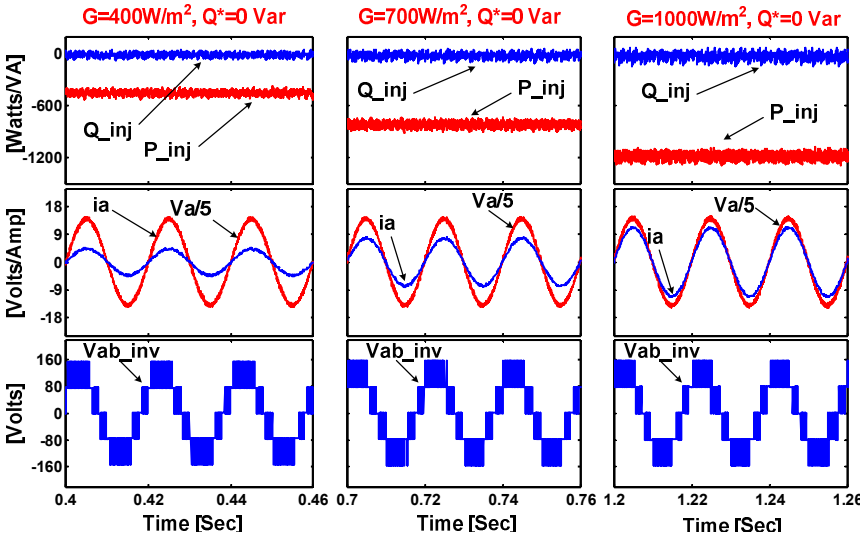

(b)

Fig.5.4. Simulation results for steady-state active power at various irradiances (a) MPDPC (b) CRITIC-W-CMPC.

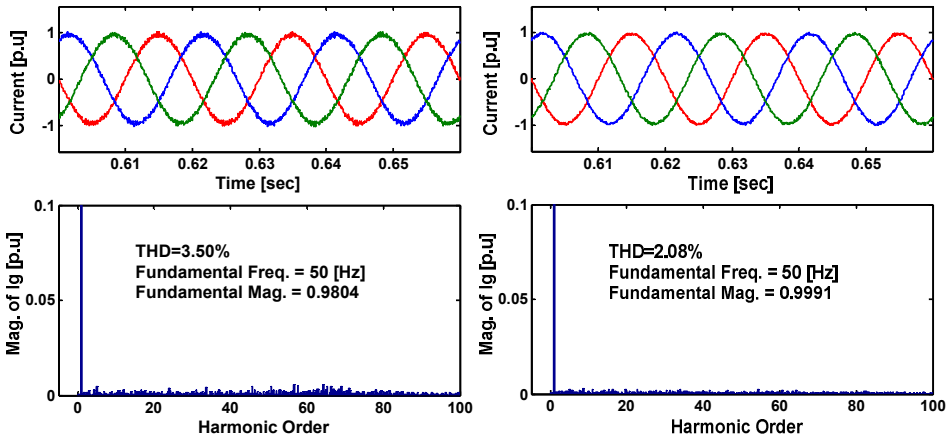

(a) (b)

Fig.5.5. Simulation results for harmonic spectra and %THD of injecting currents (a) MPDPC (b) CRITIC-W-CMPC.

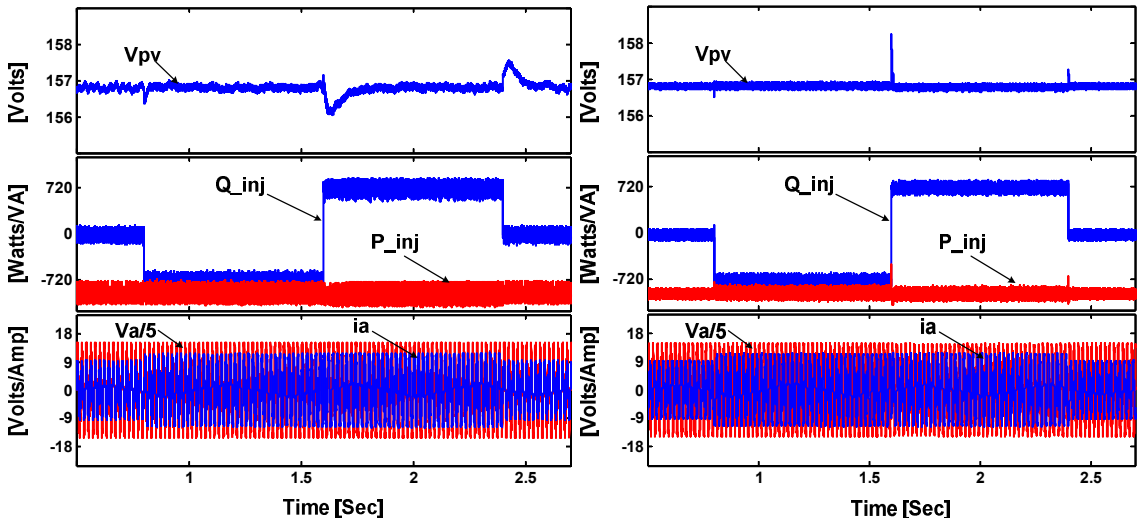

(a) (b)

Fig.5.6. Simulation results for reactive power evolution of 3L-NPC PV inverter (a) CMPDPC (b) CRITIC-W-CMPC.

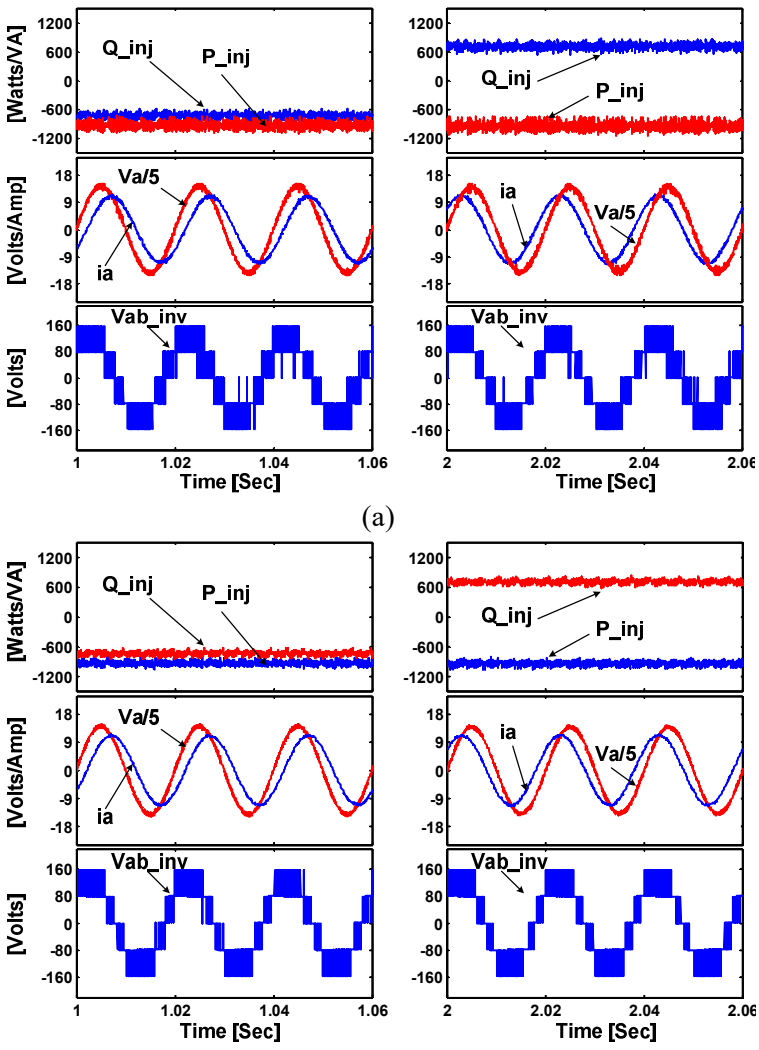

(a)

(b)

Fig.5.7. Simulation results for steady-state active-reactive power (a) MPDPC (b) CRITIC-W-CMPC.

The dynamic selection of weighting factors corresponding to the change in operating conditions of the PV inverter is shown in Fig.5.8. Initially the power tracking objective and DC-link capacitor voltage balancing objectives are considered. Similar to the reactive power evolution, a step change in reactive power reference Q^* from 0 Var to -720 Var and then to +720 Var and back to 0 Var is applied during [0-0.7] s. The weighting factors λ_{pq} and λ_{dc} corresponding to the power tracking and DC-link voltage balancing are calculated online. At 0.7 s the third objective of CMV reduction is enabled where the λ_{cmv} is also calculated online along with λ_{pq} and λ_{dc}. The zoomed view of dynamically selected weighting factors is shown in the subplot of Fig.5.8. The results validate the dynamic adaption of weighting factor corresponding to operating conditions to meet the required objectives.

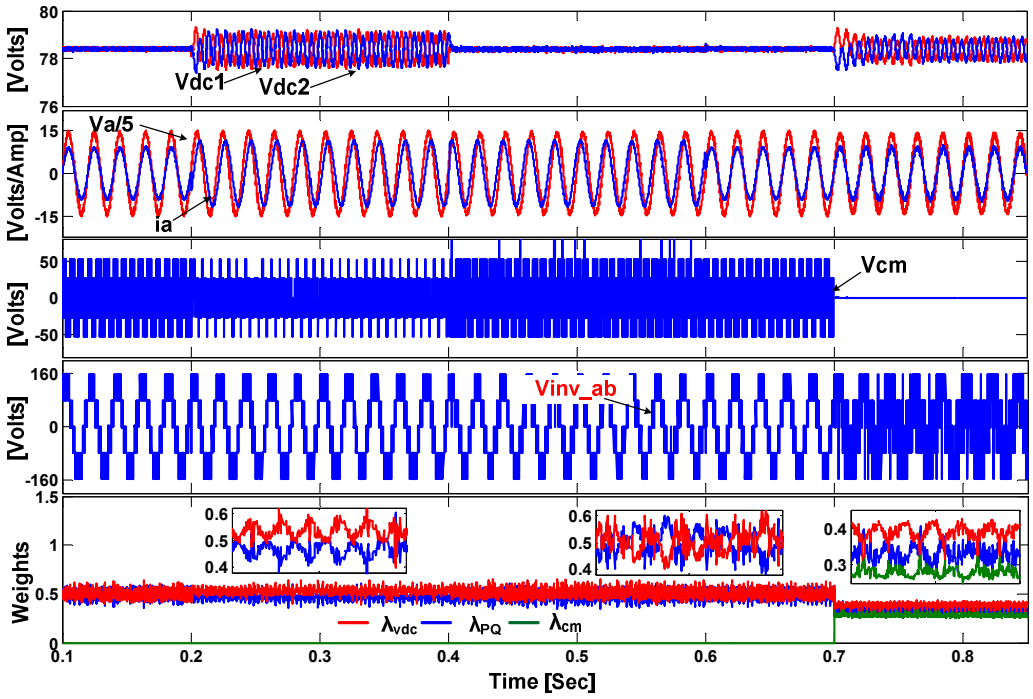

Fig.5.8. Simulation results illustrating the dynamic selection of weighting factors change in operating condition.

The impact of weighting factor selection on the dynamic performance of power tracking and DC-link capacitor voltage balancing objectives are investigated individually. Fig.5.9 illustrates the results for dynamic performance of both the control approaches for step change of reactive power reference from -720 Var to +720 Var. The time taken for the measured power to track the reference by using the proposed control scheme is 0.1 ms which is almost similar to that of the classical. Similarly, Fig.5.10 illustrates the DC-link capacitor voltage balancing capabilities of both the control approaches. Initially an intentional voltage

difference of 40 V is applied till 0.4 s and then commanded to balance the voltages V_{dc1}, and V_{dc2}. The results show that both the control approaches balances the capacitor voltages; however, the proposed control scheme is fast compared to the classical.

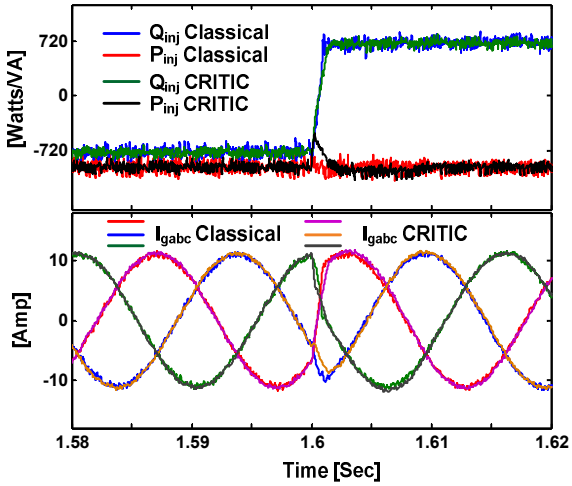

Fig.5.9. Simulation results for dynamic performance of both the control approaches for step change in reactive power.

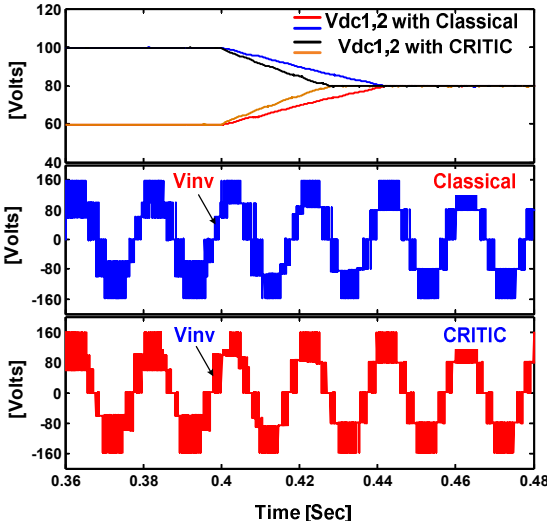

Fig.5.10. Simulation results for dynamic performance of both the control approaches for capacitor voltage balancing.

5.5 Experimental results

Experiments are conducted on the developed laboratory scale prototype as shown in Fig.2.20 under various operating conditions to validate the simulations of conventional MPDPC and the proposed CRITIC-W-CMPC. Results are presented for dynamic evolution of active power to validate the maximum power extraction, reactive power to validate the grid-support with centralized approach, and finally the steady-state results for evaluating the improved tracking performance of each control objective. Further, dynamic selection of

weighting factors with various operating conditions is also presented. In classical MPDPC, the initial values of weighting factor used for power tracking (λ_{PQ}) and DC-link voltage balancing (λ_{vdc}) are selected based on empirical approach. Further, they are tuned to obtain proper results. On the other hand, the proposed approach dynamically selects the weighting factors based on CRITIC approach in accordance with the operating conditions of the system.

To verify the proposed CMPC, the test scenario of maximum power extraction with 1) rapid change in irradiance by keeping the reactive power reference Q^*=0 Var and 2) changing the reactive power reference by keeping irradiance constant at 800 Watts/m^2 are illustrated in Fig.5.11 and Fig.5.12, respectively. In order to validate the effectiveness of the proposed control scheme, the results are compared with the classical PI based MPDPC. In case of classical approach, the PI controller regulates the DC-link voltage to track its reference MPPT voltage. Whereas, the proposed CMPC scheme utilizes the model based decoupled active-reactive power reference generation based on gradual approaching manner. It can be observed that, the power evolution of the PV inverter with both the control approaches is quite similar. Despite of eliminating the outer DC-voltage control loop, the proposed control scheme has tightly regulated the DC-link voltage to its MPPT reference even after sudden application of reactive power change. The steady state waveforms of active power, reactive power, injecting currents, PV voltage and the inverter line voltage at various operating conditions for both the control approaches are shown in Fig.5.13 to Fig.5.16.

The steady state results for classical MPDPC and proposed CRITIC-W-CMPC at 400 Watts/m^2, 700 Watts/m^2 and 1000 Watts/m^2 are shown in Fig.5.13 and Fig.5.14, respectively. Similarly, the steady state results for reactive power reference Q^* for ±720 Var with constant irradiance of 800 Watts/m^2 are shown in Fig.5.15 and Fig.5.16, respectively. By comparing the results, it can be clearly observed that the power ripples obtained with the proposed CRITIC-W-CMPC approach is very less compared to the classical MPDPC. Table.5.1 illustrate the quantitative comparison (simulation and experimental) of active power ripple, reactive power ripple and % THD of injecting currents for both the control approaches.

Further, the dynamic selection of weighting factor corresponding to change in the operating conditions is shown in Fig.5.17. In order to investigate the dynamic selection of

weighting factor, the inverter operating power factor is changed from unity power factor to the lagging power factor with Q^*=+720 Var at 800 Watts/m^2 irradiance as shown in Fig.5.17 (a). Similarly, in Fig.5.17 (b) the results for leading power factor with Q^*=-720 Var at 800 Watts/m^2 irradiance is shown. The influence of weighting factor selection on the dynamics of DC-link capacitor voltage balancing is shown in Fig.5.18. Initially, the DC-link voltages V_{dc1}, V_{dc2} have a voltage difference of 40 V, after 0.06 s the voltages are commanded to balance. Both the control approaches has balanced the DC-link voltages, however the proposed CRITIC-W-CMPC has balanced the capacitor voltages quickly compared to the classical approach without deviating from the reference.

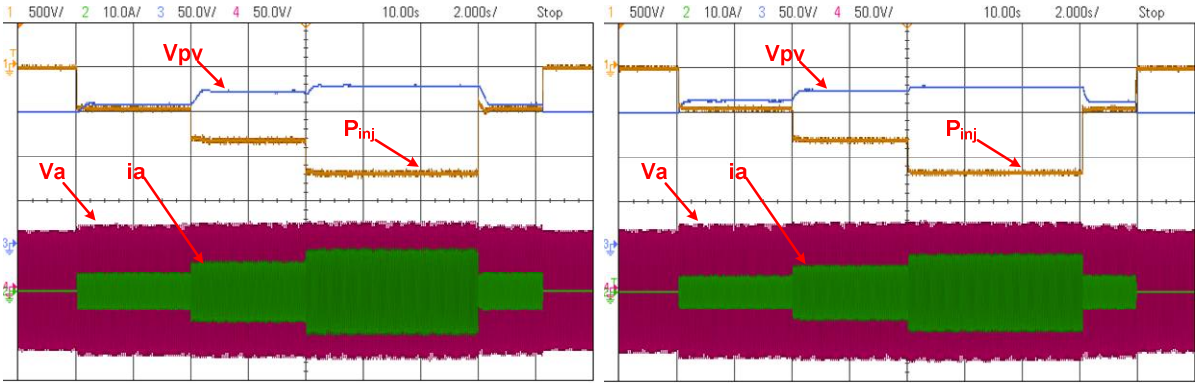

(a) (b)

Fig.5.11. Experimental results for active power evolution of 3L-NPC PV inverter (a) MPDPC (b) CRITIC-W-CMPC.

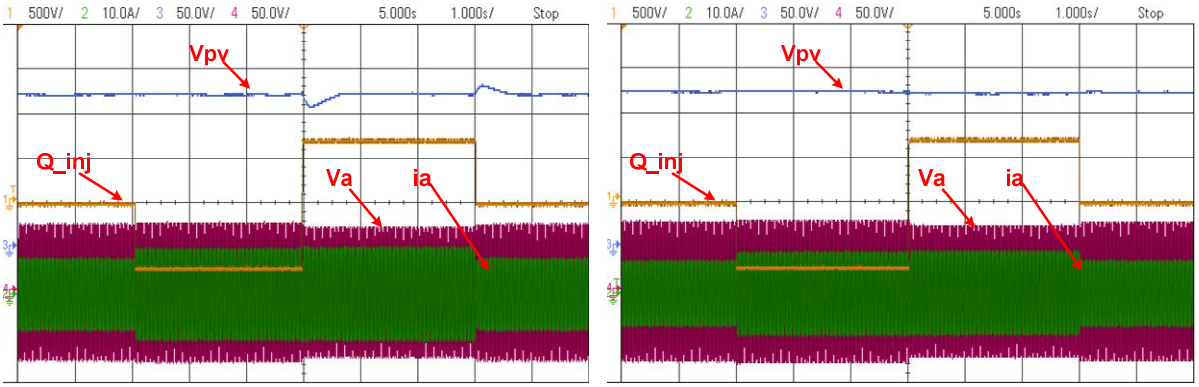

(a) (b)

Fig.5.12. Experimental results for reactive power evolution of 3L-NPC PV inverter (a) MPDPC (b) CRITIC-W-CMPC.

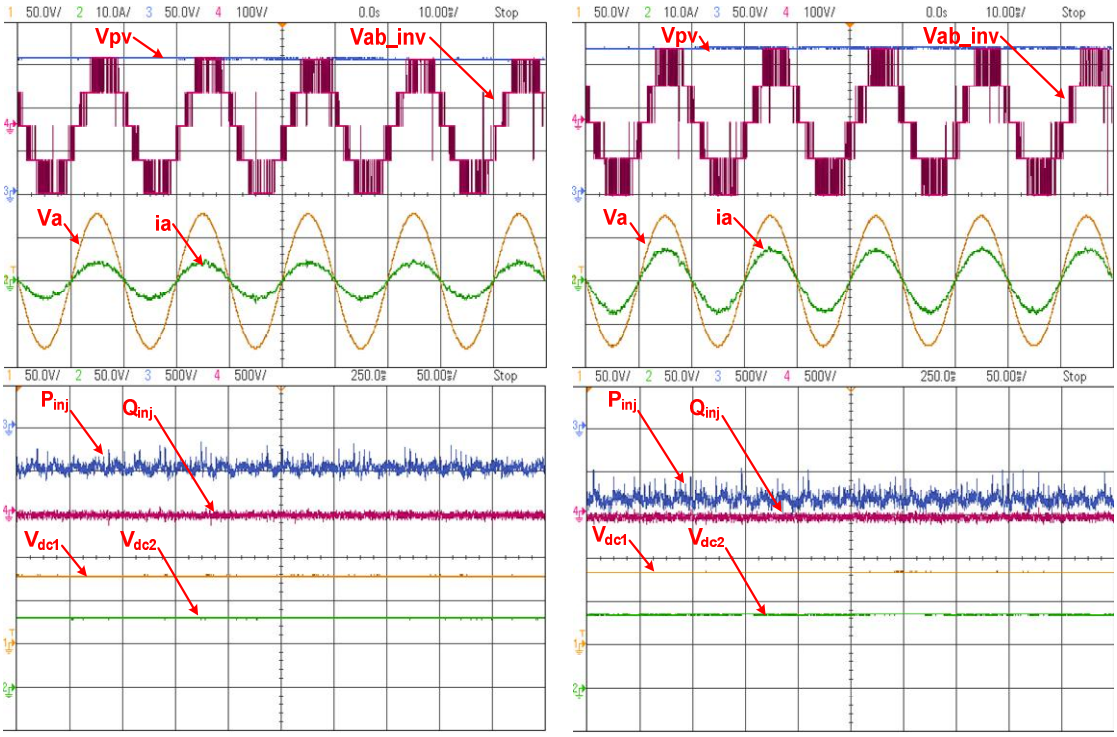

(a) (b)

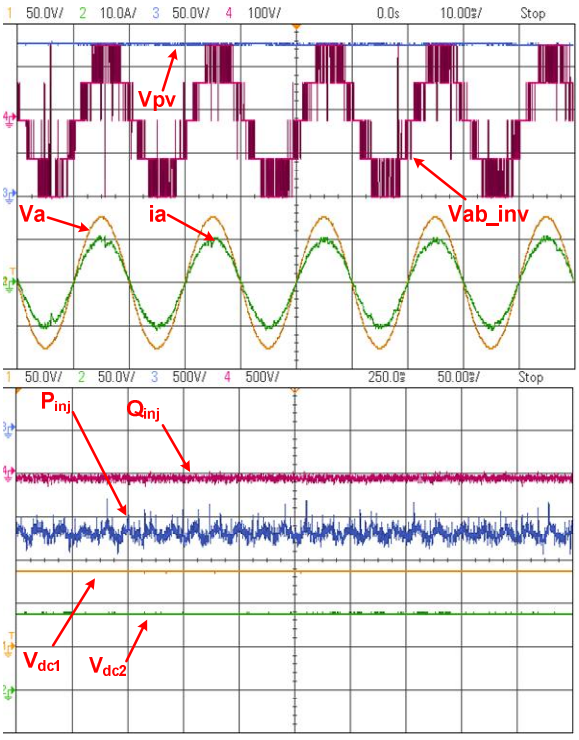

(c)

Fig.5.13. Experimental results for MPDPC at steady state with irradiances (a) 400 Watts/m^2 (b) 700 Watts/m^2 (c) 1000 Watts/m^2

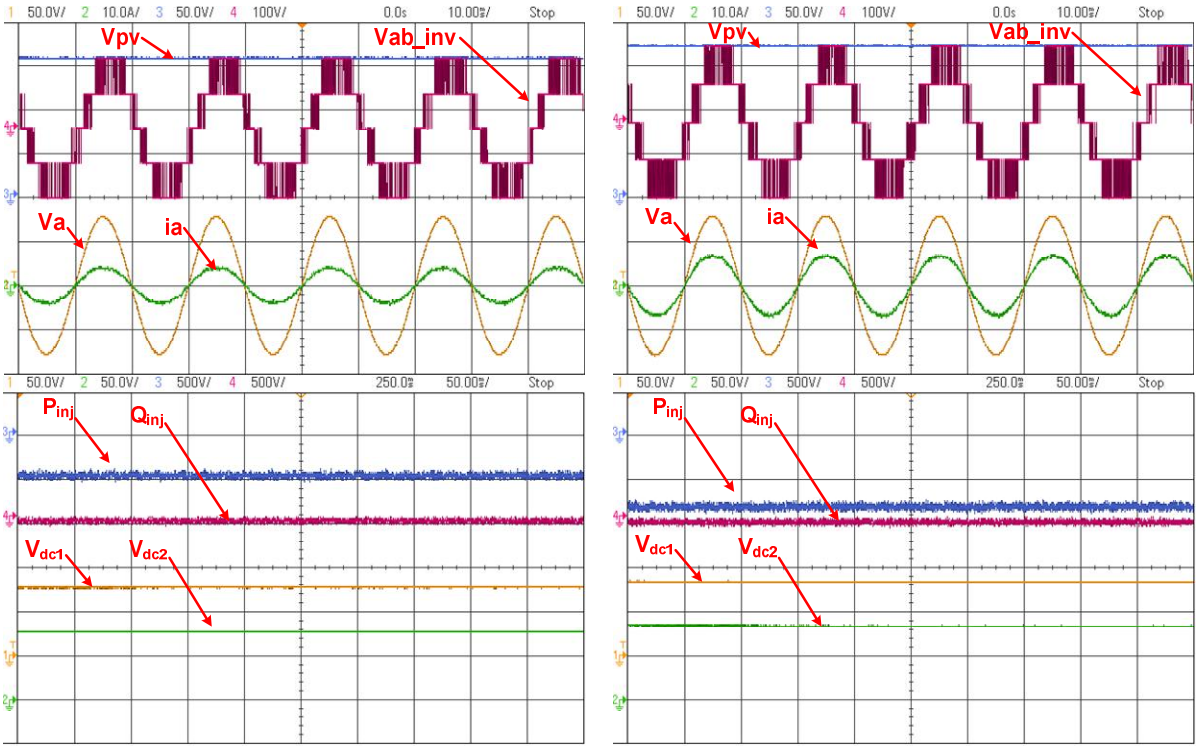

(a) (b)

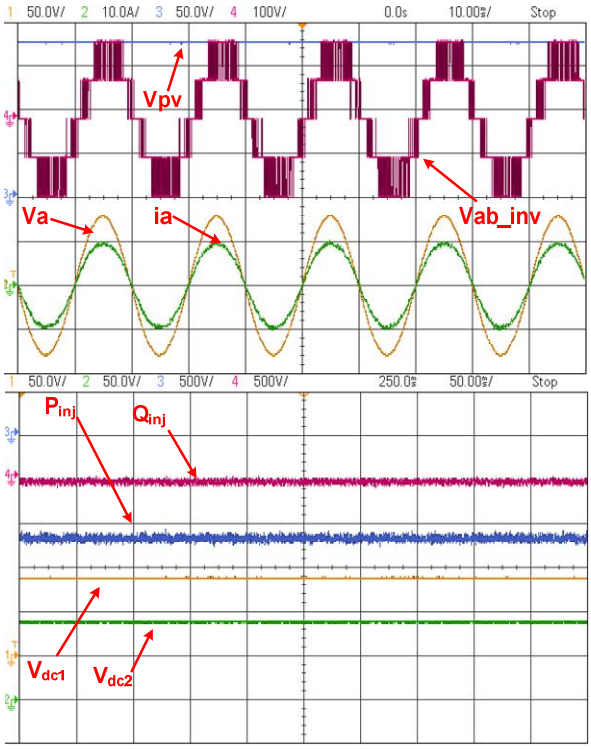

(c)

Fig.5.14. Experimental results for CRITIC-W-CMPC at steady state with irradiances (a) 400 Watts/m^2 (b) 700 Watts/m^2 (c) 1000 Watts/m^2

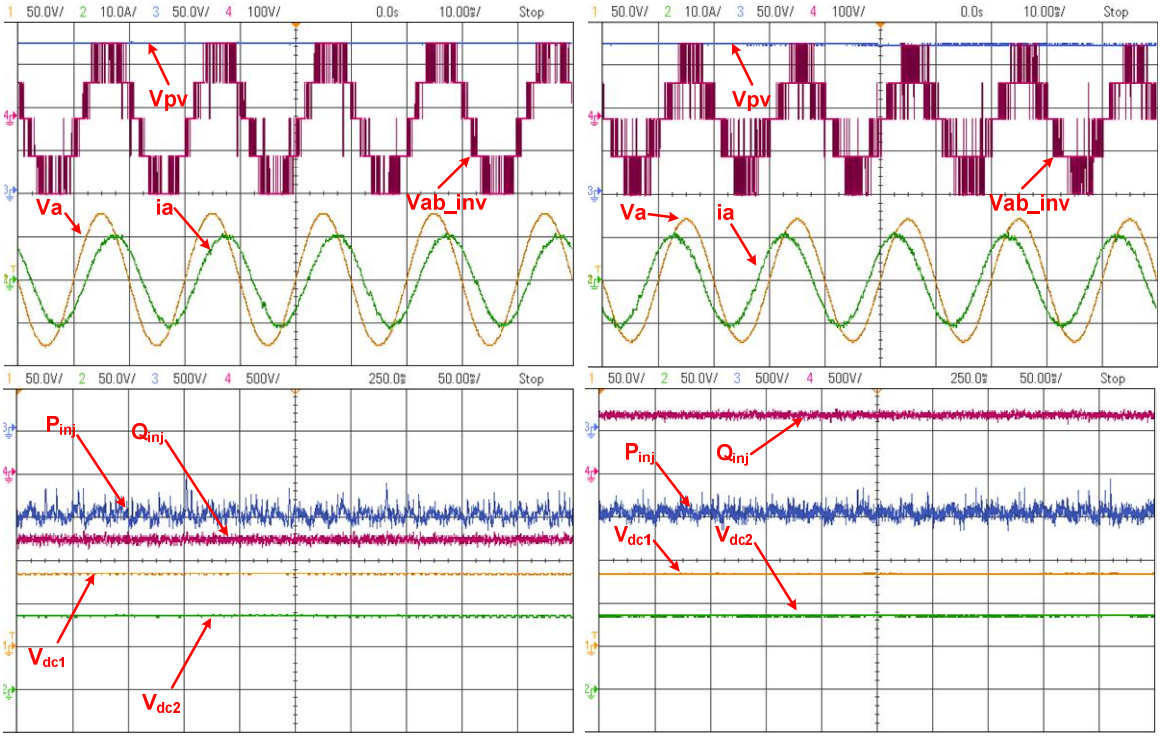

(a) (b)

Fig.5.15. Experimental results for steady-state waveforms with MPDPC (a) -720 Var at 800 Watts/m^2 (b) +720 Var at 800 Watts/m^2

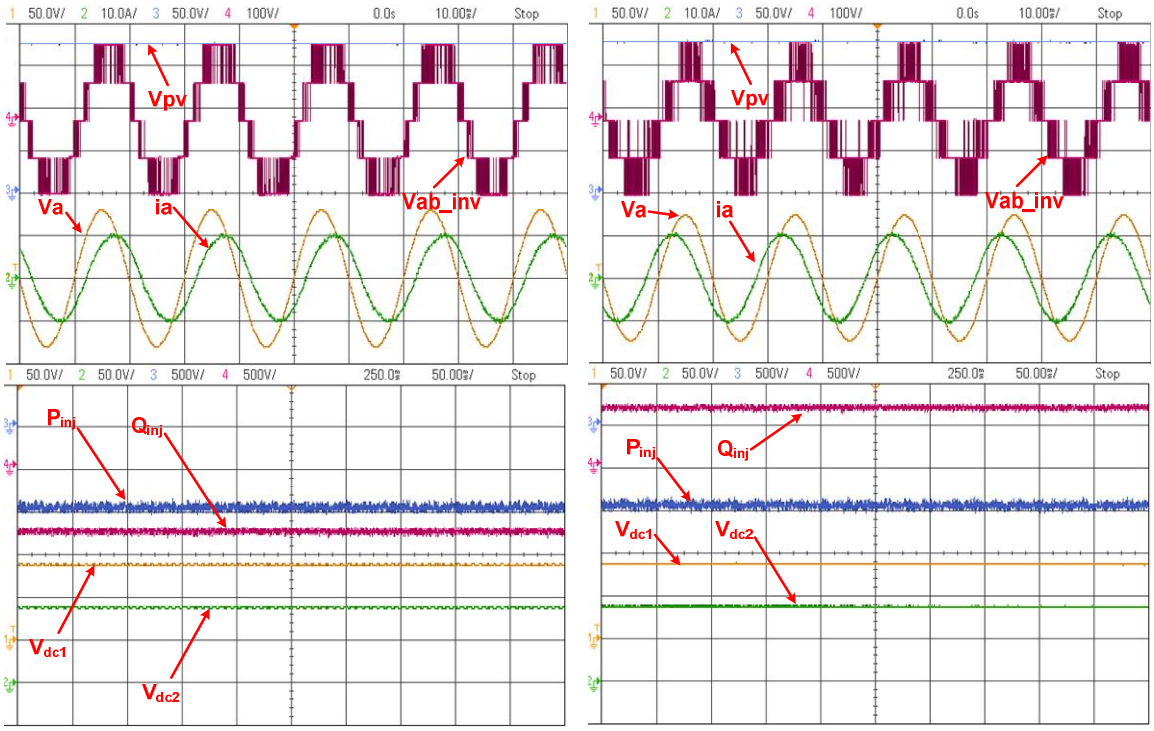

(a) (b)

Fig.5.16. Experimental results for steady-state waveforms with CRITIC-W-CMPC (a) -720 Var at 800 Watts/m^2 (b) +720 Var at 800 Watts/m^2

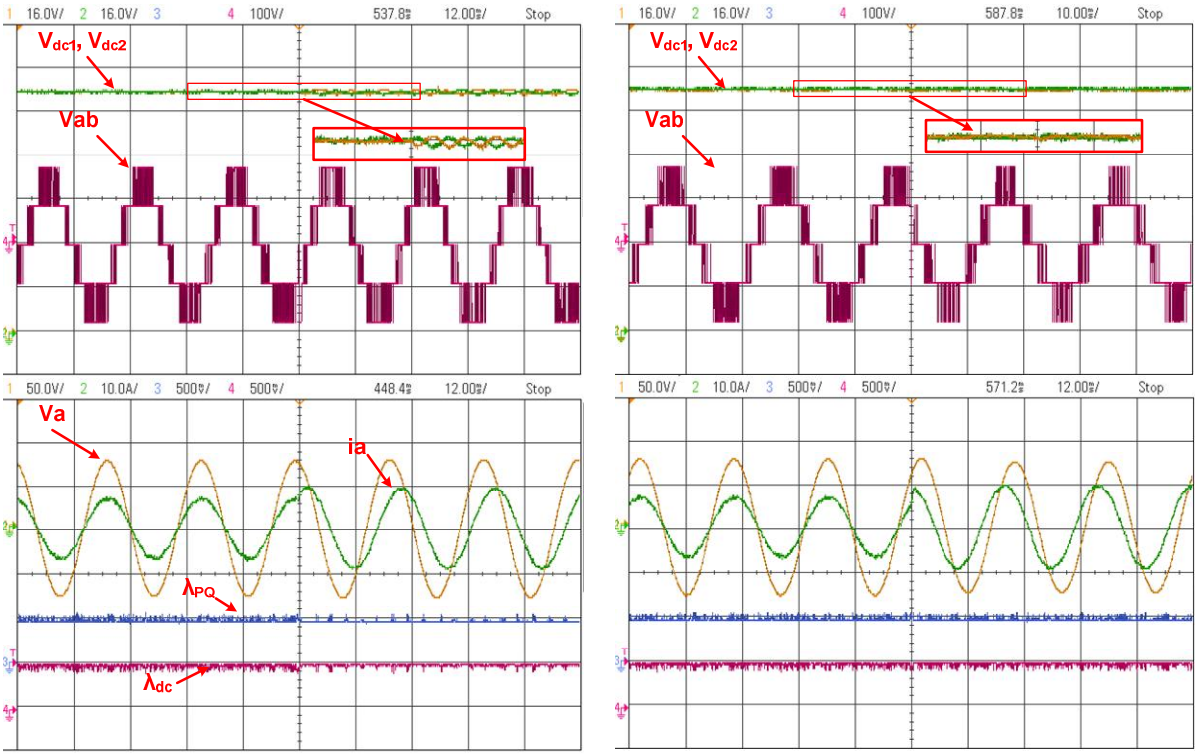

(a) (b)

Fig.5.17. Experimental results for dynamic selection of weighting factors with the change in operating power factor condition (a) UPF to +720 Var (b) UPF to -720 Var

Table.5.1. Performance comparison

Operating condition	Performance Indices	PI-MPDPC		CRITIC-W-CMPC	
		Simulation	Experimental	Simulation	Experimental
P_{inj} = 480 Watts Q_{inj} = 0 var	ΔP	35.17	35.39	18.67	20.21
	ΔQ	12.76	19.20	9.24	12.03
	%THD of i_g	8.48	8.9	5.12	5.46
P_{inj} = 1200Watts Q_{inj} = 0 var	ΔP	44.16	61.22	24.42	34.78
	ΔQ	13.75	34.10	12.46	23.38
	%THD of i_g	3.50	4.59	2.08	2.69
P_{inj} = 960 Watts Q_{inj} = -720 var	ΔP	48.15	64.95	16.23	33.02
	ΔQ	25.23	52.86	17.26	30.81
	%THD of i_g	3.24	4.84	2.6	3.16
P_{inj} = 960 Watts Q_{inj} = 720 var	ΔP	38.53	59.32	15.97	34.14
	ΔQ	19.70	50.11	14.72	32.93
	%THD of i_g	3.19	3.91	2.24	2.51

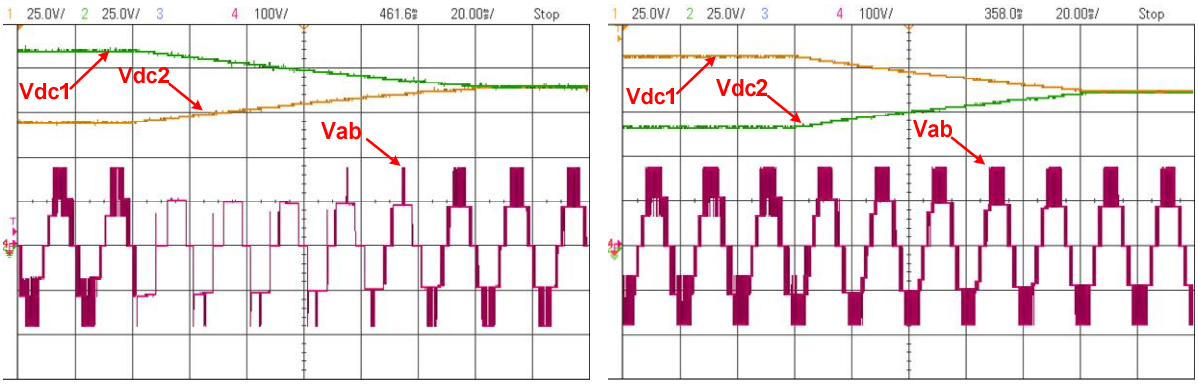

(a) (b)

Fig.5.18. Experimental results for dynamic performance of capacitor voltage balancing (a) CMPDPC (b) CRITIC-W-CMPC.

5.6 Summary

This chapter has presented a centralized model predictive control with CRITIC based dynamic weighting factor selection (CRITIC-W-CMPC) for a single-stage grid-tied SPV inverter. It has two major contributions:

1) Introduced a CRITIC based dynamic weighting factor selection method. CRITIC is an objective weighting method which establishes a quantitative relation between multiple variables and determines the weighting factors in each sampling period by using a multivariate descriptive statistical analysis of objective errors. Hence, the proposed control scheme offers an improved steady-state and dynamic tracking performance of each control objectives as demonstrated by the results. The generalized steps for the implementation of CRITIC method can be extended to various applications.

2) Development of a CMPC for a floating DC-link structure of grid-tied inverter. The proposed CMPC approach has eliminated the cascaded structure of single-stage grid-tied solar photovoltaic inverter control by a decoupled active-reactive power based dynamic reference generation. The results confirm the regulation of floating DC-link to its reference for extracting maximum power without the additional controller. The effectiveness of the proposed control scheme is validated by comparing the results with classical PI based MPDPC.

Chapter-6
PSI Weighted Centralized-MPC for Single-Stage Grid-Tied SPECS

6.1 Introduction

Selection of suitable weighting factors in the multi-objective control is one of the significant aspects in the design of FCS-MPC. In general, branch and bound algorithm based empirical method is used for the selection of suitable weighting factor which requires number of simulation and experimental trials. This heuristic approach is a time consuming and tedious task. Further, selection of weighting factors becomes more complex with each inclusion of additional control objective into the objective-function. Therefore, it is necessary to introduce a generic procedure for the selection of weighting factors. MCDM methods have drawn the attention of researchers to simplify the weighting factor selection in the multi-objective model predictive control. MCDM methods are widely used to find the optimal solution for problems associated with conflicting criteria and complex decision making. Preference Selective Index (PSI) is one of the objective methods in the weighting factor selection. PSI is popular due to its simplicity and straightforward approach [139]–[144].

In this chapter, a PSI weighted centralized model predictive control (PSI-W-CMPC) approach for a grid-tied 3L-NPC PV inverter is presented. The modified CMPC handles both outer DC-link voltage regulation to the MPPT reference and inner power control to inject maximum power extracted from the PV array as a single objective in the objection function as discussed in Chapter 5. The objectives of power tracking, DC-link capacitor voltage balancing has a conflict in obtaining the correlation among them, but is equally important for the proper operation of the inverter. To address this, a PSI based dynamic weighting factor selection approach is presented in this chapter. PSI offers an improved steady-state and dynamic tracking performance of each control objective.

6.2 General implementation steps for PSI-based approach

PSI is one of the objective weighing approaches of MCDM methods. These MCDM methods are used to identify the optimal solution from the available alternatives to achieve the desired criteria. The objective weighting factor selection approaches of MCDM methods utilises the multivariate analysis of descriptive statistics for determining the weights. However, unlike most of the MCDM methods the PSI approach does not require the relative significance between various criteria; hence it can also be applicable in the cases where there is a conflict in obtaining the correlation among criteria. In this study, the evaluation of the

objective function defined with various control objectives is viewed as a MCDM problem, where the optimal control action is obtained by using the PSI-based objective prioritisation approach. Generalised steps to find the objective weights of the individual criterion are given as follows

Step 1: Initially a decision matrix is formulated for *m* number of alternatives and *n* number of criteria as follows:

$$X_{ij} = \begin{bmatrix} x_{11} & x_{12} & \cdots & x_{1n} \\ x_{21} & x_{22} & \cdots & x_{2n} \\ \vdots & \vdots & \ddots & \vdots \\ x_{m1} & x_{m2} & \cdots & x_{mn} \end{bmatrix} \tag{6.1}$$

Where, x_{ij} belongs to the i^{th} alternative and j^{th} criterion.

Step 2: Normalization of data is required for the implementation of PSI method because of conflicting criteria. Based on the dataset obtained in (6.1), normalization of data can be computed to a scale of 0 to 1 based on the benefit criteria (i.e., larger the better) or cost criteria (i.e., smaller the better) and it can be obtained as

$$r_{ij} = \frac{x_{ij} - x_j^{\min}}{x_j^{\max} - x_j^{\min}} \text{ for benefit criteria} \tag{6.2}$$

$$r_{ij} = \frac{x_j^{\max} - x_{ij}}{x_j^{\max} - x_j^{\min}} \text{ for cost criteria} \tag{6.3}$$

Where $x_j^{\min} = \min\left\{x_{1j}, x_{2j} \ldots\ldots\ldots x_{mj}\right\}$

$x_j^{\max} = \max\left\{x_{1j}, x_{2j} \ldots\ldots\ldots x_{mj}\right\}$

Step 3: Based on the obtained normalised values, a preference variation value can be obtained for each criterion by using the following relation:

$$PV_j = \sum_{i=1}^{m}\left[r_{ij} - \overline{r}_j\right]^2 \tag{6.4}$$

where $\overline{r}_j$ is the mean of normalized value of the j^{th} criterion and it can be given as follows:

$$\overline{r}_j = \frac{1}{m}\sum_{i=1}^{m} r_{ij} \tag{6.5}$$

Step 4: Overall preference value (i.e. the weight assigned) of each criterion can be obtained by using the following relation:

$$\lambda_j = \frac{\varphi_j}{\sum_{j=1}^{n} \varphi_j} \tag{6.6}$$

Where φ_j gives the deviation in the preference value, $P\mathrm{v}_j$, and it is given as follows:

$$\varphi_j = 1 - P\mathrm{v}_j \tag{6.7}$$

Step 5: Obtaining the PSI I_i

$$I_i = \sum_{j=}^{n} \lambda_j r_{ij} \tag{6.8}$$

6.3 PSI based objective prioritization for grid-tied 3L-NPC inverter

To implement PSI method in objective function optimization, a single objective function is divided into individual objective function for each control objective as follows:

$$\xi_{pq}\left(S_i\right)\Big|_{i=1,2,\ldots,27} = \left|P^*\left(k+1\right) - P^p\left(k+1\right)\right| + \left|Q^*\left(k+1\right) - Q^p\left(k+1\right)\right| \tag{6.9}$$

$$\xi_{vdc}\left(S_i\right)\Big|_{i=1,2,\ldots,27} = \left|V_{dc1}^p\left(k+1\right) - V_{dc2}^p\left(k+1\right)\right| \tag{6.10}$$

The schematic of single-stage grid tied 3L-NPC PV inverter with PSI-W-CMPC approach is shown in Fig.6.1. In order to formulate the objective prioritisation of FCS-MPC as a decision-making problem, the terms criteria and alternatives associated with PSI method are framed as control objectives and the admissible switching states of the converter. The following steps are used to obtain the optimal switching state for next sampling period.

Step 1: Data generation for decision matrix X_{ij}, where $i = S_1,\ldots,S_{27}$ ($m = 27$ switching states/alternative) and $j =$ 1, 2 ($n =$ 2 control objectives/criteria given as ξ_{pq} and ξ_{vdc})

$$X_{ij} = \begin{bmatrix} \xi_{S1pq} & \xi_{S1vdc} \\ \xi_{S2pq} & \xi_{S2vdc} \\ \vdots & \vdots \\ \xi_{S27pq} & \xi_{S27vdc} \end{bmatrix} \tag{6.11}$$

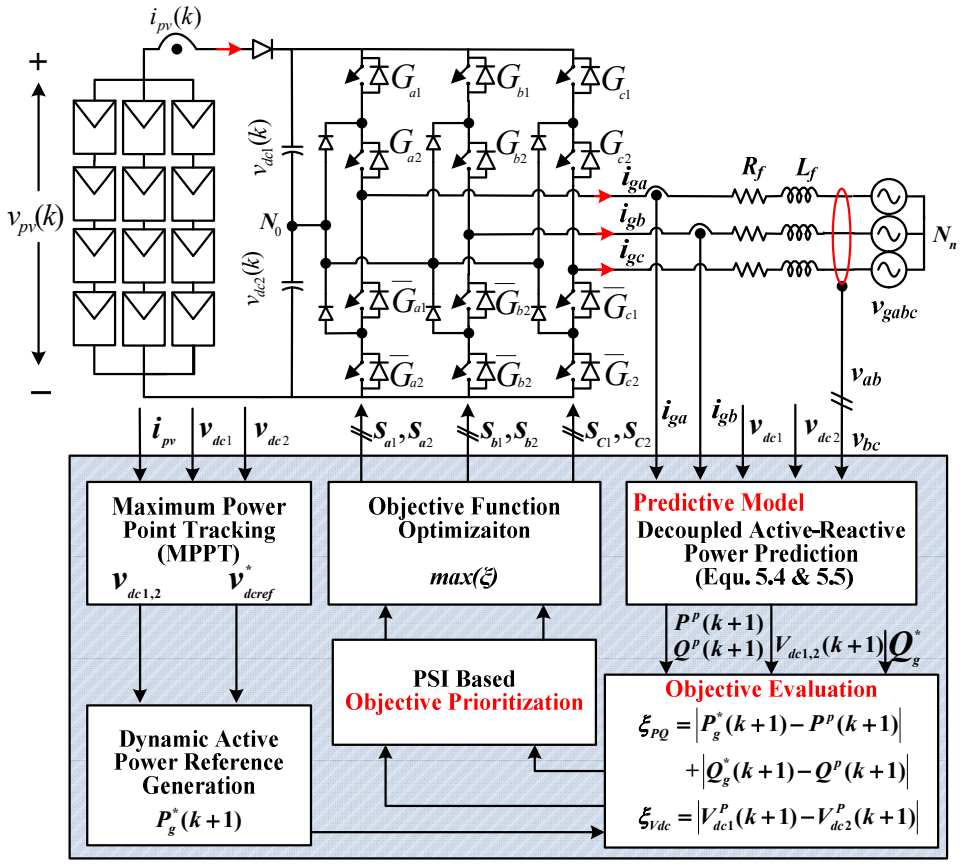

Fig.6.1. Schematic of single-stage grid tied 3L-NPC PV inverter with PSI-W-CMPC approach.

Step 2: Normalisation of generated data in decision matrix using Eq. (6.3) i.e. r_{ipq}, r_{ivdc} for $i = S_1, \ldots, S_{27}$.

$$r_{ipq} = \frac{\xi_{pq}^{\max} - \xi_{ipq}}{\xi_{pq}^{\max} - \xi_{pq}^{\min}} \tag{6.12}$$

$$r_{ivdc} = \frac{\xi_{vdc}^{\max} - \xi_{ivdc}}{\xi_{vdc}^{\max} - \xi_{vdc}^{\min}} \tag{6.13}$$

Where

$$\xi_{pq}^{\min} = \min\left\{\xi_{S1pq}, \xi_{S2pq}, \ldots\ldots\ldots \xi_{S27pq}\right\}$$

$$\xi_{pq}^{\max} = \max\left\{\xi_{S1pq}, \xi_{S2pq}, \ldots\ldots\ldots \xi_{S27pq}\right\}$$

$$\xi_{vdc}^{\min} = \min\left\{\xi_{S1vdc}, \xi_{S2vdc}, \ldots\ldots\ldots \xi_{S27vdc}\right\}$$

$$\xi_{vdc}^{\max} = \max\left\{\xi_{S1vdc}, \xi_{S2vdc}, \ldots\ldots\ldots \xi_{S27vdc}\right\}$$

Step 3: Calculation of preference variation of each control objective using Eq. (6.4), i.e. Pv_{pq} and Pv_{vdc}

$$Pv_{pq} = \sum_{i=S_1}^{S_{27}} \left[r_{ipq} - \overline{r}_{pq} \right]^2 \tag{6.14}$$

$$Pv_{vdc} = \sum_{i=S_1}^{S_{27}} \left[r_{ivdc} - \overline{r}_{vdc} \right]^2 \tag{6.15}$$

Where $\overline{r}_{pq}$ and $\overline{r}_{vdc}$ are the mean of normalized values of r_{ipq} and r_{ivdc} and they are given as

$$\overline{r}_{pq} = \frac{1}{27} \sum_{i=S_1}^{S_{27}} r_{ipq} \tag{6.16}$$

$$\overline{r}_{vdc} = \frac{1}{27} \sum_{i=S_1}^{S_{27}} r_{ivdc} \tag{6.17}$$

Step 4: Calculation of the overall preference value of each objective using Eq. (6.6), i.e. λ_{pq} and λ_{vdc}.

$$\lambda_{pq} = \frac{\varphi_{pq}}{\varphi_{pq} + \varphi_{vdc}} \tag{6.18}$$

$$\lambda_{vdc} = \frac{\varphi_{vdc}}{\varphi_{pq} + \varphi_{vdc}} \tag{6.19}$$

Where φ_{pq} and φ_{vdc} gives the deviation in the preference values Pv_{pq}, and Pv_{vdc}. They are given as follows:

$$\varphi_{pq} = 1 - Pv_{pq} \tag{6.20}$$

$$\varphi_{vdc} = 1 - Pv_{vdc} \tag{6.21}$$

Step 5: Obtaining the PSI I_i, using Eq. (6.8) for $i = S_1, \ldots, S_{27}$

$$I\left(S_i\right)\Big|_{i=1,2,\ldots,27} = \lambda_{pq} r_{ipq} + \lambda_{vdc} r_{vdc} \tag{6.22}$$

The alternative with the highest PSI is selected as the optimal control alternative.

$$I_{opt} = \arg \max_{i=S_1,..S_{27}} I_i \tag{6.23}$$

The detailed flowchart for this control approach is shown in Fig.6.2.

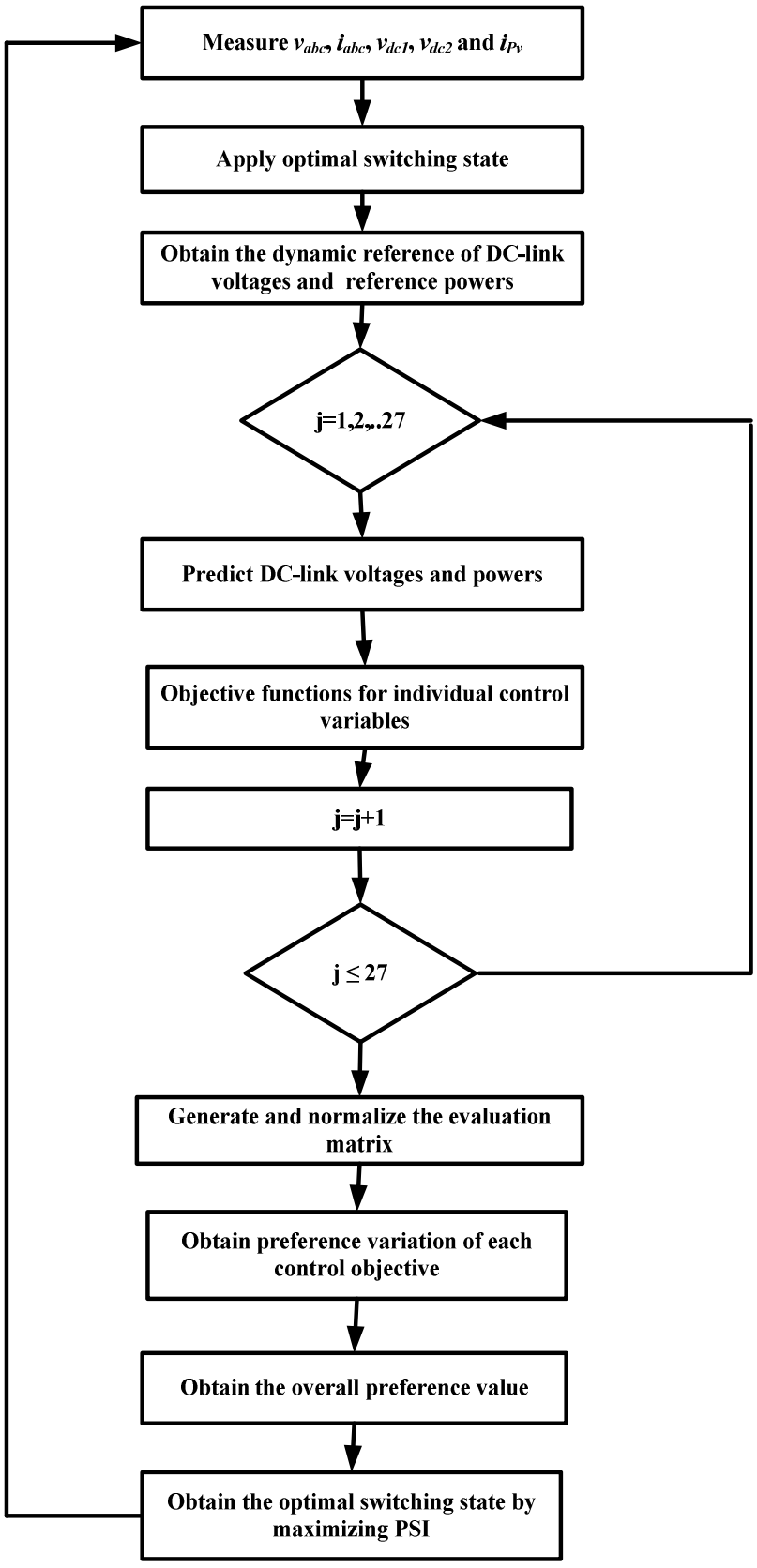

Fig.6.2. Flowchart for single-stage grid tied 3L-NPC PV inverter with PSI-W-CMPC approach

6.4 Simulation results

To examine the performance of proposed PSI-W-CMPC control scheme, a detailed model of single-stage grid-tied 3LNPC SPV inverter is designed in MATLAB/Simulink software. The nominal power of the PV inverter is taken as 1.2 kVA. The simulations are carried with one-step prediction horizon for a sampling period of T_s = 80μs. The system parameters for both the simulation and experimental studies are given in Table.3.1. For evaluating the performance, the system is subjected to various operating conditions and the results are compared with the classical PI-based MPDPC. The performance of the proposed control scheme is assessed in terms of active power ripple, reactive power ripple and percentage total harmonic distortion (%THD) of injecting currents.

In order to validate the centralized control of proposed scheme, the active power evolution of the SPV system with both the control approaches are investigated. The PV array in the system is subjected to varying irradiance while keeping the reactive power reference Q^* = 0 Var. The objective function in both the control approaches is defined with the active-reactive power tracking and DC-link capacitor voltage balancing. The scenario of irradiance variation is as follows: initially the irradiance is kept at zero Watts/m^2 for a time interval of [0-0.2] s during which the DC-link voltage is maintained at 150 V (V_{min}). At 0.2 s, the irradiance is changed to 400 Watts/m^2 and is kept constant until 0.6 s; then it is increased to 700 Watts/m^2 at 0.6 s and then to 1000 Watts/m^2 at 1 s. After 1.45 s the irradiance is brought down to 400 Watts/m^2 and then to zero Watts/m^2 at 1.75 s. The DC-link voltage is tracked to 153.2 V, 156.4 V and 157.4 V at 400 Watts/m^2, 700 Watts/m^2 and 1000 Watts/m^2, as a result the maximum power of 460 Watts, 840 Watts and 1200 Watts are extracted, respectively. From Fig.6.3, it can be observed that the proposed control scheme tracked the reference MPPT voltage without using the outer DC-link voltage controller. Both the control approaches are found to have similar power evolution; on the other hand the power ripple with the proposed control approach is reduced compared to the classical. The steady state waveforms of phase voltage, phase current, inverter line voltage and the active-reactive powers of both the control approaches at 400 Watts/m^2, 700 Watts/m^2 and 1000 Watts/m^2 are shown in Fig.6.4.

The harmonic spectrum of the injecting currents for both the methods at 1000 Watts/m^2 is shown in Fig.6.5. The THD is calculated up to 100^{th}-harmonic order. It can be seen that the proposed PSI-W-CMPC exhibits the %THD of 2.91% which is much smaller than 3.50% of

classical MPDPC. The results show that the proposed scheme has better harmonic performance compared to the classical method.

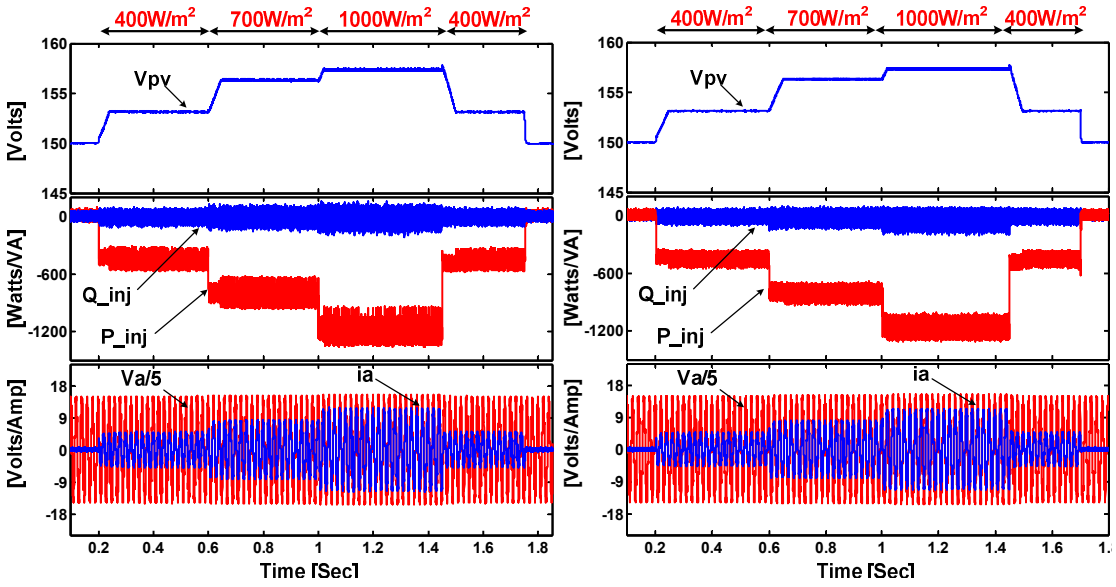

Fig.6.3. Simulation results for active power evolution of 3L-NPC PV inverter (a) MPDPC (b) PSI-W-CMPC.

Similar to the active power, the reactive power evolution of PV inverter with both the control approaches is shown in Fig.6.6. The scenario of change in reactive power reference Q^* is as follows: a step change from zero Var to -720 Var is applied at 0.8 s, then from -720 Var to +720 Var at 1.6 s and back to zero Var at 2.4 s. During this change in reactive power, a constant 960 Watts of active power is injected by maintaining the irradiance constant at 800 Watts/m^2. It can be seen that, both the control approaches has regulated the DC-link voltage of the inverter to 156.9 V even after the application of step change in reactive power. In the classical approach the transient seen in the DC-link voltage depends on the choice of controller gains. Whereas, in case of proposed control scheme, the DC-link voltage is strictly regulated to the reference MPPT voltage by using the proposed CMPC which has eliminated the need for outer DC-link voltage controller and the efforts required for its tuning. Further, the results confirm that the influence of change in reactive power reference on maximum power tracking is minimized with the decoupled active-reactive power control. The steady state waveforms of phase voltage, phase current, inverter line voltage and the active-reactive powers of both the control approaches at an irradiance of 800 Watts/m^2 with ±720 Var are shown in Fig.6.7. The results confirm that the active and reactive power ripples of proposed PSI-W-CMPC have lesser power ripple compared to the classical MPDPC.

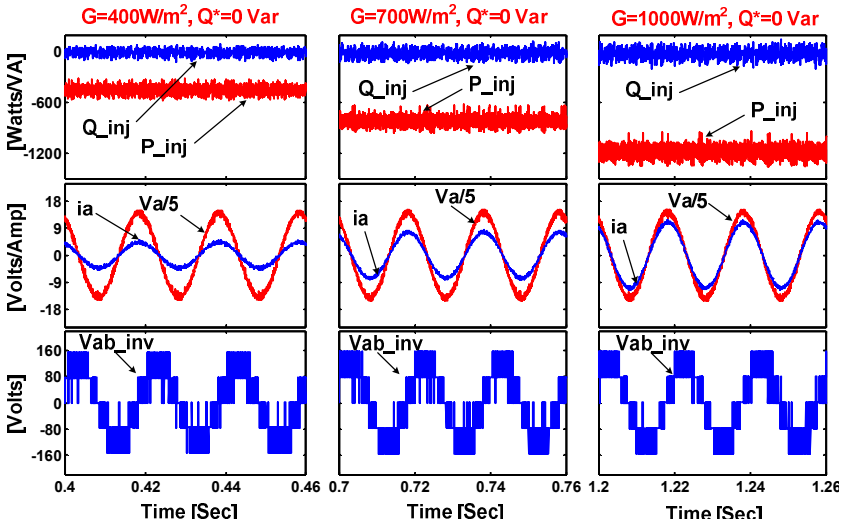

(a)

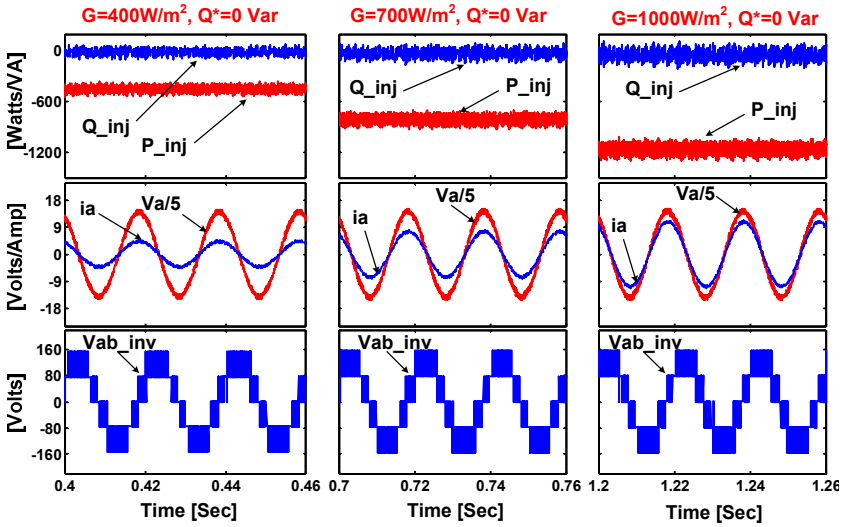

(b)

Fig.6.4. Simulation results for steady-state active power at various irradiances (a) MPDPC (b) PSI-W-CMPC.

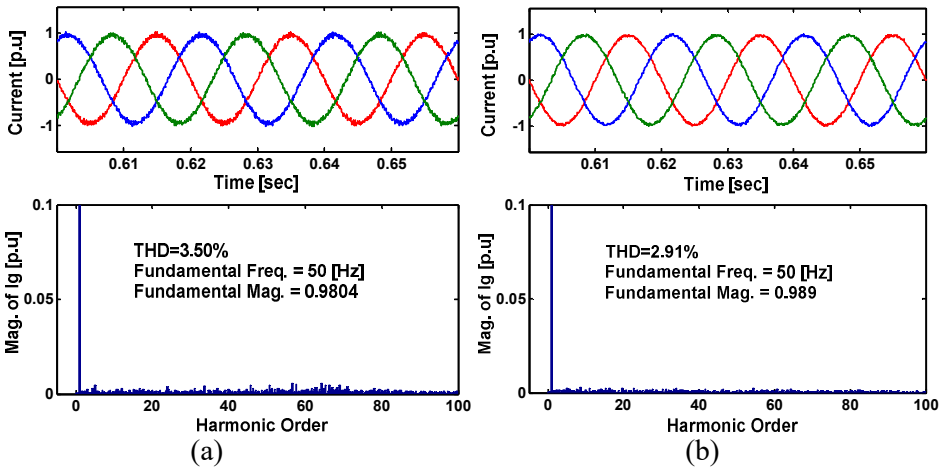

(a) (b)

Fig.6.5. Simulation results for harmonic spectra and %THD of injecting currents (a) MPDPC (b) PSI-W-CMPC.

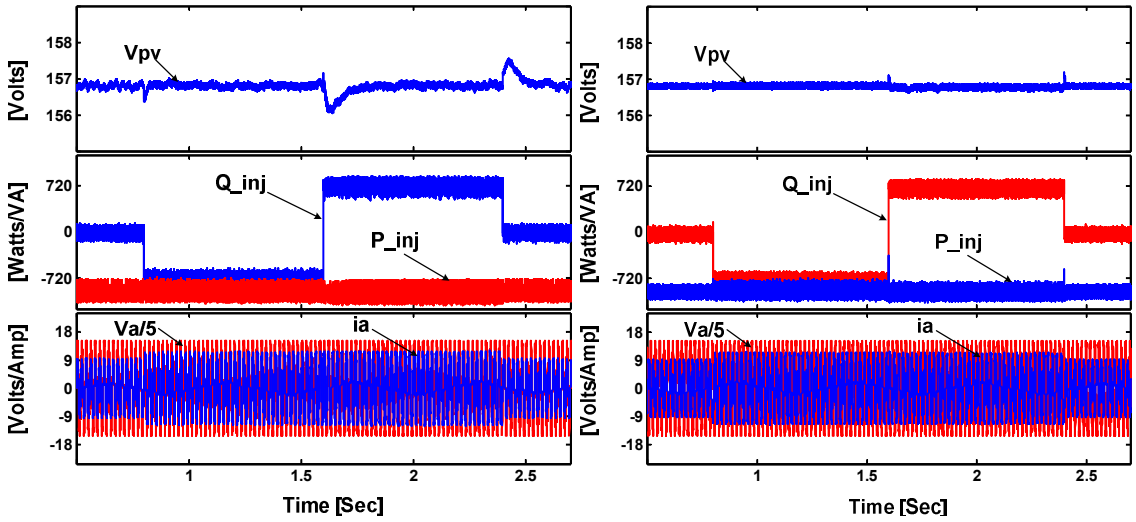

(a) (b)

Fig.6.6. Simulation results for reactive power evolution of 3L-NPC PV inverter (a) MPDPC (b) PSI-W-CMPC.

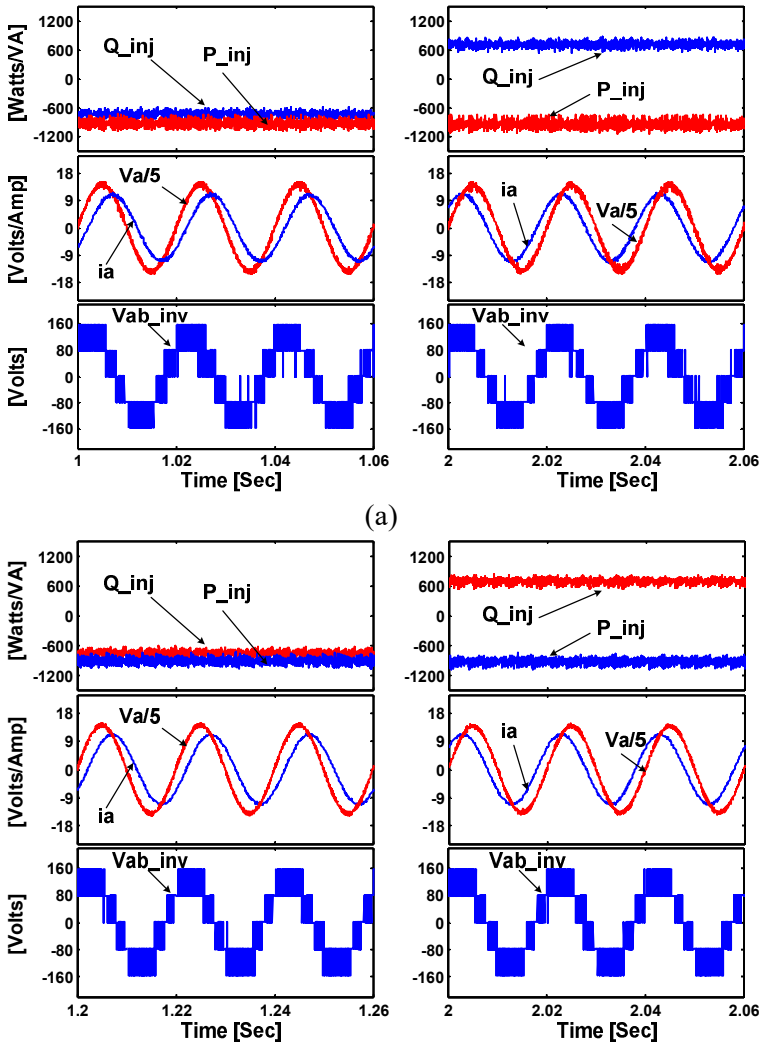

(a)

(b)

Fig.6.7. Simulation results for steady-state active-reactive power (a) MPDPC (b) PSI-W-CMPC.

The dynamic selection of weighting factors corresponding to the change in operating conditions of the PV inverter is shown in Fig.6.8. Initially, the power tracking objective and DC-link capacitor voltage balancing objectives are considered. Similar to the reactive power evolution, a step change in reactive power reference Q^* from zero Var to -720 Var and then to +720 Var and back to zero Var is applied during [0-0.7] s. The weighting factors λ_{pq} and λ_{dc} corresponding to the power tracking and DC-link voltage balancing are calculated online. At 0.7 s the third objective of CMV reduction is enabled where the λ_{cmv} is also calculated online along with λ_{pq} and λ_{dc}. The zoomed view of dynamically selected weighting factors is shown in the subplot of Fig.6.8. The results validate the dynamic adaption of weighting factor corresponding to operating conditions to meet the required objectives.

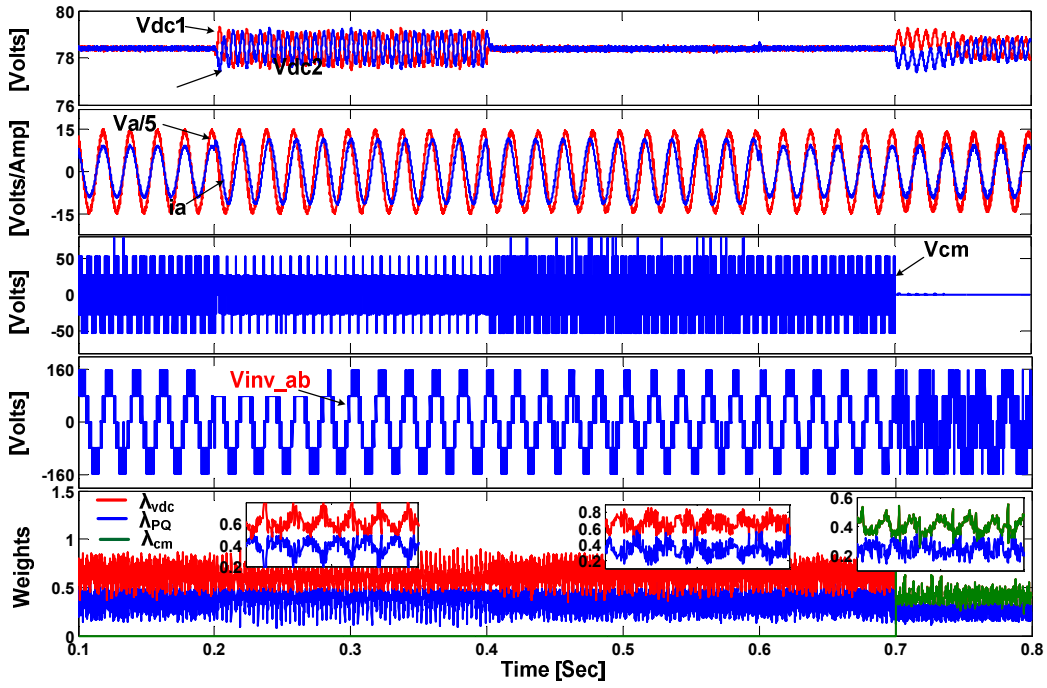

Fig.6.8. Simulation results for the dynamic selection of weighting factors with PSI for change in operating condition.

The impact of weighting factor selection on the dynamic performance of power tracking and DC-link capacitor voltage balancing objectives are investigated individually. Fig.6.9 illustrates the results for dynamic performance of both the control approaches for step change of reactive power reference Q^* from -720 Var to +720 Var. The time taken for the measured power to track the reference by using the proposed control scheme is 0.1 ms which is almost similar to that of the classical. Similarly, Fig.6.10 illustrates the DC-link capacitor voltage balancing capabilities of both the control approaches. Initially, an intentional voltage

difference of 40 V is applied till 0.4 s and then commanded to balance the voltages V_{dc1}, and V_{dc2}. The results show that both the control approaches balances the capacitor voltages; however, the proposed control scheme is fast compared to the classical.

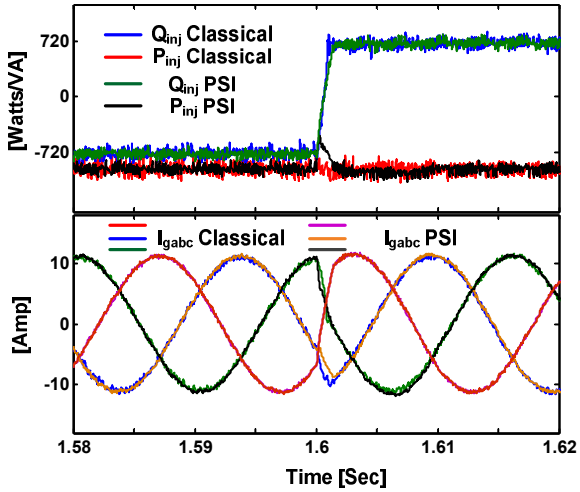

Fig.6.9. Simulation results for dynamic performance of both the methods for step change in reactive power

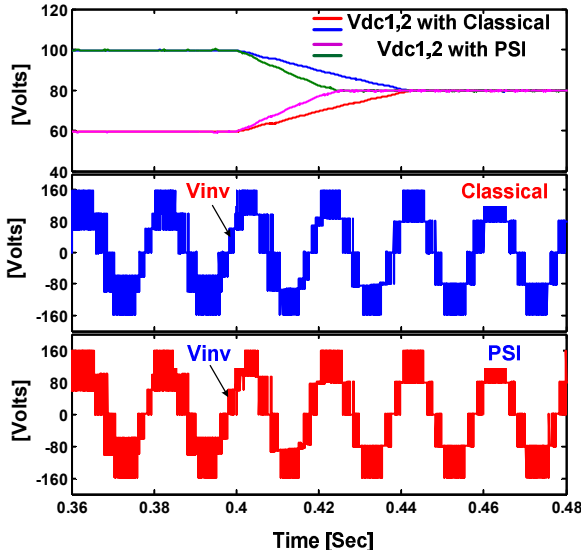

Fig.6.10. Simulation results for dynamic performance of both the methods for capacitor voltage balancing

6.5 Experimental results

Experiments are conducted on the developed laboratory scale prototype as shown in Fig.2.20 under various operating conditions to validate the simulations of conventional MPDPC and the proposed PSI-W-CMPC. Results are presented for evolution of active power to validate the maximum power extraction and reactive power to validate the grid-support with the centralized approach, dynamic selection of weighting factors with various

operating conditions and finally the steady-state results for evaluating the improved tracking performance of each control objective. In classical MPDPC, the initial values of weighting factor used for power tracking (λ_{PQ}) and DC-link voltage balancing (λ_{vdc}) are selected based on empirical approach. Further, they are tuned to obtain proper results. On the other hand, the proposed approach dynamically selects the weighting factors based on PSI method in accordance with the operating conditions of the system.

To verify the proposed CMPC, the test scenario of maximum power extraction with 1) rapid change in irradiance by keeping the reactive power reference Q^*=0 Var and 2) changing the reactive power reference by keeping irradiance constant at 800 Watts/m^2 are illustrated in Fig.6.11 and Fig.6.12, respectively. In order to validate the effectiveness of the proposed control scheme the results are compared with the classical PI based MPDPC. In case of classical approach, the PI controller regulates the DC-link voltage to track its reference MPPT voltage, whereas the proposed CMPC scheme utilizes the model based decoupled active-reactive power reference generation based on gradual approaching manner. It can be observed that the power evolution of the PV inverter with both the control approaches is quite similar. Despite of eliminating the outer DC-voltage control loop, the proposed control scheme has tightly regulated the DC-link voltage to its MPPT reference even after sudden application of reactive power change. The steady state waveforms of active power, reactive power, injecting currents, PV voltage and the inverter line voltage at various operating conditions for both the control approaches are shown in Fig.6.13 to Fig.6.16.

The results for classical MPDPC and proposed PSI-W-CMPC at 400 Watts/m^2, 700 Watts/m^2 and 1000 Watts/m^2 are shown in Fig.6.13 and Fig.6.14 respectively, whereas ±720 Var with constant irradiance of 800 Watts/m^2 are shown in Fig.6.15 and Fig.6.16, respectively. By comparing the results, it can be clearly observed that the power ripples obtained with the proposed PSI-W-CMPC approach is very less compared to the classical MPDPC. Table.6.1 illustrate the quantitative comparison (simulation and experimental) of active power ripple, reactive power ripple and % THD of injecting currents for both the control approaches.

Further, the dynamic selection of weighting factor corresponding to change in the operating conditions is shown in Fig.6.17. In order to investigate the dynamic selection of weighting factor, the inverter operating power factor is changed from unity power factor to

the lagging power factor with Q^*=+720 Var at 800 Watts/m^2 irradiance as shown in Fig.6.17 (a). Similarly, in Fig.6.17 (b) the results for the leading power factor with Q^*=-720 Var at 800 Watts/m^2 irradiance is shown. The influence of weighting factor selection on the dynamics of DC-link capacitor voltages for balancing is shown in Fig.6.18. Initially, the DC-link voltages V_{dc1}, V_{dc2} have a voltage difference of 40 V, after 0.06 s the voltages are commanded to balance. Both the control approaches has balanced the DC-link voltages, however the proposed PSI-W-CMPC has balanced the capacitor voltages quickly compared to the classical without deviating from the reference.

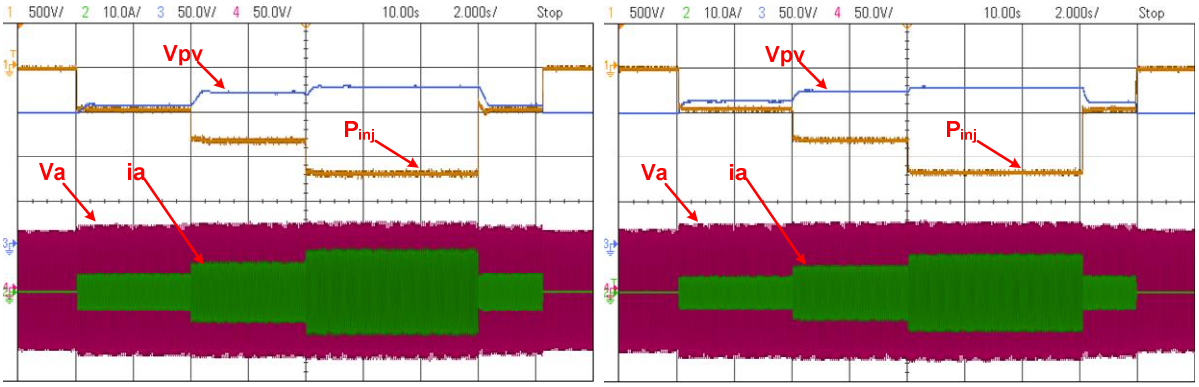

(a) (b)

Fig.6.11. Experimental results for active power evolution of 3L-NPC PV inverter (a) MPDPC (b) PSI-W-CMPC.

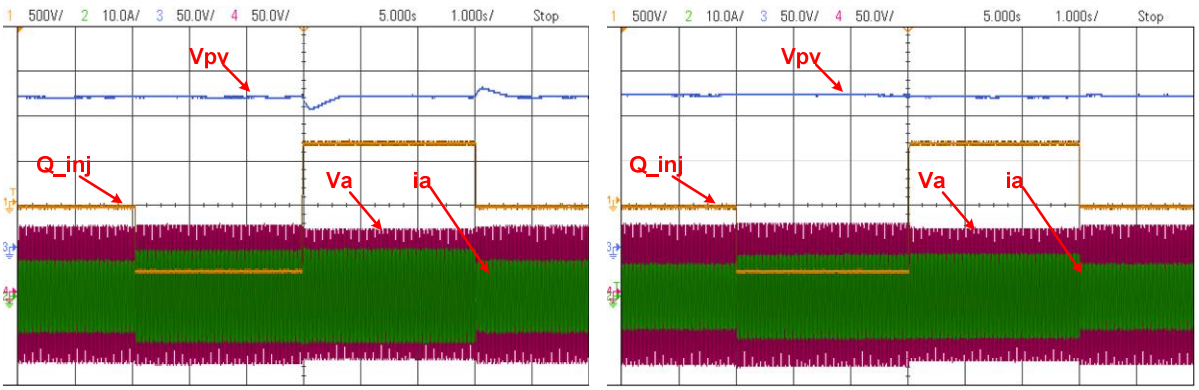

(a) (b)

Fig.6.12. Experimental results for reactive power evolution of 3L-NPC PV inverter (a) MPDPC (b) PSI-W-CMPC.

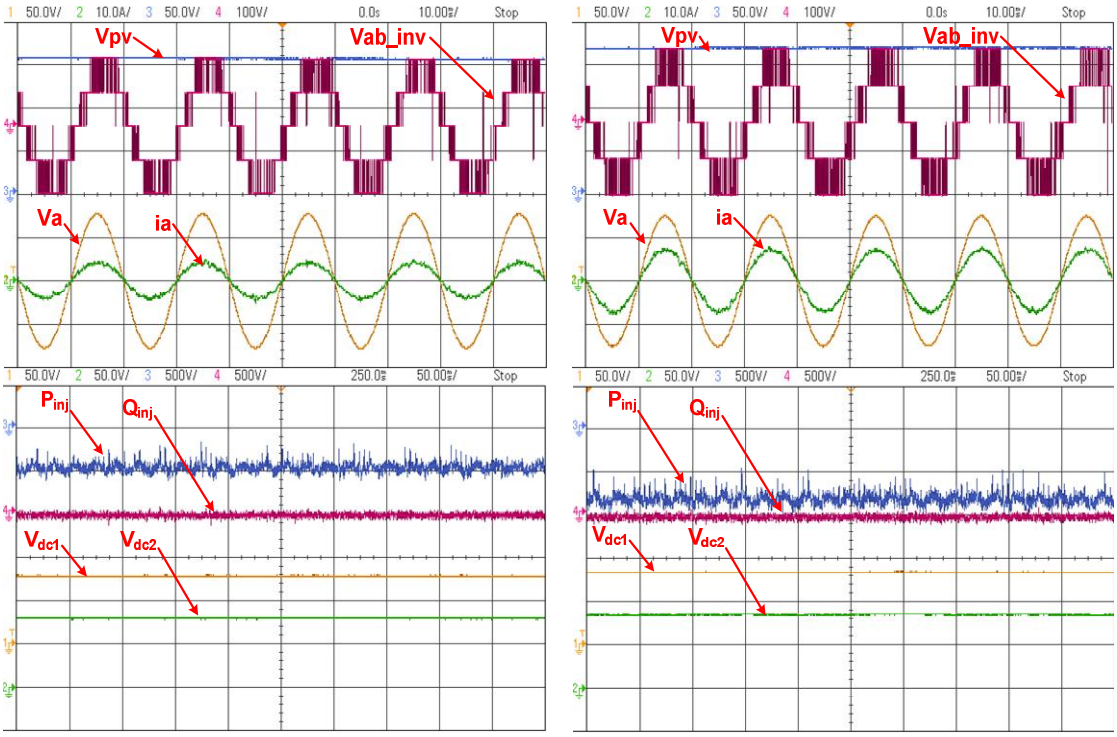

(a) (b)

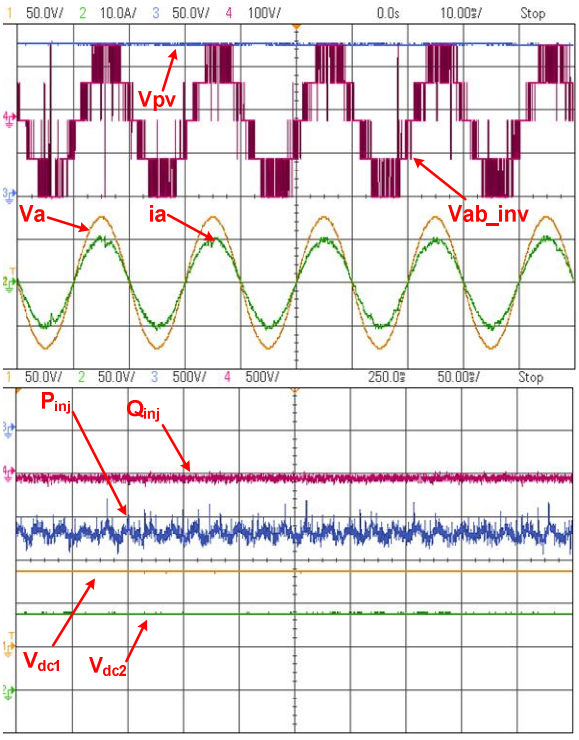

(c)

Fig.6.13. Experimental results of Classical MPDPC at steady-state waveforms for (a) 400 Watts/m^2 (b) 700 Watts/m^2 (c) 1000 Watts/m^2

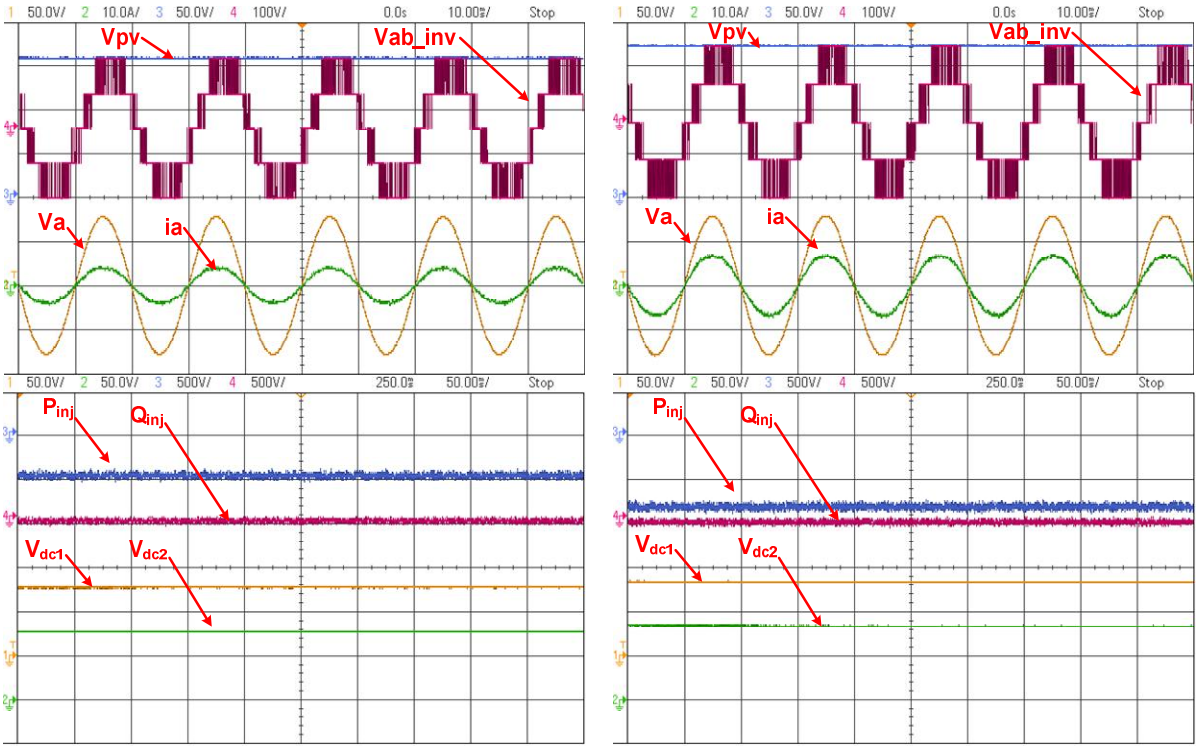

(a) (b)

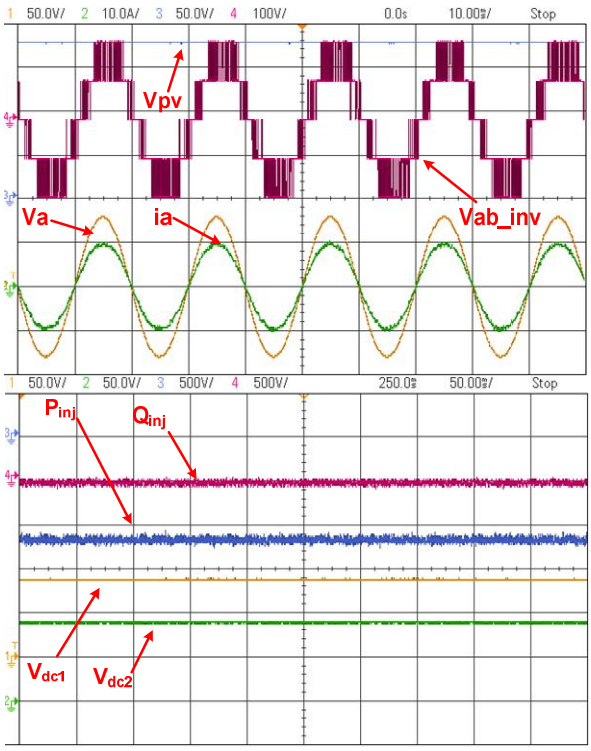

(c)

Fig.6.14. Experimental results of PSI-W-CMPC at steady-state waveforms for (a) 400 Watts/m^2 (b) 700 Watts/m^2 (c) 1000 Watts/m^2

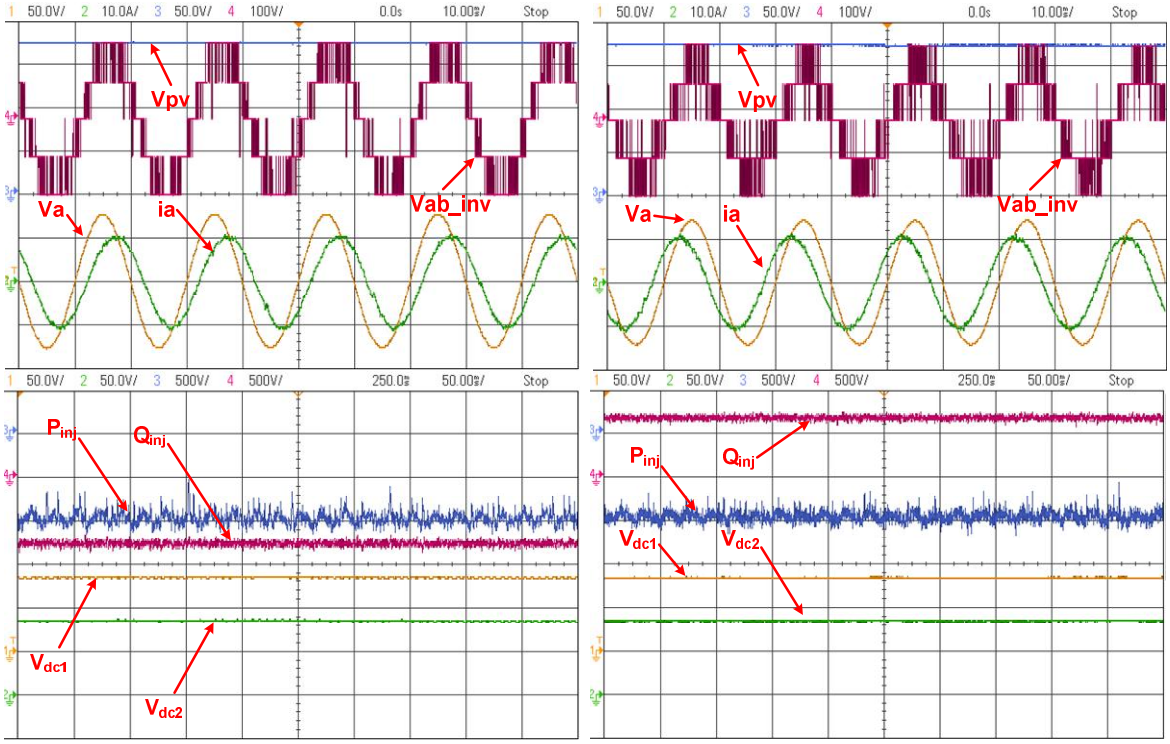

(a) (b)

Fig.6.15. Experimental results for steady-state waveforms with MPDPC (a) -720 Var at 800 Watts/m^2 (b) +720 Var at 800 Watts/m^2.

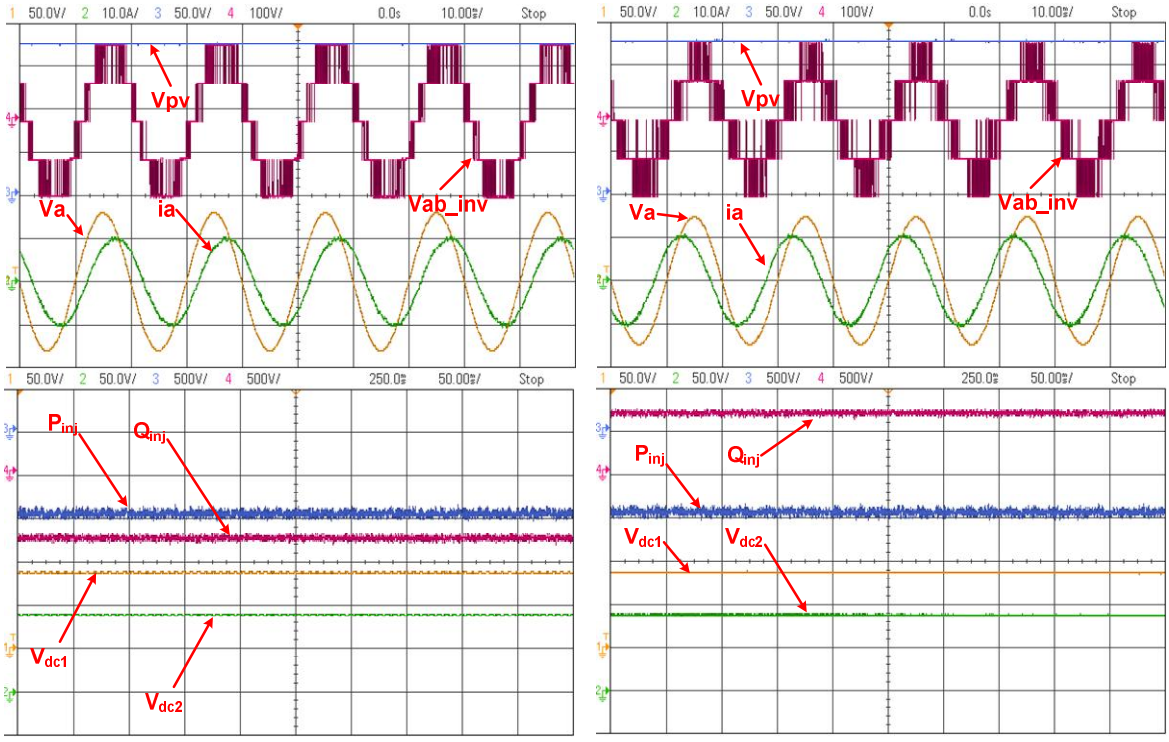

(a) (b)

Fig.6.16. Experimental results for steady-state waveforms with PSI-W-CMPC (a) -720 Var at 800 Watts/m^2 (b) +720 Var at 800 Watts/m^2.

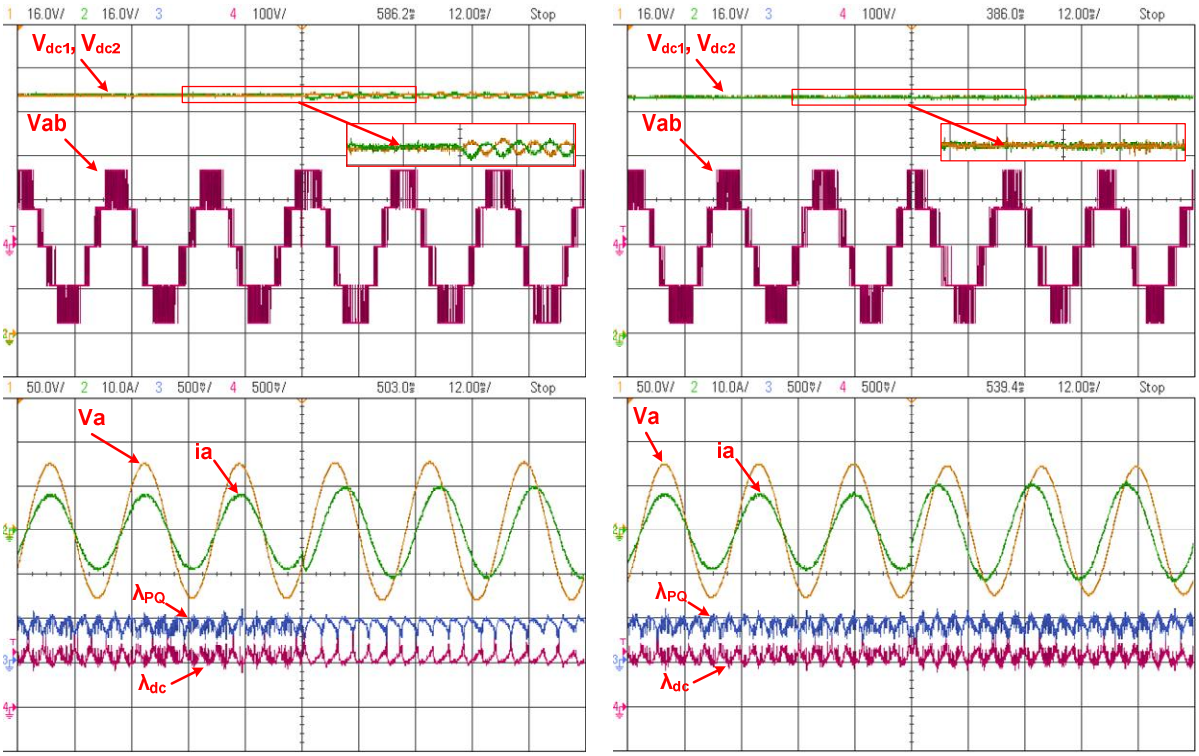

(a) (b)

Fig.6.17. Experimental results illustrating the dynamic selection of weighting factors for change in operating power factor condition (a) UPF to +720 Var (b) UPF to -720 Var.

Table.6.1. Performance comparison

Operating condition	Performance Indices	PI-MPDPC		PSI-W-CMPC	
		Simulation	Experimental	Simulation	Experimental
P_{inj} = 480 Watts Q_{inj} = 0 Var	ΔP	35.17	35.39	20.84	24.01
	ΔQ	12.76	19.20	9.73	13.11
	%THD of i_g	8.48	8.9	5.24	5.93
P_{inj} = 1200Watts Q_{inj} = 0 Var	ΔP	44.16	61.22	28.73	40.92
	ΔQ	13.75	34.10	11.00	26.33
	%THD of i_g	3.50	4.59	2.91	3.70
P_{inj} = 960 Watts Q_{inj} = -720 Var	ΔP	48.15	64.95	18.72	38.43
	ΔQ	25.23	52.86	19.13	35.83
	%THD of i_g	3.24	4.84	2.97	3.68
P_{inj} = 960 Watts Q_{inj} = 720 Var	ΔP	38.53	59.32	17.70	40.10
	ΔQ	19.70	50.11	15.96	35.97
	%THD of i_g	3.19	3.91	2.46	2.96

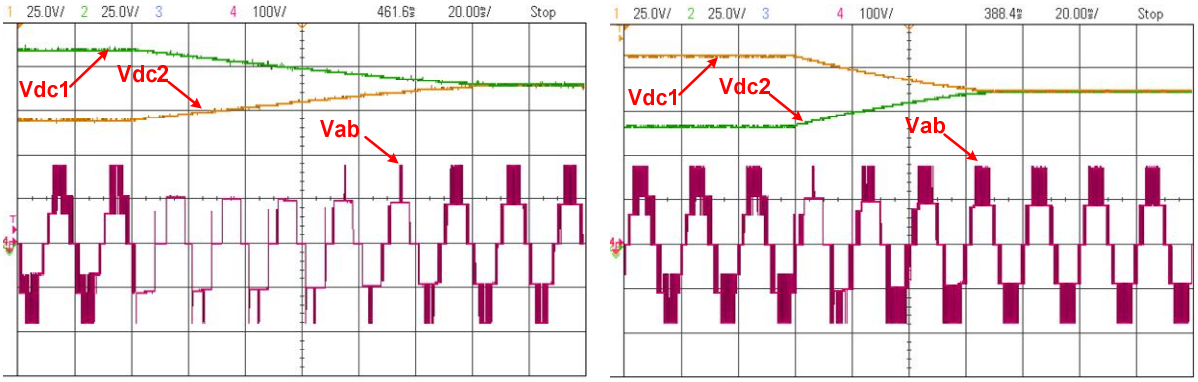

(a) (b)

Fig.6.18. Experimental results for dynamic performance of capacitor voltage balancing (a) MPDPC (b) PSI-W-CMPC.

6.6 Summary

In this chapter, a PSI-based centralised model predictive decoupled active–reactive power control for a single-stage grid-tied 3L-NPC PV inverter is proposed and demonstrated by using lab-scale experimental setup. The proposed CMPC approach incorporates the DC-link voltage regulation constraint into the objective function with a dynamic reference generation approach. A decoupled active-reactive power control is used to eliminate the impact of reactive power exchange on the maximum power tracking. In addition, a PSI-based objective prioritisation approach is introduced to dynamically select the weighting factors. This PSI method determines the weighting factor based on a descriptive statistical approach in each sampling period, as a result, an improved steady-state and dynamic tracking performance is achieved. From the results, it can be observed that the proposed control approach has eliminated the cascading structure and regulated the DC-link voltage to its reference without any effect of reactive power exchange. The steady state and dynamic tracking performance of each control objective have improved with the dynamic selection of weighting factors.

Chapter-7
Conclusions and Future Scope

7.1 Overview and summary of results

By considering the control capabilities and the merits of FCS-MPC, an investigation on multi-objective model predictive control of single-stage grid tied solar photovoltaic system is presented in this research work. Selection of weighting factors in the objective function is the only parameter to be tuned in the multi-objective model predictive control which has direct impact on system performance. Further, despite of the multi-objective control capability of FCS-MPC, the control of single-stage grid-tied solar photovoltaic inverter has cascaded control structure which includes a classical linear PI controller to regulate the outer DC-link voltage of the inverter. The outer DC-link voltage has to be regulated to its reference obtained from the MPPT algorithm to extract the maximum power from the PV array. The dynamics of this DC-link voltage controller influences the overall system performance. Hence, in order to address these limitations new control strategies are proposed in this research work. The details of contributions are as follows:

1. Initially, a direct optimization method based on selective finite-states is introduced to simplify the prioritization between the equally important objectives of current tracking and DC-link capacitor voltage balancing in single-stage grid tied 3L-NPC PV inverter. In this approach, the DC-link capacitor voltage balancing is inherently achieved by the selective switching states defined based on position of reference voltage vector in space vector plane, charge status of DC-link capacitors and direction of inverter phase current. As a result, the selection of optimal switching state to track the reference current is simplified, efforts required to select the weighting factor is eliminated and due to the limited number of switching states the computational burden on the processor is reduced. In addition to these, the proposed FS-MPC has retained the steady-state tracking and dynamic response of the system.

   The proposed selective FS-MPC scheme for a 3L-NPC inverter based SPECS is experimentally verified. From the results, it is observed that the capacitor voltage balancing has been achieved inherently, indeed has eliminated the weighting factor selection issue for equally important control objectives. The overall computation time required for the real-time implementation is reduced by 34.4% in comparison with the classical MPCC and 88.89% for each objective which validates the significant reduction in computational burden on the processor. The %THD of the injecting currents is 3.52% which is well below the IEEE Std. 1547 which is comparable with MPCC approach.

Despite of selective FS-MPC merits, the complexity in selection of weighting factors for secondary control objectives are still exists. Due to the availability of limited switching states, the inclusion of secondary control objectives in the objective function doesn't meet required operating conditions. Further, the FS-MPC also uses a PI controller to regulate the floating DC-link of the inverter which influences the dynamics of the system performance. In order to overcome these problems, two generic methods for selection of dynamic weighting factors along with the CMPC approach to regulate the outer DC-link voltage of the inverter are proposed.

2. A CRITIC based objective prioritization approach for dynamic selection of weighting factors in the objective function of FCS-MPC is proposed. CRITIC is an well established objective prioritization approach of MCDM methods which establishes a quantitative relation between various individual criteria's by using a multivariate descriptive statistical analysis of objective errors. The evaluation of multiple objectives in the objective function of FCS-MPC is framed as a multi-objective decision making problem, where the switching states are considered as the control alternatives and control objectives as the criteria's. The detailed steps to determine the dynamic weights of the objectives are presented.

   Further, a centralized model predictive control (CMPC) approach is presented to regulate the floating DC-link of the inverter without using any additional controller or control loop. The CMPC approach utilizes the model of the system to determine the dynamic reference power based on gradual approaching manner. The dynamic reference power includes the power required to regulate the charge of DC-link in addition to the maximum power which is required to be injected into the grid. Thus the proposed CMPC eliminates the cascaded structure and includes the DC-link voltage regulation into the power reference in the objective function.

3. A PSI based objective prioritization approach for dynamic selection of weighting factors in the objective function of FCS-MPC is proposed. PSI is also a popular objective prioritization approach of MCDM methods. However, in contrast to the general objective prioritization methods the PSI approach does not require relative significance between various criteria's. Hence, this approach is more popular in the cases where there is a conflict in obtaining the correlation among the criteria's. The control objectives of single-stage grid tied 3L-NPC inverter are active-reactive power tracking,

DC-link capacitor voltage balancing and CMV reduction. Obtaining a correlation between these objectives are difficult hence, PSI approach is preferred to prioritise these objectives. Similar to the previous approach, the switching states are considered as the control alternatives and control objectives as the criteria's. The detailed steps to determine the dynamic weights of the objectives are presented.

The CRITC and PSI weighting approaches along with the CMPC approach is implemented on a laboratory scale experimental setup. The results are compared with the classical PI based MPDPC, where the weighting factors are selected based on the empirical approach. Comparative results between the objective weighting methods are summarised in the Table.7.1.

Table.7.1. Performance comparison of objective weighting methods

Operating condition	Performance Indices	PI-MPDPC		CRITIC-W-CMPC		PSI-W-CMPC	
		Sim.	Exp.	Sim.	Exp.	Sim.	Exp.
P_{inj} = 480 Watts Q_{inj} = 0 Var	ΔP	35.17	35.39	18.67	20.21	20.84	24.01
	ΔQ	12.76	19.20	9.24	12.03	9.73	13.11
	%THD of i_g	8.48	8.9	5.12	5.46	5.24	5.93
P_{inj} = 1200Watts Q_{inj} = 0 Var	ΔP	44.16	61.22	24.42	34.78	28.73	40.92
	ΔQ	13.75	34.10	12.46	23.38	11.00	26.33
	%THD of i_g	3.50	4.59	2.08	2.69	2.91	3.70
P_{inj} = 960 Watts Q_{inj} = -720 Var	ΔP	48.15	64.95	16.23	33.02	18.72	38.43
	ΔQ	25.23	52.86	17.26	30.81	19.13	35.83
	%THD of i_g	3.24	4.84	2.6	3.16	2.97	3.68
P_{inj} = 960 Watts Q_{inj} = 720 Var	ΔP	38.53	59.32	15.97	34.14	17.70	40.10
	ΔQ	19.70	50.11	14.72	32.93	15.96	35.97
	%THD of i_g	3.19	3.91	2.24	2.51	2.46	2.96

7.2 Conclusion

In this research work, alternative techniques based on direct optimisation and dynamic objective prioritisation approaches based on MCDM methods are proposed for simplifying the selection of weighting factors in the objective function of multi-objective FCS-MPC. The proposed techniques are namely: selective FS-MPC under direct optimisation, CRITIC and PSI based objective prioritisation approaches under MCDM methods. All the proposed techniques eliminate the heuristic offline selection of weighting factors. The detailed mathematical modelling, implementation steps, simulation results and experimental results are presented for both the conventional and proposed techniques in the corresponding chapters. All the proposed techniques offer an improved objective tracking and comparative

dynamic response with respect to the classical approaches.

7.3 Future Scope

- Multi-vector approach with switching instant optimization techniques can be implemented along with the proposed techniques for further improving the performance of multi-objective model predictive control of grid tied inverters.
- Fixed switching frequency implementation for multi-objective model predictive control of grid-tied inverters.

Appendix

Appendix

- **Euler's Discretization**

The real-time implementation of FCS-MPC technique requires conversion of continuous time model of the system to a discrete-time model of the system. This process is usually known as discretization. The discretization of first order state equation by using the forward Euler's discretization is given as follows

$$\frac{d\vec{x}(t)}{dt} \approx \frac{\vec{x}_{k+1} - \vec{x}_k}{T_s} \tag{A.1}$$

Where, $\vec{x}$ is the state variable, T_s is the sampling period and k is the sampling instant.

- **Clark's transformation**

Coordinate transformation of three-phase stationary *abc* – reference frame to stationary $\alpha\beta$ - orthogonal reference frame is shown in Fig A.1. The transformation can be done by using the following relation

$$\begin{bmatrix} x_\alpha \\ x_\beta \end{bmatrix} = \Gamma \begin{bmatrix} x_a \\ x_b \\ x_c \end{bmatrix} \tag{A.2}$$

Where, 'Γ' is the conversion matrix $\Gamma = \sqrt{\frac{2}{3}} \begin{bmatrix} 1 & -\frac{1}{2} & -\frac{1}{2} \\ 0 & \frac{\sqrt{3}}{2} & -\frac{\sqrt{3}}{2} \end{bmatrix}$

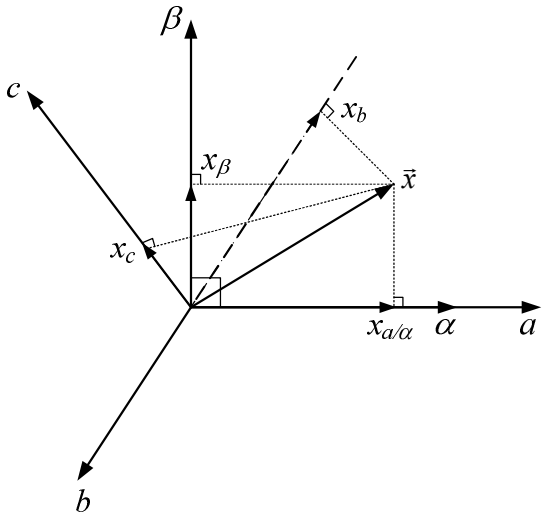

Fig.A.1 Three phase to stationary orthogonal transformation

- **Park's transformation**

Coordinate transformation of three-phase stationary *abc* – reference frame to *dq* – synchronous reference frame is shown in Fig A.2. The transformation can be done by using the following relation

$$\begin{bmatrix} x_d \\ x_q \end{bmatrix} = \hat{\Gamma} \begin{bmatrix} x_a \\ x_b \\ x_c \end{bmatrix} \tag{A.3}$$

Where, '$\hat{\Gamma}\,P$' is the conversion matrix

$$\mathrm{P} = \sqrt{\frac{2}{3}} \begin{bmatrix} \cos(\theta) & \cos\left(\theta - \frac{2\pi}{3}\right) & \cos\left(\theta + \frac{2\pi}{3}\right) \\ \sin(\theta) & \sin\left(\theta - \frac{2\pi}{3}\right) & \sin\left(\theta + \frac{2\pi}{3}\right) \end{bmatrix}$$

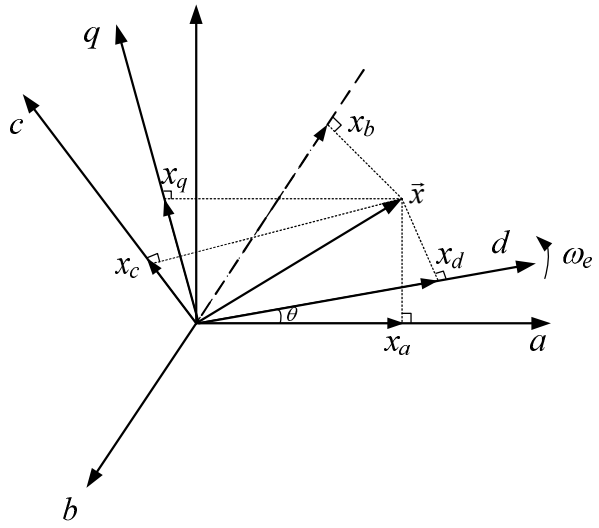

Fig.A.2 Three-phase to rotating reference frame

- **Voltage oriented control (VOC)**

VOC is one of the popular techniques used for the control of grid tied inverters. This control algorithm is designed in the synchronous reference frame with grid-voltage as the reference. The design of VOC includes the dynamics of grid side circuit as given below

$$\frac{d\vec{i}_{dg}(t)}{dt} = \frac{1}{L_f}\left(\vec{v}_{dg}(t) - \vec{v}_{di}(t) + \omega L_f i_{qg}\right) \tag{A.4a}$$

$$\frac{d\vec{i}_{qg}(t)}{dt}=\frac{1}{L_f}\left(\vec{v}_{qg}(t)-\vec{v}_{qi}(t)-\omega L_f i_{dg}\right) \tag{A.4b}$$

Where, ω is the angular frequency of the grid.

Form the above Eq. (A.4), it can be observed that, derivative of *d*-axis current is related to *d*-axis and q-axis components, and similarly for the *q*-axis current. Hence, the above system is said to be cross coupled and leads to the unsatisfactory performance during dynamic operating conditions. To avoid this problem a decoupled controller can be implemented as shown in Fig. A.3.

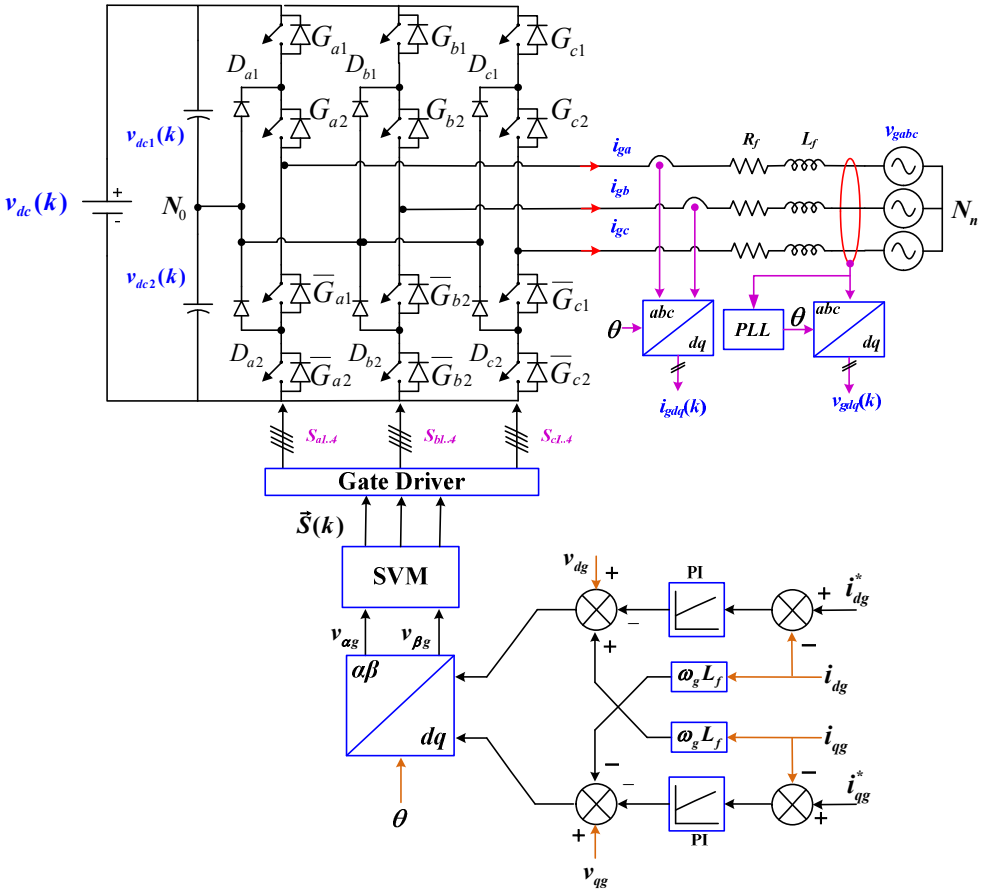

Fig.A.3 Schematic of 3L-NPC inverter with VOC with decoupled control

The outputs of the PI controllers are expressed as follows,

$$v_{di}=-\left(k_p+k_i/S\right)\left(i^*_{dg}-i_{dg}\right)+\omega L_f i_{qg}+v_{dg} \tag{A.5a}$$

$$v_{qi}=-\left(k_p+k_i/S\right)\left(i^*_{qg}-i_{qg}\right)-\omega L_f i_{dg}+v_{qg} \tag{A.5b}$$

Where, k_p+k_i/S is the transfer function of PI controller.

By substituting Eq. (A.5) in Eq. (A.4) yields

$$\frac{di_{dg}}{dt} = \left(k_p + k_i / S\right)\left(i_{dg}^{*} - i_{dg}\right)\Big/ L_f \tag{A.6a}$$

$$\frac{di_{qg}}{dt} = \left(k_p + k_i / S\right)\left(i_{qg}^{*} - i_{qg}\right)\Big/ L_f \tag{A.6b}$$

The above equations confirm the decoupled control of both currents.

- **Lookup table based direct power control**

This section presents the lookup table based direct power control (DPC) approach for grid-tied 3L-NPC inverter. By using the nonlinear hysteresis controllers along with predefined switching table, instantaneous active and reactive powers of grid-tied 3L-NPC inverter can be controlled. In addition to the active and reactive power the DC-link capacitor voltage are also balanced with LUT-DPC. In this approach, active and reactive powers are estimated based on the measured grid quantities. These estimated quantities are compared with corresponding reference values. The error terms of powers and difference in DC-link capacitor voltages are given to hysteresis controllers. The responses from the hysteresis controllers are given to a predefined switching table. Based upon these responses and location of the voltage vector in complex plane, a suitable switching state will be selected.

The implementation diagram for is shown in Fig. A.1. The grid side three phase quantities i_{gx} and v_{gx} for $x \in \{a, b, c\}$ in *a-b-c* reference frame are transformed to stationary orthogonal α-β reference frame quantities $i_{g\alpha\beta}$ and $v_{g\alpha\beta}$ by using a Clarke's transformation matrix 'Γ'.

The instantaneous active and reactive powers can be obtained as

$$P_g = Re\left(1.5 v_{g\alpha\beta} * i_{g\alpha\beta}^{*}\right) \tag{A.7a}$$

$$Q_g = \mathrm{Im}\left(1.5 v_{g\alpha\beta} * i_{g\alpha\beta}^{*}\right) \tag{A.7b}$$

The hysteresis controller outputs for active power, reactive power and DC-link voltages are as follows

$$H_P = \begin{cases} 1, & \Delta P \in (B_P, \infty) \\ 0, & \Delta P \in (0, B_P) \\ -1, & \Delta P \in (-\infty, 0) \end{cases} \tag{A.8}$$

$$H_Q = \begin{cases} 2, & \Delta Q \in (B_Q, \infty) \\ 1, & \Delta Q \in (0, B_Q) \\ -1, & \Delta Q \in (-B_Q, 0) \\ -2, & \Delta Q \in (-\infty, -B_Q) \end{cases} \tag{A.9}$$

$$H_{V_{dc}} = \begin{cases} 1, & \Delta V_{dc} \in (B_{V_{dc}}, \infty) \\ -1, & \Delta Q \in (-\infty, -B_{V_{dc}}) \end{cases} \tag{A.10}$$

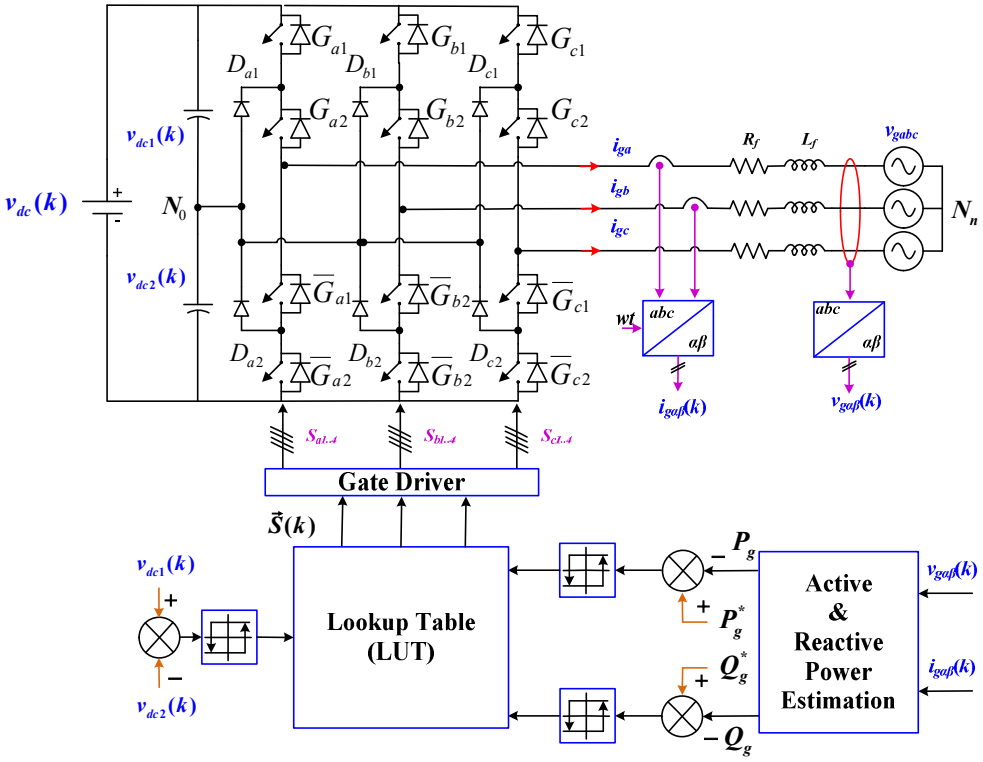

Fig.A.4 Schematic of 3L-NPC inverter with LUT-DPC with decoupled control

The location of the voltage vector can be obtained as

$$\theta_g = \text{arc2tan}\left(\frac{v_{g\alpha}}{v_{g\beta}}\right) \tag{A.11}$$

$$(n-1).\frac{\pi}{6} \le \theta_g \le n.\frac{\pi}{6},\ n \in \{1,2,3,\ldots 12\}$$

Where, *n* is the sector number.

The predefined switching table for the selection of switching state is given in Table A.1

Table A.1 Switching table for LUT-DPC

H_P	H_Q	H_{Vdc}	Sector number											
			1	2	3	4	5	6	7	8	9	10	11	12
1	2	-1	NON	NPO	OPP	NOP	NNO	ONP	POP	PNO	ONN	PON	PPO	OPN
		1	OPO	NPO	NOO	NOP	OOP	ONP	ONO	PNO	POO	PON	ONN	OPN
	1	-1	OPP	OPP	NNO	NNO	POP	POP	ONN	ONN	PPO	PPO	NON	NON
		1	NOO	NOO	OOP	OOP	ONO	POP	POO	POO	OON	OON	OPO	OPO
	-1	-1	NNO	POP	POP	ONN	ONN	PPO	PPO	NON	NON	OPP	OPP	NNO
		1	OOP	ONO	ONO	POO	POO	ONN	ONN	OPO	OPO	NOO	NOO	OOP
	-2	-1	NNP	PNP	PNP	PNN	PNN	PPN	PPN	NPN	NPN	NPP	NPP	NNP
		1	NNP	PNP	PNP	PNN	PNN	PPN	PPN	NPN	NPN	NPP	NPP	NNP
0	2	-1	OPN	NPN	NPO	NPP	NOP	NNP	ONP	PNP	PNO	PNN	PON	PPN
		1	OPN	NPN	NPO	NPP	NOP	NNP	ONP	PNP	PNO	PNN	PON	PPN
	1	-1	PPO	PPO	NON	NON	OPP	OPP	NNO	NNO	POP	POP	ONN	ONN
		1	OON	OON	OPO	OPO	NOO	NOO	OOP	OOP	ONO	ONO	POO	POO
	-1	-1	ONN	ONN	PPO	PPO	NON	NON	OPP	OPP	NNO	NNO	POP	POP
		1	POO	POO	ONN	OON	OPO	OPO	NOO	NOO	OOP	OOP	ONO	ONO
	-2	-1	PNP	PNP	PNN	PNN	PPN	PPN	NPN	NPN	NPP	NPP	NNP	NNP
		1	PNP	PNP	PNN	PNN	PPN	PPN	NPN	NPN	NPP	NPP	NNP	NNP
-1	2	-1	PON	PPN	OPN	NPN	NPO	NPP	NOP	NNP	ONP	PNP	PNO	PNN
		1	PON	PPN	OPN	NPN	NPO	NPP	NOP	NNP	ONP	PNP	PNO	PNN
	1	-1	PON	PPN	OPN	NPN	NPO	NPP	NOP	NNP	ONP	PNP	PNO	PNN
		1	PON	PPN	OPN	NPN	NPO	NPP	NOP	NNP	ONP	PNP	PNO	PNN
	-1	-1	PNN	PON	PPN	OPN	NPN	NPO	NPP	NOP	NNP	ONP	PNP	PNO
		1	PNN	PON	PPN	OPN	NPN	NPO	NPP	NOP	NNP	ONP	PNP	PNO
	-2	-1	PNN	PON	PPN	OPN	NPN	NPO	NPP	NOP	NNP	ONP	PNP	PNO
		1	PNN	PON	PPN	OPN	NPN	NPO	NPP	NOP	NNP	ONP	PNP	PNO

- **System design**

Sl. No	Parameter	Calculation
1	Minimum DC-link Voltage	$V_{dc\_\min} = \frac{2\sqrt{2}V_{L-L}}{\sqrt{3}m_{mi}} = \frac{2\sqrt{2}*85}{\sqrt{3}*0.92} = 150.085\ V$
2	DC-link Capacitance	$C_{eff} = \frac{2K_S S_{rated} T_{trans}}{\left(V_{dc,\max}^2 - V_{dc,\min}^2\right)} = \frac{2*0.6*1200*0.02}{\left(180^2 - 140^2\right)} = 2250\mu F$ $C_1 = C_2 = 2C_{eff} = 4500\mu F$
3	Interfacing filter inductor	$L_f = \frac{\sqrt{3}m_{mi}V_{dc}}{12af_{sm}\Delta i_{rp}} = \frac{\sqrt{3}*0.92*180}{12*1.5*5000*0.1} = 3.18mH$
4	Proportional controller gain	$k_p = \frac{C_{dc}}{a2T_{i\sigma}} = \frac{4700\mu F}{0.9*2*0.0058} = 0.45$

References

[1] "Trends in photovoltaic applications 2018," *IEA (International Energy Agency)*, pp. 1–88, 2018.

[2] Y.-K. Wu, J.-H. Lin, and H.-J. Lin, "Standards and Guidelines for Grid-Connected Photovoltaic Generation Systems: A Review and Comparison," *IEEE Trans. Ind. Appl.*, vol. 53, no. 4, pp. 3205–3216, 2017.

[3] J. M. Carrasco, L. G. Franquelo, J. T. Bialasiewicz, E. Galván, R. C. P. Guisado, M. Ángeles, M. Prats, J. I. León, and N. Moreno-alfonso, "Power-Electronic Systems for the Grid Integration of Renewable Energy Sources : A Survey," *IEEE Trans. Ind. Electron.*, vol. 53, no. 4, pp. 1002–1016, 2006.

[4] H. A. Rub, M. Malinowski, and A. Kamal, *Power electronics for renewable energy systems, transportation and industrial applications*. Wiley, United Kingdom, 2014.

[5] T. Kerekes, D. Sera, and L. Mathe, "Three-phase photovoltaic systems : structures , topologies , and control," *Electr. Power Components Syst.*, no. July, pp. 1364–1375, 2015.

[6] E. Romero-cadaval, G. Spagnuolo, L. G. Franquelo, C.-A. Ramos-Paja, T. Suntio, and W.-M. Xiao, "Grid-connected photovoltaic generation plants components and operation," *IEEE Ind. Electron. Mag.*, vol. 7, no. 3, pp. 6–20, Sep. 2013.

[7] S. Kouro, J. I. Leon, D. Vinnikov, and L. G. Franquelo, "Grid-connected photovoltaic systems an overview of recent research and emerging PV converter technology," *IEEE Ind. Electron. Mag.*, vol. 9, no. 1, pp. 47–61, Mar. 2015.

[8] K. Zeb, W. Uddin, M. Adil, Z. Ali, M. Umair, N. Christo, and H. J. Kim, "A comprehensive review on inverter topologies and control strategies for grid connected photovoltaic system," *Renew. Sustain. Energy Rev.*, vol. 94, no. November 2017, pp. 1120–1141, 2018.

[9] Z. Ozkan and A. M. Hava, "Three-phase inverter topologies for grid-connected photovoltaic systems," in *2014 International Power Electronics Conference (IPEC-Hiroshima 2014 - ECCE ASIA)*, 2014, pp. 498–505.

[10] J. A. Anderson, L. Schrittwieser, M. Leibl, and J. W. Kolar, "Multi-Level Topology Evaluation for Ultra-Efficient Three-Phase Inverters," in *2017 IEEE International Telecommunications Energy Conference (INTELEC)*, 2017, pp. 456–463.

[11] T. Kheng, S. Freddy, N. A. Rahim, W. Hew, and H. S. Che, "Comparison and analysis of single-phase transformerless grid-connected PV inverters," *IEEE Trans. Power Electron.*, vol. 29, no. 10, pp. 5358–5369, 2014.

[12] W. Li, Y. Gu, H. Luo, W. Cui, X. He, and C. Xia, "Topology review and derivation methodology of single phase transformerless photovoltaic inverters for leakage current suppresion," *IEEE Trans. Ind. Electron.*, vol. 62, no. 7, pp. 4537–4551, 2015.

[13] L. Zhang, K. Sun, L. Feng, H. Wu, and Y. Xing, "A family of neutral point clamped full-bridge topologies for transformerless photovoltaic grid-tied inverters," *IEEE Trans. Power Electron.*, vol. 28, no. 2, pp. 730–739, Feb. 2013.

[14] S. Ray, N. Gupta, and R. A. Gupta, "A comprehensive review on cascaded h-bridge inverter-based large-scale grid-connected photovoltaic," *IETE Tech. Rev.*, vol. 34, no. 5, pp. 463–477, 2017.

[15] R. Islam, Mahfuz-ur-rahman, kashem M. Muttaqi, and D. Sutanto, "State of the art of the medium - voltage power converter technologies for grid integration of solar photovoltaic power plants," *IEEE Trans. Energy Convers.*, vol. 34, no. 1, pp. 372–384, 2018.

[16] K. Alluhaybi, I. Batarseh, H. Hu, and X. Chen, "Comprehensive review and comparison of single-phase grid-tied photovoltaic microinverters," *IEEE J. Emerg. Sel. Top. Power Electron.*, vol. PP, no. d, p. 1, 2019.

[17] Q. Li and P. Wolfs, "A review of the single phase photovoltaic module integrated converter topologies with three different DC link configurations," *IEEE Trans. Power Electron.*, vol. 23, no. 3, pp. 1320–1333, 2008.

[18] T. J. Liang, Y. C. Kuo, and J. F. Chen, "Single-stage photovoltaic energy conversion system," *IEE Proc. - Electr. Power Appliications*, vol. 148, no. 4, pp. 339–344, 2001.

[19] H. Ghoddami and A. Yazdani, "A single-stage three-phase photovoltaic system with enhanced maximum power point tracking capability and increased power rating," *IEEE Trans. Power Deliv.*, vol. 26, no. 2, pp. 1017–1029, 2011.

[20] V. N. Lal and S. N. Singh, "Control and performance analysis of a single-stage utility-scale grid-connected PV system," *IEEE Syst. J.*, vol. 11, no. 3, pp. 1601–1611, 2015.

[21] R. A. Mastromauro, M. Liserre, and A. Dell'Aquila, "Control issues in single-stage photovoltaic systems: MPPT, current and voltage control," *IEEE Trans. Ind. Informatics*, vol. 8, no. 2, pp. 241–254, 2012.

[22] L. Hassaine, E. Olias, J. Quintero, and V. Salas, "Overview of power inverter topologies and control structures for grid connected photovoltaic systems," *Renew. Sustain. Energy Rev.*, vol. 30, pp. 796–807, 2014.

[23] M. Barghi Latran and A. Teke, "Investigation of Multilevel Multifunctional Grid Connected Inverter Topologies and Control Strategies Used in Photovoltaic Systems," *Renew. Sustain. Energy Rev.*, vol. 42, pp. 361–376, 2015.

[24] A. Sinha, K. C. Jana, and M. K. Das, "An inclusive review on different multi-level inverter topologies , their modulation and control strategies for a grid connected photo-voltaic system," *Sol. Energy*, vol. 170, no. May, pp. 633–657, 2018.

[25] J. Leon, S. Kouro, L. Franquelo, J. Rodriguez, and B. Wu, "The Essential Role and the Continuous Evolution of Modulation Techniques for Voltage Source Inverters in Past, Present and Future Power Electronics," *IEEE Trans. Ind. Electron.*, vol. Early Acce, no. 5, pp. 2688–2701, 2016.

[26] V. Yaramasu, "Predictive control of multilevel converters for megawatt wind energy conversion systems," Ryerson University, 2016.

[27] M. P. Kazmierkowski and L. Malesani, "Current control techniques for three-phase voltage-source PWM converters: a survey," *IEEE Trans. Ind. Electron.*, vol. 45, no. 5, pp. 691–703, 1998.

[28] L. Malesani, P. Mattavelli, and S. Buso, "Robust dead-beat current control for PWM rectifiers and active filters," *IEEE Trans. Ind. Appl.*, vol. 35, no. 3, pp. 613–620, 1999.

[29] E. Pouresmaeil, D. Montesinos-miracle, and O. Gomis-bellmunt, "Control scheme of three-level NPC inverter for integration of renewable energy resources into AC grid," *IEEE Syst. J.*, vol. 6, no. 2, pp. 242–253, 2012.

[30] W. Chen and J. Lin, "One-dimensional optimization for proportional-resonant controller design against the change in source impedance and solar irradiation in PV systems," *IEEE Trans. Ind. Electron.*, vol. 61, no. 4, pp. 1845–1854, 2014.

[31] R. Davoodnezhad, D. G. Holmes, and B. P. Mcgrath, "A Novel Three-Level Hysteresis Current Regulation Strategy for Three-Phase Three-Level Inverters," *IEEE Trans. Power Electron.*, vol. 29, no. 11, pp. 6100–6109, 2014.

[32] L. Liu, H. Li, Y. Xue, and W. Liu, "Reactive power compensation and optimization strategy for grid-interactive cascaded photovoltaic systems," *IEEE Trans. Power Electron.*, vol. 30, no. 1, pp. 188–202, 2015.

[33] Z. Zhang, F. Wang, and T. Sun, "FPGA Based Experimental Investigation of a Quasi-Centralized Model Predictive Control for Back-to-Back Converters," *IEEE Trans. Power Electron.*, vol. 31, no. 1, pp. 662–674, 2015.

[34] M. Rezkallah, A. Hamadi, A. Chandra, and B. Singh, "Real-time HIL implementation of sliding mode control for standalone system based on PV array without using dumpload," *IEEE Trans. Sustain. Energy*, vol. 6, no. 4, pp. 1389–1398, 2015.

[35] S. Adhikari, F. Li, and H. Li, "P-Q and P-V Control of Photovoltaic Generators in Distribution Systems," *IEEE Trans. Smart Grid*, vol. 6, no. 6, pp. 2929–2941, 2015.

[36] R. K. Agarwal, I. Hussain, and B. Singh, "LMF-based control algorithm for single stage three-phase grid integrated solar PV system," *IEEE Trans. Sustain. Energy*, vol. 7, no. 4, pp. 1379–1387, Oct. 2016.

[37] M. Mirhosseini, J. Pou, B. Karanayil, and V. G. Agelidis, "Resonant versus conventional controllers in grid-connected photovoltaic power plants under unbalanced grid voltages," *IEEE Trans. Sustain. Energy*, vol. 7, no. 3, pp. 1124–1132, 2016.

[38] L. Liu, H. Li, Y. Xue, and W. Liu, "Decoupled active and reactive power control for large-scale grid-connected photovoltaic systems using cascaded modular multilevel converters," *IEEE Trans. Power Electron.*, vol. 30, no. 1, pp. 176–187, 2015.

[39] F. Blaabjerg, R. Teodorescu, M. Liserre, and A. V Timbus, "Overview of control and grid synchronization for distributed power generation systems," *IEEE Trans. Ind. Electron.*, vol. 53, no. 5, pp. 1398–1409, 2006.

[40] F. Sebaaly, H. Vahedi, H. Y. Kanann, N. Moubayed, and A. Kamal, "Sliding mode fixed frequency current controller design for grid-connected NPC inverter," *IEEE J. Emerg. Sel. Top. Power Electron.*, vol. 4, no. 4, pp. 1397–1405, 2016.

[41] N. Kumar, T. K. Saha, and J. Dey, "Sliding-mode control of PWM dual inverter-based grid-connected PV system: modeling and performance analysis," *IEEE J. Emerg. Sel. Top. Power Electron.*, vol. 04, no. 2, pp. 435–444, 2016.

[42] L. Bruno, G. Campanhol, and S. Augusto, "Dynamic performance improvement of a grid-tied PV system using a feed-forward control loop acting on the NPC inverter currents," *IEEE Trans. Ind. Electron.*, vol. 64, no. 3, pp. 2092–2101, 2016.

[43] F. Sebaaly, H. Vahedi, H. Y. Kanann, N. Moubayed, and A. Kamal, "Design and implementation of space vector modulation-based sliding mode control for grid-connected 3L-NPC inverter," *IEEE Trans. Ind. Electron.*, vol. 63, no. 12, pp. 7854–7863, 2016.

[44] Y. Yang, F. Blaabjerg, H. Wang, and M. G. Simões, "Power control flexibilities for grid-connected multi-functional photovoltaic inverters," *IET Renew. Power Gener.*, vol. 10, pp. 504–513, 2016.

[45] M. Rezkallah, S. Sharma, A. Chandra, B. Singh, and D. R. Rousse, "Lyapunov Function and Sliding Mode Control Approach for Solar-PV Grid Interface System," *IEEE Trans. Ind. Electron.*, vol. 64, no. 1, pp. 785–795, 2017.

[46] Y. Sun, S. Li, B. Lin, X. Fu, M. Ramezani, and I. Jaithwa, "Artificial neural network for control and grid integration of residential solar photovoltaic systems," *IEEE Trans. Sustain. Energy*, vol. 8, no. 4, pp. 1484–1495, 2017.

[47] N. Mahmud, A. Zahedi, and A. Mahmud, "A cooperative operation of novel PV inverter control scheme and storage energy management system based on ANFIS for voltage regulation of grid-tied PV system," *IEEE Trans. Ind. Informatics*, vol. 13, no. 5, pp. 2657–2668, 2017.

[48] G. Vscs, S. Golestan, E. Ebrahimzadeh, and J. M. Guerrero, "An adaptive resonant Regulator for single-phase grid-tied VSCs," *IEEE Trans. Power Electron.*, vol. 33, no. 3, pp. 1867–1873, 2018.

[49] C. A. Busada, S. G. Jorge, and J. A. Solsona, "Resonant current controller with enhanced transient response for grid-tied inverters," *IEEE Trans. Ind. Electron.*, vol. 65, no. 4, pp. 2935–2944, 2018.

[50] M. Castilla, J. Miret, J. Matas, L. G. De Vicuña, and J. M. Guerrero, "Linear current control scheme with series resonant harmonic compensator for single-phase grid-connected photovoltaic inverters," *IEEE Trans. Ind. Electron.*, vol. 55, no. 7, pp. 2724–2733, 2008.

[51] N. Kumar, B. Singh, and B. K. Panigrahi, "Framework of gradient descent least squares regression based NN structure for power quality improvement in PV integrated low-voltage weak grid system," *IEEE Trans. Ind. Electron.*, vol. PP, no. c, p. 1, 2018.

[52] B. I. N. Guo, M. E. I. Su, Y. A. O. Sun, and H. U. I. Wang, "A robust second-order sliding mode control for single-phase photovoltaic grid-connected voltage source inverter," *IEEE Access*, vol. 7, pp. 53202–53212, 2019.

[53] B. Karanayil, S. Member, S. Ceballos, and J. Pou, "Maximum power point controller for large scale photovoltaic power plants using central inverters under partial shading conditions," *IEEE Trans. Power Electron.*, vol. 34, no. 4, pp. 3098–3109, 2019.

[54] R. Chilipi, N. Al Sayari, and J. Alsawalhi, "Control of single-phase solar power generation system with universal active power filter capabilities using least mean mixed-norm (LMMN)-based adaptive filtering method," *IEEE Trans. Sustain. Energy*, pp. 1–14, 2019.

[55] N. Kumar, B. Singh, and B. K. Panigrahi, "PNKLMF based neural network control and learning based HC MPPT technique for multi-objective grid integrated solar PV based distributed generating system," *IEEE Trans. Ind. Informatics*, vol. PP, no. c, p. 1, 2019.

[56] S. Benhalima, A. Chandra, and M. Rezkallah, "Real-time experimental implementation of an LMS-adaline-based ANFIS controller to drive PV interfacing power system," *IET Renew. Power Gener.*, vol. 13, no. 7, pp. 1142–1152, 2019.

[57] X. Huang, K. Wang, and B. Fan, "Robust current control of grid-tied inverters for renewable energy integration under non-ideal grid conditions," *IEEE Trans. Sustain. Energy*, p. PP, 2019.

[58] A. Timbus, M. Liserre, R. Teodorescu, P. Rodriguez, and F. Blaabjerg, "Evaluation of current controllers for distributed power generation systems," *Power Electron. IEEE Trans.*, vol. 24, no. 3, pp. 654–664, 2009.

[59] F. Fuchs, J. Dannehl, and F. W. Fuchs, “Discrete sliding mode current control of grid-connected three-phase PWM converters with LCL filter,” in *2010 IEEE International Symposium on Industrial Electronics*, 2010, pp. 779–785.

[60] R. Kadri, J. Gaubert, and G. Champenois, “An improved maximum power point tracking for photovoltaic grid-connected inverter based on voltage-oriented control,” *IEEE Trans. Ind. Electron.*, vol. 58, no. 1, pp. 66–75, 2011.

[61] J. Hu, L. Shang, Y. He, and Z. Q. Zhu, “Direct active and reactive power regulation of grid-connected DC/AC converters using sliding mode control approach,” *IEEE Trans. Power Electron.*, vol. 26, no. 1, pp. 210–222, 2011.

[62] Y. A. I. Mohamed, E. F. El-saadany, and S. Member, “A robust natural-frame-based interfacing scheme for grid-connected distributed generation inverters,” *IEEE Trans. ENergy Convers.*, vol. 26, no. 3, pp. 728–736, 2011.

[63] F. Filho, L. M. Tolbert, Y. Cao, and B. Ozpineci, “Real-time selective harmonic minimization for multilevel inverters connected to solar panels using artificial neural network angle generation,” *IEEE Trans. Ind. Appl.*, vol. 47, no. 5, pp. 2117–2124, 2011.

[64] B. P. Mcgrath and D. G. Holmes, “Multicarrier PWM strategies for multilevel inverters,” *IEEE Trans. Ind. Electron.*, vol. 49, no. 4, pp. 858–867, Aug. 2002.

[65] J. Rodríguez, J. Lai, and F. Z. Peng, “Multilevel inverters: a survey of topologies, controls, and applications,” *IEEE Trans. Ind. Electron.*, vol. 49, no. 4, pp. 724–738, Aug. 2002.

[66] S. Kouro, P. Lezana, M. Angulo, and J. Rodriguez, “Multicarrier PWM with DC-link ripple feedforward compensation for multilevel inverters,” *IEEE Trans. Power Electron.*, vol. 23, no. 1, pp. 52–59, 2008.

[67] J. Rodriguez, leopoldo G. Franquelo, S. Kouro, J. I. Leon, R. C. Portillo, M. A. M. Prats, and M. A. Pérez, “Multilevel converters : an enabling technology for high-power applications,” *Proc. IEEE*, vol. 97, no. 11, pp. 1786–1817, 2009.

[68] H. Abu-rub, J. Holtz, J. Rodriguez, and G. Baoming, “Medium-voltage multilevel converters-state of the art, challenges, and requirements in industrial applications,” *IEEE Trans. Ind. Electron.*, vol. 57, no. 8, pp. 2581–2596, 2010.

[69] A. Shukla, A. Ghosh, and A. Joshi, “Hysteresis modulation of multilevel inverters,” *IEEE Trans. Power Electron.*, vol. 26, no. 5, pp. 1396–1409, 2011.

[70] J. S. Lee and K. B. Lee, “New modulation techniques for a leakage current reduction and a neutral-point voltage balance in transformerless photovoltaic systems using a three-level inverter,” *IEEE Trans. Power Electron.*, vol. 29, no. 4, pp. 1720–1732, Apr. 2014.

[71] U. Choi, F. Blaabjerg, and K. Lee, “Method to minimize the low-frequency neutral-point voltage oscillations with time-offset injection for neutral-point-clamped inverters,” *IEEE Trans. Ind. Appl.*, vol. 51, no. 2, pp. 1678–1691, 2015.

[72] U. Choi, J. Lee, and K. Lee, “New modulation strategy to balance the neutral-point voltage for three-level neutral clamped inverter systems,” *IEEE Trans. Energy Convers.*, vol. 29, no. 1, pp. 91–100, 2014.

[73] J. Shen, S. Schröder, S. Member, B. Duro, and R. Roesner, “A Neutral-Point Balancing Controller for a Three-Level Inverter With Full Power-Factor Range and Low Distortion,” *IEEE Trans. Ind. Appl.*, vol. 49, no. 1, pp. 138–148, 2013.

[74] J. Alonso-martı, J. Eloy-Garcia, and S. Arnaltes, “Direct power control of grid connected PV systems with three level NPC inverter,” *Sol. Energy*, vol. 84, pp. 1175–1186, 2010.

[75] Z. Ben Mahmoud, M. Hamouda, and A. Khedher, “Direct power control with common mode voltage reduction of grid-connected three- level NPC inverter,” *IET Power Electron.*, vol. 12, no. 3, pp. 400–409, 2019.

[76] S. Rivera, S. Kouro, B. Wu, S. Alepuz, M. Malinowski, P. Cortes, and J. Rodriguez, “Multilevel direct power control — a generalized approach for grid-tied multilevel converter applications,” *IEEE Trans. Power Electron.*, vol. 29, no. 10, pp. 5592–5604, 2014.

[77] J. Rodriguez, A. N. A. M. Llor, and H. A. Young, “Model predictive control: MPC’s role in the evolution of power electronics,” *IEEE Ind. Electron. Mag.*, vol. 9, no. December, pp. 8–21, 2015.

[78] J. Rodriguez, M. P. Kazmierkowski, J. R. Espinoza, P. Zanchetta, H. Abu-rub, S. Member, H. A.

Young, and C. A. Rojas, “State of the art of finite control set model predictive control in power electronics,” *IEEE Trans. Ind. Informatics*, vol. 9, no. 2, pp. 1003–1016, 2013.

[79] S. Kouro, P. Cortés, R. Vargas, U. Ammann, and J. Rodríguez, “Model Predictive Control — A Simple and Powerful Method to Control Power Converters,” *IEEE Trans. Ind. Electron.*, vol. 56, no. 6, pp. 1826–1838, Jun. 2009.

[80] C. Bordons and C. Montero, “Basic principles of MPC for power converters: bridging the gap between theory and practice,” *IEEE Ind. Electron. Mag.*, vol. 9, no. september, pp. 31–43, 2015.

[81] D. Bao-Cang, *Modern predictive control*. Baca Raton: CRC, 2009.

[82] J. Richalet, A. Rault, J. L. Testud, and J. Papon, “Model predictive heuristic control : applications to industrial processes *,” *Automatica*, vol. 14, no. 5, pp. 413–428, Sep. 1978.

[83] J. M Maciejowski, “Predictive control with constraints.” Prentice Hall, London, 2002.

[84] R. Kennel and D. Schrooer, “Predictive control strategy for converters,” in *IFAC Control in Power Electronics*, 1983, pp. 415–422.

[85] J. Holtz and S. S, “A predictive controller for the stator current vector of AC machines fed from a switched voltage source,” in *IEEE International Power Electronics Conference*, 1983, pp. 1665–1675.

[86] P. Cortés, M. P. Kazmierkowski, R. M. Kennel, D. E. Quevedo, and J. Rodríguez, “Predictive Control in Power Electronics and Drives,” *IEEE Trans. Ind. Electron.*, vol. 55, no. 12, pp. 4312–4324, Dec. 2008.

[87] J. Rodriguez and P. Cortes, *Predictive Control of Power Converters and Electrical Drives*. United Kingdom: Wiley, United Kingdom, 2012.

[88] C. Bordons and C. Montero, “Basic Principles of MPC for Power Converters: Bridging the Gap between Theory and Practice,” *IEEE Ind. Electron. Mag.*, vol. 9, no. 3, pp. 31–43, 2015.

[89] S. Vazquez, J. I. Leon, L. G. Franquelo, J. Rodriguez, H. A. Young, A. Marquez, and P. Zanchetta, “Model Predictive Control: A Review of Its Applications in Power Electronics,” *IEEE Ind. Electron. Mag.*, vol. 8, no. 1, pp. 16–31, Mar. 2014.

[90] S. Kouro, M. Malinowski, K. Gopakumar, J. Pou, L. G. Franquelo, B. Wu, J. Rodriguez, M. A. Pérez, and J. I. Leon, “Recent advances and industrial applications of multilevel converters,” *IEEE Trans. Ind. Electron.*, vol. 57, no. 8, pp. 2553–2580, 2010.

[91] P. Cortes, S. Kouro, B. La Rocca, R. Vargas, J. Rodriguez, J. I. Leon, S. Vazquez, and L. G. Franquelo, “Guidelines for weighting factors design in Model Predictive Control of power converters and drives,” *2009 IEEE Int. Conf. Ind. Technol.*, pp. 1–7, 2009.

[92] P. Acuna, R. P. Aguilera, A. M. Y. M. Ghias, M. Rivera, C. R. Baier, and V. G. Agelidis, “Cascade-free model predictive control for single-phase grid-connected power converters,” *IEEE Trans. Ind. Electron.*, vol. 64, no. 1, pp. 285–294, 2017.

[93] J. Liu, S. Cheng, Y. Liu, and A. Shen, “FCS-MPC for a single-phase two-stage grid- connected PV inverter,” *IET Power Electron.*, vol. 12, no. 4, pp. 915–922, 2019.

[94] X. Wang, J. Zou, J. Zhao, C. Xie, K. Li, L. Meng, and J. M. Guerrero, “Model predictive control methods of leakage current elimination for a three-level T-type transformerless PV inverter,” *IET Power Electron.*, vol. 11, no. 8, pp. 1492–1498, 2018.

[95] P. Kakosimos and H. Abu Rub, “Predictive control of a grid-tied cascaded full-bridge NPC inverter for reducing high-frequency common-mode voltage components,” *IEEE Trans. Ind. Informatics*, vol. 14, no. 6, pp. 2385–2394, 2018.

[96] C. A. Rojas, M. Aguirre, S. Kouro, T. Geyer, and E. Gutierrez, “Leakage current mitigation in photovoltaic string inverter using predictive control with fixed average switching frequency,” *IEEE Trans. Ind. E*, vol. 64, no. 12, pp. 9344–9354, 2017.

[97] X. Li, H. Zhang, M. B. Shadmand, and R. S. Balog, “Model predictive control of a voltage-source inverter with seamless transition between islanded and grid-connected operations,” *IEEE Trans. Ind. Electron.*, vol. 64, no. 10, pp. 7906–7918, 2017.

[98] M. B. Shadmand, S. Jain, and R. S. Balog, “Autotuning technique for the cost function weight factors in model predictive control for power electronic interfaces,” *IEEE J. Emerg. Sel. Top. Power Electron.*, vol. 7, no. 2, pp. 1408–1420, 2019.

[99] Luis M A Caseiro, A. M. S. Mendes, and S. M. A. Cruz, “Dynamically weighted optimal switching vector model predictive control of power converters,” *IEEE Trans. Ind. Electron.*, vol. 66, no. 2, pp.

1235–1245, 2019.

[100] O. Machado, F. J. Rodriguez, E. J. Bueno, and P. Martin, “A Neural Network-Based Dynamic Cost Function for the Implementation of a Predictive Current Controller,” *IEEE Trans. Ind. Informatics*, vol. 13, no. 6, pp. 2946–2955, 2017.

[101] T. Dragicevic and M. Novak, “Weighting factor design in model predictive control of power electronic converters: an artificial neural network approach,” *IEEE Trans. Ind. Electron.*, vol. PP, no. c, p. 1, 2018.

[102] X. Liu, D. Wang, and Z. Peng, “Cascade-free fuzzy finite-control-set model predictive control for nested neutral point-clamped converters with low switching frequency,” *IEEE Trans. Control Syst. Technol.*, vol. PP, pp. 1–8, 2018.

[103] P. Acuña, L. Morán, M. Rivera, R. Aguilera, R. Burgos, and V. G. Agelidis, “A single-objective predictive control method for a multivariable single-phase three-level NPC converter-based active power filter,” *IEEE Trans. Ind. Electron.*, vol. 62, no. 7, pp. 4598–4607, 2015.

[104] Y. Yang, H. Wen, M. Fan, R. Chen, and M. Xie, “Fast finite-switching-state model predictive control method without weighting factors for T-type three-level three-phase inverters,” *IEEE Trans. Ind. Informatics*, vol. 15, no. 3, pp. 1298–1310, 2019.

[105] Y. Yang, H. Wen, M. Fan, M. Xie, R. Chen, and Y. Wang, “A constant switching frequency model predictive control without weighting factors for T-type single-phase three-level inverters,” *IEEE Trans. Ind. Electron.*, vol. 66, no. 7, pp. 5153–5164, 2019.

[106] S. R. Mohapatra and V. Agarwal, “Model predictive controller with reduced complexity for grid tied multilevel inverters,” *IEEE Trans. Ind. Electron.*, vol. PP, no. c, p. 1, 2018.

[107] J. Wang, Y.-Y. Jing, C.-F. Zhang, and J.-H. Zhao, “Review on multi-criteria decision analysis aid in sustainable energy decision-making,” *Renew. Sustain. Energy Rev.*, vol. 13, no. 9, pp. 2263–2278, Dec. 2009.

[108] N. H. Zardari, K. Ahmed, S. M. Shirazi, and Z. Bin Yusop, *Weighting methods and their effects on multi-criteria decision making model outcomes in water resources management*. London: Springer, 2015.

[109] X. Liu, D. Wang, and Z. Peng, “A computationally efficient FCS-MPC method without weighting factors for NNPCs with optimal duty cycle control,” *IEEE/ASME Trans. Mechatronics*, vol. 23, no. 5, pp. 2503–2514, 2018.

[110] F. Villarroel, J. R. Espinoza, C. A. Rojas, J. Rodriguez, M. Rivera, and D. Sbarbaro, “Multiobjective Switching State Selector for Finite-States Model Predictive Control Based on Fuzzy Decision Making in a Matrix Converter,” *IEEE Trans. Ind. Electron.*, vol. 60, no. 2, pp. 589–599, 2013.

[111] D. E. Quevedo, R. P. Aguilera, A. P. Marcelo, P. Cortés, and R. Lizana, “Model Predictive Control of an AFE Rectifier With Dynamic References,” *IEEE Trans. Power Electron.*, vol. 27, no. 7, pp. 3128–3136, Jul. 2012.

[112] L. Tarisciotti, A. Formentini, A. Gaeta, M. Degano, P. Zanchetta, R. Rabbeni, and M. Pucci, “Model Predictive Control for Shunt Active Filters with Fixed Switching Frequency,” *IEEE Trans. Ind. Appl.*, vol. 53, no. 1, pp. 296–304, 2017.

[113] J. Z. Zhang, T. Sun, F. Wang, J. Rodriguez, and R. Kennel, “A Computationally Efficient Quasi-Centralized DMPC for Back-to-Back Converter PMSG Wind Turbine Systems Without DC-Link Tracking Errors,” *IEEE Trans. Ind. Electron.*, vol. 63, no. 10, pp. 6160–6171, 2016.

[114] J. Rodriguez, S. Bernet, P. K. Steimer, and I. E. Lizama, “A survey on neutral-point-clamped inverters,” *IEEE Trans. Ind. Electron.*, vol. 57, no. 7, pp. 2219–2230, 2010.

[115] R. Vargas, P. Cortés, U. Ammann, J. Rodríguez, and J. Pontt, “Predictive control of a three-phase neutral-point-clamped inverter,” *IEEE Trans. Ind. Electron.*, vol. 54, no. 5, pp. 2697–2705, 2007.

[116] J. Rodríguez, J. Pontt, C. A. Silva, P. Correa, P. Lezana, P. Cortés, and U. Ammann, “Predictive Current Control of a Voltage Source Inverter,” *IEEE Trans. Ind. Electron.*, vol. 54, no. 1, pp. 495–503, 2007.

[117] J. Scoltock, T. Geyer, and U. Madawala, “Model Predictive Direct Power Control for Grid-Connected Neutral-Point-Clamped Converters,” *IEEE Trans. Ind. Electron.*, vol. 62, no. 9, pp. 5319–5328, Mar. 2015.

[118] P. Cortes, J. Rodriguez, C. Silva, and A. Flores, “Delay Compensation in Model Predictive Current

Control of a Three-Phase Inverter," *IEEE Trans. Ind. Electron.*, vol. 59, no. 2, pp. 1323–1325, 2012.

[119] J. Rodriguez and P. Cortes, "Delay Compensation," in *Predictive Control of Power Converters and Electrical Drives*, John Wiley & Sons, Ltd, 2012, pp. 177–189.

[120] V. Yaramasu, M. Rivera, M. Narimani, B. Wu, and J. Rodriguez, "Finite State Model-Based Predictive Current Control with Two-Step Horizin for Four-Leg NPC Converters," *J. Power Electron.*, vol. 14, no. 6, pp. 1178–1181, Nov. 2014.

[121] F. Villarroel, J. R. Espinoza, C. A. Rojas, J. Rodriguez, M. Rivera, and D. Sbárbaro, "Multiobjective switching state selector for finite-states model predictive control based on fuzzy decision making in a matrix converter," *IEEE Trans. Ind. Electron.*, vol. 60, no. 2, pp. 589–599, 2013.

[122] V. Kumar, P. Gaur, and A. P. Mittal, "Finite-state model predictive control of NPC inverter using multi-criteria fuzzy decision-making," *Int. Trans. Electr. Energy Syst.*, vol. 25, no. 5, pp. 876–897, 2014.

[123] V. P. Muddineni, S. R. Sandepudi, and A. K. Bonala, "Improved weighting factor selection for predictive torque control of induction motor drive based on a simple additive weighting method," *Electr. Power Components Syst.*, vol. 45, no. 13, pp. 1450–1462, 2017.

[124] V. P. Muddineni, S. R. Sandepudi, and A. K. Bonala, "Finite control set predictive torque control for induction motor drive with simplified weighting factor selection using TOPSIS method," *IET Electr. Power Appl.*, vol. 11, no. 5, pp. 749–760, 2017.

[125] V. P. Muddineni, A. K. Bonala, and S. R. Sandepudi, "Enhanced weighting factor selection for predictive torque control of induction motor drive based on VIKOR method," *IET Electr. Power Appl.*, vol. 10, no. 9, pp. 877–888, 2016.

[126] N. Mohan, T. M. Undeland, and W. P. Robbins, *Power electronics converters, applications and design*. John Wiley & Sons, Inc., 2003.

[127] T. Messo, J. Jokipii, J. Puukko, and T. Suntio, "Determining the value of DC-link capacitance to ensure stable operation of a three-phase photovoltaic inverter," *IEEE Trans. Power Electron.*, vol. 29, no. 2, pp. 665–673, Feb. 2014.

[128] A. Khoshooei, J. S. Moghani, I. Candela, and P. Rodriguez, "Control of D-STATCOM during unbalanced grid faults based on DC voltage oscillations and peak current limitations," *IEEE Trans. Ind. Appl.*, vol. 54, no. 2, pp. 1680–1690, Mar. 2018.

[129] M. K. Mishra and K. Karthikeyan, "An investigation on design and switching dynamics of a voltage source inverter to compensate unbalanced and nonlinear loads," *IEEE Trans. Ind. Electron.*, vol. 56, no. 8, pp. 2802–2810, Aug. 2009.

[130] R. N. Beres, X. Wang, M. Liserre, F. Blaabjerg, and C. L. Bak, "A review of passive power filters for three-phase grid-connected voltage-source converters," *IEEE J. Emerg. Sel. Top. Power Electron.*, vol. 4, no. 1, pp. 54–69, Mar. 2016.

[131] V. Blasko and V. Kaura, "A new mathematical model and control of a three-phase AC-DC voltage source converter," *IEEE Trans. Power Electron.*, vol. 12, no. 1, pp. 116–123, 1997.

[132] P. Rodriguez, A. V Timbus, R. Teodorescu, M. Liserre, and F. Blaabjerg, "Flexible active power control of distributed power generation systems during grid faults," *IEEE Trans. Ind. Electron.*, vol. 54, no. 5, pp. 2583–2592, 2007.

[133] M. B. Shadmand, X. Li, R. S. Balog, and H. Abu Rub, "Constrained Decoupled Power Predictive Controller for a Single-Phase Grid-Tied Inverter," *IET Renew. Power Gener.*, vol. 11, no. 5, pp. 659–668, 2017.

[134] D. Diakoulaki, G. Mavrotas, and L. Papayannakis, "Determining objective weights in multiple criteria problems: the CRITIC method," *Pergamon*, vol. 22, no. 7, pp. 763–770, 1995.

[135] Y. Wang and Y. Luo, "Integration of correlations with standard deviations for determining attribute weights in multiple attribute decision making," *Math. Comput. Model.*, vol. 51, no. 1–2, pp. 1–12, 2010.

[136] Z. Lin, F. Wen, H. Wang, G. Lin, T. Mo, and X. Ye, "CRITIC-based node importance evaluation in skeleton-network reconfiguration of power grids," *IEEE Trans. Circuits Syst. II Express Briefs*, vol. 65, no. 2, pp. 206–210, 2017.

[137] N. Yalçın and U. Ünlü, "A multi-criteria performance analysis of Initial Public Offering (IPO) firms using CRITIC and VIKOR methods," *Technol. Econ. Dev. Econ.*, vol. 24, no. 2, pp. 534–560, 2017.

[138] mehdi keshavarz Ghorabaee, M. Amiri, E. Z. Kazimieras, and J. Antucheviciene, “Assessment of third-party logistics providers using a CRITIC-WASPAS approach with interval type-2 fuzzy sets,” *Transport*, vol. 32, no. 1, pp. 66–78, 2017.

[139] D. Petković, M. Madić, M. Radovanović, and V. Gečevska, “Application of the performance selection index method for solving machining MCDM problems,” *FACTA Univ.*, vol. 15, no. 1, pp. 97–106, 2017.

[140] B. Vahdani, S. M. Mousavi, and S. Ebrahimnejad, “Soft computing-based preference selection index method for human resource management,” *J. Intell. Fuzzy Syst.*, vol. 26, no. 1, pp. 393–403, 2014.

[141] R. Attri and S. Grover, “Application of preference selection index method for decision making over the design stage of production system life cycle,” *J. King Saud Univ. - Eng. Sci.*, vol. 27, no. 2, pp. 207–216, 2015.

[142] M. Madic, J. Antucheviciene, M. Radovanovic, and D. Petkovic, “Determination of laser cutting process conditions using the preference selection index method,” *Opt. Laser Technol.*, vol. 89, no. March, pp. 214–220, 2017.

[143] O. A. Joseph and R. Sridharan, “Ranking of scheduling rule combinations in a flexible manufacturing system using preference selection index method,” *Int. J. Adv. Oper. Manag.*, vol. 3, no. 2, pp. 201–216, 2011.

[144] K. D. Maniya and M. G. Bhatt, “The selection of flexible manufacturing system using preference selection index method,” *Int. J. Syst. Eng.*, vol. 9, no. 3, pp. 330–349, 2011.

Publications

Journals:

1. **Anil Kumar Bonala**, Srinivasa Rao Sandepudi and Vishnu Prasad Muddineni "Selective finite-states model predictive control of grid interfaced three-level neutral point clamped photovoltaic inverter for inherent capacitor voltage balancing," **IET Power Electronics** 2018, vol. 11, issue 13, pp 2072-2080.
2. **Anil Kumar Bonala**, Srinivasa Rao Sandepudi "Centralised model-predictive decoupled active-reactive power control for three-level neutral point clamped photovoltaic inverter with preference selective index-based objective prioritisation" **IET Power Electronics** 2019, vol. 12, issue 4, pp 840-851.
3. **Anil Kumar Bonala**, Srinivasa Rao Sandepudi "Centralised model-predictive control with CRITIC based objective prioritization for grid interfaced solar photovoltaic inverter" **IEEE Transactions on Industrial Informatics, Status: revision submitted.**

Conferences:

1. **Anil Kumar Bonala**, Srinivasa Rao Sandepudi and Vishnu Prasad Muddineni "Variable Conductance Factor Based Control of Multi-Functional Grid Connected Single Stage Solar PV System" **IEEE ICPEICES-2016**July 4th to 6th 2016.
2. **Anil Kumar Bonala**, Srinivasa Rao Sandepudi and Vishnu Prasad Muddineni "Predictive Current Control with Reduced Neutral Switching for Four-Leg VSI Based Shunt Active Power Filter" **40th National Systems Conference** November 4th to 6th 2016.
3. **Anil Kumar Bonala**, Srinivasa Rao Sandepudi and Vishnu Prasad Muddineni "Model Predictive Current Control with Modified Synchronous Detection Technique for Three-Phase 3L-NPC Multi-Functional Solar Photovoltaic System". **IEEE PEDES 2016** December 14th to 16th 2016.
4. **Anil Kumar Bonala**, Srinivasa Rao Sandepudi and Vishnu Prasad Muddineni "Improved Model Predictive Current Control for Single-Phase NPC Shunt Active Power Filter". **IEEE PEDES 2016** December 14th to 16th 2016.